CARBON NANOTUBE/POLYMER COMPOSITES AND NOVEL MICRO- AND NANO- STRUCTURED ELECTROSPUN POLYMER MATERIALS

A Thesis
Presented to
The Academic Faculty

by

Jing Liu

In Partial Fulfillment
of the Requirements for the Degree
Doctor of Philosophy in the
School of Polymer, Textile & Fiber Engineering

Georgia Institute of Technology
May 2007

CARBON NANOTUBE/POLYMER COMPOSITES AND NOVEL MICRO- AND NANO- STRUCTURED ELECTROSPUN POLYMER MATERIALS

Approved by:

Dr. Satish Kumar, Advisor
School of Polymer, Textile & Fiber Engineering
Georgia Institute of Technology

Dr. Samuel Graham
School of Materials Science & Engineering
Georgia Institute of Technology

Dr. Anselm C. Griffin
School of Polymer, Textile & Fiber Engineering
Georgia Institute of Technology

Dr. Donggang Yao
School of Polymer, Textile & Fiber Engineering
Georgia Institute of Technology

Dr. Wallace W. Carr
School of Polymer, Textile & Fiber Engineering
Georgia Institute of Technology

Date Approved: [December 18, 2006]

ACKNOWLEDGEMENTS

I am very grateful to many people who helped me in this thesis work. First, I would like to express my deepest appreciation to my advisor, Dr. Satish Kumar, for his mentoring on how to work professionally in scientific areas and how to be an independent and successful researcher, for his time in critically reading the drafts of this thesis, for his encouragement and for giving me opportunities to attend academic conferences. He is a great educator. I learned a lot from him, and this will benefit me during the rest of my life. His guidance, support, and friendship made the completion of this research possible. I would like to thank my other committee members, Drs. Wallace W. Carr, Samuel Graham, Anselm C. Griffin, and Donggang Yao for their valuable suggestions and for critical reading of the thesis.

I thank my current and former labmates from whom also I learned a great deal. In particular, thanks to Tong Wang for assistance in electrospinning, to Dr. Chongfu Zhou for surface area measurement, to Marlyin Minus for transmission electron microscopy, to Han Gi Chae for providing assistance with the solubility parameter calculation and for editing the introductry chapter of the thesis, to Dr. Asif Rasheed for critical reading of the entire thesis, to Dr. Tao Liu for helpful discussions on Raman spectroscopy. I am grateful to Professor Wallace W. Carr and Dr. Hongming Dong (Georgia Tech.) for assistance with the high speed photography. I am also grateful to Professor Mark D. Dadmun (University of Tennessee) and Dr. Asif Rasheed for poly (styrene-co-4-vinyl phenol) copolymer synthesis. Finally, I want to thank my friends and family, especially my husband, who has always given me love and support through the course of this research work.

TABLE OF CONTENTS

LIST OF TABLES

LIST OF FIGURES

LIST OF SYMBOLS

δ_p	polar component of the solubility parameter
δ_d	dispersive component of the solubility parameter
δ_h	hydrogen bonding component of the solubility parameter
δ_t	total solubility parameter
G, G', and D	Raman bands of carbon nanotubes
RBM	radial breathing mode
Zylon®	commercial PBO fiber
$(E_{CNT})_{II}$	effective modulus of CNT along the composite fiber axis
E_{11}	longitudinal modulus
E_{22}	transverse modulus
G_{12}	in-plane shear modulus
ν_{12}	poisson's ratio
T_g	glass transition temperature
$(NH_2OH)(HCl)$	hydroxylamine hydrochloric acid salt
$K_2S_2O_8$	potassium persulfate
σ_c	composite conductivity
V	CNT volume fraction
V_c	CNT volume fraction at the percolation threshold
β	the critical exponent
nm	nanometer
μm	micrometer
meV	millielectron volt

kV	kilovolts
S/m	siemens per meter (Unit of conductivity)
E_{laser}	laser excitation energy
E_{ii}	van Hove transition energy
E_{22}^{s}	Semiconductor nanotube second level van Hove transition energy
eV	electron volt
MPa	megapascal
GPa	gigapascal
Pa.s	pascal second (Unit of viscosity)
J/g	joules per gram (Unit of energy)
$\overline{M_w}$	weight average molecular weight
*C*e	entanglement concentration
*C**	chain overlap concentration
η_{sp}	specific viscosity
η_s	solvent viscosity
η	solution viscosity
d_t	diameter of electrospun fiber
E_c	composite modulus
E_m	matrix modulus
l_{NT}	the length of nanotube ropes
d_{NT}	the diameter of nanotube ropes

LIST OF ABBREVIATIONS

CNT	Carbon Nanotube
SWNT	Single Wall Carbon Nanotube
DWNT	Double Wall Carbon Nanotube
MWNT	Multi Wall Carbon Nanotube
VGCNF	Vapor Grown Carbon Nano Fiber
CNF	Carbon Nano Fiber
PMMA	Poly (methyl methacrylate)
iPMMA	isotactic PMMA
aPMMA	atactic PMMA
LMW	low molecular weight
HMW	high molecular weight
PP	Polypropylene
PA6	Polyamide 6
PAN	Polyacrylonitrile
PBO	Poly (p-phenylene benzobisoxazole)
PVA	Poly (vinyl alcohol)
SEM	Scanning Electron Microscopy
TEM	Transmission Electron Microscopy
AFM	Atomic Force Microscopy
TGA	Thermogravimetry Analysis
DSC	Differential Scanning Calorimetry
TMA	Thermal Mechanical Analysis

DMA	Dynamic Mechanical Analysis
UV-vis-NIR	Ultraviolet– visible–Near-Infrared
RBM	Radial Breathing Mode
PVP	Polyvinylpyrrolidone
PS	Polystyrene
PPA	Polyphosphoric acid
AIBN	azobisisobutyronitrile
PVDF	Poly (vinylidene fluoride)
PmPV	Poly (p-phenylenevinylene-co-2,5-dioctyloxy-m- phenylenevinylene)
TGDDM	tetraglycidyldiamino diphenylmethane
DDS	4,4'-diaminodiphenyl sulfone
SDS	sodium dodecyl sulfate
PPO-co-PEO	Poly (propylene oxide)-co-poly(ethylene oxide)
PPO	Poly (propylene oxide)
PEO	Poly (ethylene oxide)
PLLA	Poly-l-lactic acid
PVDF-HFP	Poly (vinylidene fluoride-co-hexafluoropropylene)
PVP	Polyvinylpyrrolidone
PSVPh	Poly (styrene-co-4-vinylphenol)
PU	Polyurethane
EMI	Electromagnetic Interference
DMF	N, N- Dimethylformamide
NMP	N-methylpyrrolidone

SDS	Sodium Dodecyl Sulphate
PPEI-EI	Poly (propionylethylenimine-co-ethylenimine)
PVA-VA	Poly (vinyl acetate-co-vinyl alcohol)
DTAB	Dodecyltrimethylammonium bromide
TBAC	Tetrabutylammonium chloride
EPL	Electrospinning-phase separation-leaching
CTE	Coefficient of thermal expansion
CNI	Carbon Nanotechnologies Inc.
MC	Methylene chloride
THF	Tetrahydrofuran
FPS	Frames per second
MEK	Methyl ethyl ketone
ARES	Advanced Rheometric Expansion System
BET	Brunauer, Emmett and Teller
DFT	Density Functional Theory

SUMMARY

This research work focuses on single wall carbon nanotube (SWNT)/polymer composites and novel structured electrospun polymer materials. For SWNT/polymer composite study, poly (methyl methacrylate) (PMMA) is used as the polymer matrix. Obtaining SWNT/PMMA composite with enhanced mechanical and electrical properties is one of the research goals of this study. The first important step is to figure out a method for achieving uniform SWNT dispersion in PMMA. Eight different solvents with various solubility parameters were used to disperse SWNT in PMMA. It is found that the polar component of the solubility parameter (δ_p) of the solvent affects SWNT dispersion in PMMA. SWNT dispersion in PMMA improves with increasing solvent δ_p value, and the most uniform dispersion is obtained in nitromethane, which is the most polar solvent employed in this study. Based on this dispersion study, SWNT/PMMA composite films at various SWNT concentrations were processed using nitromethane. Mechanical and electrical property enhancements are observed. Processing, structure, morphology, and properties of these composites are discussed. A comparison between reinforcement efficiency of SWNT, multiwall carbon nanotubes (MWNT), and vapor grown carbon nano fibers (VGCNF) in PMMA is also discussed.

In order to electrospin SWNT/PMMA/nitromethane solution into composite nanofibers, first PMMA was electrospun over a wide concentration range. With increasing solution concentration, morphology of the electrospun polymer changed from particles to fibers. At relatively low solution concentrations, micro- and nano-structured polymer particles (including cups), and at higher solution concentrations, porous and solid nanofibers are observed. SWNT/PMMA/nitromethane solution was electrospun into

polymer shell-SWNT core nanofibers. Solvent characteristics play an important role on particle or fiber mat morphology during electrospinning. The qualitative relationship between solvent properties (evaporation rate, dielectric constant, surface tension, and viscosity) and particle morphologies is discussed. By tailoring solution properties and electrospinning conditions, one can produce particles or fibers with controlled morphology for specific applications.

Carbon nanotube, polymer/carbon nanotube composites, and electrospinning literature is briefly reviewed in Chapter 1. SWNT dispersion study in PMMA is presented in Chapter 2, followed by a detailed structure, processing and properties study on PMMA/carbon nanotube composite films in Chapter 3. PMMA and poly(styrene-co-vinyl phenol) (PSVPh) electrospinning study resulting in various morphology particles is presented in Chapter 4 followed by atactic and isotactic PMMA as well as limited polystyrene electrospinning resulting in solid and porous fibers in Chapter 5. SWNT core-polymer shell composite nanofiber electrospinning is presented in Chapter 6. Conclusions of this study and recommendations for future work are given in Chapter 7.

CHAPTER 1

INTRODUCTION

1.1 CNT/Polymer Composites

1.1.1 Introduction

In the 1990s, carbon nanotubes (CNT), which consist of single wall (SWNT)[1, 2], double wall (DWNT)[3, 4], and multi walls (MWNT)[5] were developed. By comparison, vapor grown carbon nano fibers (VGCNF) were developed in 1980s[6, 7]. CNT possess highly anisotropic electrical[8], optical[9], mechanical[10], and thermal[11] properties. Table 1.1 compares the properties of CNTs with those of the selected commercial high performance fibers. This comparison suggests that there is potential for producing CNT/polymer composites with higher electrical conductivity and mechanical properties than the current state of the art high performance fibers.

Table 1.1. Typical properties of carbon nanotubes and commercial high performance fibers[12].

	SWNT[10, 13-17]	DWNT [18]	MWNT [19-22]	Carbon fiber[6]	Zylon® [23, 24]	Kevlar 49®[24, 25]
Tensile strength (GPa)	23 – 63			4 – 7	5.8	3.6 – 4.1
Tensile modulus (GPa)	640	-	1060	150 – 950	270	130
Elongation at break (%)	5.8	28	-	0.5 – 2.5	2.5	2.8
Electrical conductivity (S/m)	$\sim 10^6$			5.5×10^4 – 9×10^5	$< 10^{-13}$	
Typical diameter	1 nm	~5 nm	~20 nm	5 – 10 μm		

Due to its excellent mechanical and electrical properties (Table 1.1), SWNT is employed as the ultimate reinforcing component in polymer composites. In the carbon nantoube research, a wide range of polymer matrices have been used, which include poly (methyl methacrylate) (PMMA)[26-29], polypropylene (PP)[30, 31], polyacrylonitrile (PAN)[32-39], poly (p-phenylene benzobisoxazole) (PBO)[40] etc. Some remarkable properties have been reported. For example, super-tough SWNT/ poly (vinyl alcohol) (PVA) composite fiber[41] containing 60 wt% SWNT has a breaking energy of 570 J/g. By comparison, the breaking energies of the existing tough materials, such as spider silk, Kevlar™, and Zylon™ fibers are about 165, 34, and 70 J/g, respectively. The tensile

strength of SWNT/PVA composite fiber was reported to be about 3 GPa[42]. In this introduction, several SWNT/polymer composites with a focus towards resulting property enhancements are discussed. The challenges and opportunities in the SWNT/polymer composites research are also discussed.

1.1.2 Characterization methods for CNT and CNT/polymer composites

Various characterization methods are used for SWNT and SWNT/polymer composites. For morphology characterization, Optical Microscopy, Scanning Electron Microscopy (SEM), Transmission Electron Microscopy (TEM), and Atomic Force Microscopy (AFM) play important roles. Individual or exfoliated SWNT exhibits van Hove singularities in the ultraviolet – visible – near – infrared (UV-vis-NIR) range[43-45]. However, SWNT bundles quench van Hove transitions of individual SWNT. Therefore, the UV-vis-NIR spectrum can detect SWNT exfoliation state. In addition, Cryo-TEM also can provide the information of the SWNT exfoliation state. Rheology measurements demonstrate the viscoelastic behavior of SWNT dispersion and SWNT/polymer composite melts or solutions[7, 46, 47]. Dynamic Mechanical Analysis (DMA) shows mechanical properties as a function of temperature. Mechanical properties of SWNT fibers and films, and their composites strongly depend on the SWNT orientation in the bulk sample. Therefore, for fully understanding the properties of SWNT based materials, accurate orientation determination is needed. Raman spectroscopy can provide information about SWNT orientation.

Raman spectroscopy is an effective characterization method of CNT enabled materials. The typical Raman spectrum of SWNT is shown in Figure 1.1, which includes four main features: the tangential G band (near 1600 cm^{-1} and derived from the graphite

in-plane vibration mode), the disorder induced D band (around 1300 cm^{-1}), the G' band (at about 2600 cm^{-1} and generally taken as the overtone of D band), and the radial breathing mode (RBM) (generally in the 150 cm^{-1} ~ 500 cm^{-1} range), which corresponds to the collective out-of-plane radial displacement of the carbon atoms[48]. RBM band characterizes the diameter distribution in a given SWNT sample due to its position being inversely proportional to the nanotube diameter. Raman spectroscopy also monitors SWNT deformation effectively. The positions of both G and G' bands downshift under tensile stress and upshift upon the application of compression or with pressure[49] (G band shift constant is range from 5 to 8.7 cm^{-1}/GPa[50] and G' band shift constant is around 23 cm^{-1}/GPa[51]). Charge transfer also affects SWNT Raman spectrum[52]; n doping causes Raman bands downshift and p doping results in upshifting of Raman bands. SWNT Raman bands shift to lower wave numbers with increasing temperature due to the decrease in carbon-carbon bond force[53]. Temperature coefficient of G band (~ -0.038 cm^{-1}/K) is higher than that of the RBM band (~ -0.013 cm^{-1}/K)[54]. Recently, the relative intensity of 267 cm^{-1} RBM peak using 785 nm laser excitation was attributed to SWNT aggregation state[55].

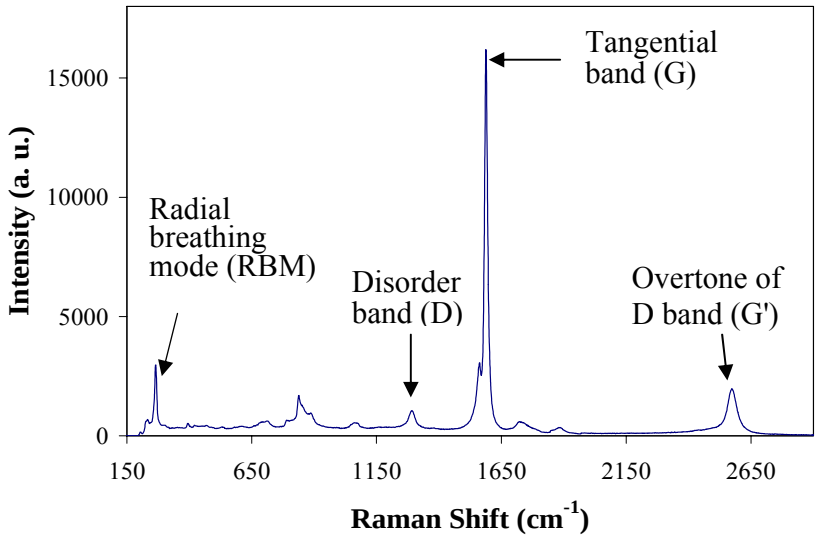

Figure 1.1. Typical Raman spectrum of SWNT with four major bands (RBM, D, G, and G') marked in the figure.

1.1.3 CNT and CNT/polymer composite mechanical properties

1.1.3.1 SWNT film and fiber

SWNT film[56], also referred to as buckypaper, is typically produced without polymer matrix or any binder by filtering SWNT dispersion in aqueous or organic media. Table 1.2. shows the typical properties of the SWNT films processed from N, N-dimethyl formamide (DMF), nitric acid, or oleum. Mechanical properties of the SWNT buckypaper can be enhanced by intercalating it with polymers such as PVA, polyvinylpyrrolidone (PVP), or polystyrene (PS)[57]. Mechanical properties of PAN/SWNT composite films are also substantially higher than either PAN film or SWNT buckypaper (Table 1.2.)[33].

Table 1.2. Typical properties of SWNT, control PAN, and PAN/SWNT (60/40) films.

	SWNT film from oleum[56]	SWNT film from nitric acid[58]	SWNT film from DMF[33]	Control PAN film[33]	SWNT/PAN (60/40) film[33]
Tensile strength (MPa)	30.0	70.0	1.1	57.0	103.0
Tensile modulus (GPa)	8.0	5.0	7.6	2.7	10.9
Elongation at break (%)	0.5	3.0	0.6	22.3	1.6
Electrical conductivity (S/m)	1.3×10^5	1.2×10^4	3.0×10^4	-----	1.5×10^4

Continuous well-aligned macroscopic SWNT fibers[59] have been solution spun from fuming sulfuric acid with tensile strength and tensile modulus of 116 MPa and 120 GPa, respectively. SWNT/polymer composites are expected to have higher mechanical properties comparing with control polymer samples at a certain amount of SWNT loading. In addition, from the cost aspect, comparing with SWNT buckypaper or fiber, making SWNT reinforced polymer composite is the direction to commercialize SWNT based materials.

1.1.3.2 CNT/polymer composites

1.1.3.2.1 Theoretical calculations

In a SWNT/polymer composite film with a random nanotube orientation and uniform SWNT dispersion in a plane, E_{11} and E_{22} are related to the E_c (composite modulus) by the Halpin-Tsai equations[60]:

$$E_C = \frac{3}{8}E_{11} + \frac{5}{8}E_{22} \quad (1)$$

$$E_{11} = \frac{1 + 2(l_{NT}/d_{NT})\eta_L V_{NT}}{1 - \eta_L V_{NT}} E_m \quad (2)$$

$$E_{22} = \frac{1 + 2\eta_T V_{NT}}{1 - \eta_T V_{NT}} E_m \quad (3)$$

$$\eta_L = \frac{E_{NT}/E_m - 1}{E_{NT}/E_m + 2(l_{NT}/d_{NT})} \quad (4)$$

$$\eta_T = \frac{E_{NT}/E_m - 1}{E_{NT}/E_m + 2} \quad (5)$$

l_{NT} and d_{NT} are the length and the diameter of nanotube ropes, respectively. V_{NT} is the volume fraction of SWNT in the SWNT/polymer film. The axial modulus of SWNT (E_{NT}) is 640 GPa[13]. E_m is the modulus of the polymer matrix and E_c is the modulus of the composite. Based on measured E_m and E_c values, by using the Halpin-Tsai equations, l_{NT}/d_{NT} can be calculated.

1.1.3.2.2 PMMA/CNT

Due to its large consumption, PMMA reinforcement becomes a critical problem in order to meet some specific application requirements. SWNT is considered as the ideal reinforcing candidate due to its excellent electrical and mechanical properties. A lot of efforts were put on dispersing SWNT in PMMA in solution[26, 61], in melt[27], as well

as via in-situ polymerization[62, 63]. The reported mechanical property improvements in CNT/PMMA composites vary over a wide range.

There are a number of studies on SWNT/PMMA composites in the literature. In one study, 8 wt% SWNT loading results in 100 % enhancement in the tensile modulus[27], while in another case, only 2 wt% SWNT was needed to achieve 100 % enhancement in tensile modulus[64]. Addition of less than 0.1 wt% SWNT in PMMA fibers increases the low temperature (-150 ^{o}C) modulus from 5 to 7 GPa, while at the temperature above T_g, the modulus essentially remains unchanged. The author attributed these changes to PMMA/SWNT cohesive interactions at low temperature and not to any morphological changes in PMMA[64]. SWNT (1 wt%) containing drawn PMMA fiber exhibits dramatic 700 % increase in the strain failure when compared to the PMMA fiber of similar draw ratio[65]. In this case, SWNT was dispersed in solution of hydroxylamine hydrochloric acid salt [$(NH_2OH)(HCl)$] and then mixed into PMMA matrix.

In addition to pristine SWNT, functionalized SWNT has also been utilized to reinforce PMMA matrix. For example, amide-functionalized SWNT/PMMA films[66] with 1 wt% SWNT loading show significantly improved mechanical properties. The storage modulus increases by 48 % for unmodified SWNT (3.1 GPa) and 86 % for amide-functionalized SWNT (3.9 GPa) composite compared to that of the control PMMA film (2.1 GPa). Modulus results indicate a significant difference between functionalized and non-functionalized tubes in the composite. Functionalized tubes result in a composite in which tan δ is shifted by 30 °C from that of the matrix material, while un-functionalized composites demonstrate a broadening of relaxation modes, but still retain the signature of bulk PMMA properties. These data suggest a morphological difference

with a discrete interphase layer in un-functionalized composites and a fully transformed matrix in the case of functionalization.

Doped SWNTs are also used as the reinforcement component in the polymer matrix. The electrical conductivity and mechanical characteristics of nanocomposites from pristine SWNT and doped SWNT with PMMA films[67] are measured. In pristine SWNT/PMMA composite, a percolation threshold as low as 0.17 wt% is found with the conductivity value reaching 1700 S/m. If SWNT is doped with $SOCl_2$, the percolation threshold does not change but the saturation conductivity rise to about 10,000 S/m. A small content of $SOCl_2$ doped SWNT (0.114 wt%) dramatically increases the toughness to 6 GJ/m^3, which is 30 times the toughness of the pure PMMA.

The interaction between PMMA and SWNT has also been examined. In some studies, it has been suggested that PMMA intercalates SWNT bundles and as a result, the distance between SWNT increases[26, 51, 68-70]. However, no direct evidence of the increased intertube distance has so far been reported. With the incorporation of PMMA, RBM up shifts. The up shift of the RBM is cited as the evidence of PMMA intercalation into SWNT bundles. It is suggested that at low SWNT content, SWNT bundles may be fully exfoliated[26, 69].

MWNT/PMMA composites have also attracted significant attention. With the presence of 1.5 wt% MWNT, modulus of PMMA film at 50 ^oC increased from 1.2 GPa to 2.2 GPa when 0.5 wt% poly(vinylidene fluoride) (PVDF) is added[71]. The increased properties are attributed to PMMA/MWNT interaction assisted by PVDF. However, no spectroscopic evidence of the interaction is provided. By incorporating 26 wt% MWNT, T_g increased by more than 15 °C and the composite modulus increased by a factor of 2

(from 0.7 to 1.4 GPa) at room temperature and by a factor of 27 (from about 20 MPa to above 540 MPa) at 120 °C when compared with the control specimen[72].

In-situ polymerized PMMA containing 7 wt% MWNT show increased tensile strength (from 55 to 72 MPa), hardness (from 19 to 28 Kg/m^2), and heat deflection temperature (from 388 to 429 K). It is suggested that the π bonds in MWNT open with azobisisobutyronitrile (AIBN) and react with PMMA to form covalent bonds. PMMA/MWNT composite exhibits a new infrared absorption peak at 1665 cm^{-1} and is proposed to be due to shift in the carbonyl PMMA peak resulting from PMMA/MWNT reaction[62, 63, 73]. PMMA grafted MWNT is synthesized using cetyltrimethylammonium bromide aqueous solution and potassium persulfate ($K_2S_2O_8$). Evidence of efficient load transfer is observed in PMMA/MWNT fibers. The telescopic effect in the MWNT pull out is also observed[74]. The orientation of MWNT in PMMA proves to be an effective way to substantially toughen the composite; 1 wt% MWNT in PMMA (oriented composite) exhibits 170 % increase in tensile toughness over the oriented PMMA. This is attributed to MWNT being perpendicular to the direction of the craze propagation[75].

1.1.4 CNT and CNT/polymer composite electrical properties

The large aspect ratio and high conductivity makes SWNT excellent candidates for conducting composites. According to the percolation theory, $\sigma_c \propto (V - V_c)^{\beta}$, where σ_c is the composite conductivity, V is the SWNT volume fraction, V_c is the SWNT volume fraction at the percolation threshold, and β is the critical exponent. β = 1 – 1.3 in two dimension, β = 1.6 to 2 in three dimension, and β >2 have been observed in anisotropic systems. The electrical conductivity of SWNT films and fibers are in the range of 10^4-10^5

S/m[56, 59], while the conductivity of the individual nanotube and nanotube bundles has been measured to be on the order of 10^6 S/m[13]. SWNT reinforced polymer composites percolate at very low SWNT concentration, which possess excellent electrical conductivity without compromising the host polymer's other preferred physical properties and processability.

Different systems give percolation values within a wide range, even for the same system such as epoxy/SWNT, various percolation values are obtained due to different preparation methods resulting in various composite morphologies (Table 1.3). Gum arabic stabilized SWNT combining with a PVA emulsion[76] gives a percolation threshold well below 0.1 wt%. Homogeneous polymer/SWNT composites by noncovalently functionalized soluble SWNT show percolation threshold at 0.05 ~ 0.1 wt% SWNT concentration[77]. The percolation threshold for PP/MWNT composites is between 1 and 2 wt% MWNT[78]. Epoxy/MWNT composites with weight fractions ranging from as low as 0.001 wt% up to 1 wt% exhibits the percolation threshold at 0.04 wt%[79]. Electrical conductivity of the PMMA/SWNT composite film increase from 0.118 to 11.5 S/m as the SWNT concentration increases from 1.3 wt% to 6.6 wt%[27]. When PMMA/MWNT nanocomposites at the same MWNT concentrations is electrospun in DMF into nanofibrous membrane (the diameter of the electrospun fibers ranged between 120 ± 30 nm and 710 ± 20 nm), the conductivity is reduced to ~10^{-8} S/m. The dispersion of the MWNT in the electrospun nanofibers is superior to the conventional CNT/polymer composites and MWNT in the electrospun nanofibers embedded in the polymer matrix and are aligned along the fiber axis, which decreases the contact points between MWNT, resulting in low electrical conductivity[63]. The electrical conductivity

of the composites not only strongly depends on the dispersion, exfoliation and orientation of CNT, but also on the length of the CNT. Figure 1.2 shows schematic descriptions of three different states of nanotube dispersion and orientation in polymer matrix, where nanotube loading required for electrical percolation would be the highest in Figure 1.2 (a) and the lowest in Figure 1.2 (c).

Table 1.3. Electrical conductivity of CNT enabled materials[12].

	V_c (vol%)	β	Maximum conductivity* (S/m)
PPE/PS/SWNT[77]	0.045	1.5	10 (10 wt%)
PPE/PC/SWNT[77]	0.11	2.8	4.8×10^{2} (10 wt%)
P3OT/SWNT[80]	11	2.0	$\sim10^{-3}$ (35 wt%)
Epoxy/SWNT[81]	0.074	1.3	1.2×10^{-3} (0.2 wt%)
Eopxy/MWNT-1[79]	0.01	-	5×10^{-1} (0.1 wt%)
Epoxy/MWNT-2[79]	0.0025	1.2	2 (1 wt%)

*Nanotube loading at which maximum conductivity is reported in parenthesis.

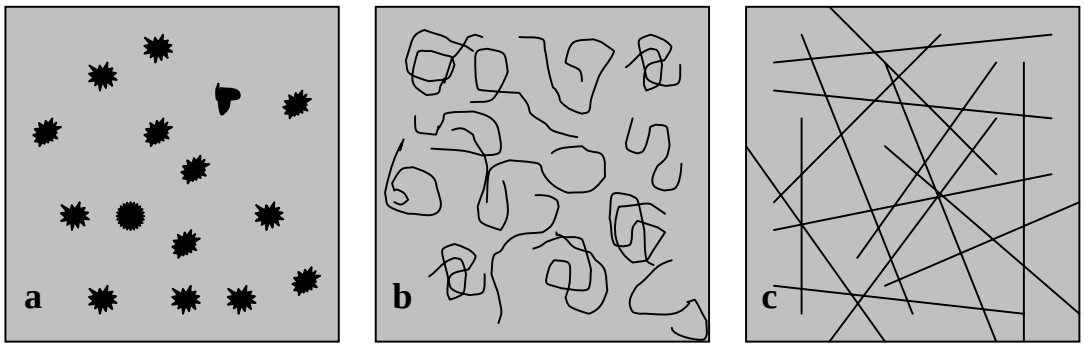

Figure 1.2. Schematics of various SWNT morphologies in polymer matrix (a) SWNT globules, (b) well dispersed coiled SWNT, and (c) well dispersed extended SWNT[12].

Electrically conducting composites have applications in electrostatic painting, antistatic shielding on airplane, electromagnetic interference (EMI) shielding, and as a transparent conductor[82]. MWNT/PMMA composite thin films act as gas and chemical sensors by monitoring the change in the film resistance when exposed to vapors of dichloromethane, chloroform, acetone, methanol, ethyl acetate, toluene and hexane[83].

1.1.5 Effects of CNT on decomposition temperature of polymer matrix

To date, both promoting and hindering effects of CNT on the thermal stability of polymer matrix have been reported.

1.1.5.1. Increase in polymer decomposition temperature upon addition of CNT

Several papers have reported increase in the decomposition temperature (T_d) of polymer matrix upon addition of CNT. The details of the composite systems, CNT loadings and increments in decomposition temperature are given in Table 1.4. The enhancement in the decomposition temperature has been attributed to the interaction between CNT and polymer matrix.

Table 1.4. Composite systems exhibiting increase in polymer decomposition temperature with CNT loading.

Composite	CNT Loading	Increase in T_d	Notes about CNT
MWNT/PU film[84]	2 wt%	9 °C	Diameter: 10 nm~ 30 nm Purity: 95 wt%
MWNT/polyamide 6 (PA6) film[85]	0.1 wt% 2.0 wt%	5 °C 18 °C	Diameter: 10 nm~ 60 nm Length: > the order of microns.
MWNT/PE[86]	10.0 wt%	20 °C	Diameter: 10 nm~30 nm, Length: 1 μm ~10 μm, Purity: >85%.
MWNT/PLLA[87]	3 wt%	10 °C	MWNT synthesized by pyrolysis of $Fe(CO)_5$ and C_2H_2 mixture in a quartz tube
MWNT/PP[88]	3 wt%	44 °C	-----
MWNT/atactic PP film[89]	5 wt%	70 °C	-----
MWNT/PMMA[90]	3 wt%	62 °C	Purity: 90-95%
SWNT/nylon 6[91]	1.5 wt%	13 °C	SWNT is functionalized containing ~3-4% carboxylic acid groups, Purity: 80~90%.
SWNT/PU[92]	1 wt%	5 °C	Washed with HCl to remove the catalyst and further purified with HNO_3 to remove the amorphous carbon.
VGCNF/polycarbonate [93]	TGA was carried out in nitrogen. The decomposition features are similar at around 350 °C, then the decomposition of the composites shifts to higher temperature with increasing VGCNF concentration		
CNF/TGDDM/DDS epoxy[94]	1 wt% 5 wt%	Slightly increase	
VGCNF/PMMA[95]	5 wt%	60 °C	Bought from Applied Sciences, Inc.

1.1.5.2. Decrease in polymer decomposition temperature upon addition of CNT

There are a few papers in the literature that report decrease in polymer decomposition temperature upon CNT addition. The details of the composite systems, CNT loading and the decrease in polymer matrix decomposition temperature are given in Table 1.5. There is no clear explanation available for the decrease in the polymer decomposition temperature with the addition of CNT.

Table 1.5. Composite systems exhibiting decrease in polymer decomposition temperature with CNT loading.

Composite	CNT Loading	Decrease in T_d		Notes about CNT
SWNT/ABS(acrylonitrile–butadiene–styrene)[96]	In air:	T_{d1}*	T_{d2}*	SWNT was purchased in toluene slurry from Tubes@rice.
	0.5 wt%	9 °C	+ 50 °C	
	1.0 wt%	11 °C	+ 21 °C	
	3.5 wt%	7 °C	+ 17 °C	
	5.0 wt%	15 °C	10 °C	
	10.0 wt%	17 °C	18 °C	
	In nitrogen:			
	0.5 wt%	0 °C	+ 51 °C	
	1.0 wt%	22 °C	11 °C	
	2.0 wt%	0 °C	57 °C	
	3.5 wt%	6 °C	26 °C	
	5.0 wt%	27 °C	38 °C	
	10.0 wt%	29 °C	36 °C	
SWNT/PVDF[97]	5 wt%	25 °C		Purity: 60% by volume
	10 wt%	45 °C		
	19 wt%	100 °C		
	29 wt%	150 °C		
	39 wt%	200 °C		
	49 wt%	225 °C		
SWNT/PMMA[66]	1 wt%	Decrease (no specific value)		Purified SWNT from CNI
SWNT/PVA[98]	0.1 wt%	3 °C		Diameter: ~0.8 nm
	1.0 wt%	3 °C		

*ABS shows two decomposition temperatures, positive values mean decomposition temperature increasing upon adding SWNT.

1.1.6 Dispersion and processing issues

SWNT agglomerates into 5 to 100 nm diameter bundles[99, 100], and forms hexagonal lattice within the bundle with binding energy between the tubes of the order of 900 meV/nm[101]. Figure 1.3(a)[100] shows the TEM image of one single SWNT bundle, which composes of many individual SWNTs. In addition, SWNT bundles have highly entangled network structure shown in Figure 1.3 (b)[100]. Therefore, counterbalancing the van der Waals interaction is one of the challenges for dispersing and exfoliating SWNT. SWNT dispersion, orientation, and exfoliation determine SWNT based materials properties enhancements. Physical and chemical approaches employed to unentangle, disperse, and exfoliate nanotubes are briefly summarized in this section.

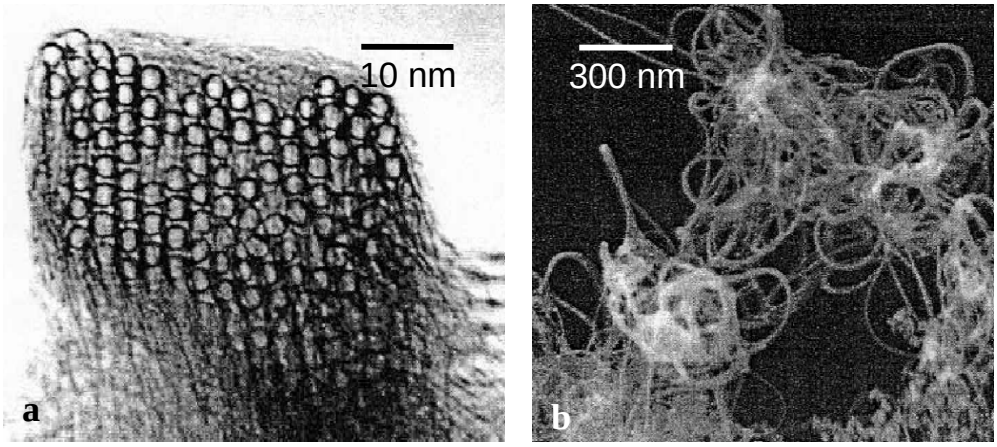

Figure 1.3. TEM image of (a) one single SWNT bundle and (b) SWNT bundles entangled network[100].

Most SWNT/polymer composite studies to date carried out in solution have employed sonication to disperse SWNT. However, sonication introduces defects, including buckling, bending, and dislocations in the carbon structure. Prolonged

sonication increases disorder, reduces nanotube length, and ultimately leads to the formation of amorphous carbon[101]. In addition, high shear mixing, in the presence of selected polymers, can unentangle ropes, yielding homogeneous dispersion.

Solvents such as 1,2-dichlorobenzene, chloroform, DMF and N-methylpyrrolidone (NMP)[102] are examples of good nanotube solvents/dispersants while acetone, ethanol, and toluene are example of poor solvents. Ausman et al.[103] investigated the room-temperature solubility of SWNT in a variety of solvents. Good SWNT solvents are characterized by high electron pair donicity, high solvatochromic parameter, and negligible hydrogen bonding[103]. CNT dispersed well in water using anioinic, cationic, and nonionic surfactants[104-107]. The size of the hydrophilic group of nonionic surfactant or polymer is the major factor for suspending nanotubes. For example, a diblock copolymer of poly(propylene oxide)-co-poly(ethylene oxide) (PPO-co-PEO), where poly(propylene oxide) (PPO) is hydrophobic and poly (ethylene oxide) (PEO) is hydrophilic, can disperse nanotubes in water[106]. TEM study shows that sodium dodecyl sulphate (SDS) is absorbed on the SWNT surface in an extremely ordered manner[108]. Certain kinds of salts (radical-anions of naphthalene, benzophenone, fluorenone, anthraquinone and benzoquinone, with Li^+ as a counter ion) [109-111] can disperse and exfoliate SWNT. The idea is that positive ions have good affinity to electron rich nanotubes.

Oxidation, for example, in nitric acid or in a mixture of sulfuric and nitric acid, can introduce oxygen-containing functional groups such as -OH and -COOH on the nanotube surface[104, 112]. Nanotube ends can be opened in the oxidizing media. Oxidized tubes form a well dispersed electrostatically stabilized colloid in water as well

as in ethanol[113]. CNT can be functionalized at end caps or at the sidewall[114, 115] to enhance their dispersion in solvents and in polymer matrices. SWNTs dissolved in organic solvents have been derivatized with thionylchloride and octadecylamine. Reaction of soluble SWNT with dichlorocarbene leads to the nanotubes functionalization. For instance, by functionalizing the end caps with long aliphatic amines[116] nanotubes become soluble. SWNTs have been solubilized by functionalizing their sidewalls by nitrene[117], fluorination[118], alkylation[119], and arylation[116].

SWNTs have been dispersed using in-situ polymerization in a number of polymers including polyaniline, poly(p-phenylene benzobisoxazole) [40], PMMA[68], and polypyrrole, etc. Well dispersed SWNT/polyaniline composite film by electrochemical polymerization has been reported[120]. A homogeneous SWNT/polyimide composite prepared by in-situ polymerization, exhibits electrical percolation at 0.1 vol % SWNT[121].

The polymer grafted SWNTs are particularly important for processing polymer/SWNT nanocomposites[122-124]. Aminopolymers can attach to SWNT-bound carboxylic acids via the formation of amide linkages[125]. Poly(styrene-*co*-*p*-(4-(4'-vinylphenyl)-3-oxabutanol)) functionalized both SWNT and MWNT[126]. Polymer bound SWNT can be formed by covalently attaching nanotubes to highly soluble linear polymers, such as poly (propionylethylenimine-co-ethylenimine) (PPEI-EI) via amide linkages or poly (vinyl acetate-co-vinyl alcohol) (PVA-VA) via ester linkages[127]. The samples of polymer bound nanotubes are soluble in both organic solvents and water, and can form highly homogenous solutions[127].

1.1.7 CNT based materials applications

SWNT enabled materials have many potential applications. There includes chemical and physical sensors, probe tips for the AFM, electrically and thermally conducting fibers for functional textiles, nanowires, quantum wires, nanoscopic levers and other components in molecular motors and molecular devices. Other promising applicable directions lie in biomedical field including scaffolds for tissue growth[128], substrate for neuron growth, actuators[129], novel micro and meso-porous carbon structures for filtration[130], field emission display devices[131], photovoltaic materials[132], electromagnetic interference shielding, packaging materials for thermal management, and supercapacitors[133, 134] as charge storage devices.

Although many successful results have been reported, dispersion of nanotubes and fabrication of homogenous polymer composites remain the main technical challenge in processing bulk nanotube based materials. In this thesis, SWNT/PMMA composites are studied with a focus on dispersion. After achieving a homogeneous SWNT/PMMA/solvent dispersion, SWNT/PMMA composite films with enhanced mechanical and electrical properties are processed. In order to process SWNT core-PMMA shell nanofibers, electrospinning is also conducted on the homogeneous SWNT/PMMA/solvent dispersion.

1.2 Electrospinning

1.2.1 Introduction

Electrospinning[135-138] can be considered as the variant of electrospraying [139] process. In electrospraying, small droplets or particles are formed as a result of the varicose break-up of the electrified jet that is often present with a solution of low viscosity. Electrospraying has found widespread use in many areas including mass

spectrometry, painting, inkjet printing, and manufacturing of particles with various sizes and compositions[139-142]. In electrospinning, a fiber is generated as the electrified jet is continuously stretched, and then polymer nanofibers with diameters ranging from tens of nanometers to a few micrometers can be produced from polymer solutions[143] or melts[144, 145]. For one specific polymer/solvent solution, with increasing solution concentration, the morphology changes from electrosprayed particles to electrospun fibers. Electro processing polymer solutions into particles is named electrospraying, while processing into fibers is named as electrospinning.

Electrospinning, first patented in 1934[146], is a very simple and versatile process. Electrospinning can produce aligned nanofibers[147-149], continuous core/shell nanofibers[150-152], as well as continuous hollow nanofibers[151, 153, 154] from polymer solutions(or melts). It can also produce continuous metal[155], ceramic[156], and composite nanofibers[157, 158]. Electrospinning has already been demonstrated on more than 50 kinds of polymers including PAN[159], PVA[160], nylon-6[161], and PEO[162] etc. Despite this progress, several challenges still remain including improving the models of the electrospinning process for better understanding its mechanism, modeling nanofibers deposition on the substrate, diameter control, especially for nanofibers with less than 100 nm diameter[163, 164], scaling up the productivity, and recycling the solvents etc.

1.2.2 Electrospinning setup and process

Figure 1.4 [165] shows the typical electrospinning setup, which includes three major parts: high voltage power supply, syringe pump including a metal spinneret, and the grounded collecting target. Direct current is usually used for electrospinning. The

spinneret is connected to a syringe which contains polymer solution (or melt). Polymer solution (or melt) can be fed through the spinneret at a controllable rate by using the syringe pump. Upon applying high voltage (usually ranging from 1 kV to 30 kV), the pendent drop of the polymer solution at the nozzle of the spinneret becomes highly charged. Once the strength of the electric field can overcome the surface tension of the polymer solution, a charged liquid jet ejects from the nozzle. This electrified jet undergoes stretching and whipping process, leading to the formation of a long and thin thread. Combining the liquid jet's continuous elongation and the evaporation of the solvent, the diameter of the filament can be greatly reduced from hundreds of micrometers to tens of nanometers during electrospinning. Attracted by the grounded collection target, the charged fibers are often deposited as randomly oriented, nonwoven fiber mat.

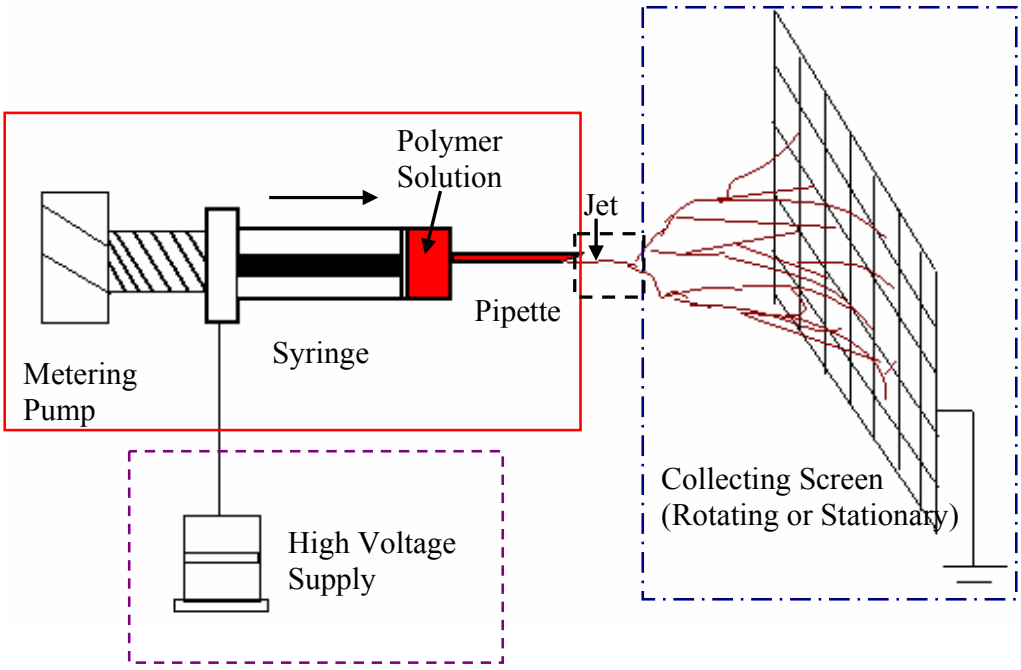

Figure 1.4. Typical electrospinning setup (Red area: syringe pump including a metal spinneret part; dotted purple area: high voltage power supply part; dotted dash blue area: grounded collecting target) (Reproduced from reference [165]).

1.2.3 Electrospinning mechanism

Although the electrospinning setup and process seem extremely simple, the mechanism is rather complicated due to a number of parameters. The formation of nanometer diameter fiber via electrospinning is based on the uniaxial stretching of a charged viscoelastic jet derived from a polymer solution (or melt). Electrospinning technique is similar to the commercial process for microscale fibers drawing except for the use of electrostatic repulsions between surface charges rather than a mechanical or shear force as the drawing force. When polymer solution (or melt) is delivered to the needle tip from the reservoir by a syringe pump, a droplet will suspend at the tip of the needle. After applying high voltage to the needle, an electrical force exerts on the

solution (or melt). Further increasing the applied voltage, the electrical force becomes large enough to overcome the surface tension; a jet ejects from the apex of this conical protrusion called “Taylor cone”, which was first observed by Geoffrey Ingram Taylor in 1964[166, 167].

Taylor theoretically derived that the requirements to form a perfect cone under such conditions required a semi-vertical angle of 49.3° and demonstrated that the shape of such a cone approached the theoretical shape just before the jet formation[166, 167]. While, Yarin et al. [168] showed that as a liquid surface developed a critical shape, its configuration approached the shape of a cone with a half angle of 33.5°, rather than a Taylor cone of 49.3°.

After initiating from the apex of Taylor cone, the electrically charged jet travels in a straight line for a few centimeters. After traveling in a straight line for a certain distance, the jet undergoes whipping instability, resulting in bending and stretching, and finally gets to the grounded target to form a fiber mat. In some specific cases, such as CNT/polymer solution at high CNT concentration, splaying of the electrified jet might also be observed, though it is never a dominant process during electrospinning[168, 169].

Based on the experimental observations and the electrohydrodynamic theories, several mathematical models have been developed to roughly investigate the electrospinning process. Reneker and his co-workers took the charged liquid jet as a system of connected, viscoelastic dumbbells and provided an interpretation for the formation of bending instability[168]. They calculated the three-dimensional trajectory for the jet using a linear Maxwell equation and the computed results were in agreement with the experimental results. Rutledge and co-workers treated the jet as a long, slender

object and thereby developed a different model to explain the electrospinning process[170-173]. Their experimental and theoretical studies clearly show that the electospinning process only involve whipping of a liquid jet. The whipping instability is mainly caused by the electrostatic interactions between the external electric field and the surface charges on the jet. The formation of the fibers with fine diameters is mainly achieved by the stretching and accelerating the fluid filament in the instability region. They further showed that the model could be extended to predict the saturation of whipping amplitude, as well as the diameter of resultant fibers[170]. Feng proposed another model to describe the motion of a highly charged liquid jet in an electric field, and the role of non-Newtonian rheology in the stretching of an electrified jet was also examined[174, 175]. All these models provide a better understanding of the mechanism responsible for the electrospinning process despite their limitations.

1.2.4 Controlling the electrospun material morphology

The morphology and the diameter of the electrospun fibers are dependent on a number of parameters[176, 177], mainly intrinsic solution properties and electrospinning conditions. Intrinsic solution properties[178] include the type of polymer, conformation of polymer chain, solvent, solution elasticity, evaporation rate of the solvent, viscosity (or concentration), surface tension, and conductivity. These parameters are mainly dominated by the properties of the solvent and the polymer. Electrospinning conditions [179] include applied voltage, flow rate, distance between the needle tip and the grounded collecting target, humidity, and temperature. By tailoring these electrospinning parameters, electrospun material morphology can be controlled.

In general, solvent[180, 181] plays an important role on the electrospun material morphology. Solvents with large evaporation rate help to get porous fibers. Surface tension keeps the surface area per unit mass small, and as a result beads and beaded fibers are formed under high surface tension condition. Hence reducing surface tension favors formation of fibers without beads, which is confirmed in Reneker's paper[162]. Large dielectric constant solvent results in small diameter fiber. For a given polymer/solvent system, viscosity has the greatest effect on fiber diameter, which is mainly determined by solution concentration[182]. At relatively low viscosity, jet breaks up into droplets, resulting in the formation of beads; above a critical viscosity, continuous fibers form. As viscosity increases further, the diameter of the fiber also increases. The electrospinning conditions also affect the morphology of electrospun material.

Rutledge and co-workers have proposed a model to include the influence of various processing parameters on the diameter of the electrospun fibers[170]. In their model, the final diameter of a spinning jet depends on the interplay between the surface tension and the electrostatic repulsions. The balance point is related to the flow rate, the strength of the electric field, and the surface tension of the liquid phase.

1.2.5 Electrospun polymer particles

Electrospinning at low polymer solution concentrations produces polymer particles. PMMA/ethyl acetate solution [183] was ejected from a reservoir tip to form suspended droplets using the force of a controllable syringe pump. Poly (ethylene terephthalate) (PET) film was used as the substrate. The relationship between the applied voltage or flow rate and droplet size was examined. With increasing applied voltage, the size of the droplet decreases, while with increasing flow rate, the size of the particles

increases. From their optical microscopy images, the droplets' dimension is around 100 μm. Thin polymer films of poly(vinylidene fluoride) (PVDF) [184] were prepared by electrospinning its DMF solution. It was concluded that the droplet size is controlled by the conductivity and flow rate of the solution.

Silica nanocups (Figure 1.5) were produced by electrospinning PVP–sol–gel solution (50-50% mixture of ethanol and water)[185] followed by calcination. Due to the low viscosity and high surface tension of the blended polymer-sol-gel solutions, the electrostatically extruded continuous liquid jet from the spinning source became tiny droplets with diameters of less than 1 μm. These droplets dried in transit and were collected at the counter electrode. The collected material was calcinated at 850 °C for 3 hours to eliminate polymer, as well as the cross-link sol-gel material. The ability of electrospinning to repeatedly generate very small and uniform volumes of liquid droplets makes it one of the important tools of nanotechnology. However, obtaining uniform sized polymer particle is still a major problem. The effect of solvent on particle morphology needs further investigation.

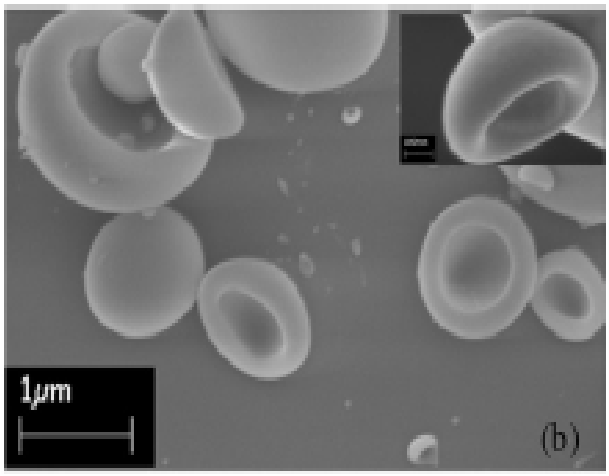

Figure 1.5. Silica nanocups (Reproduced from reference[185]).

1.2.6 Electrospun polymer fibers

In recent years, various polymers have been successfully electrospun into ultra-fine fibers with different morphologies mostly from solution and some from melts. Here we discuss bead free fibers, aligned fibers, and porous fibers as the examples to show the progress to date in the field of electrospun polymeric fibers.

1.2.6.1 Bead free fibers

Only particles can be produced by electrospinning very dilute solutions. As the concentration increases, the fiber morphology evolves from a beads-on-string structure to a uniform fiber structure. By increasing concentration, the diameter of the fiber also increases. To obtain bead free fibers of small diameter is a critical issue. Formation of beads could be attributed mainly to the interplay among three factors, surface tension, electrostatic repulsion force, and viscoelastic force. Surface tension tends to convert the liquid jet into spherical droplets. On the other hand, the electrostatic repulsion between

charges on the jet surface tends to increase the surface area, and thus favors the formation of a thin jet rather than beads. Viscoelastic force also resists rapid changes in shape and supports the formation of fibers with smooth surfaces. In general, the formation of beads can be eliminated whenever the influence of surface tension is suppressed by the effects of the last two forces.

Under a certain surface tension solution, the formation of beaded fibers is attributed to an insufficient stretch of the filaments during the whipping of the jet due to a low charge density. The addition of certain inorganic salts results in an increase in the solution conductivity, which helps in obtaining small diameter bead free fibers. Park et al. prepared smaller diameter and narrow diameter distribution PEO fibers by addition of LiCl[186]. The addition of salt increases the net charge density on the jet, and induces larger drawing force[187]. Addition of the cationic surfactants improves the net charge density that enhances the whipping instability. The jet is stretched under stronger charge repulsion and at a higher speed, resulting in an exhaustion of the bead structure. Polystyrene (PS) nanofibers[187] were electrospun with the inclusion of cationic surfactants, dodecyltrimethylammonium bromide (DTAB) (0.1 ~ 10 mmol/l) or tetrabutylammonium chloride (TBAC) (0.1 ~ 10 mmol/l), in the polymer solution. A small amount of cationic surfactant effectively stops the formation of beaded fibers during the electrospinning. In this study[187], the cationic surfactants are found to improve the solution conductivity, but have no effect on the solution viscosity.

1.2.6.2 Aligned fibers

Because of the bending instability associated with a spinning jet, electrospun fibers are often deposited randomly on the collector as the nonwoven fiber mats. Well

aligned nanofibers are required for many applications. In the past few years, a number of approaches have been used to collect aligned electrospun nanofibers arrays. A high speed rotating drum can help align the fibers[147]. Li et al.[148] have recently demonstrated that the nanofibers can be uniaxially aligned by introducing an insulating gap into the conductive collector. By modeling the electrostatic forces acting on the fiber, it has been established that the fibers tend to be oriented along a direction such that the net torque of electrostatic forces applied to the two ends of a discrete segment of the fiber is minimized[148]. By varying the design of electrode pattern, it is possible to control both alignment and assembly of the electrospun nanofibers. Recently, a new method named conjugate electrospinning[188] is used for producing continuous aligned yarns from oppositely charged nanofibers by using a rotating collector drum (Figure 1.6). The fibers from the two oppositely charged electrospinning spinnerets attract each other forming neutralized nanofibers. These fibers are drawn and stretched by the rotating drum, resulting in the continuous aligned nanofiber yarn. Poly-l-lactic acid (PLLA), poly(vinylidene fluoride-co-hexafluoropropylene) (PVDF-HFP), PAN, and polyurethane (PU) were successfully electrospun into aligned fiber mats using conjugated electrospinning method. By increasing the number of the opposite spinnerets pairs, the productivity is scaled up, but the fiber diameter is also increased at the same time[188].

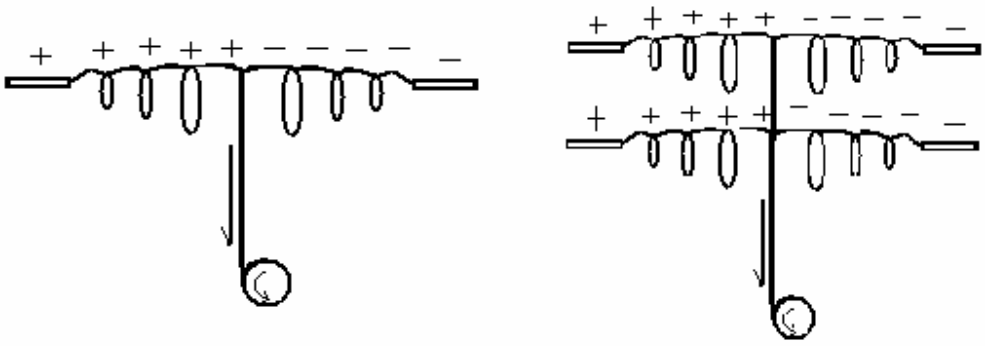

Figure 1.6. The schematic setup used for conjugate electrospinning (Reproduced from reference [188]).

1.2.6.3 Porous fibers

Compared to the conventional fiber spinning, electrospun fibers are generally much smaller in diameter and thus possess a larger surface area. The surface area can be further increased when its structure is porous rather than solid one. The porous fibers have a wide range of potential applications in encapsulation, controlled release, superhydrophobic coating, and lightweight reinforcement, etc. Two different approaches have been reported for introducing a porous structure into electrospun nanofiber. One of them is selective removal of a component from nanofibers made of a composite or blend materials. The other one is using phase separation during electrospinning under the application of proper electrospinning parameters.

Nano-porous ultra-high specific surface ultra-fine fibers[189] are created by the method of "electrospinning-phase separation-leaching" (EPL), which is based on selective removal of one component from nanofibers. Firstly, polymer solutions of PAN and polyvinylpyrrolidone (PVP) blends dissolved in co-solvent are electrospun to make ultra-fine fibers. The incompatibility of PAN and PVP induces phase separation to form

microdomains of PVP in the polymer blend ultra-fine fibers. Then, PVP microdomains in the blend fibers are leached out in water, and porous PAN ultra-fine fibers are obtained[189].

Choice of a volatile solvent[151, 190] can also help in obtaining porous fibers. For example, ultra-fine porous cellulose triacetate (CTA) fibers were prepared by electrospinning with methylene chloride (MC)(Figure 1.7(a))[191]. The pore size in ultra-fine CTA fibers electrospun with MC at 5 wt% concentration showed a bimodal pore size distribution centered at ~17 and ~64 nm (Figure 1.7(b)). The authors attributed these porous structures to phase separation resulting from the rapid evaporation of solvent during the electrospinning process[191].

Kim et al.[190] reported a new approach to fabricate electrospun polymer nonwoven mats with porous surface morphology by varying the collector temperature. PS, PAN, poly(vinylidene fluoride) (PVDF), and poly(ε-caprolactone) were all electrospun into highly porous fibers using liquid nitrogen bath[192], which freezes the fibers, inducing a phase separation between the polymer and the solvent. When the solvent is removed in vacuum, highly porous fibers are obtained (Figure 1.8).

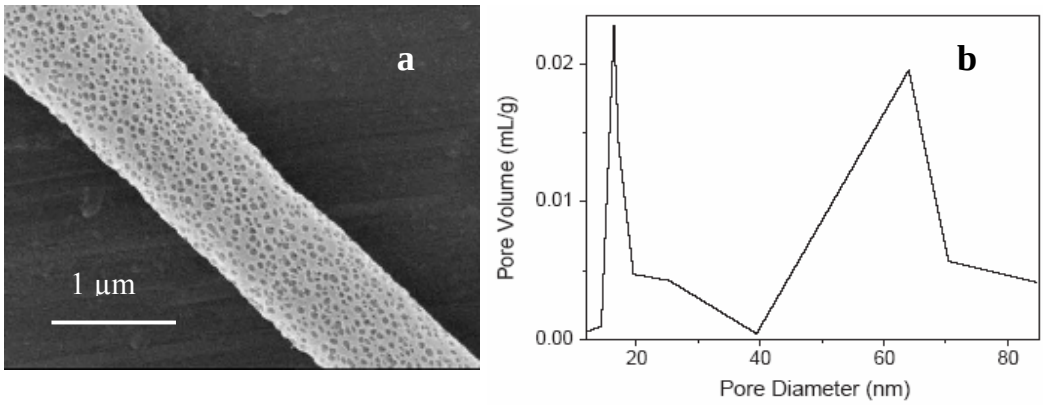

Figure 1.7. Ultrafine cellulose triacetate fibers electrospun from in methylene chloride solution at 5.0 wt% concentration (a) SEM image of porous fiber (b)The pore size distribution for this porous fiber (Reproduced from reference [191]).

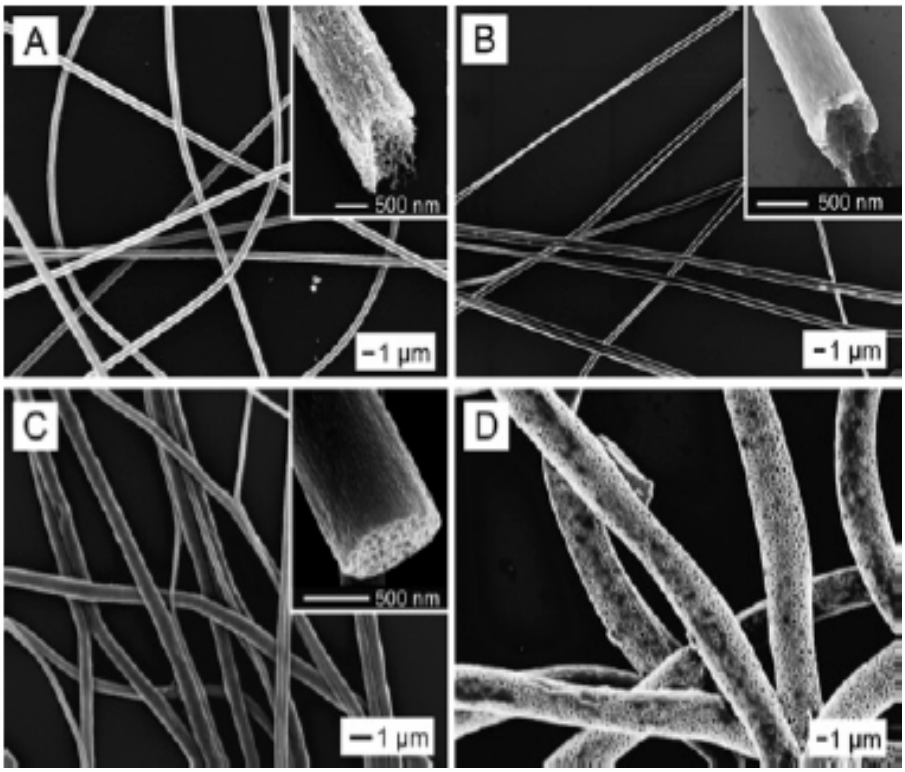

Figure 1.8. (A) PAN fibers electrospun into liquid nitrogen from DMF solution. The inset shows the end of a broken fiber, clearly indicating a highly porous structure. (B) Porous carbon fibers obtained by carbonization of the PAN fibers. (C) PVDF and (D) Poly (ε-caprolactone) fibers obtained by electrospinning into liquid nitrogen followed by drying in vacuum (Reproduced from reference [192]).

1.2.7 Electrospun CNT/polymer composite fibers

The idea of incorporating CNT into nanofibers to form novel structured composite materials seems to be very promising for they are expected to have good processability characteristics of the polymer and excellent functional properties of CNT.

In the conventional spun PAN/SWNT composite fiber with micro sized diameter, SWNT exhibits much higher orientation than PAN, such as 10 wt% PAN/SWNT composite fiber, PAN has an orientation factor of 0.66, while the orientation factor of SWNT is 0.92[32]. Relatively high orientation of CNT in polymer matrix can also be produced through electrospinning. Reneker and co-workers[193] observed that the orientation of the surface-oxidized MWNT within the electrospun nanofibers was much higher than that of the PAN polymer. The composite nanofiber sheets possess enhanced electrical conductivity, mechanical properties, thermal stability, and dimensional stability. At 20 wt% MWNT loading, the electrical conductivity of the composite nanofibers is enhanced to 100 S/m. The tensile modulus values of the compressed composite nanofiber sheets are improved significantly to 14.5 GPa (4 times that of the pure PAN nanofibers) along the fiber winding direction. The coefficient of thermal expansion (CTE) of the composite nanofiber sheets is $13*10^{-6}$/°C along the axis of the aligned nanofibers[193].

MWNT/PAN well aligned[194] nanofibers show enhanced mechanical properties. TEM observation shows that MWNT is parallel and oriented along the axes of the nanofibers. Long, continuous, and well aligned PMMA/MWNT electrospun fibers[195] are obtained by rotating drum at a speed of 1500 rpm. TEM images show that MWNT are

aligned in the direction of the fiber axis. The conductivity of the fiber increases from 4.5×10^{-3} to 5.3×10^{-2} S/m with the concentration of the MWNT increasing from 0.05 wt% to 2 wt%[195]. The composites show percolation behavior below 0.05 wt% loading[195]. Ko et al.[36] have prepared the continuous SWNT filled nanofibers and reported that the modulus improved 120% in nanofibers containing 4 wt% SWNT. Dror et al.[196] have achieved well-dispersed MWNT and SWNT, and successfully prepared the electrospun MWNT/PEO nanofibers in which MWNT alignment could be observed using TEM. The use of CNT to reinforce and enhance the performance of polymer composite can produce a new generation of nanocomposite materials. The polymer shell-SWNT core naofibers have many potential applications, such as AFM tips, nano sensors, etc.

1.2.8 Electrospun material applications

Although electrospinning has more than seventy years of history, only in recent years, it begins to attract significant attention - a result of progress in the field of nanotechnology. It is realized that electrospinning might be an effective way to bridge the dimensional and property gap between nano- and micro- structures. With increasing solution concentration, electrospun morphology changes from particles to fibers. Both electrospun particles and fibers have potential applications in biomedical field due to their various morphologies and small size. Electrospun particles can be used as controlled drug delivery system, etc. Electrospun fiber mats have a very high surface area to mass ratio, potentially offering performance advantages in fields ranging from tissue engineering[197] to protective clothing to wound dressing and to membranes for chemical processing[18, 189, 198-201].

Electrospinning represents a good approach to incorporate and align SWNT into polymer matrix[196, 202, 203]; therefore, one can get novel structured materials with excellent properties. These materials open up a wide route to functionalizing surfaces which can enable the fabrication of new types of optical, electric, and magnetic devices. PAN based carbon nanofibers prepared by electrospinning is promising for making electrodes for supercapacitors[204]. For selected applications, it is desirable not only to control the fiber diameter, but also the internal morphology. Porous fibers are of interest for applications such as filtration. By adjusting the size of the pores in the electrospun fibers, superhydrophobic materials[205, 206] can be processed. Electrospun particles can be decorated on the smooth surface to increase the surface roughness, which can then mimic the lotus leaf to obtain the superhydrophobic materials.

1.3 Thesis objectives

The key objectives of this study are:

- To systematically study carbon nanotube reinforced PMMA composites.
- To compare the reinforcement efficiency of SWNT, MWNT, and VGCNF in PMMA.
- To study the structure, processing, and properties of PMMA/CNT composites at various carbon nanotube loading.
- To understand the electrospinning process in the broad solution concentration range and to understand various factors affecting electrospun particle and fiber morphologies.

CHAPTER 2

SWNT DISPERSION IN PMMA

2.1. Introduction

Uniform dispersion in a polymer matrix is the first key step to obtain effective CNT reinforcement in the composite. Various methods have been employed to disperse nanotubes. These can be categorized into chemical and physical approaches. Functionalization of CNT, a chemical approach, enhances nanotube dispersion in many solvents. However, functionalization introduces defects on the nanotubes. Physical methods include stirring, sonication etc. Both methods have been discussed in chapter 1. Most of the reports of CNT-polymer composite preparation involve dispersing CNT in a solvent and the addition of polymer in solution. In this chapter, we study the role of solvent on SWNT dispersion in PMMA matrix. Eight different solvents with varying solubility parameters are used to prepare SWNT/PMMA composites. The three dimensional solubility parameters values of the solvents used are listed in Table 2.1.

Table 2.1. Solubility parameters of various solvents and PMMA at room temperature[207].

	Molecular formula	δ_d ($MPa^{0.5}$)	δ_p ($MPa^{0.5}$)	δ_h ($MPa^{0.5}$)	δ_t ($MPa^{0.5}$)
Toluene	C_7H_8	18.0	1.4	2.0	18.2
Methylene chloride	CH_2Cl_2	18.2	6.3	6.1	20.3
Methyl ethyl ketone	$CH_3COCH_2CH_3$	16.0	9.0	5.1	19.0
Acetone	CH_3COCH_3	15.5	10.4	7.0	20.1
Formic acid	HCOOH	14.3	11.9	16.6	25.0
DMF	$HCON(CH_3)_2$	17.4	13.7	11.3	24.8
Acrylonitrile	H2C=CHCN	16.5	17.4	6.8	24.8
Nitromethane	CH_3NO_2	15.8	18.8	5.1	25.1
PMMA	$(CH_2C(CH_3)CO_2CH_3)_n$	18.6	10.5	7.5	22.7

δ_t: total solubility parameter, which is defined as: $\delta_t^2 = \delta_d^2 + \delta_p^2 + \delta_h^2$

δ_d: dispersive contribution, δ_p: polar contribution, and δ_h: hydrogen bonding contribution

2.2. Experimental

HiPCO™ nanotubes received from Carbon Nanotechnologies, Inc. (CNI) were used without purification (Lot # R0231 and 35 wt% metal catalyst). PMMA

($\overline{M_w} = 95{,}000 \sim 150{,}000$ g/mole) was obtained from Cyro Industries and used as received. All solvents were purchased from Sigma-Aldrich Co. or from Fisher Scientific and were used as received. SWNT (10 mg) dispersed in 30 ml solvent were sonicated (the sonicator: Branson water bath sonicator by Smithkline Company, model B-22-4, power 125 W, frequency 43 KHz) for 70 hours at room temperature (water circulation was used in the bath to maintain the bath temperature at room temperature). PMMA (90 mg) was added to this dispersion, followed by sonication for another five hours. The dispersion was poured onto a glass plate, and the solvent was allowed to evaporate in the hood over several days. The resulting SWNT weight fraction in PMMA was 10 wt%. LEO 1530 field emission scanning electron microscope was used to characterize the morphology of the SWNT/PMMA composite films, and all the samples were coated with gold. The Raman spectra were collected on Holoprobe Research Raman microscope made by Kaiser Optical Systems, Inc., using 785 nm excitation wavelength (E_{laser}=1.58 eV). The laser spot diameter was a few micrometers. For each composite film, Raman spectrum was collected at different positions using an exposure time of 1 minute or exposure time of 1 second with 100 accumulations to minimize the heating effect.

2.3. Results and discussion

SWNT/PMMA dispersions are optically homogeneous when processed from nitromethane, acrylonitrile, and DMF, while other five solvents (toluene, methylene chloride, methyl ethyl ketone, acetone, and formic acid) resulted in heterogeneous dispersion. Optical micrographs of the PMMA/SWNT dispersions in nitromethane and in methyl ethyl ketone are given in Figure 2.1 as examples of homogeneous and heterogeneous dispersions, respectively.

SEM in Figure 2.2 show that composites processed from methyl ethyl ketone and methylene chloride are phase separated. Figure 2.2 also shows that the composite processed from nitromethane is more homogeneous than the one from DMF. In fact, of all the eight solvents, the composite processed from nitromethane appears to be the most homogeneous. These observations clearly suggest that solvents do play an important role in obtaining uniform SWNT dispersion in PMMA. From the SWNT/PMMA dispersion study, it is observed that when solvent polar solubility parameter component (δ_p) is higher than the corresponding δ_p value of the polymer, dispersion tends to be more homogeneous. While the total solubility parameter (δ_t), as well as the dispersive component (δ_d) and hydrogen bonding component (δ_h) do not appear to play that significant role in SWNT dispersion.

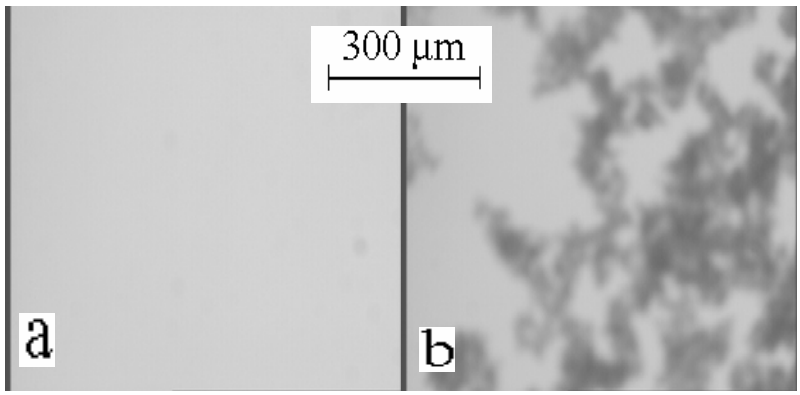

Figure 2.1. Optical micrographs of (a) SWNT/PMMA/nitromethane and (b) SWNT/PMMA/methyl ethyl ketone dispersions.

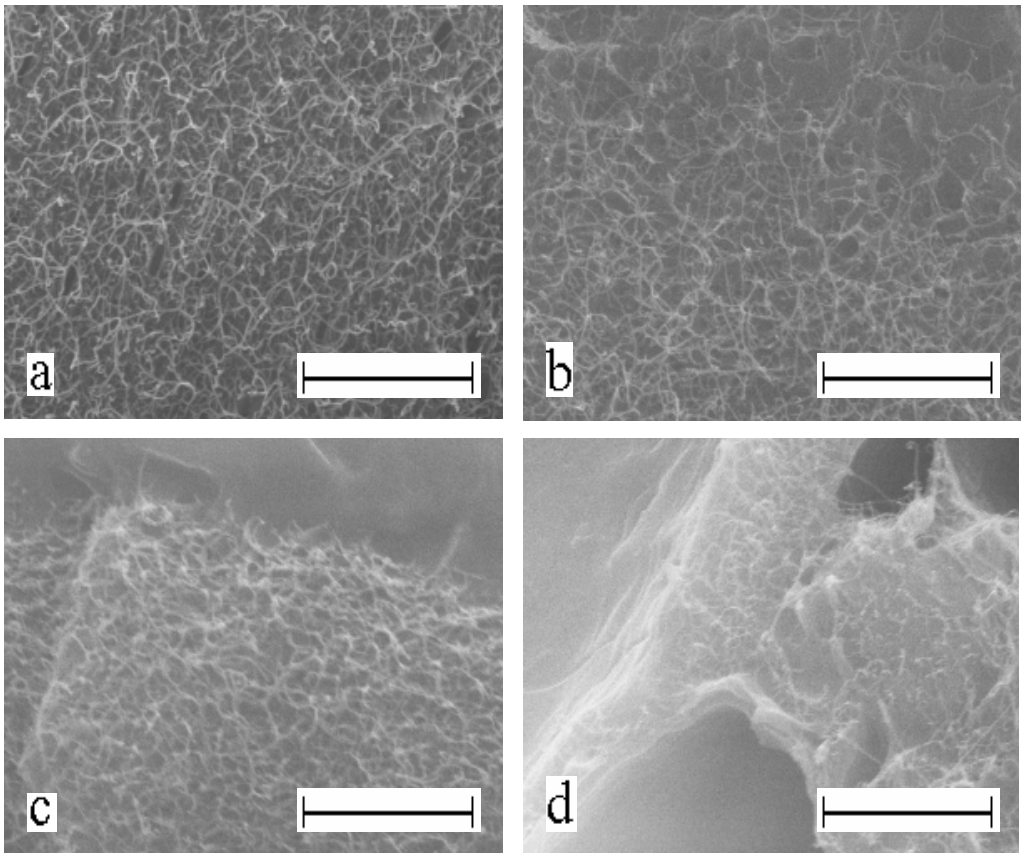

Figure 2.2. SEM images of the PMMA/SWNT composite fracture surfaces. Solvents used for (a) nitromethane, (b) DMF, (c) methyl ethyl ketone, and (d) methylene chloride. (Scale bar is 2 μm).

SWNT are hydrophobic nonpolar rigid-rods. Molecular dynamics simulation suggests continuous and spontaneous filling of a nonpolar carbon nanotube with a one-dimensionally ordered chain of water molecules[208]. There may be an ordered arrangement of polar solvents around nonpolar SWNT and the extent of solvent penetration in the interstices of the SWNT bundle may increase with solvent polarity. The presence of this solvent may become the driving force for the polymer penetration, resulting in good SWNT dispersion.

PMMA/SWNT composites have been studied using Raman spectroscopy to see if differences in SWNT dispersion give a Raman signature. For this purpose, two types of samples were prepared. The first type of samples was dried in the hood for several days. The second type of samples were prepared by heating the hood dried samples in DSC from 25 °C to 150 °C at 5 °C/min and then cooling at the same rate to room temperature, in order to relax any thermal strains in the sample as well as to ensure the removal of any residual solvent. G band shift as a function of $\Delta\delta_p$ ($\delta_{p\text{-solvent}} - \delta_{p\text{-PMMA}}$) is plotted in Figure 2.3. G band of SWNT powder was observed at 1589.5 cm^{-1} while it shifted to higher wave number for PMMA/SWNT composites processed from DMF, acrylonitrile, and nitromethane. No significant change was obtained in the G-band position for five solvents (toluene, methylene chloride, and methyl ethyl ketone, acetone, formic acid) giving optically heterogeneous dispersion, when exposure time of 1 second with 100 accumulations was used for collecting the Raman spectra. For heterogeneous samples G band downshifted when collection time for the Raman spectra was 1 minute. This down shift was a result of sample heating due to prolonged exposure (1 minute) to laser in heterogeneous samples while short exposure times (1 second) did not result in sample heating and hence no change in G band position. By comparison, for the samples exhibiting homogeneous SWNT distribution, G-band displacement was the same for both laser exposure times of 1 minute and 1 second (100 accumulations). This is a result of better heat dissipation due to homogeneous SWNT dispersion. Thus in Figure 2.3, dashed line represents heating effect while solid line is G band shift resulting from differences in SWNT dispersion in PMMA processed from different solvents. If δ_p of the solvent is less than that of the PMMA, the G band position remains the same as that for SWNT powder,

however if δ_p of the solvents is higher than that of PMMA, G band up shifts in proportion to $\Delta\delta_p$ ($\delta_{p\text{-solvent}} - \delta_{p\text{-PMMA}}$).

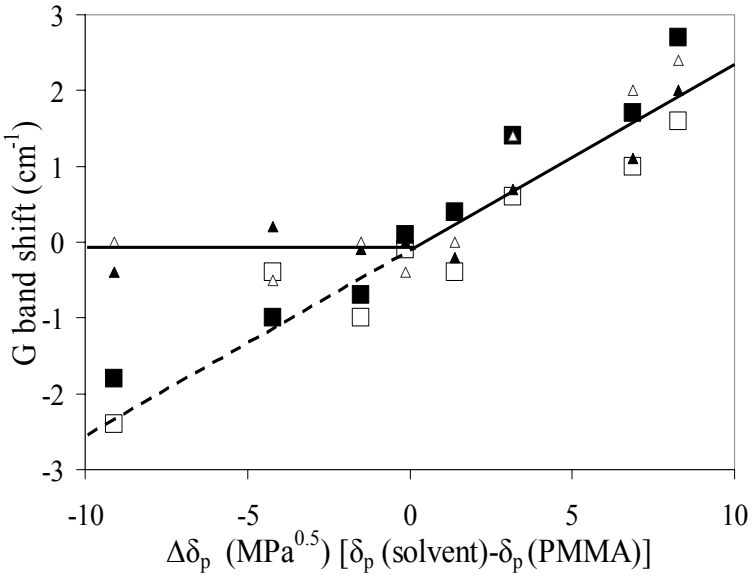

Figure 2.3. G band shift in PMMA/SWNT composites processed in different solvents as a function of $\Delta\delta_p$ (Open squares: thermally treated samples and laser exposure time one minute during Raman experiment. Solid squares: air dried samples and laser exposure time one minute. Open triangles: thermally treated samples and laser exposure time one second with 100 accumulations. Solid triangles: air dried samples and exposure time one second with 100 accumulations).

G band shift for both the air-dried and thermally treated PMMA/SWNT composite samples was the same, indicating the absence of thermal strains. G band up shift for higher solvent δp values indicate compressive strain on individual SWNT or SWNT bundles.

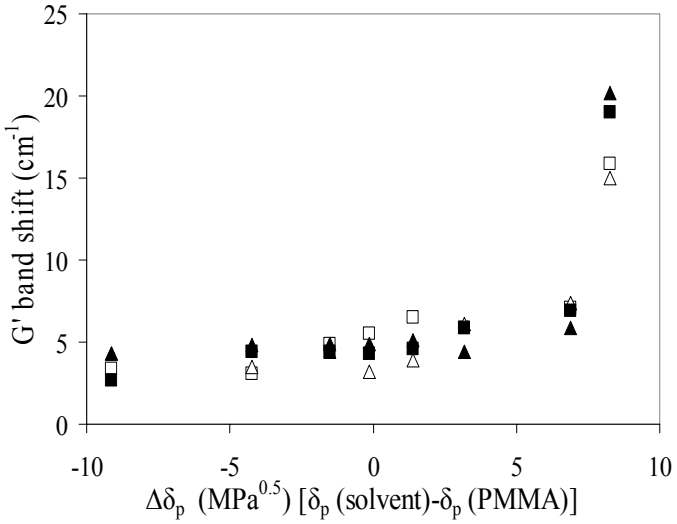

Figure 2.4. G' band shift in the PMMA/SWNT composites as a function of $\Delta\delta_p$ (the symbols have been defined in Figure 2.3).

Using the SWNT G band shift in Figure 2.3, and the G band shift constant of 5.0 cm^{-1}/GPa, about 0.14 GPa compressive stress is predicted on SWNT in PMMA/SWNT composite processed from nitromethane. Sample heating decreases the carbon - carbon bond force constant, and results in G and RBM band down shifts[209]. Temperature coefficient of G band (~-0.038 cm^{-1}/K) is higher than that for the RBM band (~-0.013 cm^{-1}/K)[210]. In qualitative agreement with this observation, for 1 minute exposure time, the difference between RBM peak positions for PMMA/SWNT samples processed from nitromethane and toluene is about 0.7 cm^{-1} wave number, while for the G band this

difference is more than 4 cm^{-1} wave numbers. For the toluene processed film (data in Figure 2.3), temperature increase of about 50 K is predicted in the Raman experiment for the 1 minute exposure time using G band temperature coefficient of ~-0.038 cm^{-1}/K. For 1 minute exposure, temperature effect dominates the $\Delta\delta_p$ less than zero region, and dispersion induced compressive strain effect dominates the $\Delta\delta_p$ greater than zero region.

Figure 2.4 gives the G' band shift of the composites as a function of $\Delta\delta_p$. As the case for G band, G' band shift also increases with $\Delta\delta_p$ and is also a result of compressive strains on the SWNT in the composite. The composite processed from nitromethane has the largest G' shift, by about 15 to 20 cm^{-1} and with absolute value as high as 2591 cm^{-1}.

The Raman spectra in RBM region for the HiPCO™ SWNT and for the PMMA/SWNT composites processed from toluene and nitromethane are plotted in Figure 2.5. No obvious shift in the RBM peak positions was observed within experimental error between the three spectra. This is consistent with the literature results suggesting that RBM peak position is not significantly affected by the strains in the film[211]. Only small variations in the relative RBM intensities were observed when spectra were obtained at different positions on the sample. For SWNT powder and eight composites films, the low-frequency Raman spectra regions were all fitted with six Lorentzian components located at 203, 226, 234, 247, 265 and 267 cm^{-1}. Each component corresponds to one type of nanotube. Using d_t (nm) = 223.5/[ω_{RBM} (cm^{-1})-12.5], which can be applied to nanotubes in bundles[212], nanotube diameters were determined to be in the range from 0.88 nm to 1.17 nm. RBM peak positions, corresponding to SWNT diameters and other properties are listed in Table 2.2.

Table 2.2. The SWNT diameters corresponding to the observed Raman RBM peaks, van Hove transition energy E_{22}^{s}, change in transition energy E_{22}^{s} under compressive strain, and nanotube structural parameters (n, m) and r.

ω_{RBM} (cm^{-1})	d_t(nm)	E_{22}^{s} (eV) *[213]	E_{22}^{s} (eV)**[214]	(n, m)	r	Change in E^{s}_{22} under compressive force
203	1.17	1.40~1.46	1.37	11,6	-1	Decrease
226	1.05	1.53~1.60	1.54	10,5	-1	Decrease
233	1.01	1.59~1.67	1.59	12,1	-1	Decrease
247	0.96	1.70~1.79	1.84	10,3	1	Increase
265	0.89	1.81~1.88	1.85	7,6	1	Increase
267	0.88	1.81~1.90	1.78	10,2	-1	Decrease

Notes: E_{22}^{s} (eV) from Ref. [194], and E_{22}^{s} (eV)** calculated value*
(n, m) are tube chiral vectors, n-m=3q+r, where q and r integer values,
Change in E_{22}^{s} is based on tight binding calculations of Lucas and Young[215], where it has been shown that the change in Van Hove singularities under uniaxial strain depends on the nanotube structure.

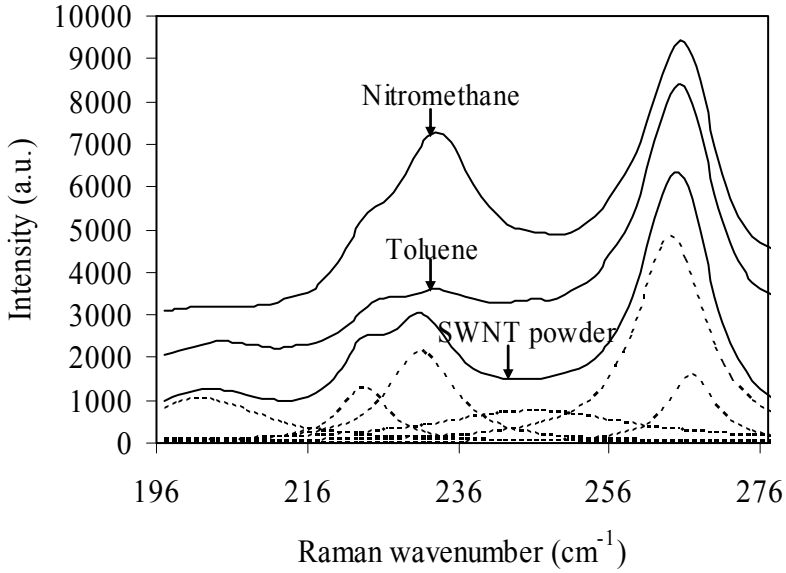

Figure 2.5. RBM bands of SWNT powder and PMMA/SWNT composite films made from toluene and nitromethane. Dotted lines show Lorentzian peak fitting to the SWNT spectra.

Change in 233 cm^{-1} band intensity with solvent δ_p values is plotted in Figure 2.6. Here 233 cm^{-1} band intensity has been normalized to G band intensity. For $\delta_{p\text{-solvent}} < \delta_{p\text{-PMMA}}$, 233 cm^{-1} band intensity remains unchanged. For $\delta_{p\text{-solvent}} > \delta_{p\text{-PMMA}}$, 233 cm^{-1} band intensity increases with increasing solvent δ_p. Same trend was observed if RBM band intensity is normalized to the totally intensity of 265 cm^{-1} and 267 cm^{-1} peaks. The RBM intensity variations in PMMA/SWNT composites result from the effect of compressive strain on resonance. SWNT electronic band structure is modified under strain. This affects resonance condition as E_{ii} shifts closer to or further away from E_{laser}. The RBM intensity increases when the difference $|E_{ii} - E_{laser}|$ decreases and vice versa. The RBM intensity is maximized when E_{ii} is equal to E_{laser}. For r = -1 (see footnote of Table 2.2 for the definition of r), E_{22}^{s} decrease under compressive strain and increase for r = 1. Under

compressive stress, E_{22}^{s} increases for 265 cm^{-1} peak and decreases for 267 cm^{-1} peak and their energy values are relatively far from E_{laser}. Therefore the other peak intensities can be normalized to the total intensity of these two peaks. E_{22}^{s} of 203 cm^{-1} decreases under compression and for the samples processed in nitromethane, the compressive force is the highest. Thus E_{22}^{s} shifts farther away from E_{laser} (1.58 eV), and the peak almost disappears for PMMA/SWNT processed in nitromethane. E_{22}^{s} of 233 cm^{-1} band is between 1.59 eV and 1.67 eV (its theoretical value is 1.59 eV). With compressive strain this energy value decreases and shifts closer to the laser energy value of 1.58 eV. This enhances resonance, and results in increased intensity for the 233 cm^{-1} peak for those samples exhibiting homogeneous SWNT dispersion in PMMA.

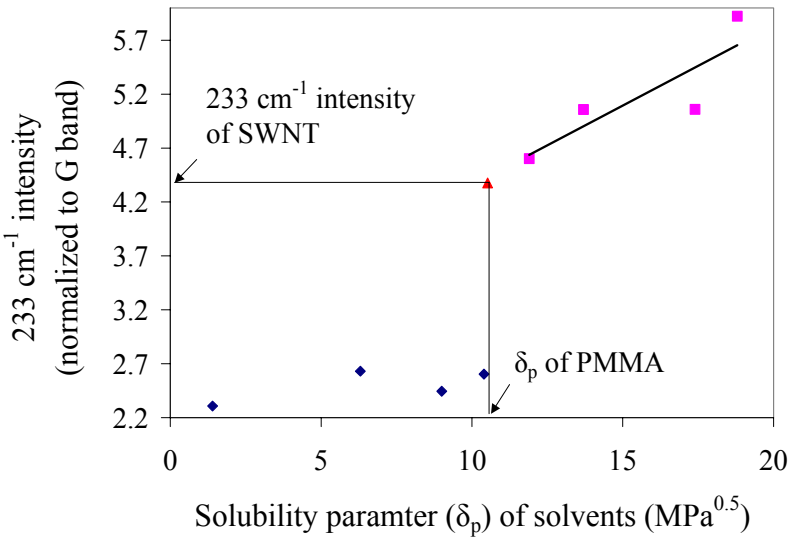

Figure 2.6. 233 cm^{-1} band intensity in the composites as a function of solvent solubility parameter (δ_p).

2.4. Conclusions

Results show that for achieving SWNT/PMMA good dispersion, the polar component (δ_p) of the solubility parameter is most important, while the other components, namely dispersive and hydrogen bonding (δ_d and δ_h), or the total solubility parameter (δ_t) do not appear to be so critical. The best SWNT/PMMA dispersion was achieved in nitromethane, the most polar solvent used in this study. SWNT/PMMA samples exhibiting different degrees of dispersion have been studied using Raman spectroscopy. The intensity variations in the RBM mode, as well as changes in the G and G' band peak positions are consistent with the qualitative dispersion observations obtained from optical microscopy and scanning electron microscopy.

CHAPTER 3

CNT/PMMA COMPOSITES

3.1. Introduction

As discussed in chapter 1, the reported mechanical properties of SWNT/PMMA composite vary over a wide range. In this chapter, a systematic study on the reinforcement of SWNT in PMMA over a wide range of SWNT concentration is reported. Based on the dispersion study in chapter 2, SWNT/PMMA composite films at various SWNT concentrations are processed from nitromethane. Two types of SWNTs are used; SWNT-A containing 35 wt% metal catalyst and SWNT-B with about 2.4 wt% metal catalyst. Electrical and mechanical properties enhancements upon adding SWNT into PMMA matrix are expected. The structure, morphology, and properties of SWNT/PMMA composites are discussed. A comparison between properties of SWNT-A/PMMA, SWNT-B/PMMA, MWNT/PMMA, and VGCNF/PMMA composites is also discussed.

3.2. Experimental

Two types of HiPCO^{TM} SWNT received from CNI, were used without further purification (SWNT-A: Lot # R0231 with 35 wt% metal catalyst and SWNT-B: Lot # XO021UA with 2.4 wt% metal catalyst). Multi wall carbon nanotube (MWNT) was purchased from Iljin Nanotech, Co. (Korea), and vapor grown carbon nanofiber (VGCNF) (PR-24-HT) was bought from Applied Sciences, Inc. (Cedarville, OH). TGA of SWNT-A, SWNT-B, MWNT, and VGCNF in air with a heating rate of 10 °C/min is shown in Figure 3.1. The decomposition temperature of SWNT-A, SWNT-B, MWNT,

and VGCNF are determined as 422 °C, 570 °C, 626 °C, and 738 °C, respectively. PMMA ($\overline{M_w} = 95{,}000 \sim 150{,}000$ g/mole) was obtained from Cyro Industries and used as received. Nitromethane and toluene were purchased from Sigma- Aldrich Co. and also used as received. CNTs were dispersed in nitromethane by sonication (Sonicator: Branson 3510, Branson Ultrasonic Corp., Danbury CT) for a certain amount of time until optically homogenous solution was achieved. To this uniform SWNT/nitromethane dispersion, PMMA/nitromethane solution (5 ml) was added and mixed by stirring. The optically homogenous PMMA/SWNT/nitromethane solution was casted onto a glass substrate to form 20 to 25 μm thick films. PMMA/SWNT composite films at different SWNT loadings were prepared. Control PMMA film was also prepared using the same procedure. The resulting films were dried under vacuum at 80 ^{o}C for 2 days to remove any traces of solvent.

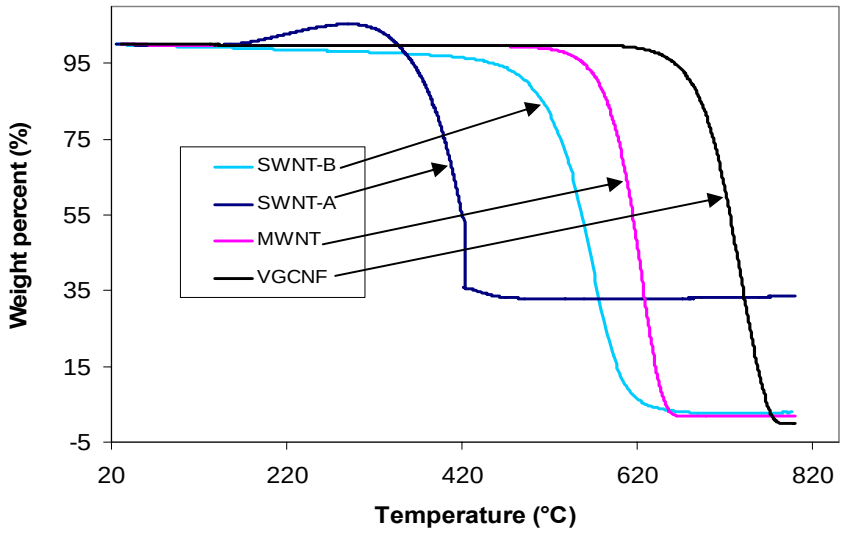

Figure 3.1. Thermogravimetry analysis (TGA) plots of SWNT-A, SWNT-B, MWNT, and VGCNF in air at a heating rate of 10 °C/min.

For SEM experiments, films were cut by a new sharp blade. SEM imaging was conducted on gold coated cross section of the films using LEO 1530 Scanning Electron Microscope. Transmission electron microscopy (TEM) was conducted using Hitachi HF-2000 (operated at 200 kV). For TEM specimen preparation, the SWNT powders were sonicated in ethanol for 10 minutes and then a droplet of the dispersion was placed on the TEM grids using a loop (lacey carbon coated copper grids, Electron Microscopy Sciences). The SWNT-B/PMMA composite film (3.53 mg) was soaked in toluene (4 ml) for 5 days to completely disintegrate the film and then additional toluene (20 ml) was used to dilute a little drop of the suspension. A droplet of the diluted suspension was collected on TEM grid using a loop. RSA III (Rheometrics Scientific) was used to measure the tensile properties and the dynamic mechanical properties. The gauge length, film width, and strain rate for the tensile test was 15 mm, 5 mm, and 10 %/min, respectively. Dynamic mechanical analysis (DMA) was conducted at 0.1, 1.0 and 10.0 Hzusing temperature increment of 2 ^{o}C/min. The glass transition temperature (T_g) of the films was measured by both DSC (TA Instruments DSC100) and DMA. Coefficient of thermal expansion (CTE) was determined using TMA (TA Instruments TMA Q400) at 0.35 MPa stress on 8 mm long and 2 mm wide films at a heating rate of 5 ^{o}C/min. Thermogravimetric analysis (TGA) (TA Instruments TGA 2950) of various films was conducted in air (or in nitrogen) at a heating rate of 10 ^{o}C/min. In plane dc electrical conductivity was measured by four-probe method. The Raman spectra were collected on Holoprobe Research Raman microscope made by Kaiser Optical Systems Inc., using 785 nm excitation wavelength (E_{laser}=1.58 eV).

3.3. Results and discussion

3.3.1 SWNT-A/PMMA

Study of SWNT-A dispersion in PMMA using different solvents (chapter 2) shows that uniform dispersion of SWNT can be achieved by using nitromethane as the solvent. The recipe of two SWNT-A/PMMA composite films prepared by using different nanotube loadings and preparation conditions are given in Table 3.1. TEM image of SWNT-A powder is given in Figure 3.2.. The average size of the metal catalyst in SWNT-A is 4 ± 1 nm. SEM images of the cross sections of these two composite films (Figure 3.3) provide clear evidence of uniform dispersion of nantoubes in PMMA matrix.

Table 3.1. Recipe and preparation conditions of PMMA and SWNT-A/PMMA composite films.

SWNT-A (wt%)	SWNT-A (mg)	PMMA (mg)	Nitromethane (ml)	Sonication time (hrs)	Stirring time (hrs)
0	0	300	15	0	4
10	30	270	40	48	4
15	45	255	60	48	4

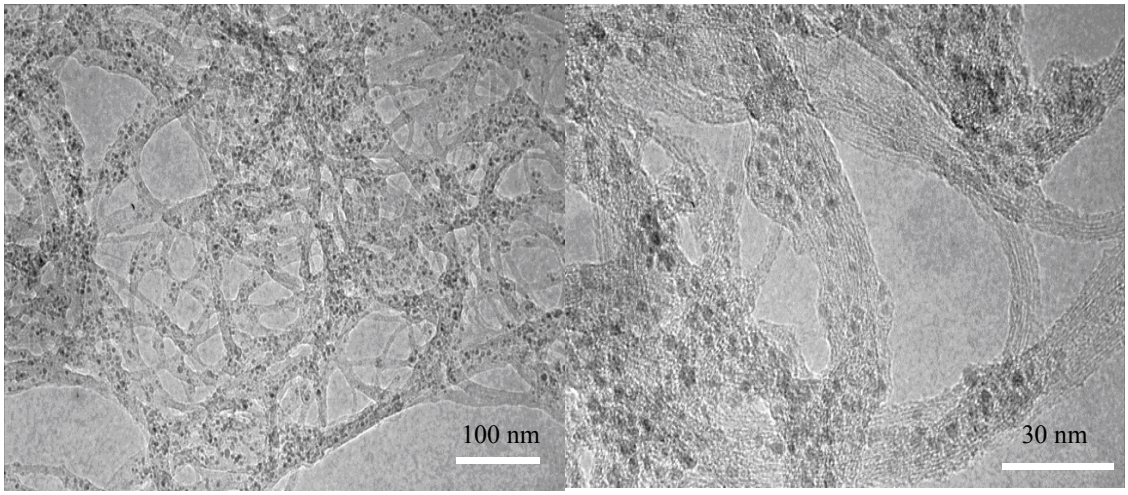

Figure 3.2. TEM images of SWNT-A powder.

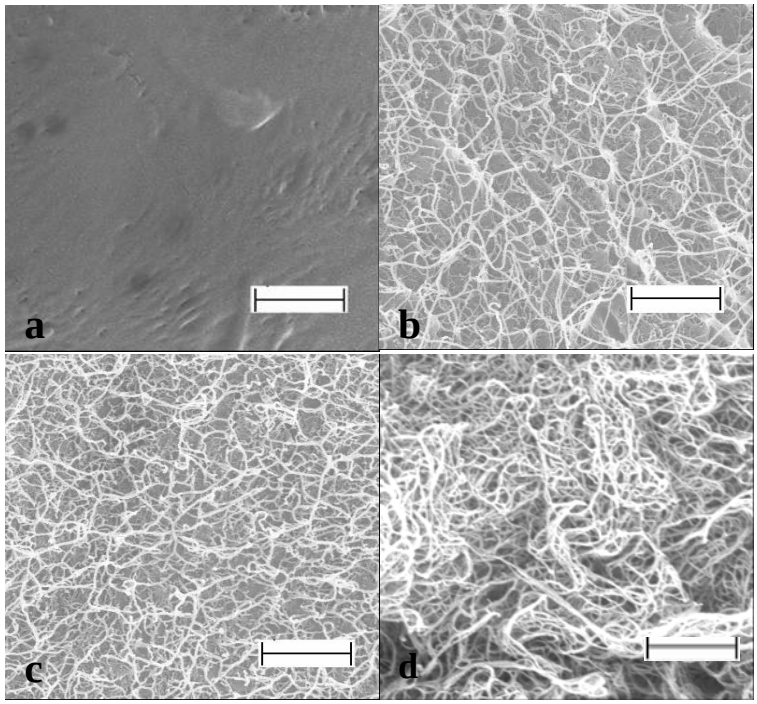

Figure 3.3. SEM images of the cross sections of SWNT-A/PMMA composite films at various SWNT-A loadings (a) 0 wt%, (b) 10 wt%, (c) 15 wt%, and (d) SWNT-A powder, respectively (scale bar is 1 μm).

The DSC curves of PMMA and SWNT-A/PMMA composite films are shown in Figure 3.4. The glass transition temperature (T_g) obtained from DSC curves are given in Table 3.2. An increment of about 3 °C in the T_g of composite with 10 wt% nanotube loading over that of pure PMMA is observed. For the composite with 15 wt% carbon nanotube loading, the enhancement in T_g is about 6 °C. Enhancement in the glass transition temperature for SWNT-A/PMMA composite indicates restricted segmental mobility of the polymer chains in the presence of nanotubes. The hindrance in polymer chain mobility in the composite could only be possible when the polymer chains are in close proximity of nanotubes.

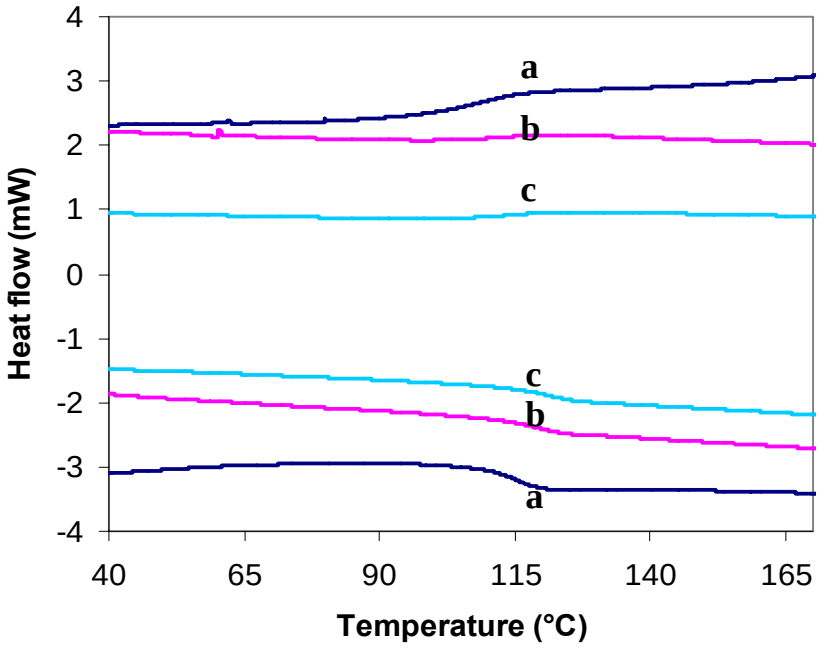

Figure 3.4. DSC curves (the second heating cycle - bottom curves and the first cooling cycle – top curves) of PMMA and SWNT-A/PMMA films at different SWNT-A loadings: (a) 0 wt%, (b) 10 wt%, and (c) 15 wt% (The curves have been vertically shifted for clarity).

Table 3.2. Glass transition temperature (T_g) of PMMA and SWNT-A/PMMA composite films determined by DSC.

	T_g (°C)	
SWNT-A (wt%)	2nd heating cycle	1st cooling cycle
0	114.6	107.5
10	118.0	110.8
15	120.2	114.4

Table 3.3. Mechanical properties and densities of control PMMA and SWNT-A/PMMA composite films.

SWNT-A (wt%)	Tensile modulus (GPa)	Tensile strength (MPa)	Elongation to break (%)	Density (g/cm^3)
0	1.8 ± 0.1	50 ± 8	3.5 ± 0.5	1.01
10	5.1 ± 0.3	51 ± 11	0.9 ± 0.2	1.05
15	4.1 ± 0.2	23 ± 12	0.6 ± 0.3	1.07

The mechanical properties of PMMA, and SWNT-A/PMMA composite films are listed in Table 3.3. The elongation to break of SWNT-A/PMMA composite films is lower when compared to the control PMMA film. This is consistent with studies on CNT composite films with PAN and PVA[33, 216]. Tensile moduli of the composite films are higher than that of control PMMA film. For the composite with 10 wt% nanotube, the tensile modulus is almost three times that of the pure PMMA. However, the reinforcement efficiency of the composite with higher loading of CNT (15 wt%) is not

that significant, indicating an optimal SWNT-A loading in reinforcing the polymer matrix under the present processing condition. This phenomenon has been observed for CNT reinforced composites[95], where an optimum CNT loading exist for a maximum enhancement in mechanical property. The tensile strength does not increase upon adding 10 wt% SWNT-A in PMMA. For composite with 15 wt% nanotube, the tensile strength decreases to 50 % of the strength of the control PMMA sample.

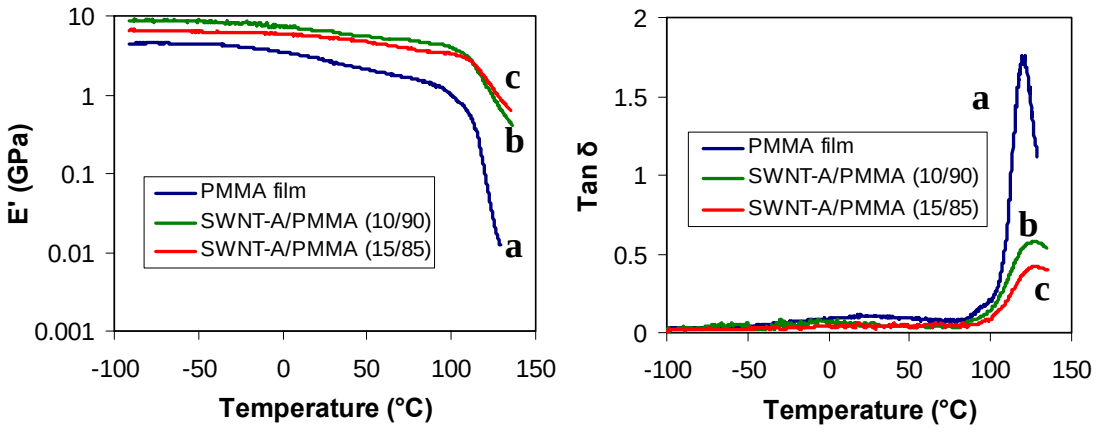

Figure 3.5. Storage modulus (E′) and tanδ behavior of PMMA and SWNT-A/PMMA composite films as a function of temperature ((a) PMMA film, (b) SWNT-A/PMMA (10/90), and (c) SWNT-A/PMMA (15/85)).

The storage modulus (E') and tan δ curves for PMMA and composite films obtained from dynamic mechanical analysis are given in Figure 3.5. Based on tan δ peak position, glass transition temperature (Tg) of the composite films with 10 wt% and 15 wt% nanotube loading is 129 ^{o}C, while that of the control PMMA film is 121 ^{o}C. Tan δ peaks of the composite films become broader and their magnitudes decrease compared to the pure PMMA film. The magnitude of tan δ peak for

PMMA film, SWNT-A/PMMA (10 wt%) film, and SWNT-A/PMMA (15 wt%) film is 1.78, 0.58, and 0.42, respectively. The decrease in tan δ magnitude for the composite films suggests suppression of PMMA molecular motion above the glass transition temperature[32, 217, 218]. SWNT-A/PMMA (10 wt%) has a storage modulus 40 times the storage modulus of PMMA at 125 ^{o}C.

Using tensile modulus of the composite (E_c) and tensile modulus of PMMA matrix (E_m) values in Table 3.3 and Halpin-Tsai equations given in chapter 1, length to diameter ratio of nanotube, l_{NT}/d_{NT} in the composite (SWNT-A/PMMA 10 wt%) is calculated to be 25, and then the average effective length of the bundle (l_{NT}) (diameter of SWNT-A bundle is 26 ± 2 nm, determined by SEM image in Figure 3.3 b) is around 652 nm. For 15 wt% SWNT-A/PMMA sample, the average effective length of the SWNT-A bundle (l_{NT}) is calculated to be 211 nm. These calculated nanotube lengths are not the true length of SWNT-A. The true length of SWNT should be the same in both samples since the same SWNT-A batch of nantoubes and the identical sample preparation methods are used in these two cases.

For 10 wt% and 15 wt% SWNT-A/PMMA composite films, the electrical conductivity values are 920 S/m and 1430 S/m, respectively. The electrical conductivity of these composite films is comparable to those of the electrically conducting polymers such as polyaniline (10^3 S/m)[219]. The high electrical conductivity values indicate formation of conducting network by nanotubes in PMMA matrix (Figure 3.3 b and c).

The poor reinforcement efficiency at higher nanotube loading is not very well understood. The presence of high concentration metal catalyst in the nanotubes is a possible reason. To exclude or minimize the possibility of any detrimental effects posed

by the presence of metal catalyst in the nanotubes, SWNT with much lower catalyst content (2.4 wt%) is used in the next phase of this study.

3.3.2 SWNT-B/PMMA

Composite films with different loadings of SWNT-B (0.5 wt%, 1.0 wt%, 5.0 wt%, 10.0 wt%, 15.0 wt%, 20.0 wt%, 35.0 wt%, and 50.0 wt%) were processed according to the experimental conditions listed in Table 3.4. A control PMMA film was also prepared.

Table 3.4. Recipe and preparation conditions for PMMA and SWNT-B/PMMA composite films.

SWNT-B (wt%)	SWNT-B (mg)	PMMA (mg)	Nitromethane (ml)	Sonication time (hrs)	Stirring time (hrs)
0	0	300	15	0	4
0.5	1.5	300	15	24	4
1	3	297	15	24	4
5	15	285	20	48	4
10	30	270	40	48	4
15	45	255	60	48	4
20	75	225	100	48	4
35	105	195	140	48	4
50	150	150	200	48	4

SWNT-B/PMMA films were processed under the same conditions as SWNT-A/PMMA films. SWNT-B was dispersed in nitromethane by sonication for a certain

amount of time. To this optically homogenous SWNT-B/nitromethane dispersion, PMMA/nitromethane solution (5 ml) was added and then mixed by magnetic stirring for four hours. Optical micrographs of SWNT-B/nitromethane and SWNT-B/PMMA/nitromethane dispersions are shown in Table 3.5., which indicate homogeneous dispersion of SWNT-B in the PMMA/SWNT-B/nitromethane solution. The optically homogenous SWNT-B/PMMA/nitromethane solution was cast onto a glass substrate to form films with the thickness ranging from 20 to 25 μm. Due to relatively large amount of solvent to SWNT is used for 0.5 wt% and 1.0 wt% samples, the sonication time is 24 hours for these two samples, while for higher nanotube loading samples, the sonication time is 48 hours. Longer sonication time might shorten the SWNT-B length. The ratio of SWNT-B to nitromethane and the sonication time are kept the same for the composites with SWNT-B loadings higher than 1.0 wt%. Due to the same carbon nanotube to solvent ratio, same sonication time, and the same stirring time, the SWNT-B length in the samples with nanotube concentration greater than 5 wt% composite samples are expected to be the same. The properties of these composites can be meaningfully compared since they have been prepared by identical procedure. For 20.0 wt% sample, a layer-by-layer method was employed for film casting. First 50 ml SWNT-B/PMMA/nitromethane solutions was casted on the glass substrate and the solvent was allowed to evaporate at room temperature. After 12 hours, another 50 ml solution was cast onto this film and allowed to dry, resulting in the final film. For both 35 wt% and 50 wt% samples, a similar layer by layer method was utilized to obtain the final film. By using layer by layer method, one can avoid the use of heating for solvent evaporation. The samples with 15 wt%, 20 wt%, 35 wt%, and 50 wt% nanotube have

one, two, three, and four layers, respectively. The SEM images of cross sections of 15 wt% and 50 wt% samples are shown in Figure 3.6. In both composite films, uniform dispersion of nanotubes in PMMA matrix is evident suggesting the quality of dispersion is similar for SWNT/PMMA composite films prepared by one-layer method or a layer-by-layer method. Control PMMA film was also prepared using the same procedure. The films were dried at room temperature in air for 4 days. The resulting films were dried under vacuum oven at 80 ^{o}C for 2 days to remove traces of solvent. SWNT-B (100 wt%) buckypaper was prepared by using DMF as solvent[220].

Table 3.5. Optical micrographs of SWNT-B/nitromethane and SWNT-B/PMMA/nitromethane dispersions.

SWNT-B (wt%)	SWNT-B/nitromethane sonication for 12 hrs	SNWT-B/nitromethane sonication for 24 hrs	SWNT-B/PMMA /nitromethane, sonication for 24 hrs, and stirring for 4 hrs
0.5			
1			
	SWNT-B/nitromethane sonication for 24 hrs	SNWT-B/nitromethane sonication for 48 hrs	SWNT-B/PMMA /nitromethane, sonication for 48 hrs, and stirring for 4 hrs
5	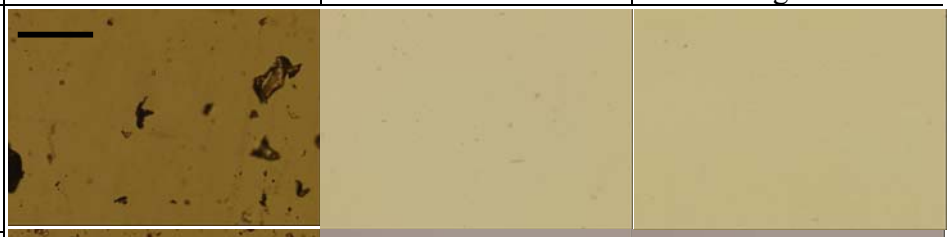		
10	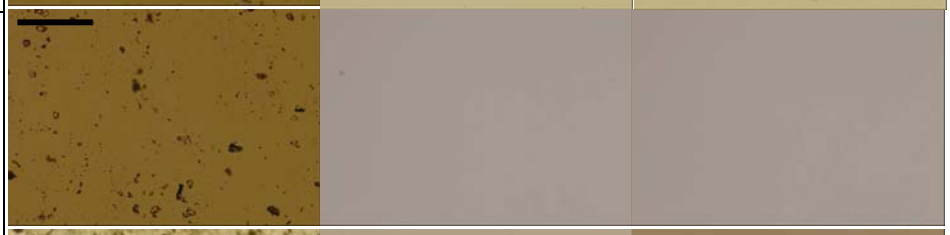		
15			

(Scale bar: 200 μm)

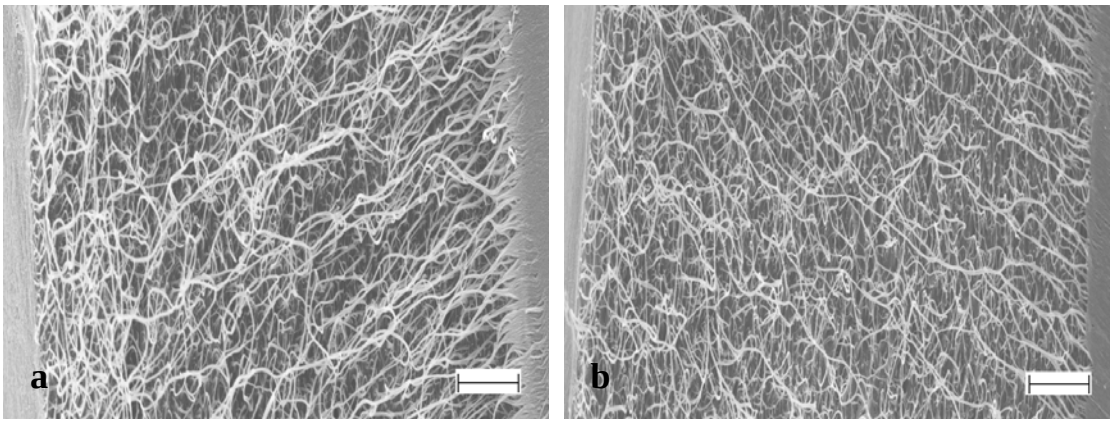

Figure 3.6. SEM images of the cross sections of the SWNT-B/PMMA composite films at different SWNT-B concentrations (a) 15 wt% and (b) 50 wt% (scale bar is 2 μm).

SEM images of the cross sections of the composite films (Figure 3.7.) show uniform dispersion of nanotubes in PMMA even at higher nanotube loadings. In all samples, diameter of SWNT-B bundles was 30 ± 5 nm.

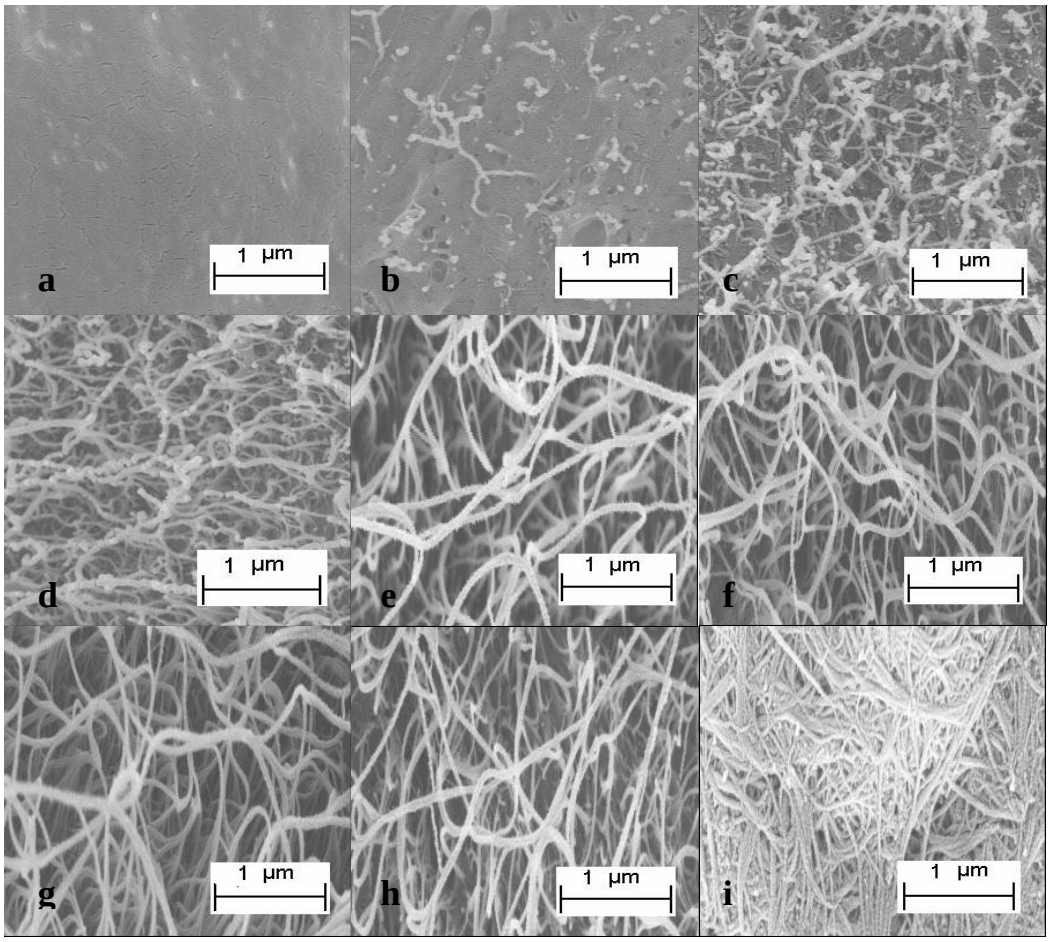

Figure 3.7. SEM images of the cross sections of SWNT-B/PMMA composite films at various SWNT-B concentrations: (a) 0.5 wt%, (b) 1.0 wt%, (c) 5.0 wt%, (d) 10.0 wt%, (e) 15.0 wt%, (f) 20.0 wt%, (g) 35.0 wt%, (h) 50.0 wt%, and (i) SWNT-B powder, respectively.

TEM images of SWNT-B powder are given in Figure 3.8 (a) and (b) and SWNT-B/PMMA (5 wt%) composite film dissolved in toluene is shown in Figure 3.8 (c) and (d). From these TEM images, one can see that there is no clear evidence of PMMA wrapping or covering onto SWNT-B bundles. In literature, several different coating of polymers onto SWNTs have been reported. These include, polyacrylonitrile[221], polycarbonate[222], polystyrene[65], and are shown in Figure 3.8 (a), (b), and (c),

respectively. The polymer coating behavior might be an indication of strong interaction between polymer and SWNT. This may suggest that the PMMA-SWNT interaction is weaker than the SWNT interaction with polyacrylonitrile, poslystyrene, or polycarbonate.

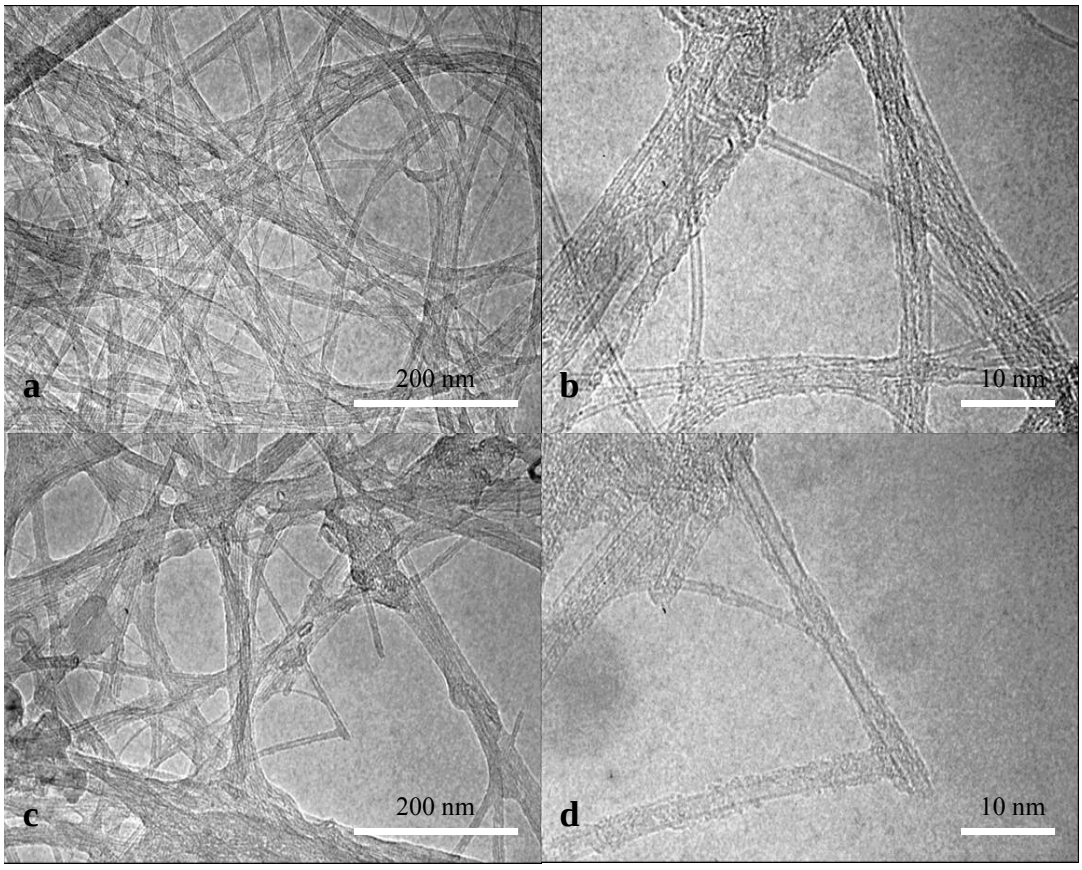

Figure 3.8. TEM images of SWNT-B powder ((a) and (b)) and SWNT-B/PMMA (5 wt% SWNT-B loading) composite film ((c) and (d)).

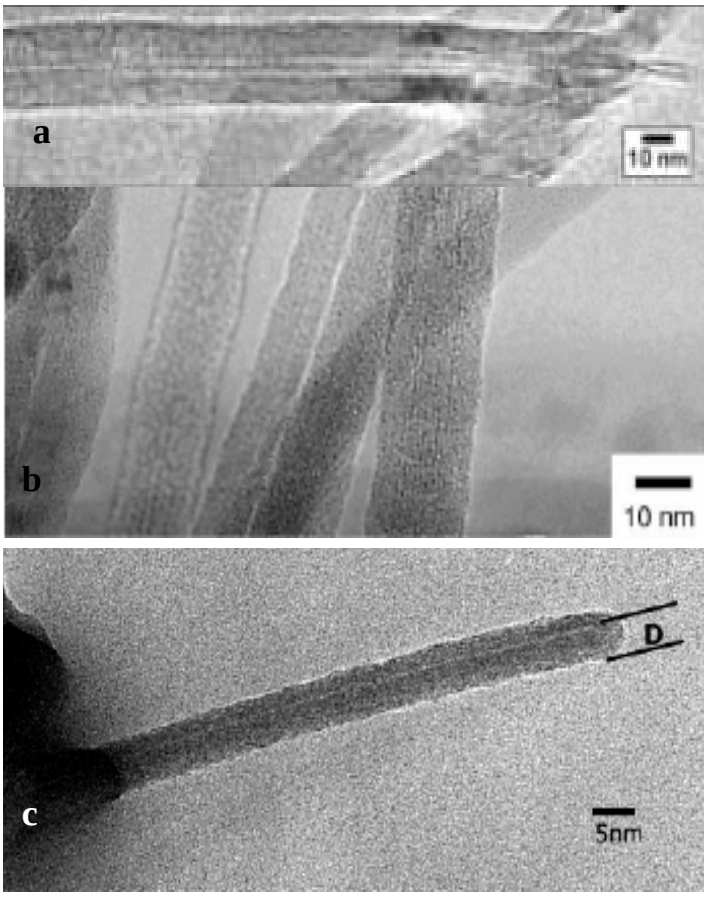

Figure 3.9. TEM images of polymer wrapping SWNT: (a) SWNT/polyacrylonitrile (Reproduced from reference [221]), (b) SWNT/polycarbonate (Reproduced from reference [222]), and (c) SWNT/polystyrene (Reproduced from reference[65]).

Table 3.6. Electrical conductivity values of SWNT-B/PMMA composite films at different SWNT-B concentrations.

SWNT-B (wt%)	Electrical conductivity (S/m)
0	1.0E-14[223]
0.5	7.9E-5
1	7
5	126
10	456 (920)*
15	854 (1430)*
20	1435
35	3574
50	5783

* Electrical conductivities of SWNT-A/PMMA composites are given in the brackets.

The electrical conductivity values of SWNT-B/PMMA composite films at different nanotube loadings are given in Table 3.6. Since the densities of PMMA and SWNT are comparable (the density of PMMA is 1.2 g/cm^3 and the density of SWNT with 1 nm diameter is 1.3 g/cm^3), the volume fraction of SWNT-B is taken to be the same as its weight fraction value. The inset of Figure 3.10 is the plot of conductivity as a function of SWNT-B volume fraction (V), from which a percolation volume (Vc) of 0.5 % is obtained. Plotting electrical conductivity as a function of (V-Vc) (Figure 3.10) results in an exponent of 1.73, which indicates three dimensional percolation behaviors.

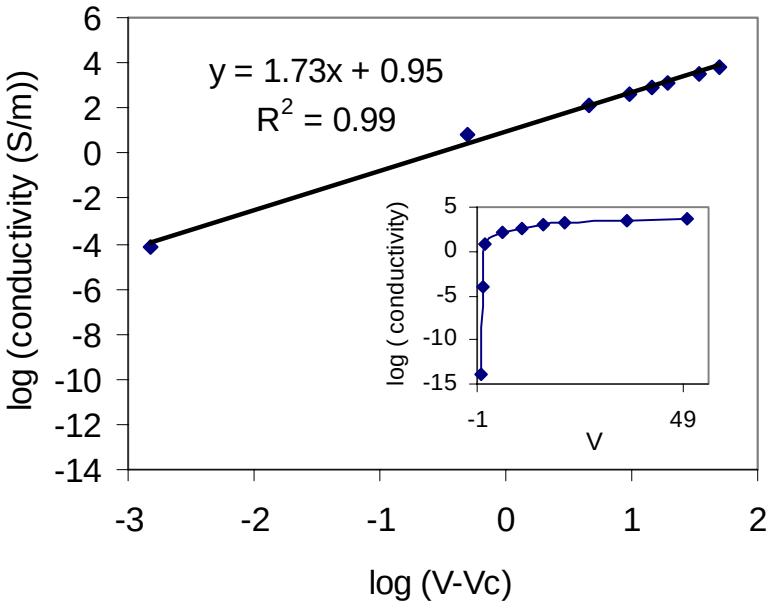

Figure 3.10. Electrical conductivity of PMMA and SWNT-B/PMMA composites.

At the same SWNT loading, SWNT-A/PMMA has higher electrical conductivity than SWNT-B/PMMA composites. The metal catalyst may contribute to this electrical conductivity difference. Carbon coated iron carbide nanoparticles with approximately 100 nm size embedded in polyvinyl chloride has a percolation value of 2.2 wt%[224]. The size of the metal catalyst in SWNT-A is about 4 nm determined from TEM image (Figure 3.2.). For SWNT-A/PMMA (10/90), the catalyst concentration in the composite is about 3.5 wt% in PMMA, while for 15 wt% SWNT-A/PMMA sample, the catalyst concentration in the composite is 5.3 wt%. The amount of metal catalyst in the composite (3.5 w% or 5.3 wt%) is already above its percolation value, which forms electrical conductivity network in PMMA matrix. SWNT-A in both 10 wt% and 15 wt% samples form an electrically conductive network in PMMA matrix. These two electrically

conductive networks (SWNT-A and metal catalyst) interplay with each other in PMMA resulting in higher electrical conductivity than SWNT-B/PMMA at the same SWNT loading.

Table 3.7. Tensile properties and densities of PMMA, SWNT-B/PMMA composites, and SWNT-B buckypaper.

SWNT-B (wt%)	Tensile modulus (GPa)	Tensile strength (MPa)	Elongation to break (%)	Density (g/cm^3)
0	1.8 ± 0.1	50 ± 8	3.5 ± 0.5	1.01
1	2.3 ± 0.2	53 ± 9	2.8 ± 0.3	1.03
5	3.4 ± 0.2	56 ± 10	2.5 ± 0.4	1.02
10	4.4 ± 0.2	63 ± 8	2.5 ± 0.7	1.06
15	5.3 ± 0.2	71 ± 1	2.4 ± 0.2	1.03
20	5.8 ± 0.2	80 ± 9	2.1 ± 0.5	1.03
35	6.7 ± 0.5	105 ± 8	2.5 ± 0.2	1.01
50	5.7 ± 0.1	86 ± 8	1.8 ± 0.1	1.01
100[220]	2.6 ± 0.2	21 ± 4	1.6 ± 0.5	----

The tensile properties of PMMA, SWNT-B/PMMA composites and SWNT-B buckypaper and their densities are given in Table 3.7. The elongation to break decreased with the addition of SWNT-B. However, at the same nanotube loading, elongation at break is higher for SWNT-B/PMMA composite as compared to SWNT-A/PMMA composite. The difference in elongation to break in the composite and buckypaper

prepared from SWNT-A and SWNT-B can be attributed to higher metal catalyst in SWNT-A. Tensile modulus and tensile strength of the composite films are higher than that of the control PMMA film or control SWNT-B buckypaper. The tensile modulus for SWNT-B/PMMA composite film containing 15 wt% SWNT-B increased by almost 300 % from 1.8 GPa for PMMA to 5.3 GPa for the composite. The tensile strength of this composite increased by 150 % from 50 MPa to 71 MPa. For the composite film containing 35 wt% nanotube, the tensile modulus increased by 400 % and tensile strength increased by ~ 100 %. With 35 wt% SWNT-B loading, the tensile modulus and tensile strength of the composite reach the maximum values. At nanotube loading of 50 wt%, tensile modulus and tensile strength values are lower than that of 35 wt% composite. This suggests that using the current processing scheme the optimum nanotube loading for reinforcing PMMA is about 35 wt%.

Effective reinforcement segment length (l_{NT}) of CNT is calculated using Halpin-Tsai equations (given in chapter 1) and the values are listed in Table 3.8.. To calculate l_{NT}, E_c (tensile modulus of the composite at various SWNT-B loading) and E_m (tensile modulus of PMMA matrix) values are considered as given in Table 3.7, E_{NT} is considered as 640 GPa[13] and d_{NT} (nanotube bundle diameter) = 30 nm as measured from the SEM images. The l_{NT} for the composite containing 1 wt% SWNT-B is calculated to be 1470 nm using equations 1-5 in chapter 1. The values of l_{NT} decreases with increasing SWNT-B loading, and at 50 wt% nanotube loading, Halpin-Tsai equations yield a negative value of l_{NT}. It should be emphasized here that l_{NT} is not the true or actual length of the nanotubes in the composite, but it can be considered as the effective nanotube length responsible for reinforcement in the composite system.

MWNT [225] was investigated as mechanical reinforcement agents in two hosts, polyvinyl alcohol (PVA) and poly (9-vinyl carbazole) (PVK). Based on Halpin–Tsai equations, the aspect ratio l_{NT}/d_{NT} was calculated to be 800 and 40 for the PVA and PVK composites, respectively. The results were unexpected as the same batch of MWNT was used in both the PVA and PVK composites. The true aspect ratio, as measured by TEM was close to 100. Based on these results, it was inferred that the interfacial bonding of nanotube is superior in case of PVA than in PVK. Other experimental evidence for MWNT/PVA and SWNT/polypropylene composites[226] have also shown disagreements in measured modulus and CNT lengths and the predicted values based on the Halpin–Tsai model.

Halpin-Tsai equation is derived based on the assumption that stress transfer between polymer matrix and nanotube is perfect. Therefore any difference in the calculated and measured values of l_{NT}/d_{NT} ratios in different composites can be attributed to differences in interfacial strength in different systems or in the same system at different nanotube loading. The difference in l_{NT}/d_{NT} for PVA and PVK[227] composites at similar CNT loading was interpreted as difference due to interfacial interaction. In this study, the difference in predicted l_{NT} can not be attributed to interaction between nanotube and polymer, since all the composite systems in this study utilize the same polymer with varying amounts of nanotube loading. The decrease in effective nanotube reinforcement length may in turn be considered a result of change in interfacial strength with varying nanotube loading.

Table 3.8. Tensile modulus of SWNT-B/PMMA composite and the calculated effective reinforcement segment length l_{NT} (nm) of SWNT-B in the composite films.

SWNT-B (wt%)	Tensile modulus (GPa)	Effective reinforcement segment length l_{NT} (nm)
1	2.3 ± 0.2	1469
5	3.4 ± 0.2	779
10	4.4 ± 0.2	556
15	5.3 ± 0.2	448
20	5.8 ± 0.2	334
35	6.7 ± 0.5	138
50	5.7 ± 0.1	-2

Table 3.9. Tan δ peak temperature (P) and tan δ magnitude (M) for PMMA and SWNT-B/PMMA films at different frequencies and the calculated activation energies.

SWNT-B (wt%)	Tan δ peak (0.1 Hz)		Tan δ peak (1 Hz)		Tan δ peak (10 Hz)		Activation energy (kJ/mole)
	P (°C)	M	P (°C)	M	P (°C)	M	
0	113	1.99	121	1.74	124	1.00	497
5	114	0.85	122	0.72	124	0.48	523
10	115	0.43	123	0.40	128	0.33	449
15	123	0.43	130	0.35	137	0.32	444
20	124	0.35	129	0.29	138	0.28	436
35	128	0.21	133	0.20	137	0.19	501
50	128	0.20	132	0.15	140	0.15	479

Tan δ and storage modulus curves of PMMA and composite films as a function of temperature are shown in Figure 3.11 and Figure 3.12. E' (GPa) of PMMA and composite films at different temperatures at a frequency of 1 Hz are given in Appendix A. 1. For a given SWMT-B/PMMA composite, tan δ peak position shifts to higher temperature upon increasing the test frequency, and its magnitude decreases (Table 3.9). At a given frequency, tan δ peak position shifts to higher temperature and its magnitude decreases with increasing SWNT-B loading. The decrease in tan δ magnitude suggests suppression of PMMA molecular motion above the glass transition temperature[32, 217, 218]. SWNT-B/PMMA (15 wt%) storage modulus is 91 times the storage modulus of PMMA at 125 °C. The ratio E'(SWNT-B/PMMA) / E' (PMMA) as a

function of temperature is plotted in Figure 3.13. E'(SWNT-B/PMMA composite)- E' (PMMA matrix) as a function of temperature is plotted in Appendix A. 2. Figure 3.13 clearly indicates that above the glass transition temperature of PMMA, the ratio E'(SWNT-B/PMMA composite) / E' (PMMA matrix) increases dramatically. The glass transition activation energies calculated from the Tan δ vs temperature plots at three frequiencies using Arrhenius Equation ($f = A\exp(\frac{-\Delta H}{RT})$; f = frequency, ΔH = activation energy, A is a constant, T = temperature, and R = gas constant (8.314 J/ (mol.K))) for various samples are listed in Table 3.9. The activation energy plots are shown in Appendix A. 3. The activation energies of SWNT-B/PMMA composites are comparable with that of PMMA film.

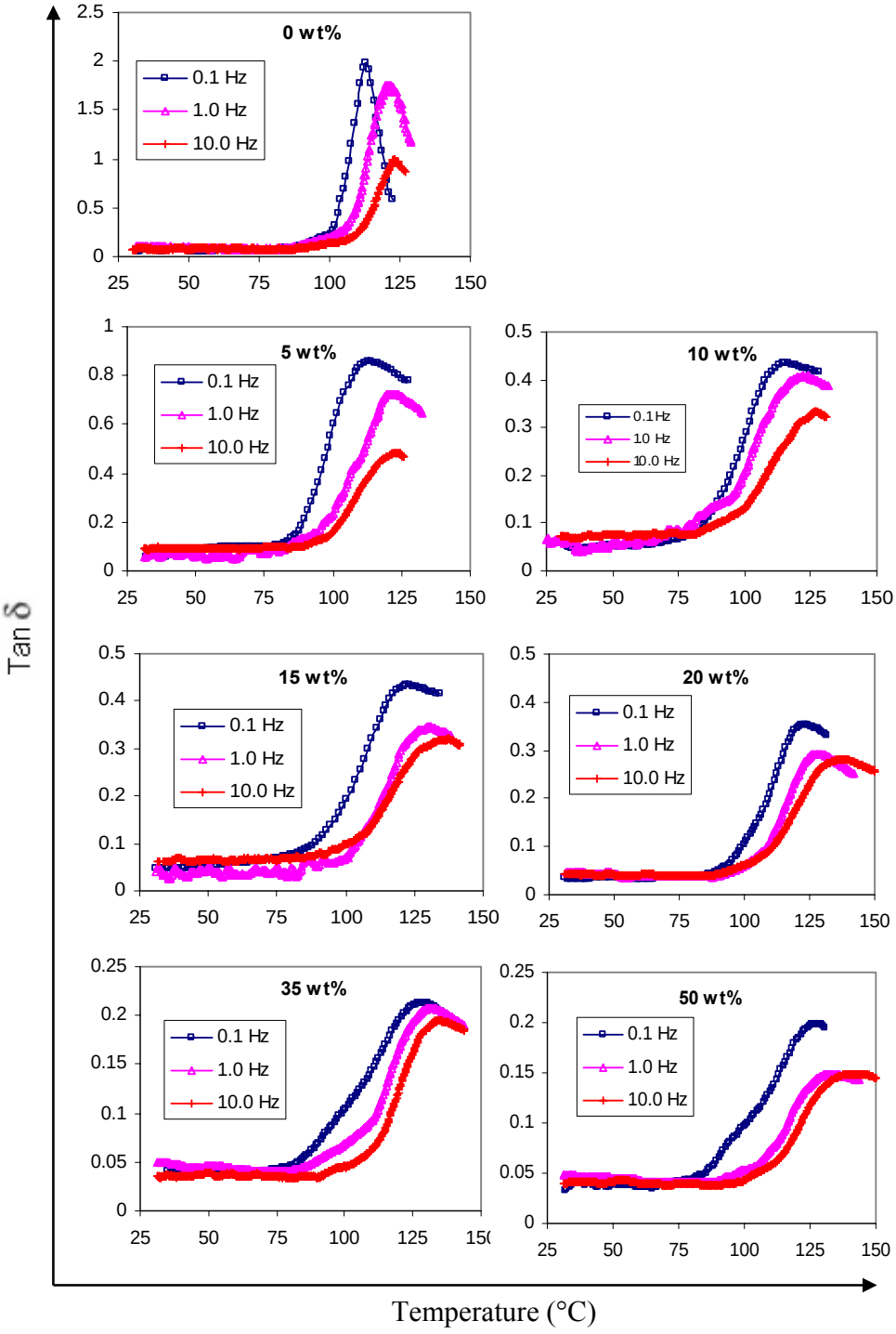

Figure 3.11. Tan δ behavior of PMMA and SWNT-B/PMMA films as a function of temperature at different frequencies. SWNT-B loading is noted on each plot.

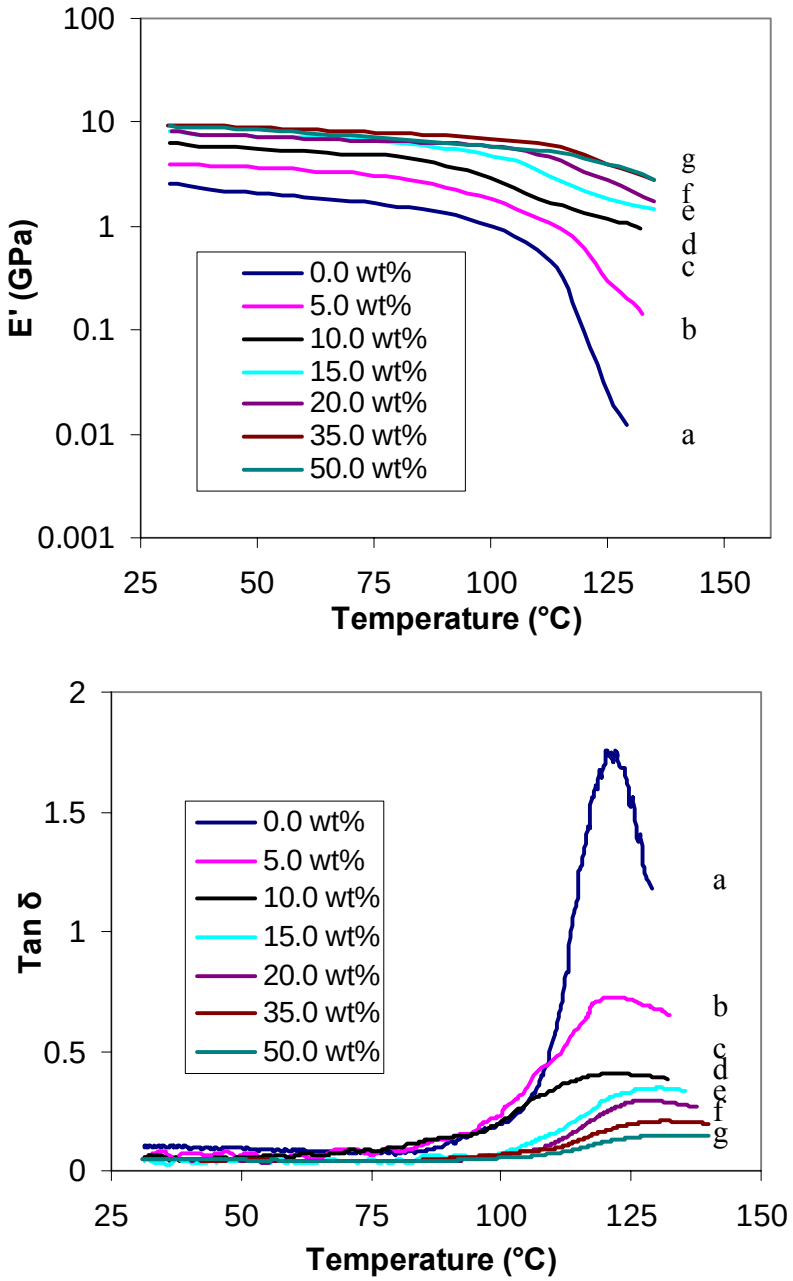

Figure 3.12. Storage modulus (E') and tan δ behavior of PMMA and SWNT-B/PMMA films as a function of temperature at 1 Hz. SWNT-B concentration as follows: (a) 0 wt%, (b) 5 wt%, (c) 10 wt%, (d) 15 wt%, (e) 20 wt%, (f) 35 wt%, and (g) 50 wt%.

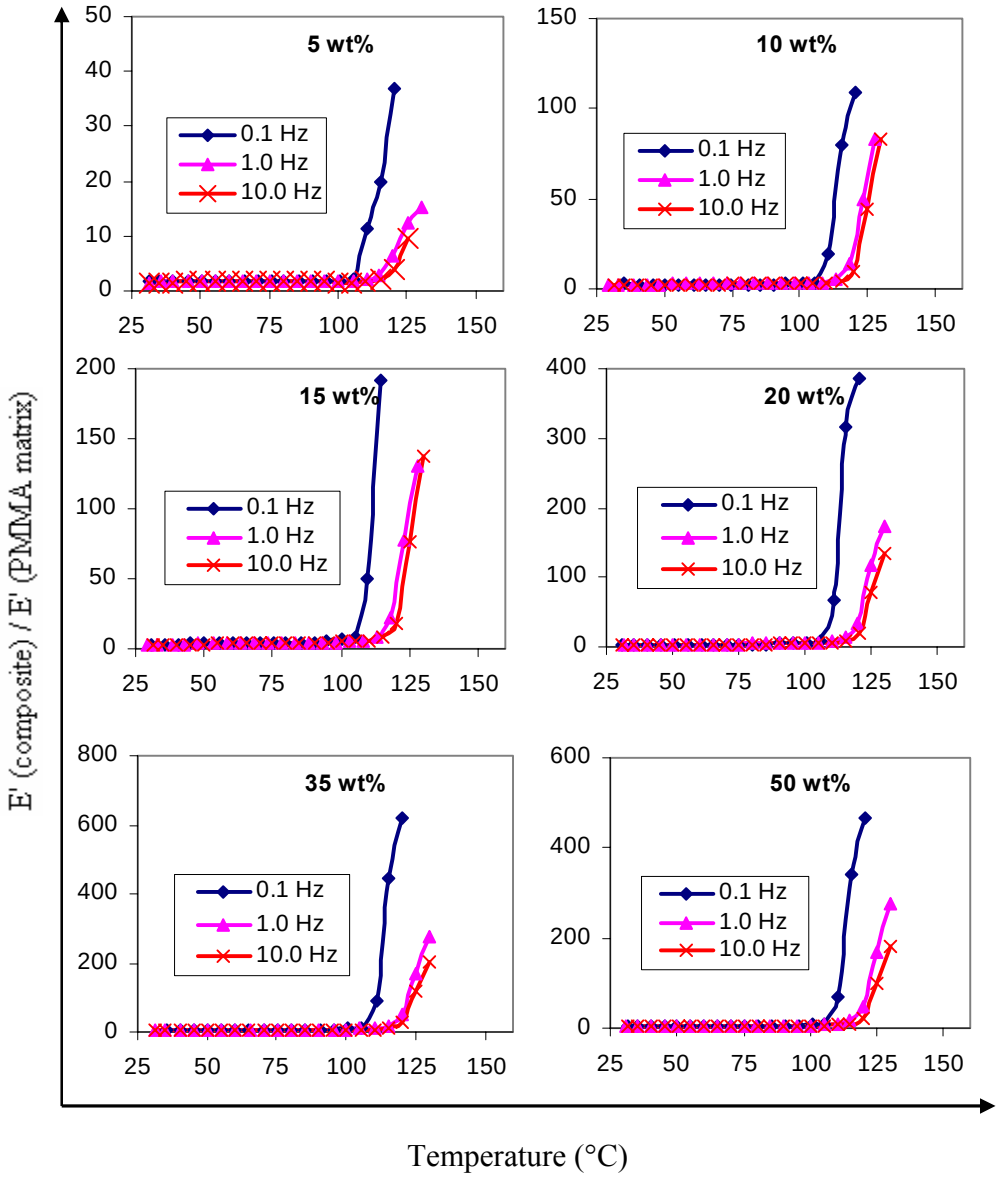

Figure 3.13. E' (composite) / E' (PMMA matrix) of SWNT-B/PMMA composites at different SWNT-B concentrations as a function of temperature.

Dimensional stability of PMMA and SWNT-B/PMMA composites are studied using TMA at 0.35 MPa stress at a heating rate of 5 ^{o}C /min. The change in sample length as a function of temperature is shown in Figure 3.14. The coefficient of thermal expansion (CTE) of PMMA and SWNT-B/PMMA composites at 30 5 ^{o}C and 105 5 ^{o}C are listed in Table 3.10. The composite films exhibit a smaller CTE compared to pure PMMA. The larger the SWNT-B loading, smaller the CTE. For having a 1% length change under 0.35 MPa stress, the temperature increases from 116 °C for pure PMMA to 211 °C for SWNT-B/PMMA with 50 wt% SWNT-B loading.

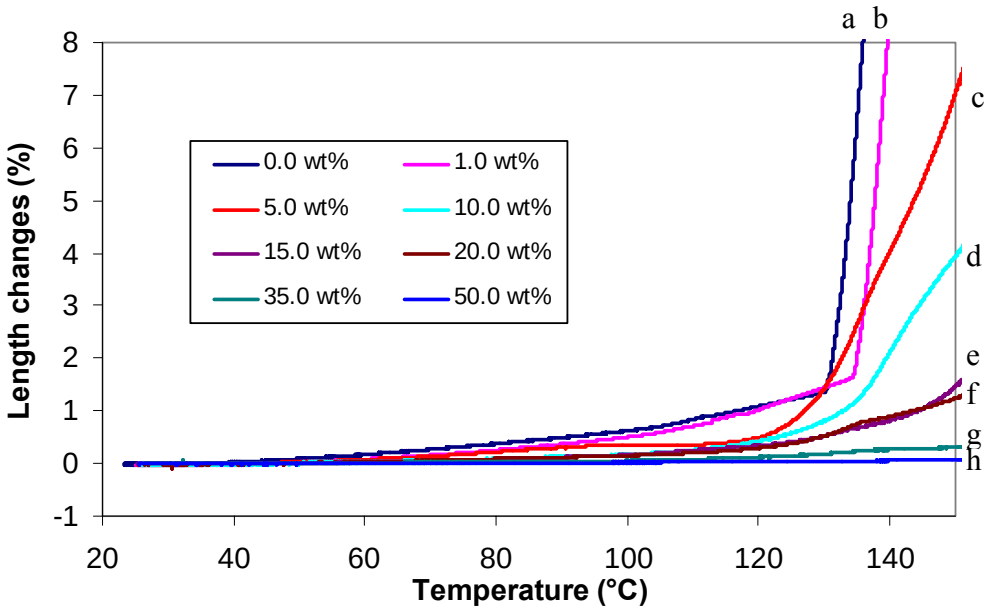

Figure 3.14. Thermal expansion of PMMA and SWNT-B/PMMA films as a function of temperature under 0.35 MPa stress. SWNT-B concentration as following: (a) 0 wt%, (b) 1 wt%, (c) 5 wt%, (d) 10 wt%, (e) 15 wt%, (f) 20 wt%, (g) 35 wt%, and (h) 50 wt%.

Table 3.10. Coefficient of thermal expansion (CTE) and temperature (°C) at 1 % length change for PMMA and SWNT-B/PMMA composite films.

SWNT-B (wt%)	CTE at 30 °C (10^{-6}/°C)	CTE at 105 °C (10^{-6}/°C)	Temperature (°C) at 1 % length change
0	50	152	116
1	32	137	119
5	18	50	127
10	11	80	133
15	9	47	144
20	8	42	144
35	3	24	183
50	2	10	211

Glass transition temperature of PMMA and composite films are obtained from DSC curves. The DSC results are shown in Figure 3.15 and the T_g values are given in Table 3.11. The results show with increasing SWNT-B loading, T_g of PMMA increases, which indicates the restricted chain mobility in the presence of nanotubes.

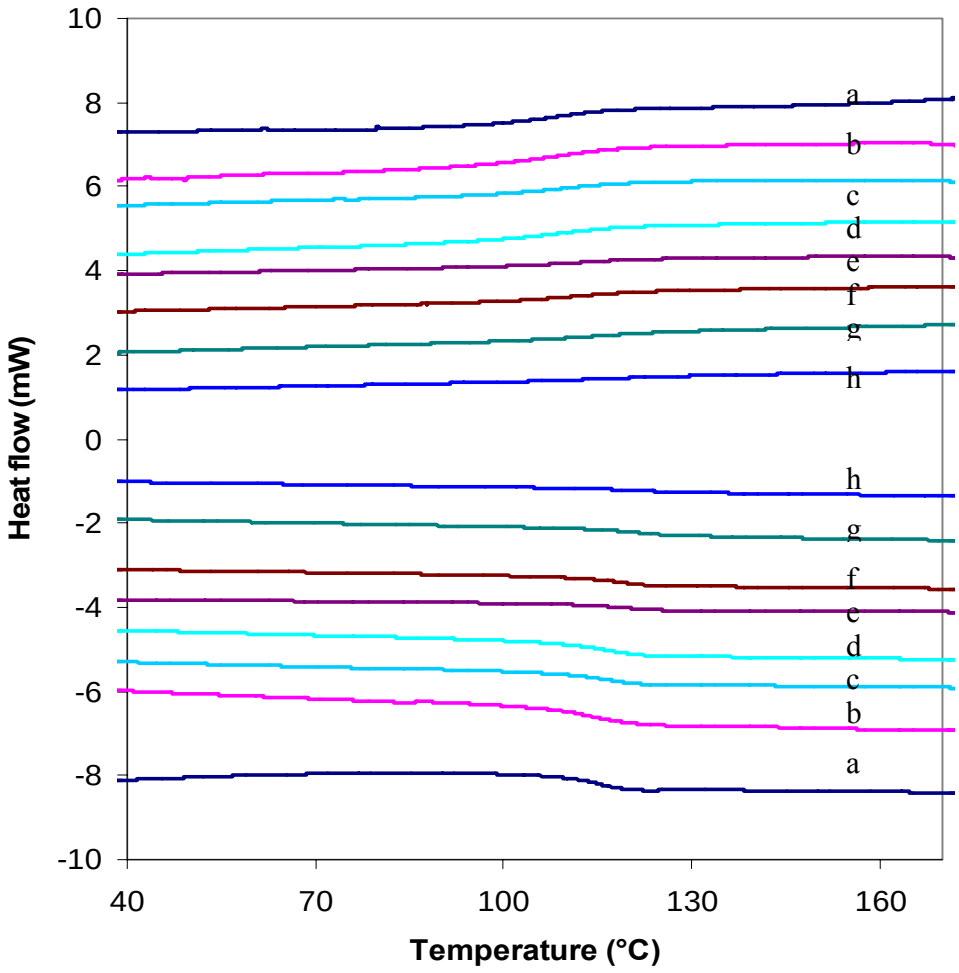

Figure 3.15. DSC curves (the second heating cycle – bottom plots and the first cooling cycle – top plots at a rate of 10 °C/min) of PMMA and SWNT-B/PMMA films at different SWNT-B concentrations ((a) 0 wt%, (b) 1 wt%, (c) 5 wt%, (d) 10 wt%, (e) 15 wt%, (f) 20 wt%, (g) 35 wt%, and (h) 50 wt%) (DSC curves are shifted vertically for clarity).

Table 3.11. Glass transition temperature (T_g) of PMMA and SWNT-B/PMMA films determined by DSC method.

	T_g (°C)	
SWNT-B (wt%)	2nd heating cycle	1st cooling cycle
0	114.6	107.5
1	114.2	108.8
5	116.7	109.8
10	116.9	111.6
15	119.9	112.1
20	119.6	112.2
35	121.6	114.9
50	121.9	115.0

As discussed in section 1.1.5 in chapter 1, studies have been reported with both increase and decrease in the polymer decomposition temperature upon adding of CNT. The increase in decomposition temperature has been interpreted due to interaction between polymer and CNT; however, no clear explanation is available for the decrease in decomposition temperature of polymer/CNT composites.

All composite samples were dried for two days in vacuum oven at 80 °C before any characterization. Thermogravimetry analysis (TGA) was conducted on these samples in air at a heating rate of 10 °C/min from 25 °C to 800 °C. In order to ensure that all the solvents were completely evaporated from these films and the samples were dried in

vacuum oven at 80 °C for 4 more days. TGA study was conducted on the re-dried samples. For one specific sample, no difference in TGA curve was observed between the sample dried for two days and the one dried for 4 extra days. The decomposition temperatures of SWNT-B, PMMA, and SWNT-B/PMMA composite are determined by TGA, which are shown in Figure 3.16 and Table 3.12.

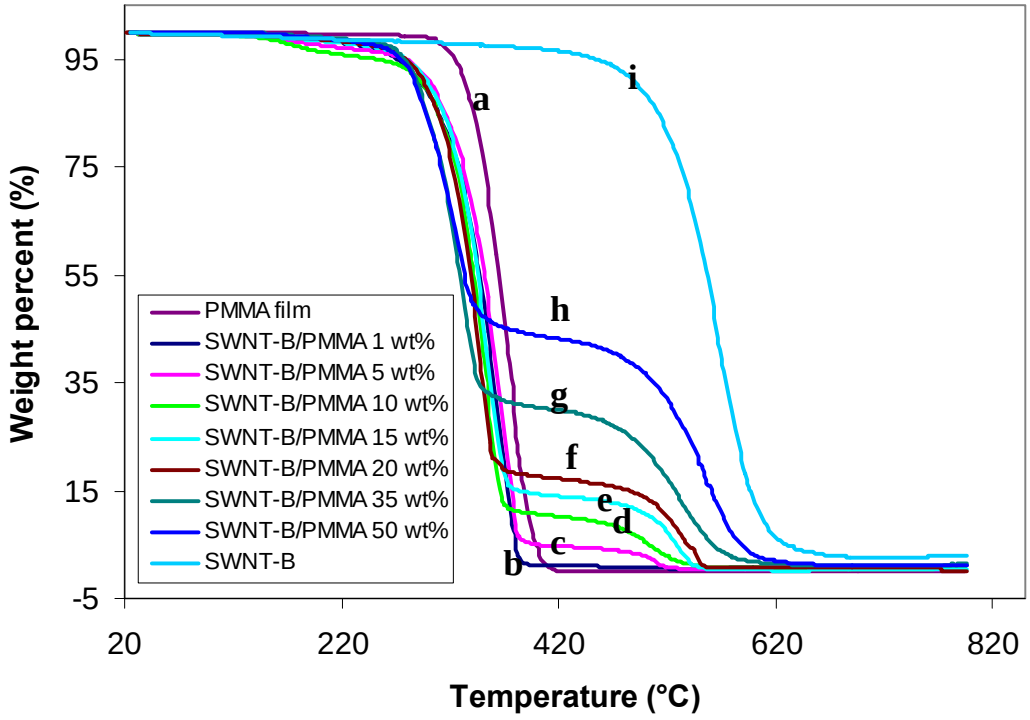

Figure 3.16. Thermogravimetry analysis (TGA) in air at a heating rate of 10 °C/min of SWNT-B/PMMA composite with increasing SWNT-B concentration ((a) 0 wt%, (b) 1 wt%, (c) 5 wt%, (d) 10 wt%, (e) 15 wt%, (f) 20 wt%, (g) 35 wt%, (h) 50 wt%, and (i) 100 wt%).

Table 3.12. Decomposition temperatures of each component in SWNT-B/PMMA composites and the residue at 800 °C determined by TGA analysis in air and in nitrogen at a heating rate of 10 °C/min.

SWNT-B (wt%)	PMMA decomposition temperature (°C)						SWNT-B decomposition temperature (°C) in air
	In air			In nitrogen			
	T_{d1}	T_{d2}	Residue (%)	T_{d1}	T_{d2}	Residue (%)	
0	328	374	0.1	353	385	0.1	----
1	313	369	0.4	334	384	1.0	501
5	319	367	0.3	327	379	4.1	508
10	312	359	0.5	329	377	9.0	509
15	311	355	0.4	329	376	14.1	525
20	308	349	0.6	337	380	18.2	529
35	290	331	1.1	330	389	32.5	538
50	279	324	1.2	320	385	46.7	559
100	----	----	2.6	----	----	----	570

T_{d1}: decomposition initiation temperature, T_{d2}: decomposition peak temperature

For TGA conducted in air, the decomposition temperature (both the decomposition initiation temperature (T_{d1}) and the decomposition peak temperature (T_{d2})) of PMMA in the composite becomes closer to that of pure PMMA with decreasing SWNT-B concentration and the decomposition temperature of SWNT-B becomes closer to that of pure SWNT-B with increasing SWNT-B concentration. For TGA conducted in nitrogen, T_{d2} of all the samples is about the same (Table 3.12 and Figure 3.17), which

indicates SWNT-B does not affect the PMMA decomposition temperature under nitrogen condition. The decomposition temperature of PMMA decreases with increasing SWNT content in air. This suggests that the presence of SWNT helps to capture more oxygen, resulting in PMMA decomposition at lower temperature.

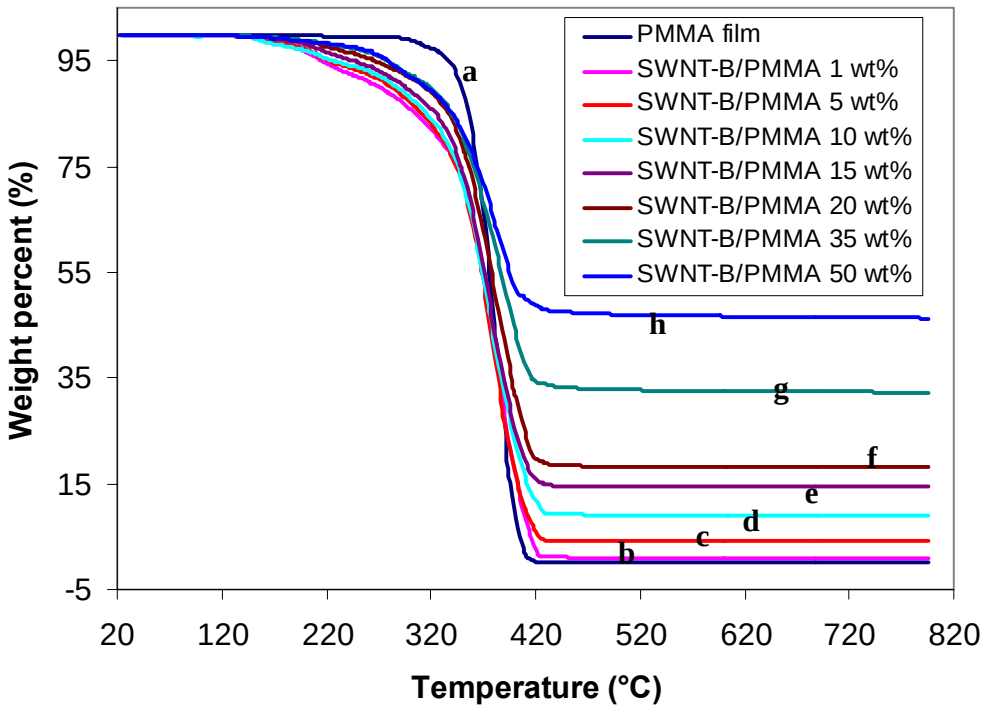

Figure 3.17. Thermogravimetry analysis (TGA) in nitrogen at a heating rate of 10 °C/min of SWNT-B/PMMA composite with SWNT-B concentration increasing ((a) 0 wt%, (b) 1 wt%, (c) 5 wt%, (d) 10 wt%, (e) 15 wt%, (f) 20 wt%, (g) 35 wt%, and (h) 50 wt%).

Raman spectra of SWNT-B, SWNT-B/PMMA 0.5 wt% film, and SWNT-B/PMMA 50 wt% film are shown in Figure 3.18. The peak position for RBM, D band, G band, and G' band for all composite are given in Table 3.13. Both RBM (Appendix A. 4 and A. 7) and D band positions remain almost the same for SWNT-B and SWNT-

B/PMMA composites, while G (Appendix A. 5 and A. 8) and G' (A. 6 and A. 9) bands upshift upon adding SWNT-B into PMMA matrix. The shifts of G (or G') band are almost the same for all the composite films irrespective of SWNT-B concentrations compared to SWNT-B powder.

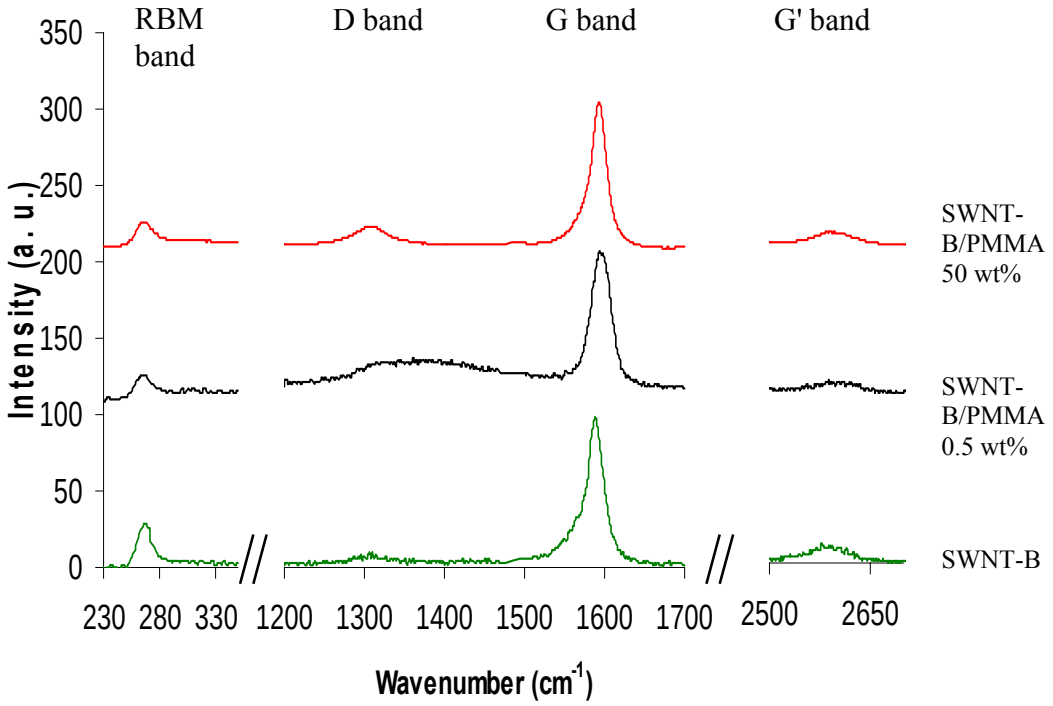

Figure 3.18. Raman spectra of SWNT-B powder, SWNT-B/PMMA 0.5 wt% film, and SWNT-B/PMMA 50 wt% film (Intensities of all the spectra have been normalized to the G band intensity).

Full width at half maximum (FWHM) of G band (Table 3.13.) decreased with increasing SWNT-B loading. In Lefrant's study[26], they observed that G band widths decreased upon adding SWNT into PMMA matrix. They hypothesized that the G band width decrease was caused by PMMA intercalation into SWNT bundles. At the same time, they observed that RBM upshifted upon embedding SWNT into PMMA matrix.

While in our case, RBM remains the same and G band widths increase after embedding SWNT into PMMA matrix. Dresselhaus et al.[213] concluded that larger the pressure on SWNT, the wider the G band. Dong et al.[228] studied G band width affected by the topological defects of pentagon-heptagon rings. The longer length of the region between the pentagon and heptagon rings means the wider width of G band. In the case of SWNT-B/PMMA, at the low SWNT-B loading sample, the average pressure from PMMA matrix may be larger than at the high SWNT-B loading. In addition, PMMA surrounds SWNT-B bundle, which might weaken the interaction between pentagon and heptagon rings making the "effective length" between these two rings smaller. Based on this hypothesis, it is reasonable to conclude that the lower the SWNT-B concentration in PMMA, the longer the "effective length" between these two rings and the larger the pressure SWNT-B experiences, resulting in wider G band peak.

Table 3.13. Raman band positions of various bands and full width at high maximum (FWHM) of G band of SWNT-B and SWNT-B/PMMA composites.

SWNT-B (wt%)	RBM (cm^{-1})	D band (cm^{-1})	G band		G' band (cm^{-1})
			Position (cm^{-1})	FWHM (cm^{-1})	
0.5	266.7	1308.1	1593.1	29	2597.2
1	266.4	1308.7	1593.0	30	2597.1
5	266.4	1309.0	1592.8	29	2597.3
10	266.5	1309.5	1592.5	28	2597.9
15	267.2	1309.7	1592.2	27	2596.0
20	266.5	1308.4	1592.0	24	2596.3
35	267.0	1309.5	1592.5	25	2596.9
50	267.5	1308.6	1592.2	23	2596.0
100	266.5	1308.8	1589.0	24	2587.7

Solvent resistance of PMMA and SWNT-B/PMMA composite films are examined by immersing these films into toluene for 30 minutes. The films were removed from toluene, and dried in vacuum oven at 80 °C for 4 days to remove any traces of toluene. The weight change in PMMA and SWNT-B/PMMA composites by exposing them in toluene are given in Table 3.14. With increasing SWNT-B loadings, the weight loss based on the weight of whole film decreased. With increasing SWNT-B concentration, the weight loss based on the weight of PMMA matrix has comparable value for 35 wt% and 50 wt% samples. The time it takes for the various samples to

completely disintegrate is also listed in Table 3.14. For 35 wt% and 50 wt% samples, it takes about 8 hours for the films to completely disintegrate. The decreased weight loss with increasing nanotube loading indicates increased solvent resistance of composite as compared to pure PMMA.

Table 3.14. Toluene resistance of PMMA and SWNT-B/PMMA composite.

SWNT-B (wt%)	Weight loss (percent) based on the whole film weight	Weight loss (percent) based on PMMA weight	Time that film disintegrate totally in toluene (hours)
0	40.1	40.1	3
1	30.0	30.3	4
5	16.6	17.5	4
10	11.4	12.6	4
15	7.7	9.1	6
20	5.8	7.2	6
35	3.7	5.7	8
50	3.0	5.9	8

3.3.3 A reinforcement efficiency comparison among SWNT-A, SWNT-B, MWNT, and VGCNF in PMMA

In order to compare the reinforcement efficiency of SWNT with MWNT and VGCNF in PMMA matrix, MWNT/PMMA (weight ratio: 15/85) and VGCNF/PMMA

(weight ratio: 15/85) were prepared following the same procedure as used for SWNT-B/PMMA (weight ratio: 15/85). SEM images of the cross sections of MWNT/PMMA and VGCNF/PMMA composites are shown in Figure 3.19. Both MWNT and VGCNF disperse uniformly in PMMA matrix.

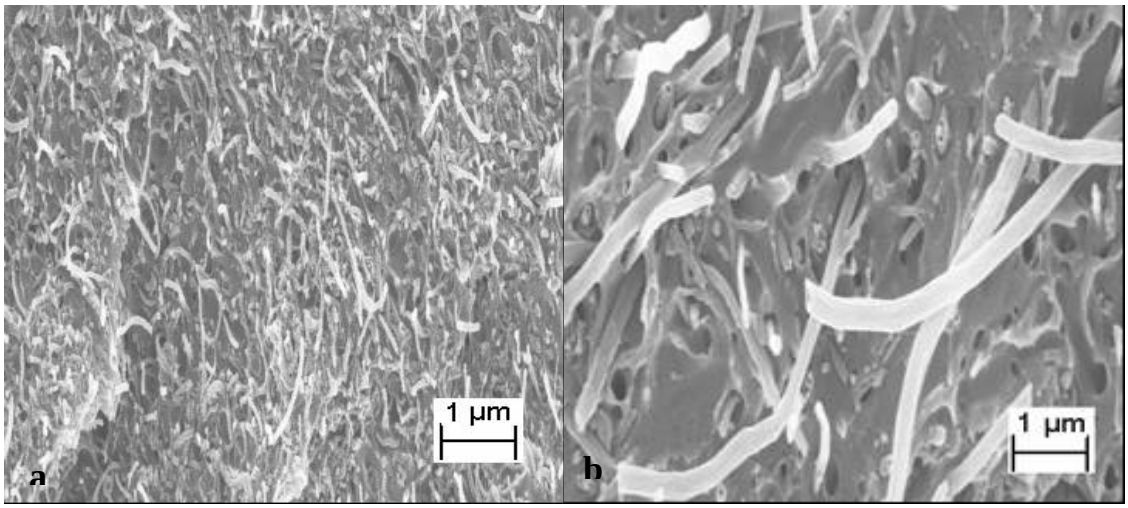

Figure 3.19. SEM images of the cross sections of (a) MWNT/PMMA (15/85 weight ratio) and (b) VGCNF/PMMA (15/85 weight ratio).

The mechanical properties of PMMA film, SWNT-A/PMMA (15/85), SWNT-B/PMMA (15/85), MWNT/PMMA (15/85), and VGCNF/PMMA (15/85) are given in Table 3.15. At the same filler loading, SWNT-B has the highest reinforcement efficiency. MWNT and VGCNF composite exhibit moderate enhancement in tensile modulus and tensile strength. The difference in reinforcing efficiency of SWNT-A and SWNT-B can be attributed to the difference in metal catalyst.

Electrical conductivity values for various films are also compared in Table 3.15. Electrical conductivities of SWNT composite films are 2 orders of magnitude higher than those of MWNT and VGCNF composite film.

Table 3.15. Tensile properties and electrical conductivity values of SWNT-A, SWNT-B, MWNT, and VGCNF reinforced PMMA composites at 15 wt% carbon nanotube content.

Samples	Tensile modulus (GPa)	Tensile strength (MPa)	Elongation to break (%)	Electrical conductivity (S/m)
PMMA film	1.8 ± 0.1	50 ± 8	3.5 ± 0.5	10^{-14}[223]
SWNT-A/PMMA (15/85)	4.1 ± 0.2	23 ± 12	0.6 ± 0.3	1430
SWNT-B/PMMA (15/85)	5.3 ± 0.2	71 ± 1	2.4 ± 0.2	854
MWNT/PMMA (15/85)	3.5 ± 0.6	54 ± 12	1.7 ± 0.4	15
VGCNF/PMMA (15/85)	3.2 ± 0.1	62 ± 21	1.9 ± 0.6	6

Tan δ peak behavior at different frequencies for PMMA, SWNT-A/PMMA, SWNT-B/PMMA, MWNT/PMMA, and VGCNF/PMMA containing 15 wt% CNT loadings are shown in Figure 3.20. and Table 3.16. At a given test frequency, the magnitude of tan δ peak decreases and its peak temperature increases in the order of PMMA, VGCNF/PMMA, MWNT/PMMA, SWNT-A/PMMA, and SWNT-B/PMMA films. Glass transition temperatures determined by tan δ peak position at 1 Hz frequency are 121 °C, 123 °C, 123 °C, 129 °C, and 130 °C for PMMA film, VGCNF/PMMA, MWNT/PMMA, SWNT-A/PMMA, and SWNT-B/PMMA, respectively. The activation energies of each sample are calculated based on tan δ peak

position at different frequencies according to Arrhenius Equation and listed in Table 3.16. The activation energies of CNT/PMMA composites are comparable with that of PMMA film.

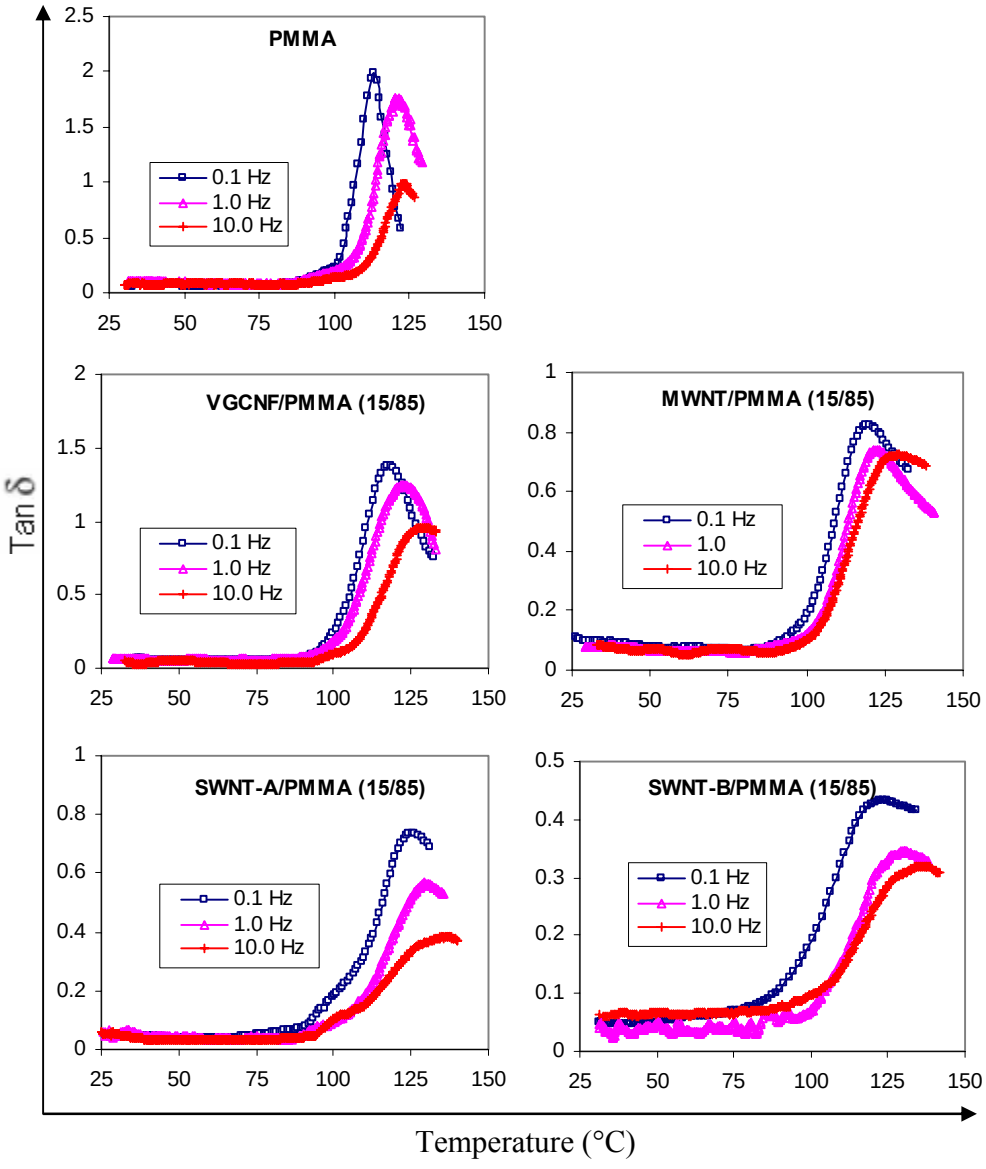

Figure 3.20. Tan δ as a function of temperature for PMMA, VGCNF/PMMA, MWNT/PMMA, SWNT-A/PMMA, and SWNT-B/PMMA films at 15 wt% filler loading at different frequencies.

Table 3.16. Tan δ peak temperature (P) and tan δ magnitude (M) for PMMA and CNT/PMMA films (15/85) at different frequencies and the calculated activation energies.

Samples	Tan δ peak (0.1 Hz)		Tan δ peak (1 Hz)		Tan δ peak (10 Hz)		Activation energy (kJ/mole)
	P (°C)	M	P (°C)	M	P (°C)	M	
PMMA	113	1.99	121	1.74	124	1.00	497
VGCNF/PMMA (15/85)	119	1.34	123	1.24	130	0.96	538
MWNT/PMMA (15/85)	120	0.82	123	0.74	131	0.72	519
SWNT-A/PMMA (15/85)	124	0.73	129	0.56	136	0.38	514
SWNT-B/PMMA (15/85)	123	0.43	130	0.35	137	0.32	444

The solvent resistance of these composite samples is examined by dipping the samples into toluene for 30 minutes. The weight losses of these samples after treating in toluene are listed in Table 3.17. At the same CNT loadings, SWNT-B/PMMA exhibits the highest solvent resistance, as evidence by small loss in weight (7.7 % and 10.8 % for SWNT-B and SWNT-A containing composite, respectively) compared to higher weight loss for composites of MWNT and VGCNF (23.9 % and 27.2 %, respectively).

Table 3.17. Toluene resistance of SWNT-A, SWNT-B, MWNT, and VGCNF reinforced PMMA composites at 15 wt% carbon naontube content.

Samples	Weight loss (percent) based on the whole film weight	Weight loss (percent) based on PMMA weight	Time that film disintegrate totally in toluene (hours)
PMMA film	40.1	40.1	3
SWNT-B/PMMA (15/85)	7.7	9.1	6
SWNT-A/PMMA (15/85)	10.8	12.7	6
MWNT/PMMA (15/85)	23.9	28.1	3
VGCNF/PMMA (15/85)	27.2	32.0	3

Thermogravimetry analysis (TGA) was conducted on PMMA and composites in air and in nitrogen at a heating rate of 10 °C/min from 25 °C to 800 °C. The decomposition temperatures of PMMA film, SWNT-A/PMMA, SWNT-B/PMMA, MWNT/PMMA, and VGCNF/PMMA composites are determined by TGA in air, which are shown in Figure 3.21 and the decomposition temperatures are listed in Table 3.18. The decomposition temperatures of PMMA in the composite films vary with the addition of different types of fillers. For example, PMMA decomposes at 355 °C in the SWNT-B/PMMA film, while it decomposes at 374 °C in VGCNF/PMMA film. The decomposition temperature of PMMA in the composite films appears to be related to the decomposition temperature of the fillers. The higher filler decomposition temperature resulted in higher PMMA decomposition temperature in the composite films. For TGA

analysis of PMMA and these four composite films in nitrogen, the decomposition temperatures are also given in Table 3.18 and Figure 3.22. All these four composites have the comparable decomposition temperature as control PMMA film, which indicates that CNT does not affect PMMA decomposition in nitrogen. This suggests that the presence of CNT helps to capture more oxygen during TGA experiments in air, resulting in PMMA decomposition at lower temperature.

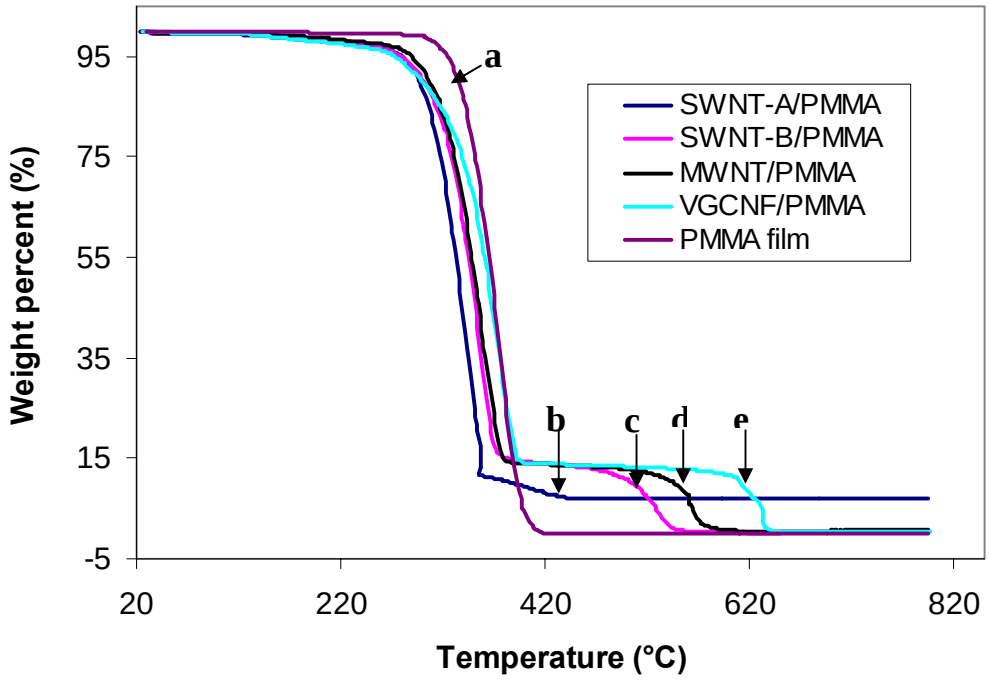

Figure 3.21. Thermogravimetry analysis (TGA) in air at a heating rate of 10 °C/min of (a) PMMA film, (b) SWNT-A/PMMA (15/85), (c) SWNT-B/PMMA (15/85), (d) MWNT/PMMA (15/85), and (e) VGCNF/PMMA (15/85).

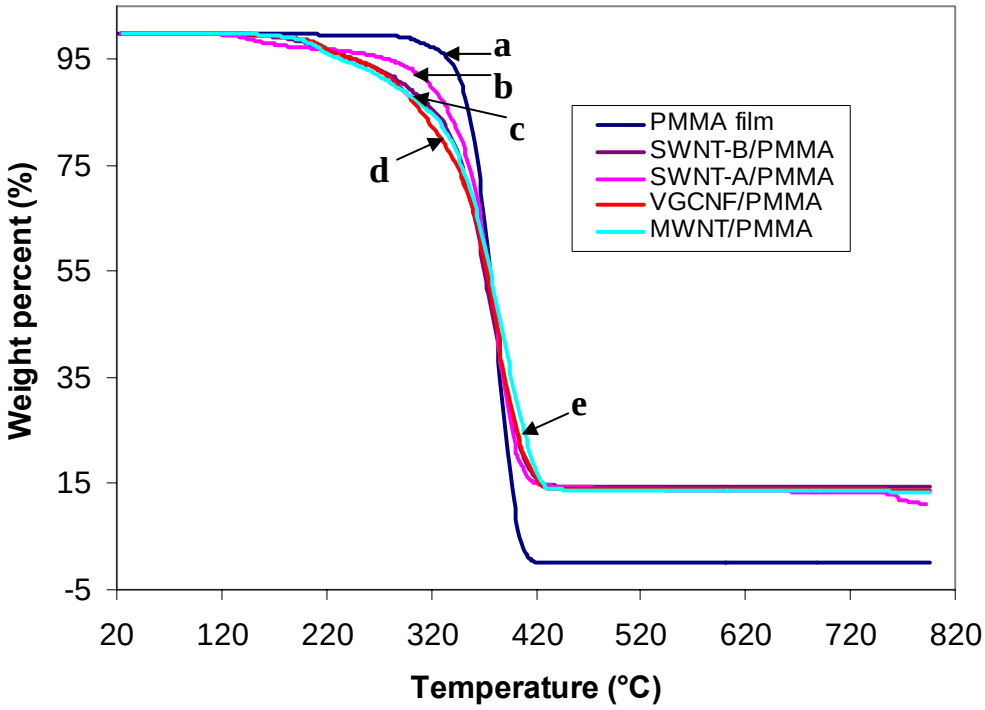

Figure 3.22. Thermogravimetry analysis (TGA) in nitrogen at a heating rate of 10 °C/min of (a) PMMA film, (b) SWNT-A/PMMA (15/85), (c) SWNT-B/PMMA (15/85), (d) MWNT/PMMA (15/85), and (e) VGCNF/PMMA (15/85).

Table 3.18. Decomposition temperatures of SWNT-A, SWNT-B, MWNT, VGCNF, SWNT-A/PMMA, SWNT-B/PMMA, MWNT/PMMA, and VGCNF/PMMA composites determined by Thermogravimetry analysis (TGA) in air and in nitrogen at a heating rate of 10 °C/min.

Samples	Decomposition temperature (°C) PMMA				Filler powder decomposition temperature (°C) in air
	In air		In nitrogen		
	T_{d1}	T_{d2}	T_{d1}	T_{d2}	
PMMA film	328	374	353	385	-----
SWNT-A/PMMA (15/85)	305	346	332	382	422
SWNT-B/PMMA (15/85)	311	355	329	376	570
MWNT/PMMA (15/85)	314	357	324	387	626
VGCNF/PMMA (15/85)	319	374	327	384	738

T_{d1}: decomposition initiation temperature, T_{d2}: decomposition peak temperature

Dimensional stability of PMMA composites with various fillers at 0.35 MPa stress at a heating rate of 5 ^{o}C /min is shown in Figure 3.23. The coefficient of thermal expansion (CTE) of these composites at 30 ^{o}C and 105 ^{o}C is given in Table 3.19. The composite films exhibit a smaller CTE compared to pure PMMA. The CTE of the composites decreases in the order of PMMA film, VGCNF/PMMA, MWNT/PMMA, SWNT-A/PMMA, and SWNT-B/PMMA. For having 1% length change under 0.35 MPa stress, the temperature increases from 119 °C for VGCNF/PMMA to 144 °C for SWNT-B/PMMA. The results indicate that the composite containing SWNT-B has the highest dimensional stability.

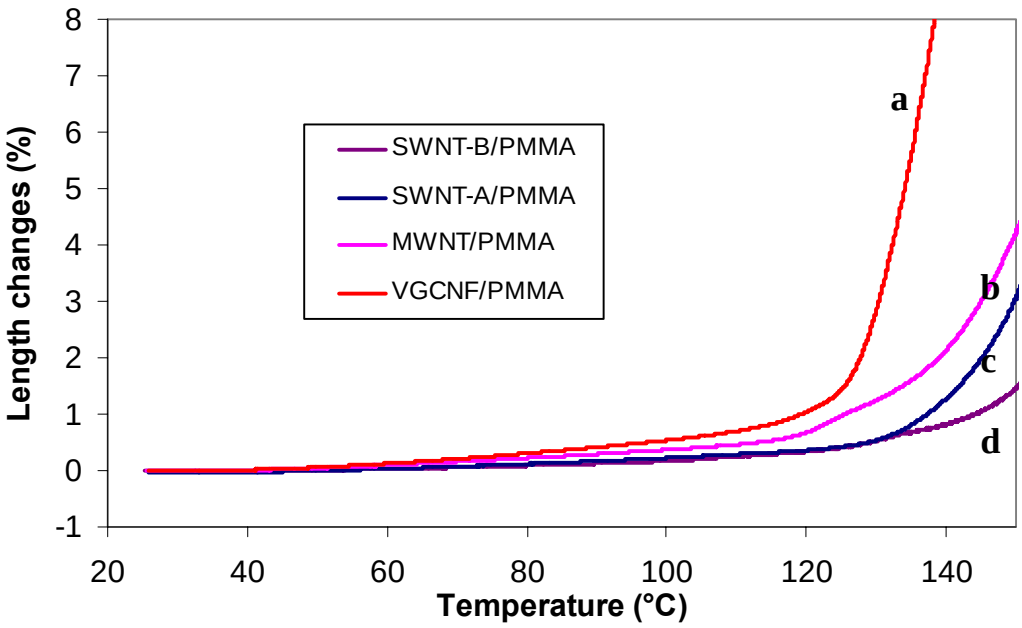

Figure 3.23. Thermal expansion of composite films as a function of temperature under 0.35 MPa stress at a heating rate of 5 °C /min ((a) VGCNF/PMMA film (15/85), (b) MWNT/PMMA (15/85), (c) SWNT-A/PMMA (15/85), and (d) SWNT-B/PMMA (15/85)).

Table 3.19. Coefficient of thermal expansion and temperature (°C) at 1 % length change of PMMA and the composite films.

	CTE at 30 °C (10^{-6}/°C)	CTE at 105 °C (10^{-6}/°C)	Temperature (°C) at 1 % length change
PMMA film	50	152	116
VGCNF/PMMA (15/85)	35	151	120
MWNT/PMMA (15/85)	30	93	126
SWNT-A/PMMA (15/85)	18	67	137
SWNT-B/PMMA (15/85)	9	47	144

A comparison of reinforcement efficiency of SWNT-A, SWNT-B, MWNT and VGCNF clearly reveals that the composites prepared with SWNT-B have the highest properties followed by composite of SWNT-A, MWNT and VGCNF. The similarity in the trend in tensile modulus, tan δ peak magnitude, solvent resistance and dimensional stability, all points towards the same conclusion; that relatively inferior properties of SWNT-A/PMMA composites are attributed to the presence of high metal catalyst in the nanotube.

3.4. Conclusions

Based on the dispersion study, nitromethane was chosen as the solvent to process CNT/PMMA composites. SWNT-A (35.0 wt% catalyst)/PMMA, SWNT-B (2.4 wt% catalyst)/PMMA, MWNT/PMMA, and VGCNF/PMMA composite films at 15 wt% CNT loadings have been processed. SWNT-B/PMMA composites at carbon nanotube loadings of 0.5, 1, 5, 10, 15, 20, 35, and 50 wt% were processed. For all these compositions, CNT dispersed uniformly into PMMA matrix as evidenced by the optical micrographs and SEM images. Among the various CNT/PMMA composites studied in this chapter, the SWNT-B/PMMA composite film exhibits the highest enhancement in tensile modulus (increased by a factor of 3), tensile strength (increased by a factor of 1.5), dimensional stability (~70 % reduction in CTE) and solvent resistance followed by composites of SWNT-A, MWNT and VGCNF. Enhancement in storage modulus for all CNT/PMMA composite films is observed. The highest increase in storage modulus is observed for SWNT-B/PMMA composite films. The magnitude of the tan δ peak decreased and shifted to higher temperature (tan δ for SWNT-B/PMMA uphifted by 9 °C) among all the CNT/PMMA composite films. SWNT-A reinforced PMMA composite has the highest

electrical conductivity among these four CNT/PMMA composites. The higher electrical conductivity in SWNT-A composites (1430 S/m) as compared to SWNT-B composites is due to additional conductivity network formed by metal catalyst. In nitrogen, PMMA has the same decomposition temperature in composites as for the control film, which indicates that CNT by itself does not affect the PMMA decomposition. While in air, PMMA degrades at lower temperature in the composite as compared to the control PMMA. This suggests that the presence of CNT assists in PMMA decomposition possibly by capturing more oxygen during TGA experiments in air.

Relatively poor mechanical properties and dimensional stability of SWNT-A composites compared to SWNT-B/PMMA composites are attributed to the presence of metal impurities. With increasing SWNT-B loading, the dimensional stability (~90 % reduction in CTE at 50 wt% SWNT-B loading) and the solvent resistance is enhanced. Enhancement in storage modulus for all CNT/PMMA composite films is observed. The electrical conductivity of SWNT-B/PMMA increased with increasing SWNT-B loading. The percolation volume is determined to be 0.5 wt%. The tensile modulus and the tensile strength do not increase linearly with increasing nanotube loading; they reach the maximum values at 35 wt% SWNT-B, and increased by a factor of 4 and 2, respectively.

CHAPTER 4

NOVEL ELECTROSPUN MICRO- AND NANO-STRUCTURED POLYMER PARTICLES

4.1 Introduction

In order to electrospin CNT/polymer/solvent dispersions, polymer solutions were electrospun first to understand the process conditions. With increasing solution concentration, electrospun material morphology changes from particles to fibers. To date, most reported electrospinning work focuses on fibers. In this chapter, a variety of polymers were elctrospun at relatively low concentrations into particles with various morphologies. PMMA was electrospun from seven different solvents and a series of poly (styrene-co-4-vinyl phenol) (PSVPh) copolymers with varying vinyl phenol component were electrospun from methyl ethyl ketone (MEK). Based on PMMA and PSVPh electrospun particles, a qualitative relationship is shown between solvent properties and electrospun particle morphologies.

4.2 Experimental

PMMA ($\overline{M_w} = 95{,}000 \sim 150{,}000$ g/mole) was obtained from Cyro Industries. Ultra low molecular weight PMMA ($\overline{M_w} = 15{,}000$ g/mole) (ULMW PMMA) was purchased from Sigma-Aldrich Co. PSVPh random copolymers were synthesized by Dr. Asif Rasheed using radical polymerization[229]. The composition, molecular weight and polydispersity index of PSVPh copolymers are listed in Table 4.1. All the solvents were purchased from Sigma-Aldrich Co. Both solvents and polymers were used as received.

Unless otherwise indicated, electrospinning was done in the horizontal mode in a chemical hood with a flow rate of 2 ml/h via an 18-gauge stainless-steel needle (inner diameter = 0.84 mm, 51 mm long) at 22,000 volts, and the distance between the needle tip and the grounded aluminum foil target was 10 cm. SEM was done on coated samples in a LEO 1530 thermally-assisted Field Emission Gun Scanning Electron Microscope at 10 KV. High-speed photographs were taken using a Photron CCD camera (Model: FASTCAM-X 1280 PSI) with a speed of 1000 frames per second (FPS). In order to obtain a sharp image on the micron-scale field of view, a pulsed Cu-vapor laser (Oxford Lasers), which emits green-yellow (510/578 nm) flash pulses with pulse duration of about 25 ns, was used.

Table 4.1. Vinyl phenol content, $\overline{M_n}$, and polydispersity index of PSVPh copolymers[229].

	Vinyl phenol mol% (measured from NMR)	$\overline{M_n}$ (g/mol) (measured by GPC)	Polydispersity index (measured by GPC)
PSVPh0	0.0	94,000	1.6
PSVPh10	13.2	118,000	1.8
PSVPh20	19.0	108,000	1.9
PSVPh30	32.5	105,000	2.4
PSVPh40	42.0	116,900	2.2

4.3 Results and discussion

4.3.1 PMMA electrospinning

Two kinds of PMMA with different molecular weights were electrospun. Molecular weight, PDI, solvents used and polymer concentrations for the electrospun samples are given in Table 4.2.

Table 4.2. A list of samples on which electrospinning is conducted in this section.

Polymer	$\overline{M_w}$ (g/mol)	Polydispersity Index	Solvents	Solution concentration (wt%)
PMMA	95,000~ 150,000	4~7	nitromethane	2, 4, 6, 8, 10, 12, 14, 16, 18, 20
			acrylonitrile	8
			acetone	8
			N,N-dimethylformamide	8
			formic acid	8
			methylene chloride	1, 8, 12
			tetrahydrofuran	1, 8
ULMW PMMA*	15,000	1.8	methylene chloride	1, 15, 30

ULMW PMMA* with a molecular weight of 15,000 g/mole could not be dissolved in nitromethane. FTIR spectrum of this ULMW PMMA (Appendix B. 1) showed a peak at 3435 cm^{-1}, which is not typically observed in PMMA.

Properties of the solvents used in electrospinning PMMA ($\overline{M_w} = 95{,}000 \sim 150{,}000$ g/mole) are listed in Table 4.3. Electrospinning of PMMA using nitromethane over a wide concentration range from 2 to 20 wt% has been discussed in chapter 5. In the concentration range of 6 to 12 wt%, formation of cups is observed (Figure 4.1). The diameter of cups at concentrations of 6, 8, 10, and 12 wt% is 3 ± 0.5 μm, 4 ± 0.5 μm, 6 ± 1.0 μm, and 7 ± 1.0 μm, respectively. These cups are also shown in Appendices B. 3 to B. 10. The relationship between cup diameter and solution concentration is shown in Figure 4.2.

Table 4.3. Properties of various solvents at room temperature[207].

	Dielectric constant	Viscosity (10^{-3} Pa · s)	Surface Tension (mN/m)	Evaporation Rate (butyl acetate=1)	R_{ij}^2 (MPa) (PMMA-solvent)
Methylene Chloride	9.1	0.44	28.1	14.5	20
Tetrahydrofuran	7.6	0.46	26.4	6.3	37
Acetone	20.7	0.30	25.2	5.6	39
DMF	38.3	3.80	37.1	0.2	30
Acrylonitrile	38.0	0.34	26.6	4.5	66
Nitromethane	39.4	0.63	36.8	1.4	106
Formic Acid	58.0	1.80	58.2	2.1	159

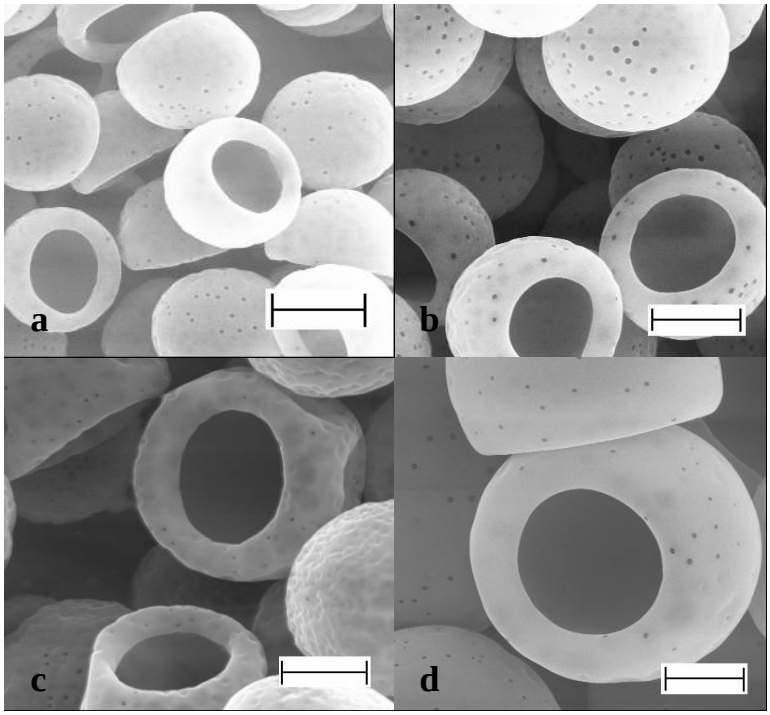

Figure 4.1. Cups electrospun from PMMA($\overline{M_w} = 95{,}000 \sim 150{,}000$ g/mole)/nitromethane solutions at different concentrations (a) 6 wt%, (b) 8 wt%, (c) 10 wt%, and (d) 12 wt% (scale bar is 2 μm).

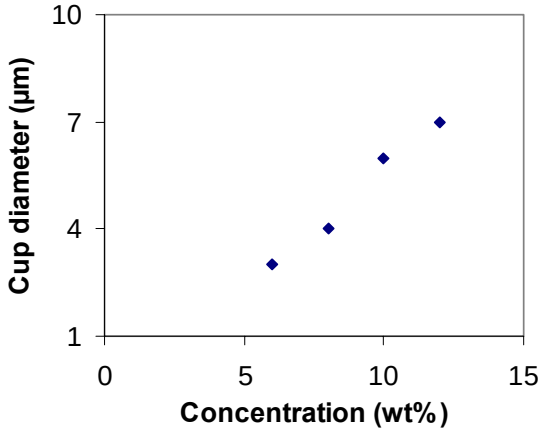

Figure 4.2. The diameter of electrospun cups as a function of PMMA($\overline{M_w} = 95{,}000 \sim 150{,}000$ g/mole) solution concentration in nitromethane.

In order to investigate the solvents effects on PMMA electrospun particle morphology, 8 wt% PMMA/different solvent solutions were electrsopun. At the same concentration and electrospinning conditions, particles with various morphologies were produced by employing different solvents (Figure 4.3 and Table 4.4).

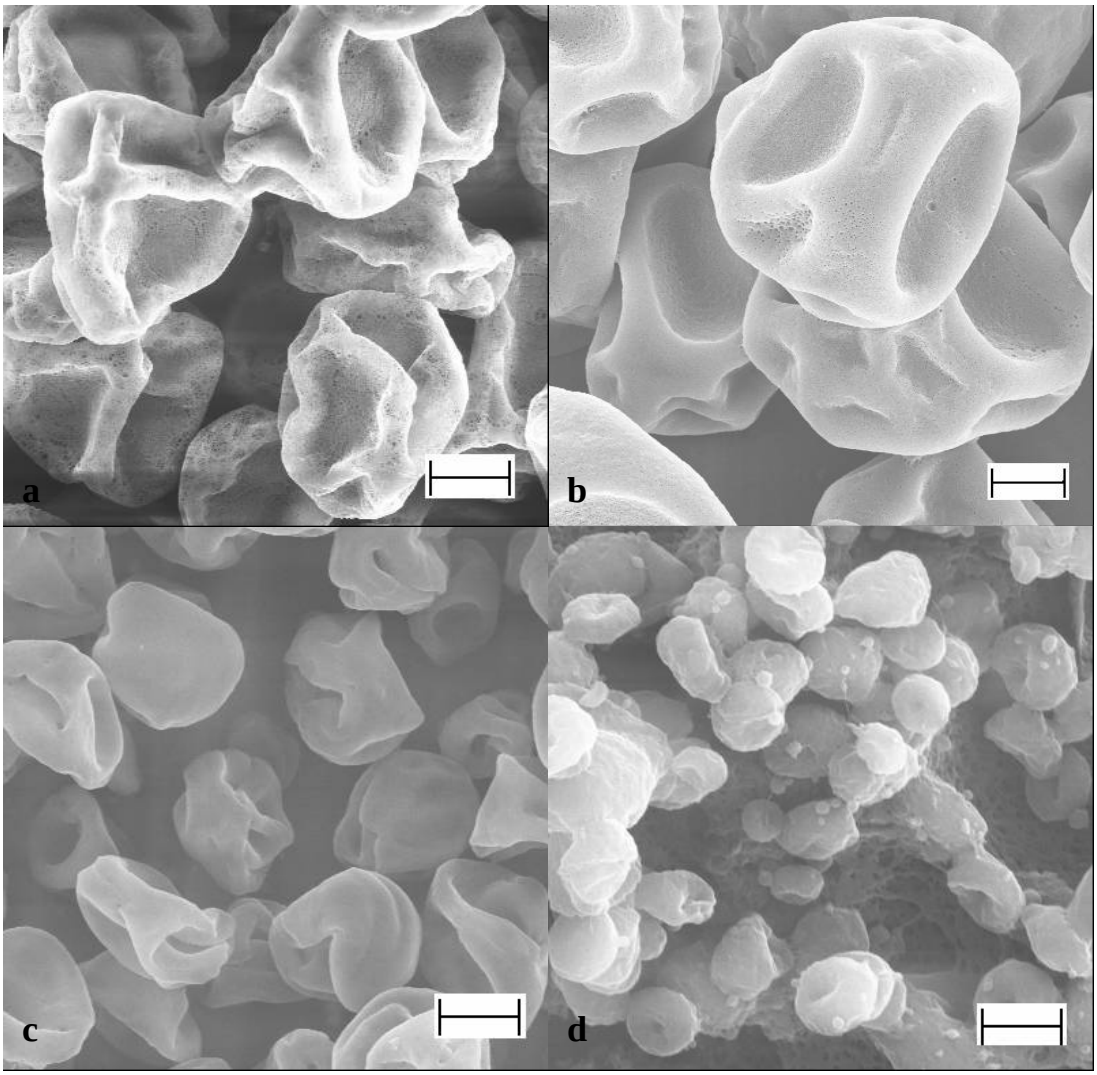

Figure 4.3. Particles electrospun from PMMA solution (8 wt%) in different solvents (a) methylene chloride, (b) tetrahydrofuran, (c) acetone, (d) N,N-dimethylformamide, (e) nitromethane, (f) acrylonitrile, (g) formic acid (scale bar of (a) and (b)is 10 μm, others are 2 μm). (To be continued).

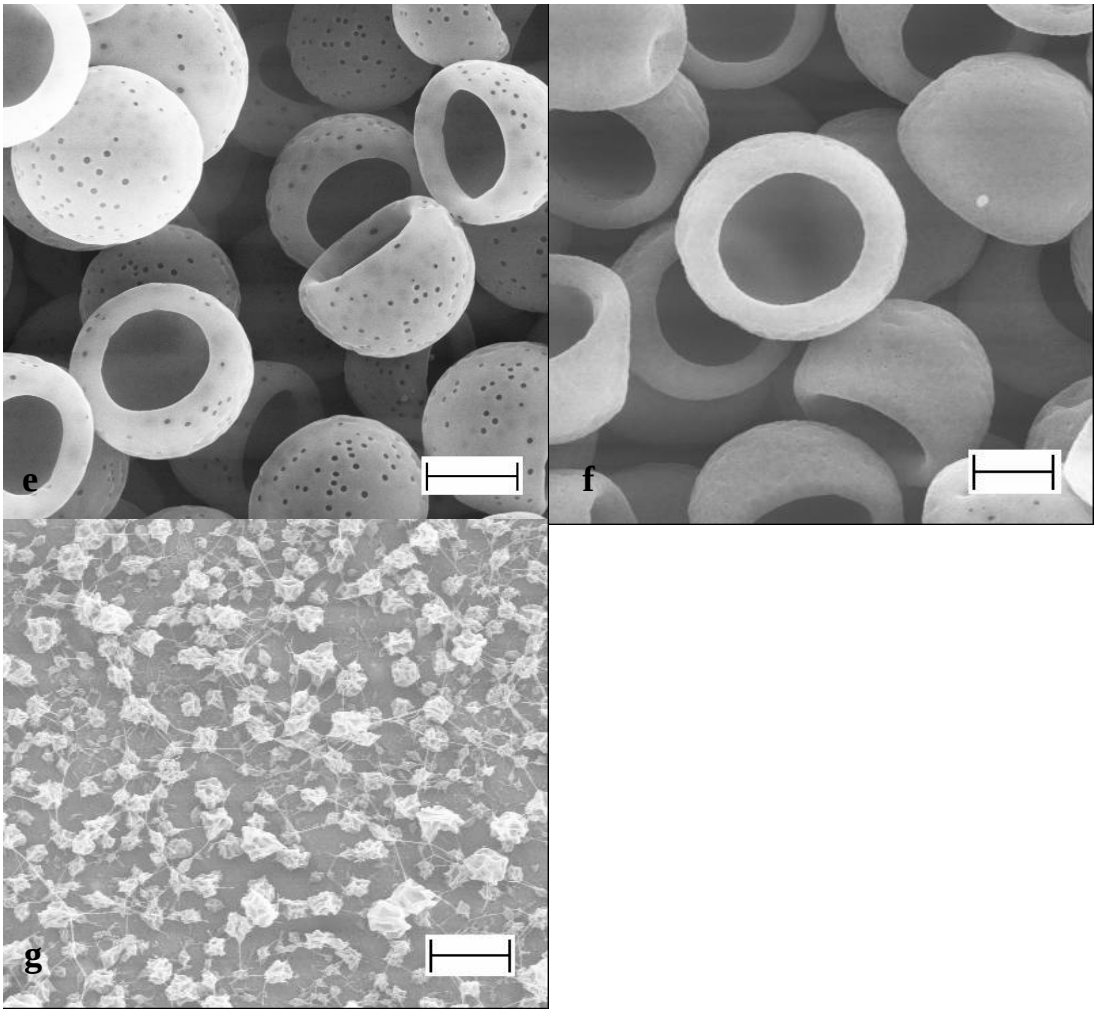

Figure 4.3 continued.

Table 4.4. The morphology and size of the electrospun PMMA particles from different solvents at 8 wt% concentration.

Solvent	Particle morphology	Particle size (μm)
Methylene chloride	Porous polygonal	~25
Tetrahydrofuran	Porous polygonal	~40
Acetone	Solid polygonal	~3
DMF	Solid polygonal	~2
Acrylonitrile	Cup	~5
Nitromethane	Cup	~4
Formic Acid	Solid polygonal with fibrous tails	~0.5 -1

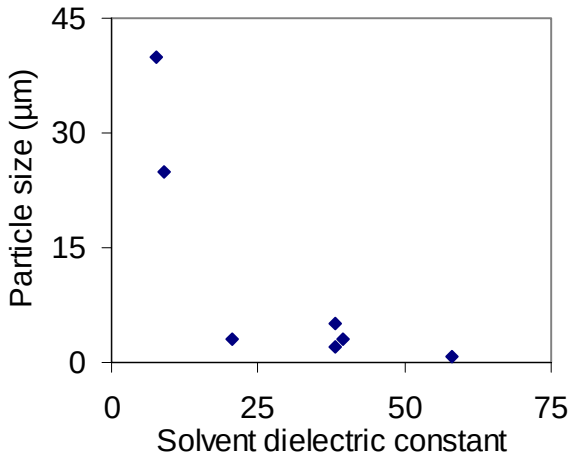

Figure 4.4. PMMA particle size (electrospun from different solvents at 8 wt% concentration using the same electrospinning conditions) as a function of solvent dielectric constant.

Particle dimension generally increases with increasing concentration. At 8 wt% concentration in methylene chloride (MC), particles of ~25 μm dimension are obtained, while at 1 wt% concentration, the particle dimension is ~ 8 μm. The dielectric constant of MC is quite small and its evaporation rate is the highest among the solvents used in the study. Solvents with intermediate dielectric constants (acetone, DMF, acrylonitrile, or nitromethane) at 8 wt% polymer concentration result in particles of 2 to 6 μm dimensions. The relationship between PMMA particle size and dielectric constant of solvents is given in Figure 4.4. The larger the dielectric constant, the smaller the particle size, which is consistent with dielectric constant effect on fiber diameter. Formic acid, the highest dielectric constant solvent, yielded particles (dimension 500 nm to 1 μm) with fibrous tails at 8 wt% concentration.

Solvent evaporation rate is another important factor. Fast evaporation will result in porous spheres, with pores forming on both inside and on the surface of the spheres. Fast evaporation introduces local phase separation, the solvent rich regions will transform into pores. PMMA electrospun using MC produces multi-porous polygonal particles. Solvents with low evaporation rate, such as DMF, result in solid spheres due to the availability of enough time for the phase separation to occur. Acetone is a good solvent for PMMA and exhibits medium evaporation rate resulting in solid particles.

The quality of the solvent (denoted by R_{ij}^2 value, listed in Table 4.3) also affects the particle morphology. The R_{ij}^2 is defined as $R_{ij}^2 = 4(\delta_{d1} - \delta_{d2})^2 + (\delta_{p1} - \delta_{p2})^2 + (\delta_{h1} - \delta_{h2})^2$ (where δ_{d1}, δ_{p1}, and δ_{h1} are the three dimensional solubility parameter values for the solvent; and δ_{d2}, δ_{p2}, and δ_{h2} for the polymer)[223]. The smaller the R_{ij}^2 value, the better the solvent for the polymer. The R_{ij}^2

of methylene chloride, acetone, and DMF for PMMA are 20, 39, and 30 (Table 4.3), respectively. These solvents are considered to be good solvents for PMMA. While acrylonitrile and nitromethane have R_{ij}^2 value of 66 and 106, respectively, and thus they are poor solvents for PMMA. As can be seen from the large R_{ij}^2 value, formic acid is the poorest PMMA solvent used in this study. At a given concentration, poor solvents result in lower viscosity, thereby allowing for jet break up into smaller particles.

Solvent plays an important role on the particle morphology. The similar morphology particles can be produced from solvents with similar properties. PMMA has been electrospun from THF or MC solvents, whose properties listed in Table 4.3, into polygonal multi-porous particles (Figure 4.5). Both THF and MC have similar dielectric constant, viscosity, surface tension, and high evaporation rate. In addition, THF and MC have smaller R_{ij}^2 value with PMMA comparing with other solvents. Both THF and MC are good solvents for PMMA, therefore during the solvent evaporation, the droplet collapses from all sides and results in polygonal particles. Due to their large evaporation rate, polygonal porous particles are produced.

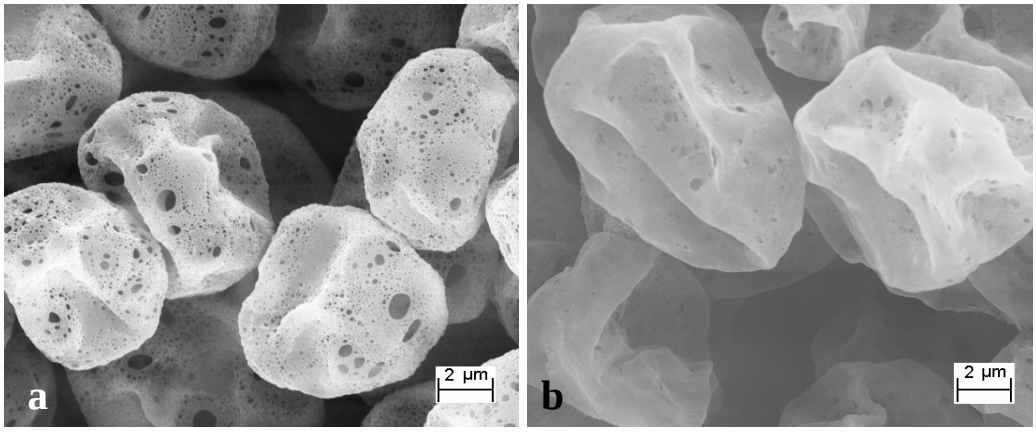

Figure 4.5. Electrospun porous polygonal PMMA particles at 1 wt% concentration from (a) methylene chloride and (b) tetrahydrofuran.

Acrylonitrile and nitromethane have similar properties given in Table 4.3, electrospinning PMMA from these two solvents produces cup shaped particles (Figure 4.6). At a given concentration and electro-processing condition, diameter of these microscopic cups is highly uniform. At 8 wt% concentration, the cup diameter from acrylonitrile is about 20 % larger and less porous than that produced from nitromethane (Figure 4.6 (a) and (b)). The low magnification SEM image of cups electrospun from acrylonitrile is shown in Appendix B. 13.The dielectric constants of acrylonitrile and nitromethane are very comparable, however based on their R_{ij}^2 values; acrylonitrile is a better solvent to PMMA than nitromethane. Therefore at the same concentration, acrylonitrile solution has higher viscosity than the nitromethane solution. Larger diameter of the cups obtained from acrylonitrile is attributed to this difference in viscosity. The cup diameter (D) to the cup height (H) ratio (Figure 4.6 (b)) decreases from ~1.5 to about ~1.2 when the polymer concentration increases from 6 to 10 wt%. The microscopic cup was cut using a razor blade. SEM of the cut cross - sections of the cup wall (Figure 4.6 (d)) shows that the walls are rounded at the tip of the cup, and for cups produced in nitromethane at 8 wt% concentration, the wall thickness is ~800 nm near the cup tip and close to 200 nm at the bottom of the cup. The nitromethane-processed cups also exhibit porosity, with pore dimensions in the 50 to 300 nm range.

The BET specific surface area of microscopic cups processed from nitromethane at 8 wt% concentration, measured by nitrogen gas adsorption is 13.7 m^2/g. Adsorbed N_2 quantity as a function of relative pressure of isothermal N_2 adsorption (77 K) is shown in

Figure 4.7(a). The pore size and pore size distribution are shown in Figure 4.7(b) from the surface area measurement.

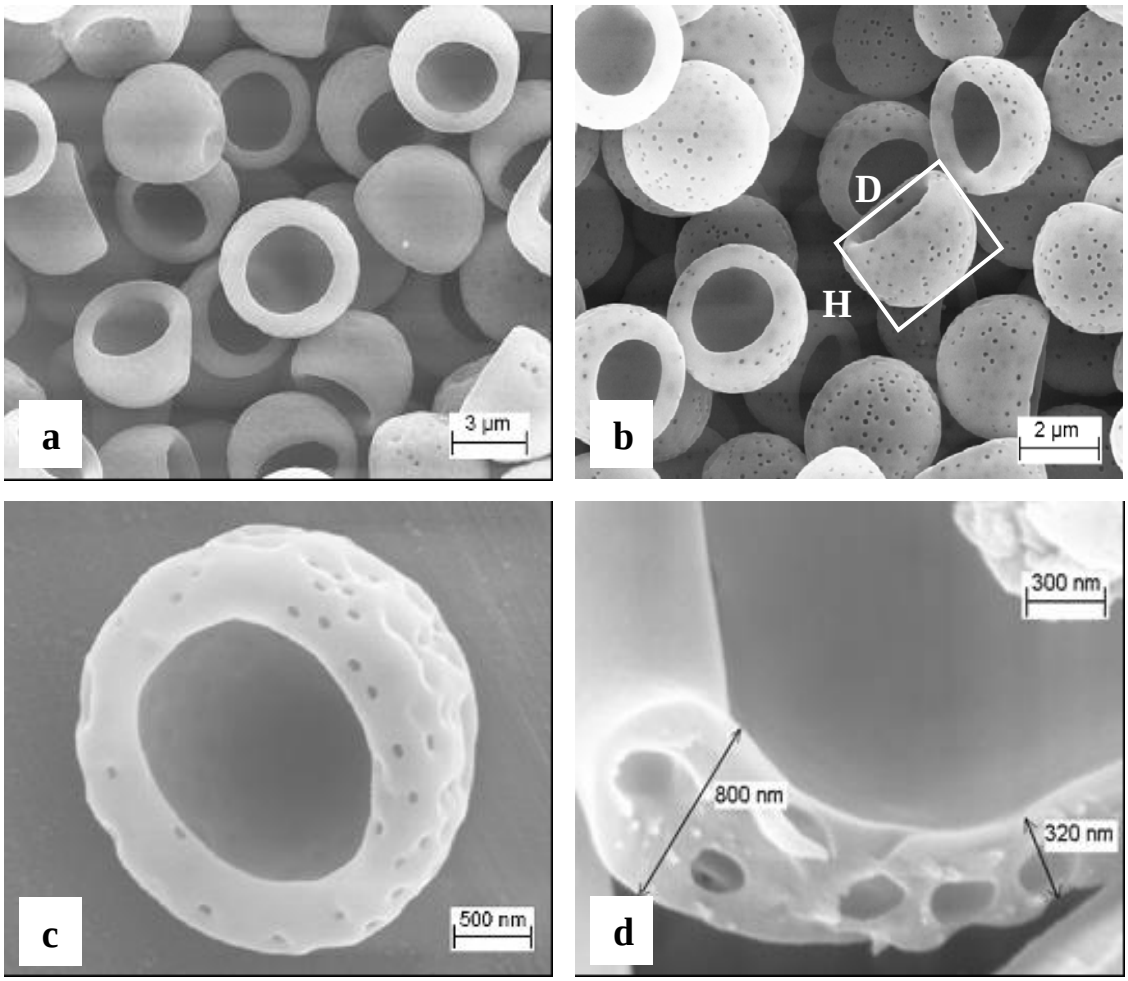

Figure 4.6. Electrospun cups from (a) 8 wt% PMMA in acrylonitrile (b), (c), and (d) 8 wt% PMMA in nitromethane (d) is the razor cut wall cross-section of the cup.

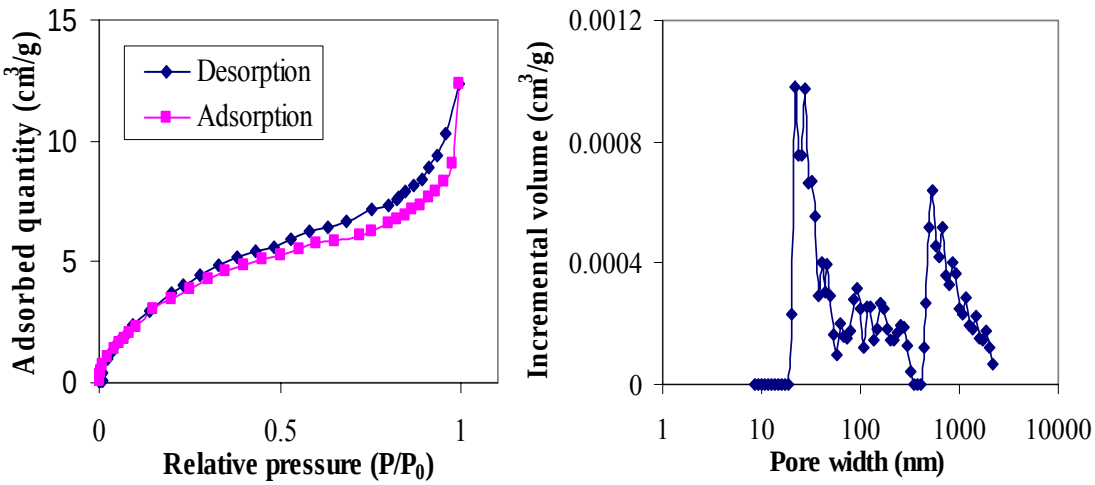

Figure 4.7. Cups electrospun from PMMA/nitromethane solution at 8 wt% concentration (a) Adsorbed N_2 quantity as a function of relative pressure of isothermal N_2 adsorption (77 K) and (b) Pore size distribution of PMMA cups.

For 6 wt% PMMA/nitromethane solution, by changing the flow rate from 2 ml/h to 0.2 ml/h, the cup diameter is decreased from ~3 μm to ~1.8 μm. At the same time, the cup size becomes less uniform, which is shown in Appendix B. 11. The working distance does not show any obvious effect on the cup diameter, which is shown in Appendix B. 12.

The entire cup formation process was visualized by high-speed photography with a speed of 1000 FPS. Photographs were taken within the black dotted square area (Figure 1.4). The distance between the needle tip and the collecting target is 10 cm. Outside this square area, due to the particles scattering or the large jet whipping, it was difficulty to capture a good image. Figure 4.8 shows the electrospinning process of PMMA/nitromethane solution at 8 wt% concentration. Figure 4.8 (a) is the charged polymer solution jet initiating from the Taylor cone. After a certain distance, which is around 0.5 cm, the jet begins whipping (Figure 4.8 (b)), and finally breaks up into

separate droplets (Figure 4.8 (c)). Each droplet looks like a circle. The phase separation into solvent rich region and polymer rich region appears to start at this stage, which leads to the formation of a hole and finally, complete evaporation of solvent results in cup formation. For PMMA/nitromethane electrospinning, the jet break up starts in the whipping region, while for PMMA/acetone, the jet breaks up within the straight region. Electrospinning process of PMMA/acetone solution at 8 wt% concentration is shown in Figure 4.9. Figure 4.9 (a) is the charged polymer solution jet initiating from the Taylor cone, and then breaks up into separate droplets (Figure 4.9 (b)). Each droplet appears as a black sphere, which turns into polygonal solid particles after complete solvent evaporation. In both cases, breakup occurs within 1 cm from the tip of the respective Taylor cones.

The Taylor cone angle is measured in the way shown in Figure 4.10. For PMMA/nitromethane solution electrospinning, with concentration increasing, the Taylor cone is shown in Figure 4.11. At the low polymer concentrations (0.0 wt%, 0.5 wt%, and 2.0 wt%), branching occurs at the Taylor cone. Branching is also observed in carbon nanotube/polyacrylonitrile/DMF solution electrospinning[230]. At these concentrations, electrospun morphology is the cup with a small tail (Figure 5.1 (a) and (b)). At moderate concentrations (6.0 wt%, 8.0 wt%, and 10.0 wt%), Taylor cone is stable with angle around 70° (this angle is consistent with Yarin's report[168]), and cup is the electrospun morphology. While, at high concentrations (14.0 wt% and 20.0 wt%), Taylor cone is stable with angle around 110°, resulting in fibers.

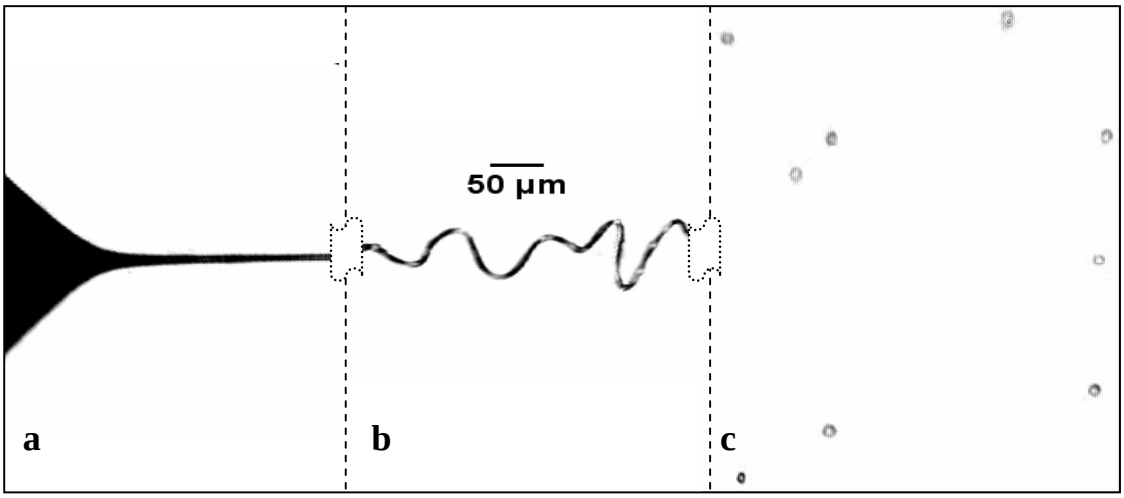

Figure 4.8. High-speed photographs of PMMA/nitromethane (8 wt%) electrospinning process (a) charged polymer solution jet initiating from the Taylor cone, (b) jet whipping, (c) jet breaking up into separate droplets.

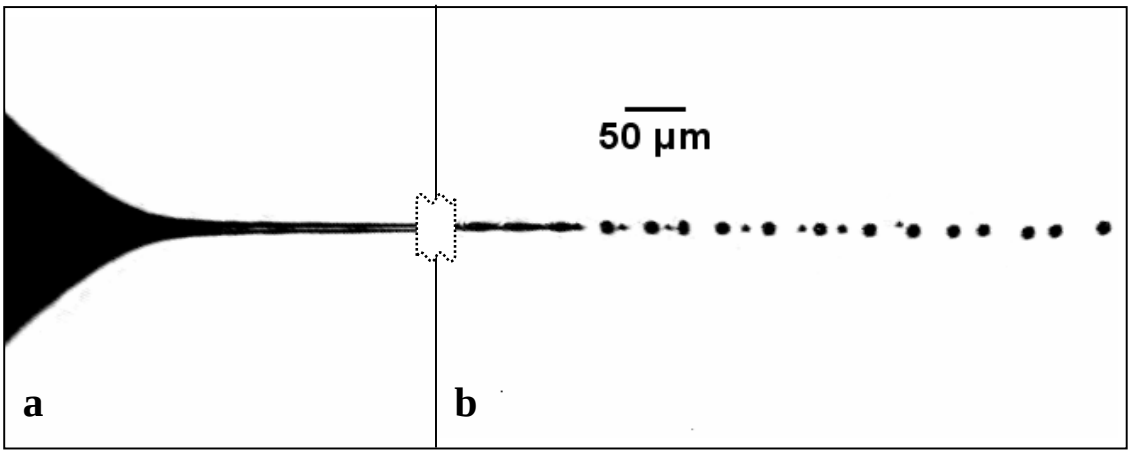

Figure 4.9. High-speed photographs of PMMA/acetone (8wt %) electrospinning process (a) charged polymer solution jet initiating from the Taylor cone, (b) jet breaking up into separate droplets.

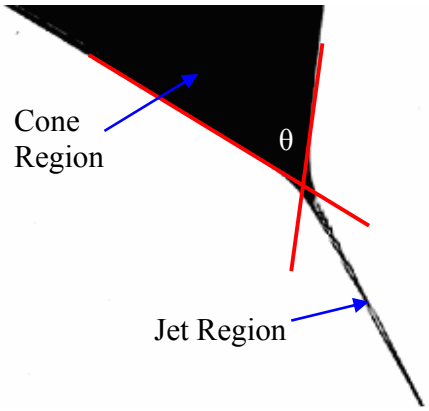

Figure 4.10. The angle θ between the two red lines is measured as Taylor cone angle.

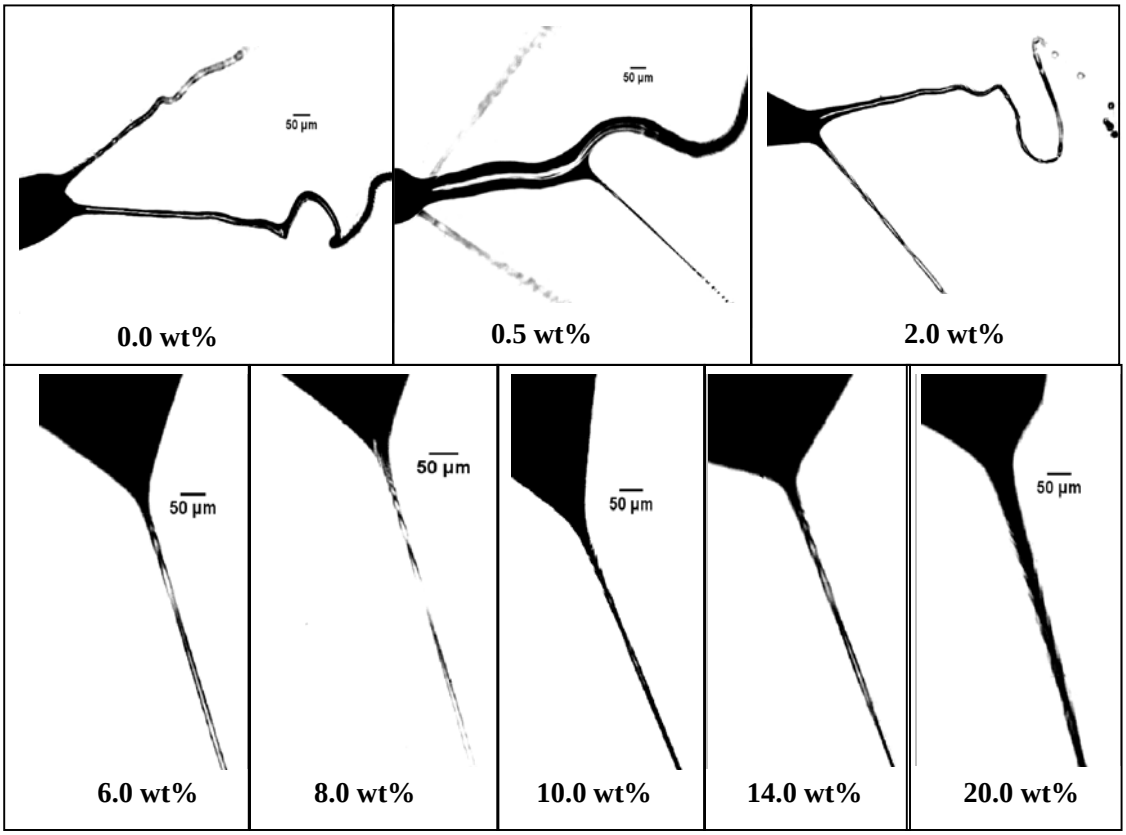

Figure 4.11. Taylor cones of electrospinning PMMA/nitromethane solutions at different polymer concentrations. Taylor angle for 6.0, 8.0, and 10.0 wt% polymer solutions is about 70 °, while for 14.0 and 20.0 wt% solutions it is about 110 °. Jet branching occurred in nitromethane, as well as in 0.5 and 2.0 wt% polymer solutions.

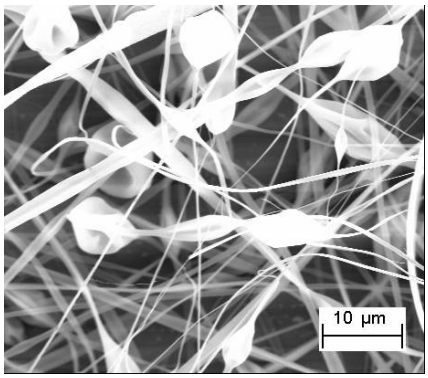

Figure 4.12. Beaded fibers electrospun from PMMA/methylene chloride at 12 wt% concentration.

PMMA ($\overline{M_w} = 95{,}000 \sim 150{,}000$ g/mole)/methylene chloride produces beaded fibers at 12 wt% concentration (Figure 4.12). In order to examine the effect of polymer molecular weight on particle formation condition, an ultra low molecular weight PMMA (ULMW PMMA) ($\overline{M_w} = 15{,}000$ g/mole) was electrospun from methylene chloride. The SEM images of the particles are given in Figure 4.13. The particle size electrospun from 1 wt%, 15 wt%, and 30 wt% solution concentrations are 4.5 ± 1.5 µm, 11.2 ± 2.1 µm, and 18.6 ± 3.5 µm, respectively. The particle size increases with increasing solution concentration. PMMA ($\overline{M_w} = 95{,}000 \sim 150{,}000$ g/mole)/methylene chloride solution produces electrospun particles with concentration < 12 wt%, while ULMW PMMA ($\overline{M_w} = 15{,}000$ g/mole)/methylene chloride solution can produce particles even at 30 wt% concentration. Lower molecular weight polymer widens the concentration range for producing electrospun particles. This ULMW PMMA (FTIR spectrum shown in Appendix B. 1) does not dissolve in nitromethane and in formic acid due to its different structure compared to typical PMMA.

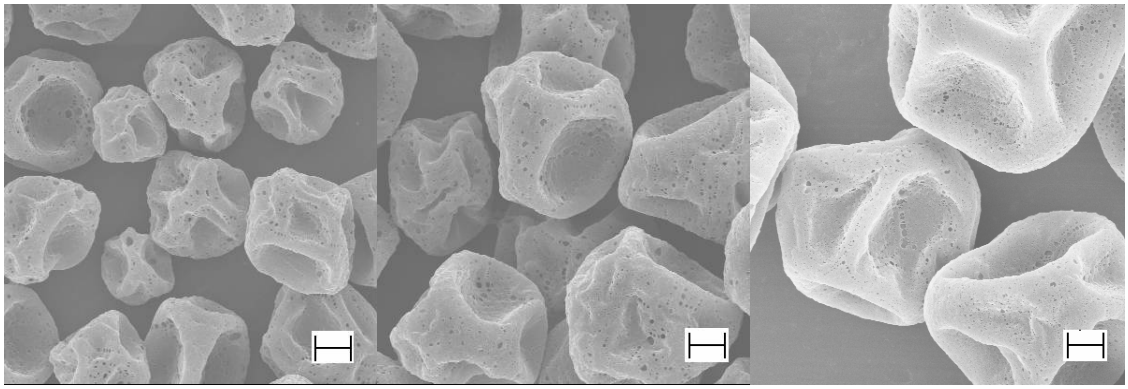

Figure 4.13. Polygonal ultra low molecular weight PMMA ($\overline{M_w} = 15{,}000$ g/mole) (ULMW PMMA) particles electrospun from solution in methylene chloride at different concentrations: (a) 1 wt%, (b) 15 wt%, and (c) 30 wt% (scale bar is 2 μm).

4.3.2 PSVPh copolymers elctrospinning

PSVPh copolymers were electrospun in methyl ethyl ketone (MEK) solutions to further explore cup formation condition.

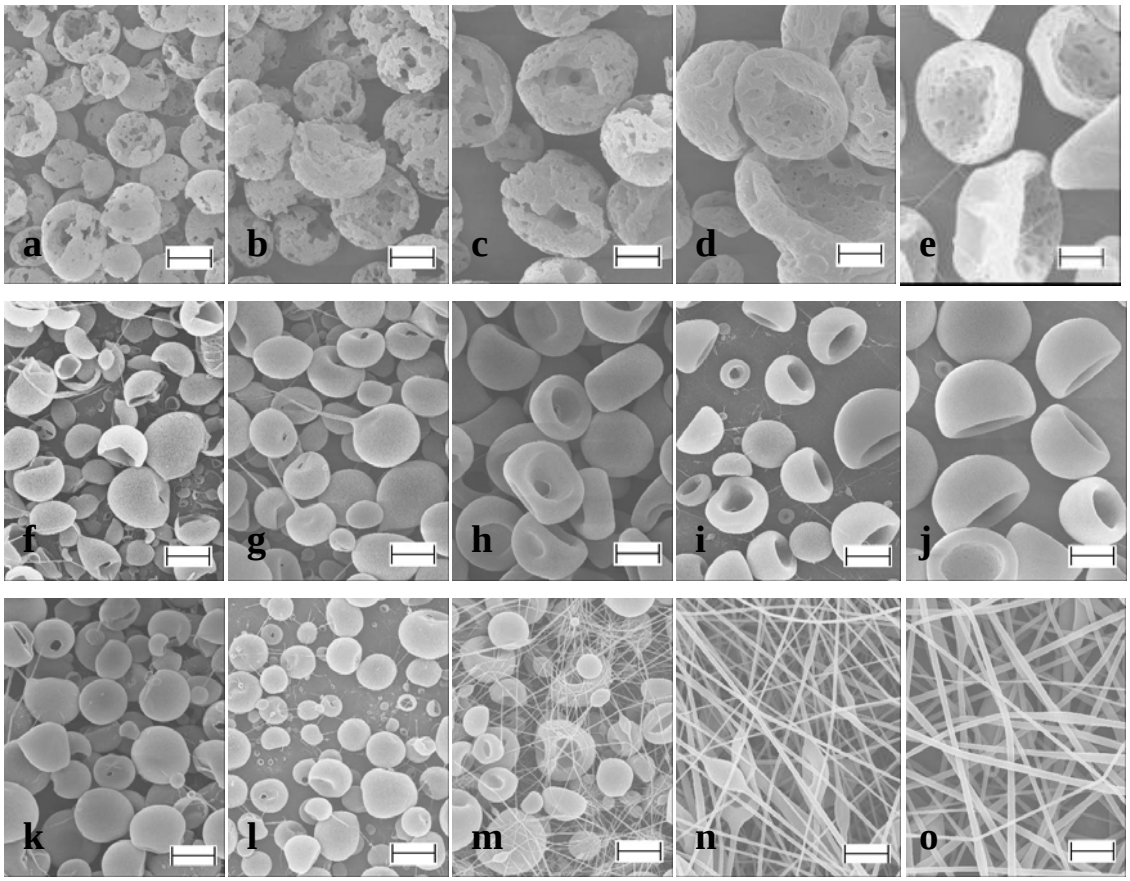

Figure 4.14. Electrospinning of PSVPh0/MEK solution, with increasing concentration (a) 1.0 wt%, (b) 2.0 wt%, (c) 4.0 wt%, (d) 6.0 wt%, and (e) 8.0 wt%. Electrospinning of PSVPh20/MEK solution, with increasing concentration (f) 1.0 wt%, (g) 2.0 wt%, (h) 4.0 wt%, (i) 6.0 wt%, and (j) 8.0 wt%. Electrospinning of PSVPh40/MEK solution, with increasing concentration (k) 1.0 wt%, (l) 2.0 wt%, (m) 4.0 wt%, (n) 6.0 wt%, and (o) 8.0 wt% (Scale bar is 2 μm).

The solvent evaporation rate of a polymer solution depends not only on the solvent's own characteristics, but also on the solution concentration and the interaction between the polymer and the solvent. With increasing concentration, the solvent is surrounded by more and more polymer molecules, which slows down the solvent evaporation[231]. In cases where hydrogen bond or other specific interaction exists between the polymer and the solvent, the solvent evaporation is further hindered.

The three dimensional solubility parameters of the PSVPh copolymers were calculated by the group contribution methods using the following equations[232]: $\delta_d = \frac{\sum F_{di}}{V}$, $\delta_p = \frac{\sqrt{\sum F_{pi}^2}}{V}$, $\delta_h = \sqrt{\frac{\sum E_{hi}}{V}}$ (F_d: dispersion component force, F_p: polar component force, E_h: hydrogen bond component energy, V: molar volume), and are listed in Table 4.5. The calculated three dimensional solubility parameter values for polystyrene (PSVPH0) are δ_d =18.05 $(MPa)^{0.5}$, δ_p =1.12 $(MPa)^{0.5}$, and δ_h= 0.00 $(MPa)^{0.5}$, while the corresponding experimental values for polystyrene are 21.3 $(MPa)^{0.5}$, 5.8 $(MPa)^{0.5}$, and 4.3 $(MPa)^{0.5}$. Solubility parameter shows difference between the theoretical calculated value and the experimental values[233, 234] in literature. Although there is a significant difference between these calculated and experimental values of the solubility parameter of PSVPh copolymers, the trend with increasing vinyl phenol component leading to the changes in solubility parameters can be meaningfully used to assess the relative solubility of various copolymers in MEK.

Table 4.5. Three dimensional solubility parameters of PSVPh copolymers and R_{ij}^2 between the copolymers and MEK.

	δ_d $(MPa)^{0.5}$	δ_p $(MPa)^{0.5}$	δ_h $(MPa)^{0.5}$	R_{ij}^2 (MPa)
PSVPh0	18.05	1.12	0.00	104.8
PSVPh10	17.82	1.58	1.76	79.5
PSVPh20	17.72	1.78	2.54	70.5
PSVPh30	17.48	2.24	4.34	55.0
PSVPh40	17.32	2.57	5.61	48.5
MEK	16.00	9.00	5.10	0.0

With increasing vinyl phenol content, R_{ij}^2 between the PSVPh copolymer and MEK decreases, indicating that MEK is becoming a good solvent for the copolymer containing more vinyl phenol component due to the increasing amount of hydrogen bonds between –OH group in the copolymer and –CO group in MEK. This is further confirmed by the dissolution rate and viscosity of the copolymer in MEK solutions. The dissolution rate of the copolymers in MEK increases with increasing vinyl phenol content. For 2 wt% concentration solutions, PSVPh0 took about 40 minutes to dissolve completely, while PSVPh40 dissolved in about 20 minutes.

Due to differences in hydrogen bonding, MEK is expected to evaporate faster in PSVPh0/MEK solution than in other copolymer/MEK solutions. Figure 4.14 (a), (b), (c), (d) and (e) show the morphology changes from porous hollow spheres to deformed cups

with increasing solution concentration of PSVPh0 in MEK. Figure 4.14 (f), (g), (h), (i), and (j) show the morphology changes from hollow porous spheres to cups with increasing solution concentration of PSVPh20 in MEK. Figure 4.14 (k), (l), (m), (n), and (o) show morphology change from hollow spheres to beaded fibers to bead free fibers with increasing PSVPh40 in MEK concentration. These morphology changes are resulting from two factors: (1) For one specific copolymer, MEK evaporation rate decreases with increasing polymer concentration. (2) Based on R_{ij}^2 calculation, MEK is a relatively poor solvent for PSVPh0, PSVPh10 and PSVPh20, while it is a relatively good solvent for PSVPh30 and PSVPh40. At the same polymer concentrations, solvent evaporation rate decreases from PSVPh0 to PSVPh40. Both PSVPh10 and PSVPh20 have similar morphology changes with increasing polymer concentration. PSVPh30 and PSVPh40 have comparable morphology changes with increasing concentration. Fibers were produced for PSVPh30/MEK or PSVPh40/MEK solutions at concentrations above 6 wt%. Due to hydrogen bond saturation between the polymer and the solvent at certain critical vinyl phenol content[235], there is no obvious electrospun morphology difference between PSVPh30 and PSVPh40 at the same concentration.

4.3.3 Electrospun particles formation conditions

Based on electrospun PMMA and PSVPh particles, qualitative relationships between solvent properties and electrospun particle morphology are shown in Figure 4.15.

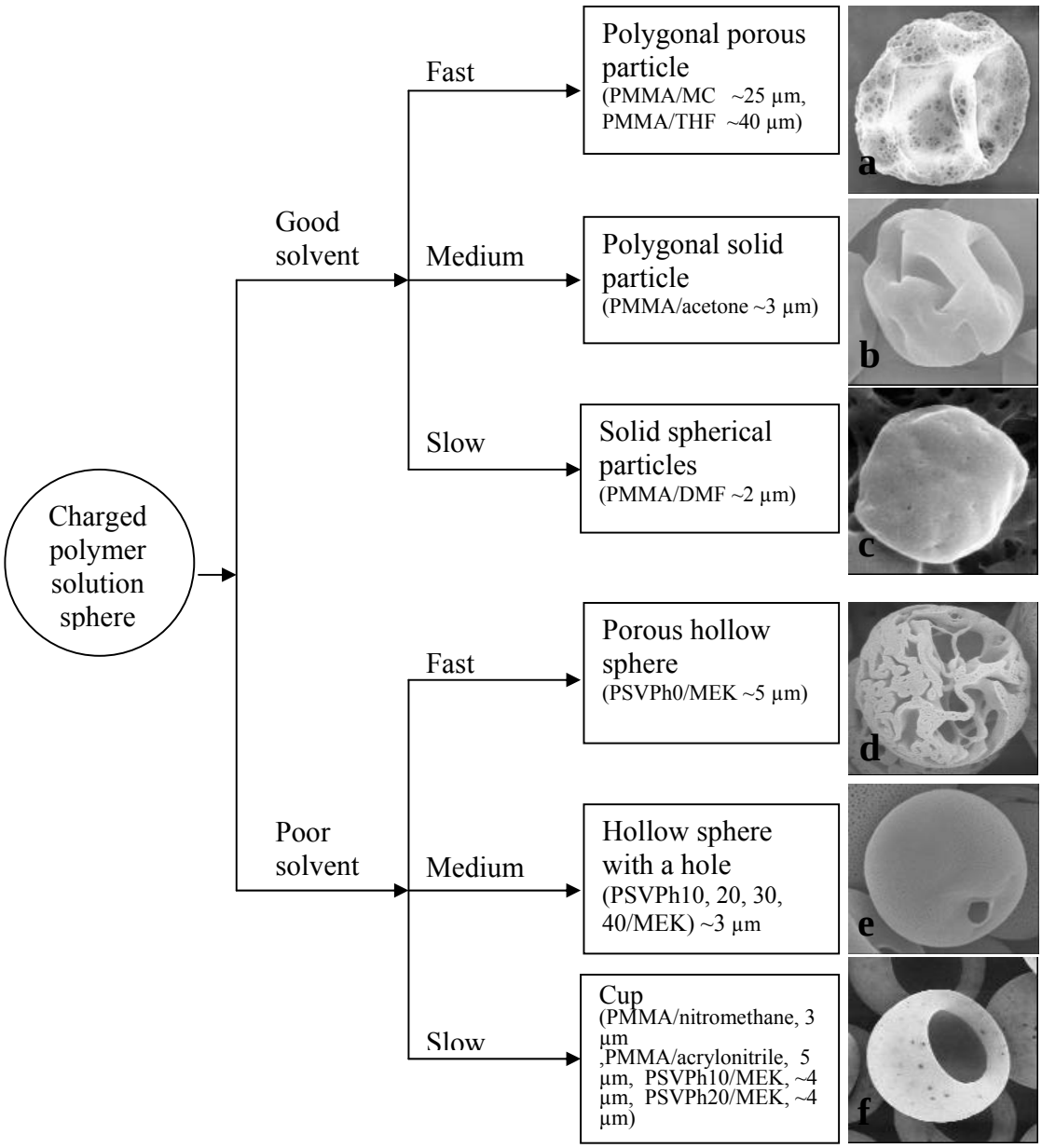

Figure 4.15. Polymer particle formation conditions. (Solvents are divided into poor and good solvent. Evaporation rate of solvents are divided in three categories: fast, medium, and slow. The particle sizes in the brackets for PMMA particle electrospun from 8 wt% concentration solutions, while for others the size is for particles electrospun from 2 wt% concentration solutions. Polygonal porous particle of PMMA electrospun from MC is from Figure 4.3a and from THF in Figure 4.3b. PMMA polygonal solid particle electrospun from acetone is in Figure 4.3c. PMMA solid spherical particle electrospun from DMF is in Figure 4.3d. PSVPh0 porous hollow sphere electrospun from MEK is in Figure 4.14a, hollow sphere with a hole in Figure 4.14g and k, and cups are in Figure 4.3e and f and Figure 4.14 j).

After the charged polymer solution jet comes out of the Taylor cone, it breaks up into separate droplets due to low viscosity and high surface tension. The charged polymer solution sphere changes into various shaped particles during solvent evaporation. The properties that determine the particle morphology and size include polymer molecular weight, solvent's dielectric constant, evaporation rate, and solvent quality. Here we discuss the effects of these factors on particle morphology. (1) Molecular weight: low molecular weight polymer broadens the concentration window suitable for producing electrospun particles, which has been demonstrated by electrospinning PMMA with different molecular weight/nitromethane under the identical electrospinning conditions. Low molecular weight PMMA ($\overline{M_w} = 95{,}000 \sim 150{,}000$ g/mol) (LMW PMMA)/nitromethane produces ladles and cups at the concentration ranges from 1 wt% ~ 12 wt%, from 14 wt%, it produces cups connected by fine fibers, while high molecular weight PMMA ($\overline{M_w} = 350{,}000$ g/mol) (HMW PMMA)/nitromethane produces cups connected by fine fibers even at very low concentrations (1 ~ 3 wt%), which is discussed in detail in chapter 5. Ultra low molecular weight PMMA ($\overline{M_w} = 15{,}000$ g/mole) (ULMW PMMA)/methylene chloride solution produces porous polygonal particles in the concentration range from 1 wt% to 30 wt% (Figure 4.13), while for LMW PMMA ($\overline{M_w} = 95{,}000 \sim 150{,}000$ g/mole)/methylene chloride solutions produce particles within 1wt% to <12 wt% concentration range. (2) Dielectric constant: high dielectric constant solvent results in smaller size particles. (3) Evaporation rate: fast evaporating solvents result in porous particles. The evaporation rate of the solvent is also affected by the concentration and the interaction between the solvent and the polymer. (4) Solvent quality: the solvent quality for the polymer can be roughly predicted by R_{ij}^2 value. By

choosing a good solvent with a fast evaporation rate for the polymer, polygonal porous particles can be produced (Figure 4.15 (a)). For medium evaporation rate solvent, solid particles with polygonal morphology are formed (Figure 4.15 (b)). For the slow evaporation rate solvent, solid near spherical particles (Figure 4.15 (c)) were obtained. If a poor solvent is used for the polymer, porous hollow spheres are produced for the fast evaporation rate solvent (Figure 4.15 (d)). For medium evaporation solvent, hollow spheres with open mouths (Figure 4.15 (e)) are processed. For the slow evaporation rate poor solvent, cups (Figure 4.15 (f)) are obtained.

Cups can be produced by adjusting the electrospinning conditions. Hollow porous spheres (Figure 4.14 (a)) from PSVPh0/MEK change into deformed cups (Figure 4.14 (e)) by increasing solution concentration. The change in morphology is attributed to hindered solvent evaporation caused by increase in concentration. PSVPh20/MEK results in hollow spheres with open mouths (Figure 4.15 (e)) at 4 wt%, while cups (Figure 4.15 (f)) are formed at 8 wt% solution concentration. The solvent evaporation is slowed down by the presence of more hydrogen bonds and increased concentration, making the solution meet the cup formation requirements. During PMMA ($\overline{M_w} = 95{,}000 \sim 150{,}000$ g/mole)/methylene chloride 1 wt% solution electrospinning, the solution temperature was decreased using dry ice (around 5 °C), as a result, electrospun particle shape changes from porous polygonal particles (Figure 4.16(a)) to cups (Figure 4.16(b)). PMMA/MC solution has an upper critical solution temperature behavior[236]. At low temperature, MC might become a poor solvent for PMMA and also the decreased temperature retards the evaporation rate. By choosing the proper solvent and by tailoring the electrospinning conditions, polymer particle morphology can be controlled.

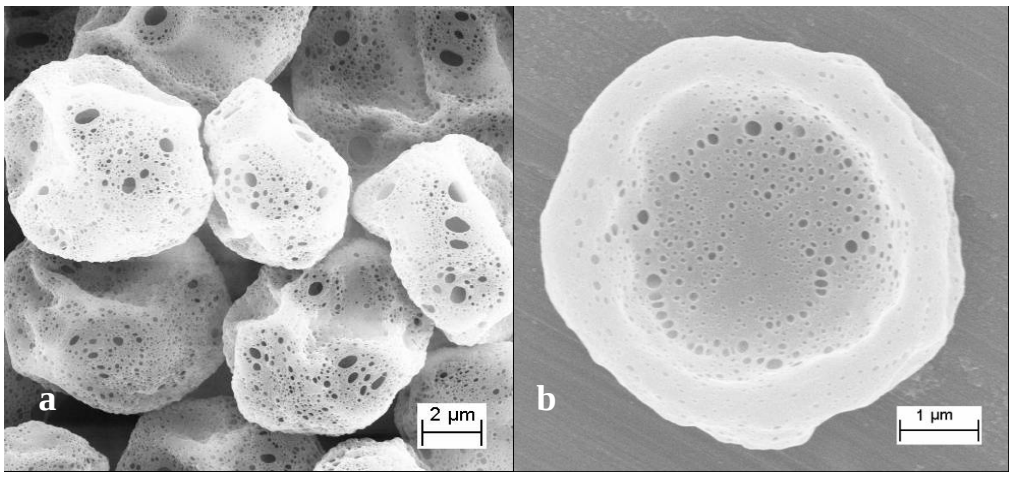

Figure 4.16. PMMA particles electrospun from methylene chloride solution at 1 wt% concentration: (a) in air and (b) under a relatively low temperature (around 5 °C) cooled by dry ice (The low magnification photograph of b is shown in Appendix B. 14).

4.4 Conclusions

Electrospinning produces particles of various morphologies at relatively low polymer concentrations. PMMA microscopic polymer cups are produced from electrospinning in nitromethane or acrylonitrile solutions. High speed photographs visualize the particle formation process. In order to further explore cup formation conditions, PSVPh random copolymers were electrospun from solutions in MEK. Cups are obtained from PSVPh10 and PSVPh20, while PSVPh30 and PSVPh40 resulted in beaded fibers at the same concentration and the same electrospinning conditions. Based on PMMA and PSVPh electrospun particles, the qualitative relationship is shown between solvent properties and electrospun particle morphologies. Electrospinning parameters determine the particle morphologies. By tailoring the solution properties and the electrospinning conditions, the particle morphology can be controlled.

CHAPTER 5

EFFECT OF SOLUTION VISCOSITY AND SOLVENT PROPERTIES ON ELECTROSPUN FIBER MORPHOLOGY

5.1 Introduction

At relatively high concentrations, fibers are produced by electrospinning. Among all the electrospinning parameters discussed in chapter 1, for a certain pair of polymer and solvent, solution viscosity, which depends on polymer concentration, has the greatest effect on electrospun fiber morphology[164]. Colby et al. measured the viscosity dependence on concentration of linear polymers in good solvents and identified four different concentration regimes including dilute, semidilute unentangled, semidilute entangled, and concentrated regimes[237, 238]. Two critical concentrations are defined. The chain entanglement concentration *C*e, is the boundary between the semidilute unentangled and semidilute entangled regimes and is defined as the point at which significant overlap of polymer chains topologically constrain the chain motion[239]. The chain overlap concentration *C**, is the boundary between the semidilute entangled and concentrated regimes and is defined as the point that polymer chain entanglements dominate the flow behavior[239].

Gupta et al. reported a series of seven linear homopolymers of PMMA with M_w ranging from 12,470 to 365,700 g/mol electrospun from their DMF solutions[240]. With increasing solution concentration, the electrospun morphology of PMMA/DMF changed from droplets, to beaded fibers, and then to uniform bead free fibers. The author also determined the dependence of fiber diameter (for all these seven different molecular

weight PMMA) on concentration to be $d_f \sim c^{3.1}$. In this chapter, two kinds of atactic PMMA with different molecular weight and one kind of isotactic PMMA were utilized to explore the scaling relationship between viscosity (or fiber diameter) and concentration. For low molecular weight atactic PMMA electrospinning, particles are produced at relatively low concentrations, which are already discussed in chapter 4. Nitromethane was chosen to be the solvent as it was found to offer uniform SWNT dispersion in PMMA.

To date, there are no literature reports on isotactic PMMA electrospinning. In this study, isotactic PMMA was electrospun using four different solvents to investigate the influence of solvents on fiber morphology. Electrospun fibers have various morphologies. High molecular weight atactic PMMA/methylene chloride and isotactic PMMA/methylene chloride were electrospun into porous fibers. In order to determine the porous fibers formation conditions, polystyrene (PS)/tetrahydrofuran solution was also electrospun.

5.2 Experimental

Low molecular weight atactic PMMA ($\overline{M_w} = 95{,}000 \sim 150{,}000$ g/mole) (LMW aPMMA) was obtained from Cyro Industries. High molecular weight aPMMA ($\overline{M_w} = 350{,}000$ g/mol, poly dispersity index (PDI) = 4~5) (HMW aPMMA) and isotactic PMMA ($\overline{M_w} = 300{,}000$ g/mol, PDI = 4~6) (iPMMA) were purchased from Sigma-Aldrich Co. PS ($\overline{M_w} = 100{,}000$ g/mol) was purchased from Dow Chemical Co. Acrylonitrile, nitromethane, formic acid, methylene chloride, and tetrahydrofuran were also purchased from Sigma-Aldrich Co. Dielectric constant and evaporation rate of these

solvents at room temperature are listed in Table 4.3. Both solvents and polymers were used as received. Electrospinning was conducted in the horizontal mode in a chemical hood with a 2 ml/h flow rate via an 18 gauge stainless steel needle at 22,000 volts, and the distance between the needle tip and the grounded aluminum foil target was 10 cm. Molecular weights, PDIs, solvents and solution concentrations are listed in Table 5.1. Scanning Electron Microscopy (SEM) was conducted on gold coated samples in LEO 1530 thermally-assisted FEG scanning electron microscope at 15 kV. Solution viscosity was measured by Rheometric Scientific's Advanced Rheometric Expansion System (ARES) with bob cup arrangement at room temperature (the inner diameter of the cup is 3.5 cm, the gap between the bob and cup is 0.2 cm). Each sample is 10 ml. The shear rate is ranging from 0.1 s^{-1} to 500 s^{-1}. To measure the surface area and the porosity of the elctrospun products, the electrospun fiber mats were degassed at 25 °C for 24 hours at 1 × 10^{-4} Pa. The isothermal N_2 gas adsorption and desorption studies were carried out at 77 K on ASAP 2020 (Micromeritics Instrument Corporation, Norcross, GA). The quantity of gas volume (V) absorbed or released at 77 K was measured as a function of gas pressure P. The specific surface area and pore size distribution of the fiber mat were evaluated by using Brunauer-Emmett-Teller (BET) and Density Functional Theory (DFT) methods, respectively.

Table 5.1. List of samples on which electrospinning is conducted in this chapter.

Polymer	$\overline{M_w}$ (g/mol)	Polydispersity Index	Solvents	Polymer Concentration (wt%)
iPMMA	300,000	4~6	nitromethane	1, 2, 3, 4, 5, 6, 7, 8, 9, 10
			acrylonitrile	4
			methylene chloride	2, 4
			formic acid	4
LMW aPMMA	95,000~ 150,000	4~7	nitromethane	2, 4, 6, 8, 10, 12, 14, 16, 18, 20
HMW aPMMA	350,000	4~5	nitromethane	1, 2, 3, 4, 5, 6, 7, 8, 9, 10, 11, 12, 13
			methylene chloride	8, 12
Polystyrene	100,000	-----	tetrahydrofuran	3, 12, 29

5.3 Results and Discussion

5.3.1 Effect of solution viscosity on electrospun fiber morphology

LMW aPMMA/nitromethane, HMW aPMMA/nitromethane, and iPMMA/nitromethane solutions were utilized to investigate the impact of the scaling relationships between viscosity and concentration on the fiber formation. Electrospinning of these solutions was carried out at identical conditions to ascertain the effects of solution concentration and viscosity on fiber formation and morphological features of the electrospun material. All three kinds of PMMA were electrospun over a wide concentration range (Table 5.1). The highest concentration for electrospinning was determined at which the solution started to clog the needle, it was difficulty to conduct electrospinning on solutions above that concentration.

For LMW aPMMA, three different morphologies resulted (Figure 5.1). At low concentrations (2 wt%~ 4 wt%), ladle structure dominates the morphology. In the middle concentration region (6 wt%~12 wt%), cups result. These two morphologies are already discussed in chapter 4. At relatively high concentrations (14 wt%~20 wt%), beaded or bead-free fibers form. For HMW aPMMA/nitromethane solutions (Figure 5.2), three different morphologies result with increasing concentration, cups connected by fine fibers are observed in the concentration ranging from 1 wt% to 3 w%. Beaded fibers are formed in the concentration range from 4 wt% to 8 wt%. For the concentration range from 9 wt% to 13wt%, bead free fibers are produced. For iPMMA, three different morphologies results with increasing solution concentration (Figure 5.3). At low concentrations (1 wt%~2 wt%), cups connected by fine fibers with ordered structure is the main morphology. In the middle concentration region (3 wt%~5 wt%), beaded fibers with ordered structure result. Randomly deposited bead free fibers are formed at relatively high concentrations (6 wt%~10 wt%). The fiber from 6 wt% solution is almost twice the

diameter of the one from 5 wt%. The ordered structure disappears at 6 wt% concentration. Solution and fiber characteristics of these three polymers electrospun from nitromethane solutions at various polymer concentrations are summarized in Table 5.2.

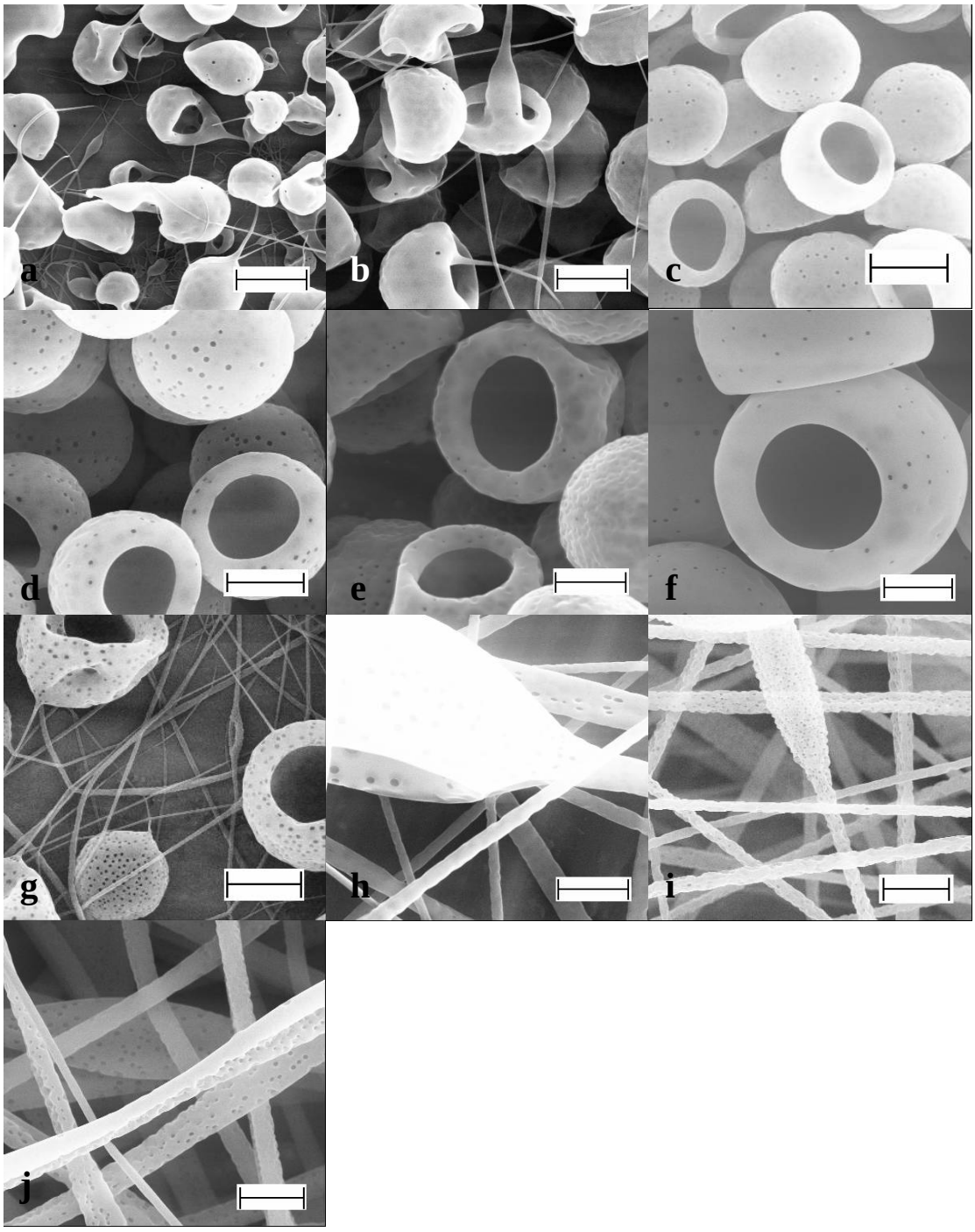

Figure 5.1. Low molecular weight aPMMA (LMW aPMMA) electrospun from nitromethane solutions at different concentrations (a) 2 wt%, (b) 4 wt%, (c) 6 wt%, (d) 8 wt%, (e) 10 wt%, (f) 12 wt%, (g) 14 wt%, (h) 16 wt%, (i) 18 wt%, and (j) 20 wt% (scale bar is 2 μm).

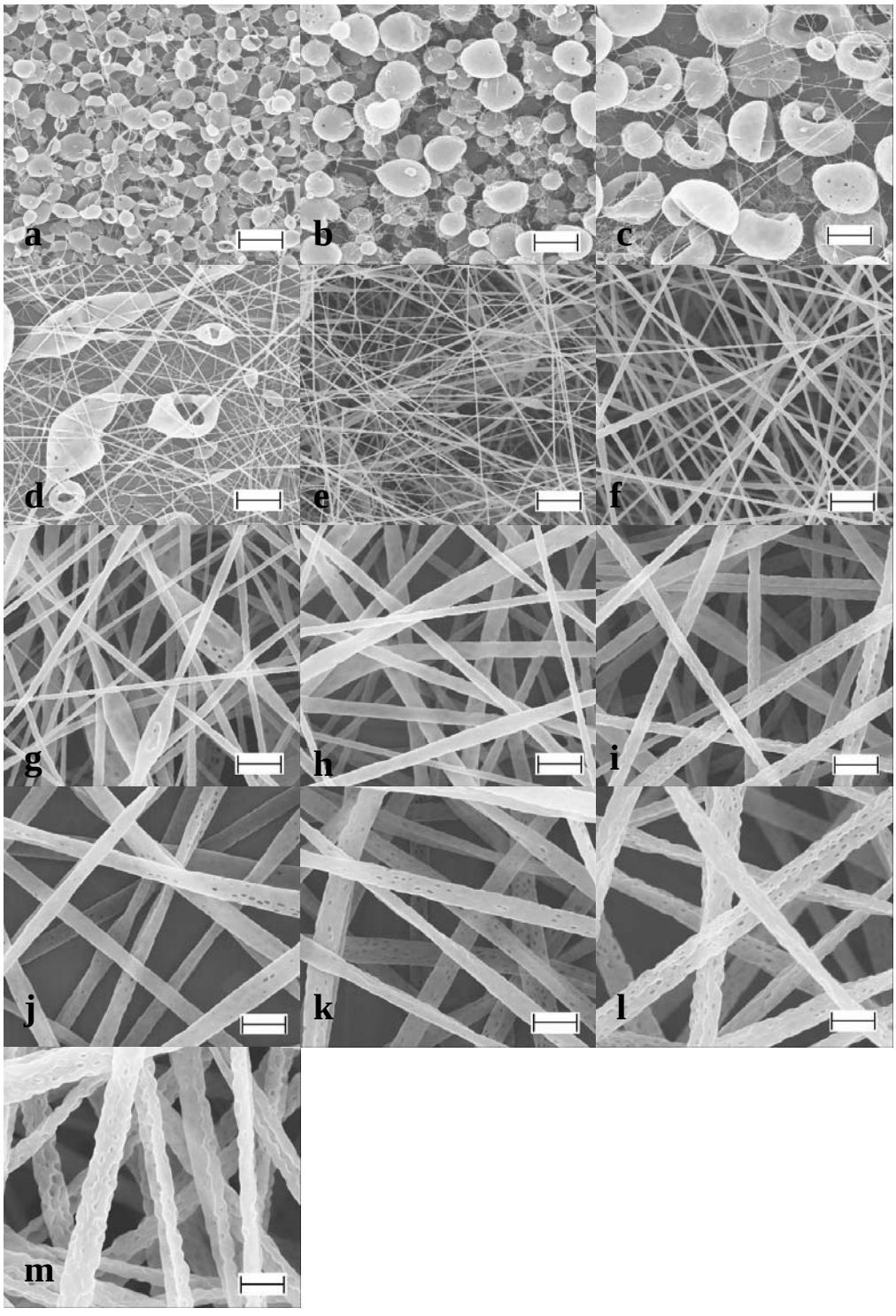

Figure 5.2. High molecular weight aPMMA (HMW aPMMA) electrospun from nitromethane solutions at different concentrations (a) 1 wt%, (b) 2 wt%, (c) 3 wt%, (d) 4 wt%, (e) 5 wt%, (f) 6 wt%, (g) 7 wt%, (h) 8 wt%, (i) 9 wt%, (j) 10 wt%, (k) 11 wt%, (l) 12 wt%, and (m) 13 wt% (scale bar is 2 μm).

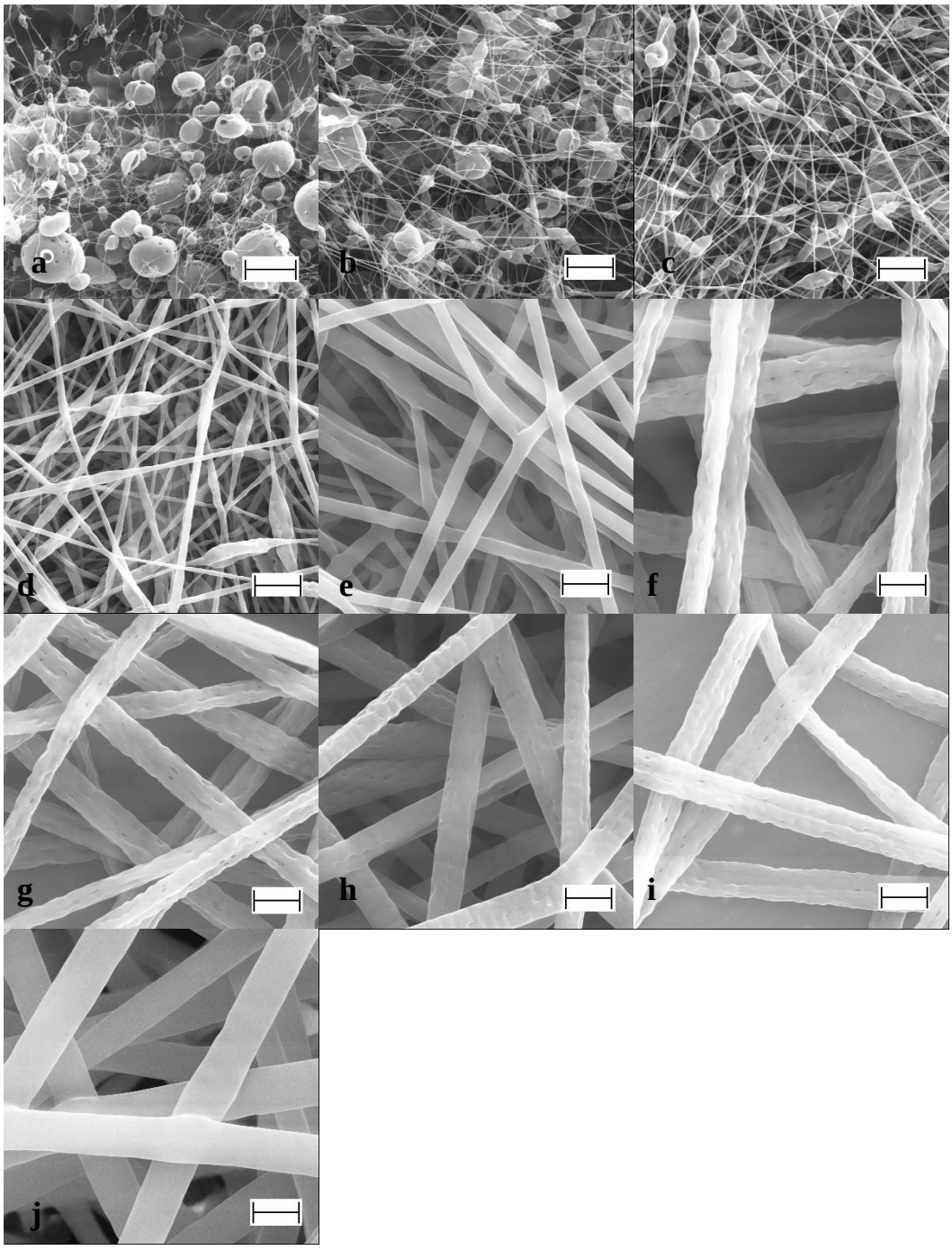

Figure 5.3. Isotactic PMMA (iPMMA) electrospun from nitromethane solutions at different concentrations (a) 1 wt%, (b) 2 wt%, (c) 3 wt%, (d) 4 wt%, (e) 5 wt%, (f) 6 wt%, (g) 7 wt%, (h) 8 wt%, (i) 9 wt%, and (j) 10 wt% (scale bar is 2 μm).

Table 5.2. PMMA/nitromethane solution viscosities and electrospun fiber mat morphology.

	Concentration (wt%)	Viscosity (Pa.s)	Exponent a ($\eta_{sp} \sim C^a$)	Exponent a ($d_t \sim C^a$)	Morphology
LMW aPMMA	2~4	0.0012~0.0023	1.9	----	Ladle
	6~12	0.0045~0.015		----	Cup
	14~20	0.0483~0.1331	2.8	3.7	Beaded fiber
HMW aPMMA	1~3	0.0014~0.0035	1.2	----	Cup connected by fine fibers
	4~8	0.0058~0.032	2.6	3.4	Beaded fibers
	9~13	0.0624~0.6438	6.5	0.8	Bead free fibers
iPMMA	1~2	0.0021~0.004	1.2	----	Cup connected by fine fibers
	3~5	0.008~0.0261	2.4	3.7	Beaded fibers
	6~10	0.0403~0.5921	5.2	0.4	Bead free fibers

η_{sp} = specific viscosity, C = polymer solution concentration, d_t = fiber diameter

The viscosity of nitromethane measured in this study at room temperature is 0.00063 Pa.s, which is consistent with literature reported value[207]. The viscosities of LMW aPMMA/nitromethane solutions at various concentrations are shown in Figure 5.4. The viscosities of HMW PMMA/nitromethane solutions at various concentrations are

shown in Figure 5.5. Shear thinning is observed at higher shear rate region for 12 wt% and 13 wt% solutions. Figure 5.6 shows the viscosities of iPMMA/nitromethane solutions. The shear thinning is observed for the solutions at concentrations higher than 6 wt%. The viscosities and fiber diameter of these three polymer systems are listed in Table 5.3. At the same concentration, iPMMA/nitromethane has a higher viscosity than HMW aPMMA/nitromethane.

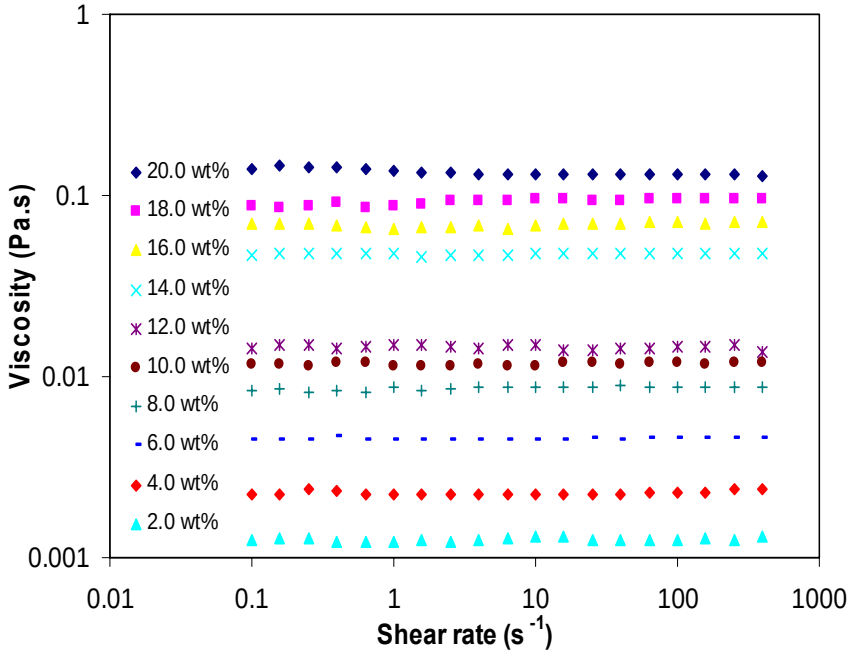

Figure 5.4. Viscosities of low molecular weight aPMMA/nitromethane solutions as a function of shear rate at various solution concentrations.

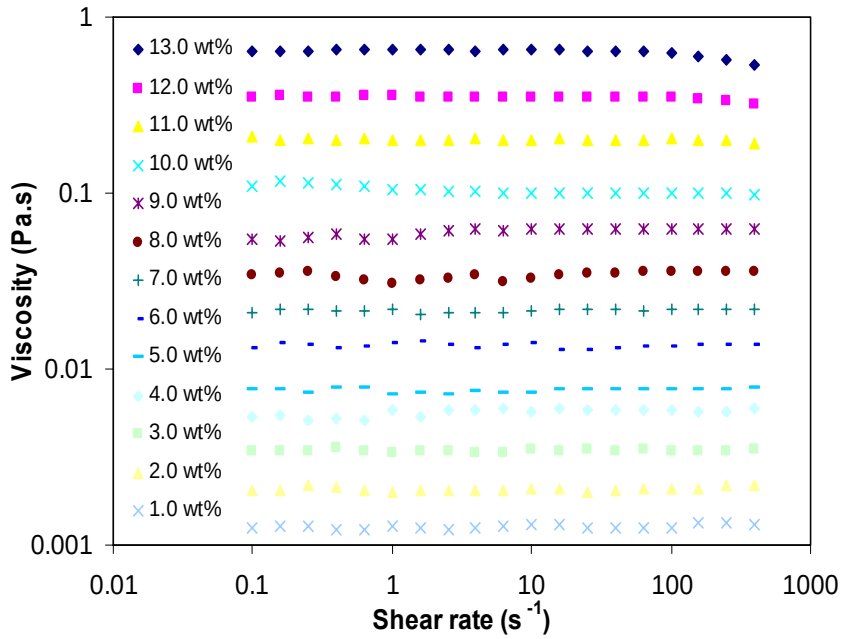

Figure 5.5. Viscosities of high molecular weight aPMMA/nitromethane solutions as a function of shear rate at various solution concentrations.

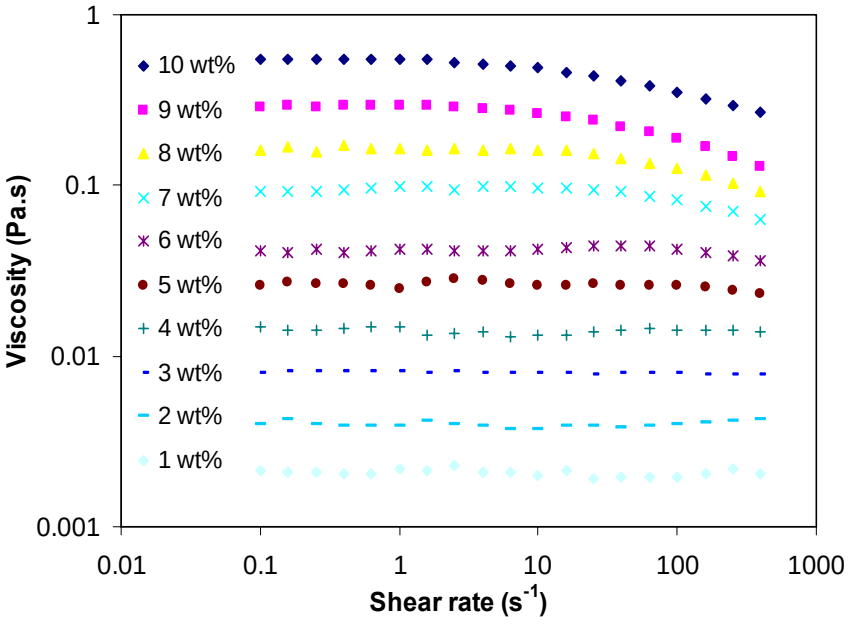

Figure 5.6. Viscosities of iPMMA/nitromethane solutions as a function of shear rate at various solution concentrations.

Table 5.3. Viscosity values of PMMA/nitromethane solutions and the electrospun fiber diameters.

Concentration (wt%)	Viscosity (Pa.s)			Fiber diameter (nm)		
	LMW aPMMA	HMW aPMMA	iPMMA	LMW aPMMA	HMW aPMMA	iPMMA
1		0.0014	0.0021			
2	0.0012	0.0021	0.004			
3		0.0035	0.008			90
4	0.0023	0.0058	0.0143		50	200
5		0.0087	0.0261		80	600
6	0.0045	0.0135	0.0403		160	1130
7		0.0217	0.0884		280	1200
8	0.0085	0.032	0.1634		550	1300
9		0.0624	0.2927		670	1390
10	0.0119	0.0995	0.5921		800	1500
12		0.2004			840	
13		0.349			890	
14	0.015			230		
16	0.0483			400		
18	0.0705			560		
20	0.1331			900		

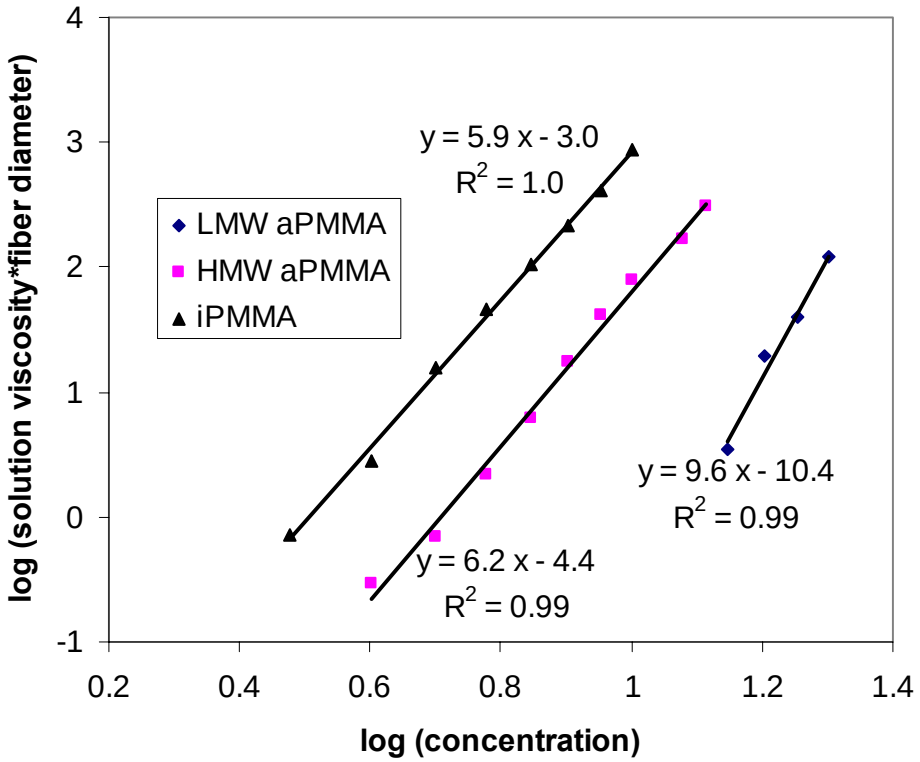

Figure 5.7. log (solution viscosity*fiber diameter) vs log (concentration) for PMMA electrospun from nitromethane.

Viscosity of PMMA/nitromethane multiplied by the electrospun fiber diameter (η*d) as a function of solution concentrations (C) are plotted in Figure 5.7. A linear relationship between log (η*d) and log (c) is shown for all the three PMMA cases. For HMW aPMMA and iPMMA, the exponent is around 6, while for LMW aPMMA has the exponent around 9.6. The similar relationship is also observed in polyacrylonitrile electrospun from DMF solutions[230]. Despite different operating voltage (Figure 5.8 (a)) and flow rates (Figure 5.8 (b)), the linear relationship between log (η*d) and log (c) has the exponent around 6[230]. The separate figures for various applied voltage and flow rates are shown in Appendices B. 15 and B. 16, respectively.

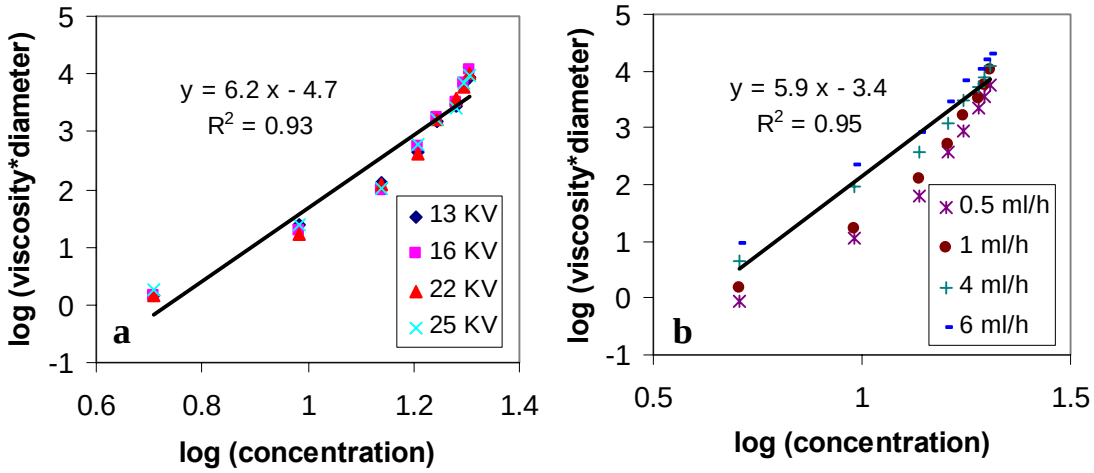

Figure 5.8. The relationship between log (solution viscosity*fiber diameter) and log (concentration) for polyacrylonitrile electrospun from DMF: (a) different applied voltages and (b) various flow rates[230].

The intrinsic viscosity [η] is given by $[\eta] = KM^a$ ("K" and "a" are constants, M is the polymer molecular weight)[223]. For aPMMA in acetonitrile, under θ condition (that is "a" = 0.5) K= 48, while for isotactic PMMA, K=75.5[223]. If both iPMMA and aPMMA have comparable molecular weight, [η] of iPMMA is larger than that of aPMMA. The persistence length of iPMMA (about 6 backbone bonds)[241, 242] is smaller than that for aPMMA (about 16-20 backbone bonds)[241, 242]. The glass transition temperature measured by DSC of iPMMA is around 50 °C and 120 °C for HMW aPMMA (provided by the manufacturers). The observed higher solution viscosity of iPMMA than that for aPMMA of same molecular weight is consistent with other molecular differences reported between these two polymers.

Specific viscosity is defined as: $\eta_{sp} = \frac{\eta - \eta_s}{\eta_s}$, where η_s is the solvent viscosity, η is the solution viscosity. The solution viscosity is obtained within the linear region at

relatively low shear rate regions. Specific viscosities of aPMMA/nitromethane and iPMMA/nitromethane solutions over a wide concentration range are calculated using the above equation.

According to de Genne's scaling concept, the polymer in a good solvent can be classified into four regimes: diluted (η_{sp}~$C^{1.0}$), semidilute unentangled (η_{sp}~$C^{1.25}$), semidilute entangled (η_{sp}~$C^{4.8}$), and concentrated (η_{sp}~$C^{3.7}$) regimes[243]. The scaling values show differences between theoretical and experimental results[244]. Gupta et al. [240] determined the scaling relationship for PMMA in DMF solution as semidilute unentangled region (η_{sp}~$C^{0.65}$), semidilute entangled region (η_{sp}~$C^{5.3}$). However, in the current work for PMMA in nitromthane, the scaling relationship was determined for HMW aPMMA as semidilute unentangled region (η_{sp}~$C^{1.2}$), semidilute entangled region (η_{sp}~$C^{2.6}$), and concentrated region (η_{sp}~$C^{6.5}$), while for iPMMA the exponent was 1.2, 2.4, and 5.2 for semidilute unentangled, semidilute entangled, and concentrated regions, repectively.

Figure 5.9 (a) shows specific viscosity and Figure 5.9 (b) shows the fiber diameter (cups and bead diameters are not considered) as a function of LMW aPMMA/nitromethane solution concentration. Figure 5.10 (a) shows specific viscosity and Figure 5.10 (b) shows the fiber diameter as a function of HMW aPMMA/nitromethane solution concentration. Figure 5.11 (a) shows specific viscosity and Figure 5.11 (b) shows the fiber diameter or as a function of iPMMA/nitromethane solution concentration. Two regimes are observed in the relationship between viscosity and solution concentration of LMW aPMMA/nitromethane solution. Three distinctive regimes are observed in the relationship between viscosity and solution concentration of

HMW aPMMA and iPMMA. Changes in the slope mark the onset of the semidilute entangled and concentrated regimes. For LMW aPMMA/nitromethane solution, the entanglement concentration (*C*e) is determined to be 13 wt%. For HMW aPMMA/nitromethane solution, the entanglement concentration (*C*e) and the concentrated concentration (*C**) are determined to be 3.5 wt% and 8.5 wt%, respectively. For iPMMA/nitromethane solution, the entanglement concentration (*C*e) and the concentrated concentration (*C**) are determined to be 2.5 wt% and 6 wt%, respectively. For both HMW aPMMA and iPMMA, with increasing concentration, the morphology changes from cups connected by fine fibers to beaded fibers occurs at Ce and morphology changes from beaded fibers to bead free fibers occurs at C*.

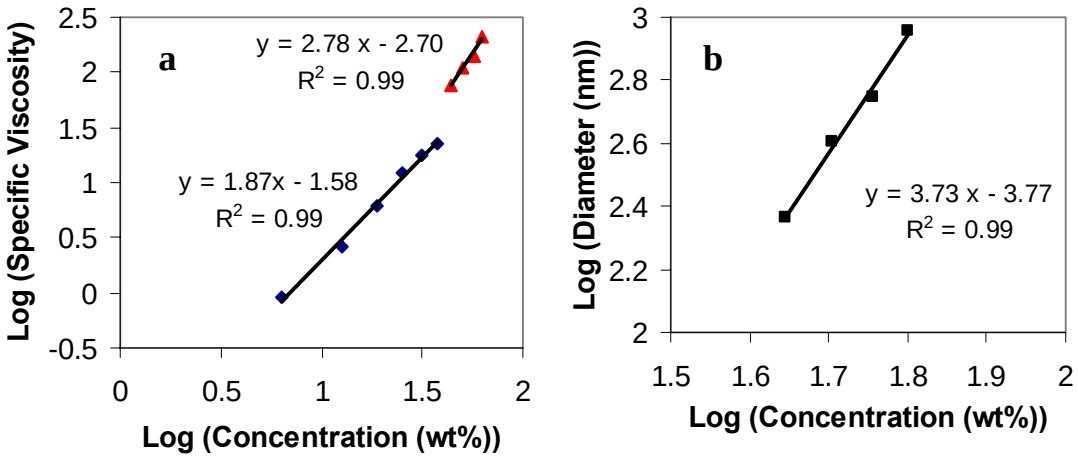

Figure 5.9. (a) Relationship between specific viscosity and concentration of low molecular weight aPMMA/nitromethane solution; (b) Relationship between average fiber diameter and low molecular weight aPMMA/nitromethane solution concentration.

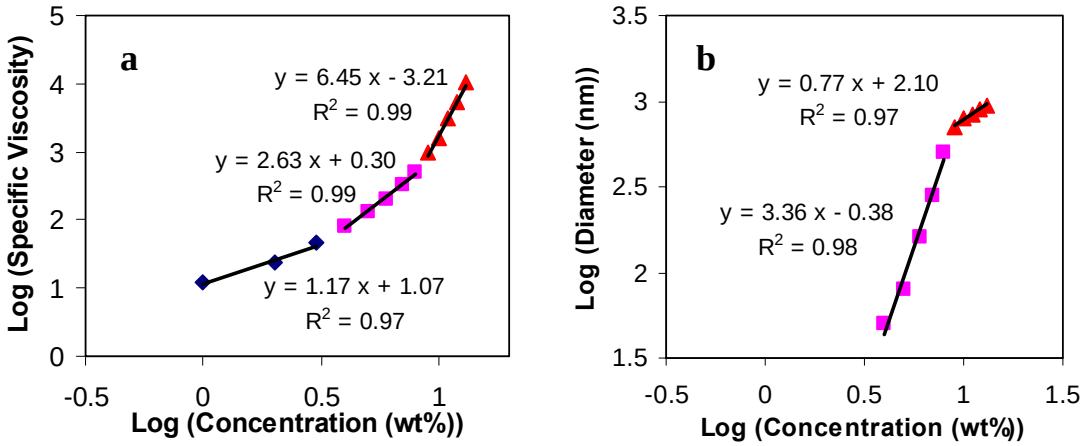

Figure 5.10. (a) Relationship between specific viscosity and concentration of high molecular weight aPMMA/nitromethane solution; (b) Relationship between average fiber diameter and high molecular weight aPMMA/nitromethane solution concentration.

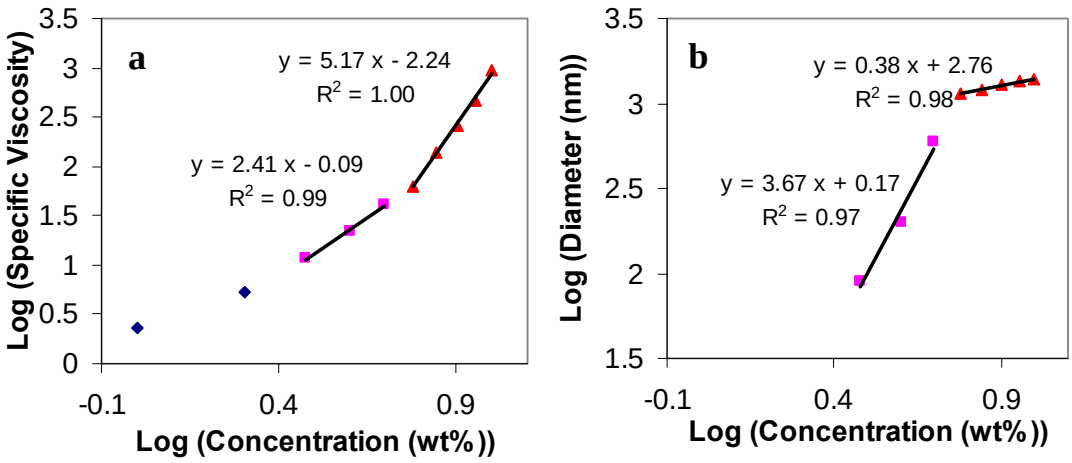

Figure 5.11. (a): Relationship between specific viscosity and concentration of iPMMA/nitromethane solution; (b): Relationship between average fiber diameter and iPMMA/nitromethane solution concentration.

For LMW aPMMA, the fiber diameter has the relationship with solution concentration as $d_t \propto C^{3.7}$ in semidilute entangled region. For both iPMMA and HMW aPMMA, in semidilute entangled region, the relationship is $d_t \propto C^{3.4\sim3.7}$. In concentrated regions, the fiber diameter has the relationship with solution concentration as $d_t \propto C^{0.4\sim0.8}$. The fiber diameter has a stronger dependence on concentration in semidilute entangled region as compared to concentrated regime. The power law relationship between the fiber diameter and the concentration has been reported for a wide range of polymers and are summarized in Table 5.4..

Table 5.4. The power law relationship between fiber diameter and solution concentration.

	Concentration (wt %)	Exponent a ($d_t \sim C^a$)
PET-co-PEI[244]	2~20	2.6
PMMA/(different solvents including cosolvent)[244]	6~10	2.7
PMMA-co-PMAA[244]	------	2.7
PMMA-co-SCMHB/DMF[244]	9~12	3.2, 4.5, 4.9
PAN (100,000 g/mol)/DMF[230]	17.5~22.1	7.5
PAN (250,000 g/mol)/DMF[230]	6.0~9.6	3.5
PAN (700,000 g/mol)/DMF[230]	2.3~3.6	2.5
PMMA/DMF[240]	------	3.1
Polyurethaneurea/DMF[245]	4~13	3.0
Fibrinogen/1,1,1,3,3,3-hexafluoro-2-propanol [246]	8~16	3.2
Polyamide-6/formic acid[164]	34~45	3.5
	22~30	3.1
	34~42	3.8
Polyethyleoxide[247]	4~10	0.5
PAN (100,000 g/mol)/DMF[230]	5.1~16.1	1.2
PAN (250,000 g/mol)/DMF[230]	3.1~5.1	0.88
PAN (700,000 g/mol)/DMF[230]	1.5~2.1	0.99
Polystyrene/DMF[248]	12~20	1.0
Poly(vinyl pyrrolidone)(ethanol/DMF)[249]	2~8	1.3

The fiber diameter shows two major dependences on concentration, which are $d_t \propto C^{1.0}$ (semidilute unentangled region and concentrated region) and $d_t \propto C^{3.0}$ (semidilute entangled region).

During electrospinning, jet thins dramatically. Sergey V. Fridrikh et al[170] predicted the terminal jet diameter (h_t) as a function of surface tension (γ), dielectric permittivity (ε), flow rate (Q), and current (I), and is given by $h_t = (\gamma \bar{\varepsilon} \frac{Q^2}{I^2} \frac{2}{\pi(2\ln\chi - 3)})^{1/3}$. The parameter χ~R/h (h is the jet diameter and R is the radius of curvature of Taylor cone) is the dimensionless wavelength of the instability responsible for the normal displacements. Then only parameter in h_t definition equation related to solution concentration is Q. According to the mass conservation rule: $m = \pi \times (d_t / 2)^{0.5} l \times \rho = \pi \times (h_t / 2)^{0.5} \times c \times l \times \rho$ (m: mass, l: fiber length, ρ: density, and c: solution concentration), the relationship between the concentration and the fiber diameter is: $d_t = h_t C^{0.5}$. Substituting h_t into the $d_t = h_t C^{0.5}$ to get $d_t \propto C^{1.17}$, which is almost consistent with experimental result of semidilute unentangled region and concentrated region. In semidilute entangled region; there might be some extra elongation, which is defined as $k \propto (\frac{C^*}{C})^n$, then: $d_t \propto C^{\frac{7+3n}{6}}$, combining with $d_t \propto C^{3.0}$, "n" is estimated to be around 5. There exists some influence on "n" value from hydrogen bond between the polymer and the solvent[244], electric field, flow rate, temperature, etc., which accounts for the range of the exponent "a" of $d_t \sim C^a$.

5.3.2 Effects of solvents on electrospun iPMMA fiber morphology

The effects of solvents on fiber morphology have been examined in several studies. Six solvents (acetic acid, acetonitrile, m-cresol, toluene, tetrahydrofuran, and dimethylformamide) were used to prepare electrospun PS fibers[180]. Different solvents resulted in various PS fiber morphologies. Among the six solvents, DMF was the best solvent that provided PS fibers with highest productivity and optimal morphological characteristics. The influence of solvents on the morphology of the poly(vinyl pyrrolidone) (PVP) micro/nanofibers prepared by electrospinning PVP solution in different solvents, including ethanol, dichloromethane, and N,N-dimethylformamide[249]. PVP fibers prepared from MC and DMF solvents at 4 wt% concentration had a shape like a bead-on-a-string. In contrast, smooth PVP nanofibers were obtained with ethanol as a solvent although the size distribution of the fibers was somewhat broadened. Poly-L-lactide produced by electrospinning from a dichloromethane solution exhibiting regular pores or pits in the 100 nm range, which indicates electrospinning can directly yield porous fibers provided that the solvents with fast evaporation speed are used[250]. PS porous fibers were electrospun from solution in THF[251].

Ordered structure fiber mat was obtained by electrospinning iPMMA/nitromethane solution at concentrations lower than 6 wt%. In order to investigate the effect of solvents on electrospun fiber morphology, iPMMA was electrospun from four different solvents. To the best of our knowledge, study on solvent effect on iPMMA electrospun fiber morphology is not available in the literature to date. Here, iPMMA was electrospun from nitromethane, acrylonitrile, methylene chloride, and

formic acid. Among these four solvents, methylene chloride has the highest evaporation rate. At iPMMA/MC concentration higher than 4 wt%, it is difficulty to electrospin due to needle clogging. Therefore, all solutions were electrospun at 4 wt% concentration and the electrospinning conditions were kept the same to ascertain the effect of solvents on fiber morphology.

Figure 5.12. shows the morphology of electrospun iPMMA fibers from four different solvents. At the same electrospinning conditions and at 4 wt% concentration, the use of volatile solvent such as methylene chloride (MC) yields iPMMA porous fibers. Solvents with lower evaporation rate such as nitromethane, acrylonitrile or formic acid reduces the tendency towards pore formation significantly. Electrospinning iPMMA in nitromethane or acrylonitrile produced ordered structured fiber mat (Figure 5.13 and Figure 5.14). It is hypothesized that the fibers carry some charges when they reach the target. The repulsive forces due to static charges arrange the fibers into ordered structure. The possible mechanism of ordered structure formation is shown in the schematic diagrams (Figure 5.15). Due to the repulsive force, the charges redistributes to the end of the fibers. Fibers with cross configuration redistribute the charges to reduce the repulsive force, which is a more stable arrangement than the parallel one. The ordered structure disappears at certain concentration due to the inability of repulsive force to arrange relatively larger diameter fibers into ordered structure.

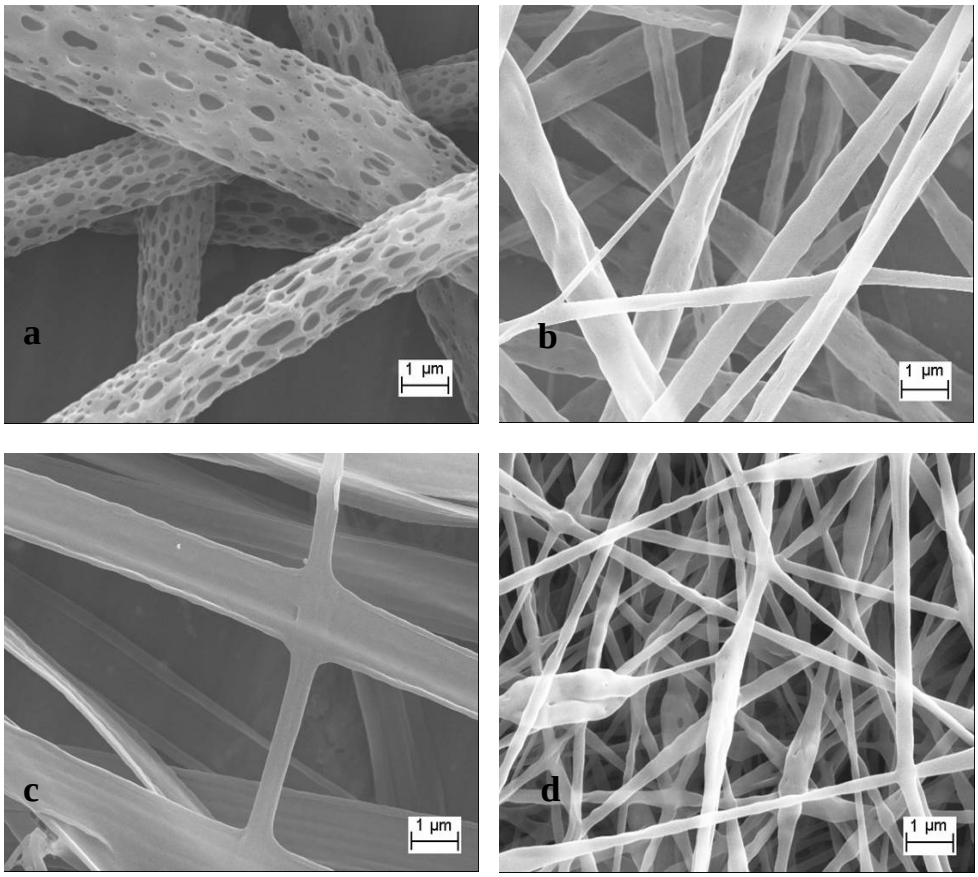

Figure 5.12. iPMMA fiber mat electrospun from four different solvents at 4 wt% concentration and at the same electrospinning conditions: (a) methylene chloride, (b) acrylonitrile, (c) formic acid, and (d) nitromethane.

iPMMA/formic acid solution produces ribbon shaped fibers. Ribbon shaped electrospun fibers have been reported by other researchers[161, 252-255]. Koombhongse et al. reported ribbon shaped electrospun fibers from 30 wt% PS in dimethylformamide, 10 wt% poly(ether imide) in hexafluoro-2-propanol, and 20 wt% poly(2-hydroxyethyl methacrylate) in ethanol[256]. Ribbon-like nanofibers of barium titanate[257] were prepared by electrospinning a solution containing barium-titanium alkoxide precursor and

poly(vinyl pyrrolidone) followed by calcination in air. The reason for ribbon shaped fibers formation is still not understood.

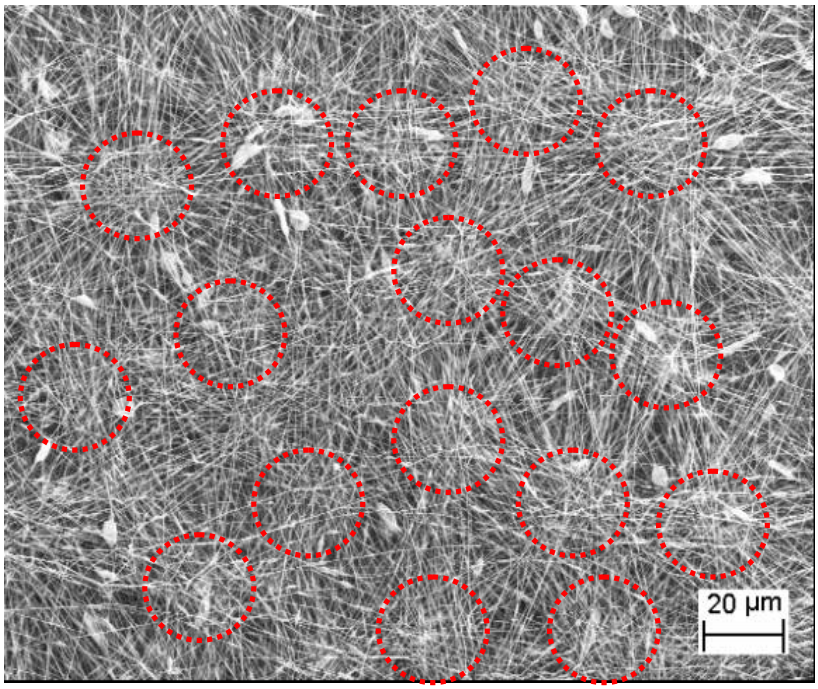

Figure 5.13. Ordered structured iPMMA fiber mats electrospinning from nitromethane solutions at 4 wt% concentration.

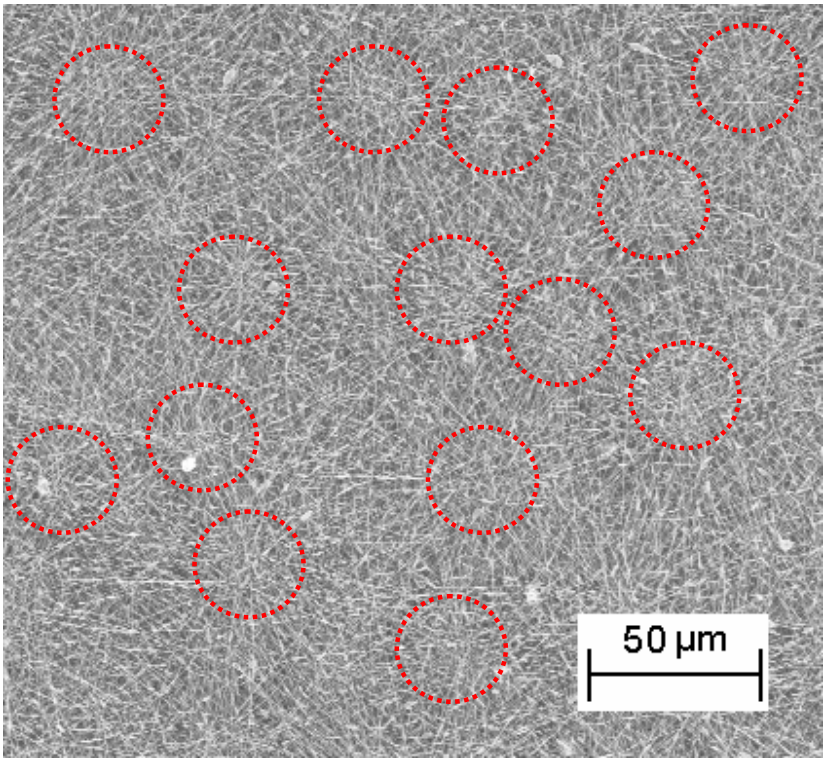

Figure 5.14. Ordered structured iPMMA fiber mats electrospinning from acrylonitrile solutions at 4 wt% concentration.

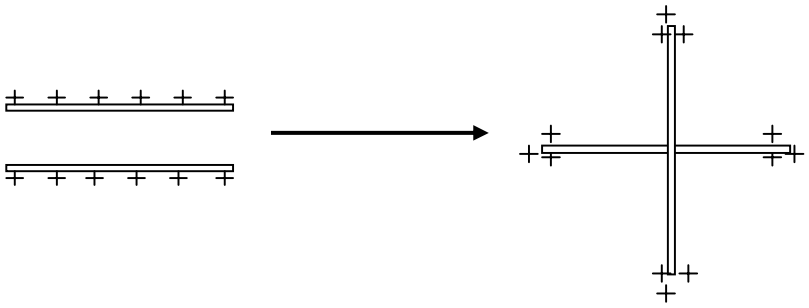

Figure 5.15. Schematic diagram of ordered structured fiber mat formation.

5.3.3 Porous fibers

Electrospinning iPMMA/methylene chloride solution results in porous fibers (Figure 5.12. (a) and Figure 5.16) directly. iPMMA porous fibers (electrospun from 2 wt% iPMMA/methylene chloride) has BET (Brunauer, Emmett and Teller) surface area of 18 m^2/g. The adsorbed N_2 quantity as a function of relative pressure of isothermal N_2 adsorption (77 K) of the 2 wt% iPMMA porous fibers is shown in Figure 5.17 (a). Surface area measurement shows the pore diameter with two major sizes with relatively broad distributions; one is within the range of 15 nm ~ 35 nm and the other one is ranging from 86 nm to 370 nm (Figure 5.17 (b)). From SEM image of the fiber fracture surface, the pores present are through the whole fiber (Figure 5.16 (d)). This porous fiber mat has a water contact angle of 151 ± 2º (Figure 5.18 (a)), belonging to superhydrophobic materials, while the water contact angle of iPMMA film is only around 74 ± 1º (Figure 5.18 (b)). The porous morphology and the roughness of fiber mat accounts for the high water contact angle[206].

HMW aPMMA/MC solution is also electrospun into porous fibers from its methylene chloride solution. At 8 wt% concentration, porous beaded fibers are produced (Figure 5.19 (a)), while 12 wt% solution results in bead free porous fibers (Figure 5.19 (b)). SEM image of the fiber cross section shows pores only on the fiber surface (Figure 5.19 (d)). Although these two kinds of PMMA have comparable molecular weight and polydispersity index (PDI) (Table 5.1), and the same electrospinning conditions, the pore morphology in the two cases appears different. iPMMA/MC has higher viscosity than aPMMA/MC solution at the same solution concentration. This results in iPMMA/MC produce fibers even at 2 wt% concentration, while aPMMA/MC results in fibers at 12

wt% concentration. For 12 wt% aPMMA/MC solution due to higher polymer concentration MC is expected to have comparatively slower evaporation rate than in 2 wt% iPMMA/MC . The difference in pore morphologies in the two cases is attributed to this difference in evaporation rate.

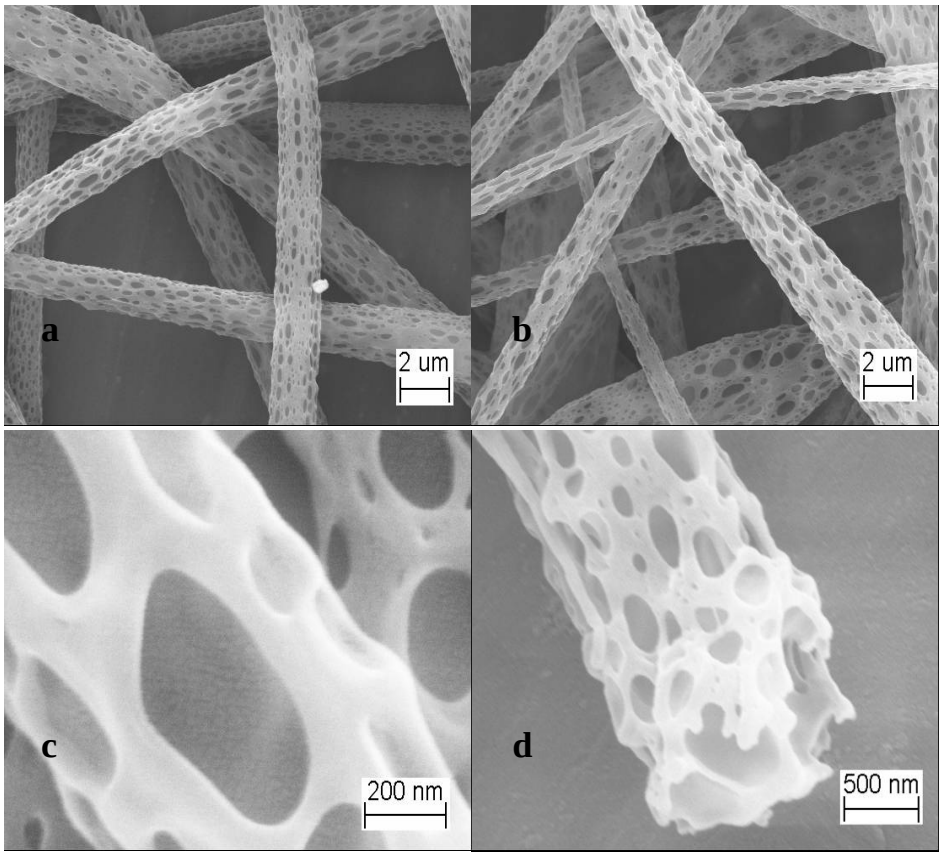

Figure 5.16. iPMMA porous fibers from electrospinning in methylene chloride solutions at different concentrations: (a) 4 wt%; (b), (c), and (d) 2wt%.

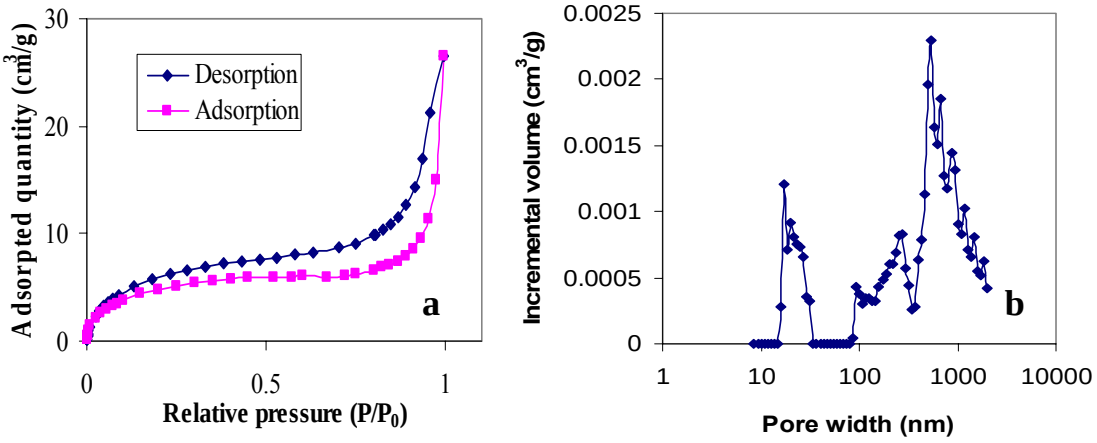

Figure 5.17. (a) Adsorbed N_2 quantity as a function of relative pressure of isothermal N_2 adsorption (77 K) and (b) Pore size distribution of iPMMA porous fibers electrospun from methylene chloride solution at 2 wt% concentration.

Figure 5.18. Water contact angles of (a) iPMMA film and (b) iPMMA porous fiber mat electrospun from methylene chloride solution at 2 wt% concentration.

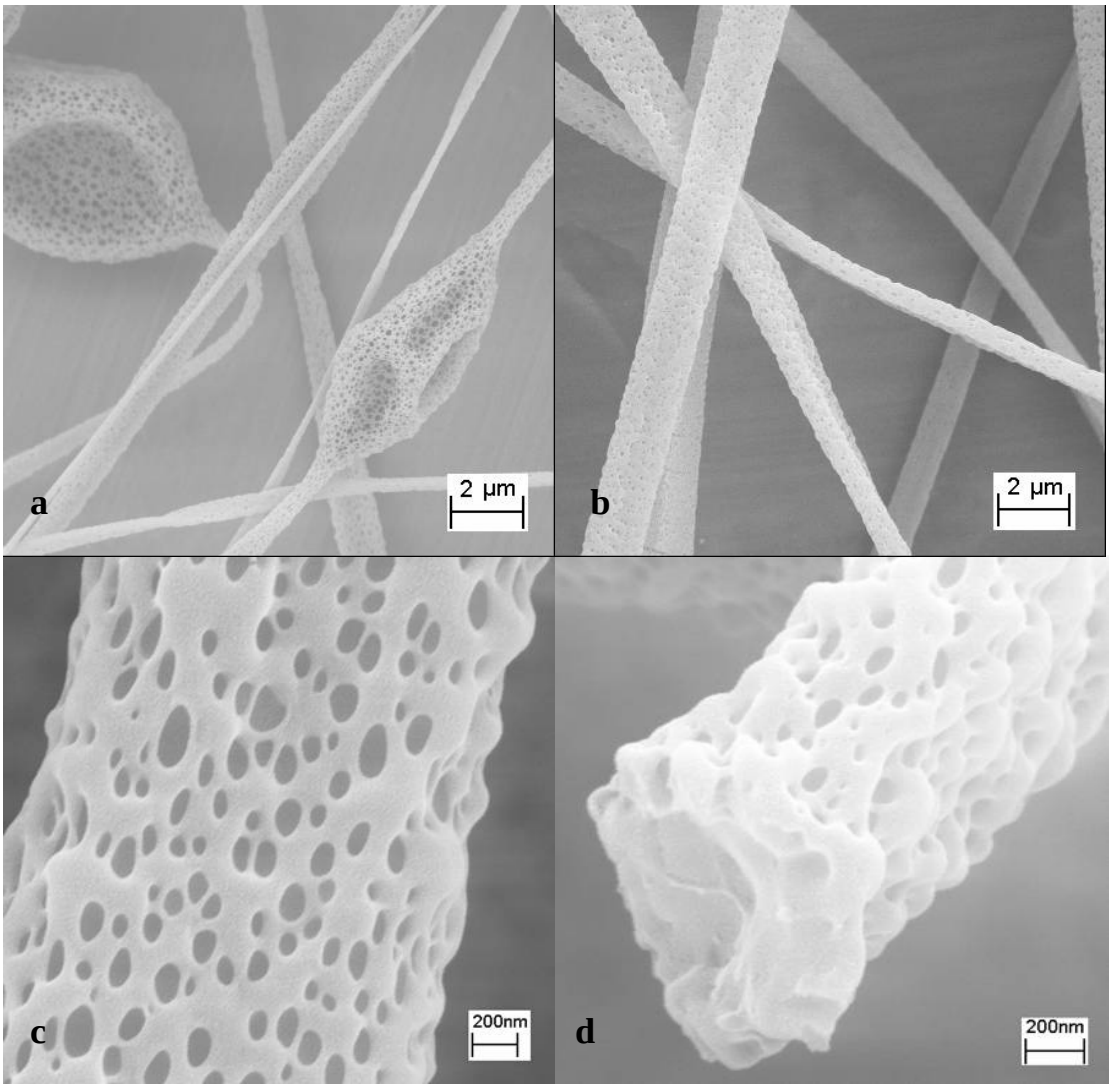

Figure 5.19. High molecular weight aPMMA porous fibers electrospun from methylene chloride solutions at (a) 8 wt%; (b), (c), and (d)12 wt% concentrations.

Both iPMMA/MC and HMW aPMMA/MC result in porous fibers. Rabolt et al.[251] have electrospun PS porous fibers from THF in the concentration range from 18 to 35 wt%. The fiber diameter was 5 to about 15 µm with pore size from 50 nm to about 150 nm. In order to further explore porous fiber formation condition, PS/THF solution was electrospun over a wide concentration range (3 wt%, 12 wt%, and 29 wt%) in this

study. With increasing concentration, the electrospun material morphology changes from particles to beaded fibers, and then to bead free fibers (Figure 5.20). The water contact angles shown in Figure 5.21 are (b) 153 ± 2°, (c) 150 ± 2°, and (d) 151 ± 2° for PS electrospun at 3, 12, and 29 wt% concentrations, respectively. The control PS film has a water contact angle of 100 ± 2° (Figure 5.21 (a)). The relatively large water contact angle of electrospun PS mats might be caused by the roughness of the surface and the pores which could trap more air in the interspace than film.

PS/THF solution was electrospun into porous beadless fibers at 29 wt% concentration (Figure 5.22). Adsorbed N_2 quantity as a function of relative pressure of isothermal N_2 adsorption (77 K) is shown in Figure 5.23 (a). The pores have a smaller diameter (22 ± 5 nm) and a narrower size distribution as shown in Figure 5.23 (b) compared to both aPMMA and iPMMA porous fibers. Due to highly porous structure, PS porous fiber mat has a large water contact angle around 151°, which has superhydrophobic property. PS porous fiber has a dog bone shaped cross section, the observation is consistent with Rabolt's work[251]. PS porous fibers have relatively more uniform sized pores compared to Rabolt's PS porous fibers. The theoretical surface area of the solid fiber mat decreases linearly with increasing fiber diameter. Although PS fibers are highly porous, due to the large diameter (5 to 10 μm) its surface area is only about 3 m^2/g. For iPMMA and HMW aPMMA porous fibers, the pores are ellipsoidal shapes oriented along the fiber axis generated by rapid phase separation due to the fast evaporation of MC during electrospinning. PS fibers, pores are round in shape.

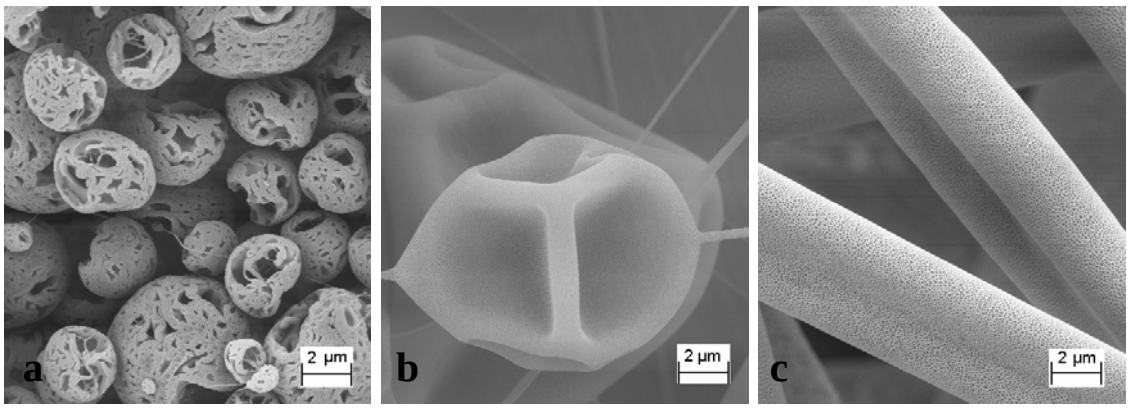

Figure 5.20. Polystyrene electrospun from tetrahydrofuran solutions at different concentrations: (a) 3 wt%, (b) 12 wt%, and (c) 29 wt%.

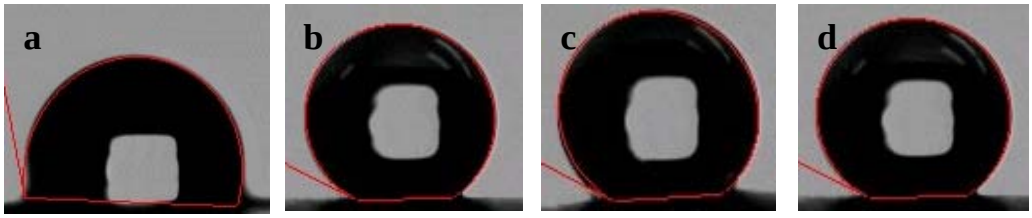

Figure 5.21. Water contact angles of (a) polystyrene film (100 ± 2°) and electrospun polystyrene from tetrahydrofuran solutions at different concentrations: (b) 3 wt % (153 ± 2°), (c) 12 wt% (150 ± 2°), and (d) 29 wt% (151 ± 2°).

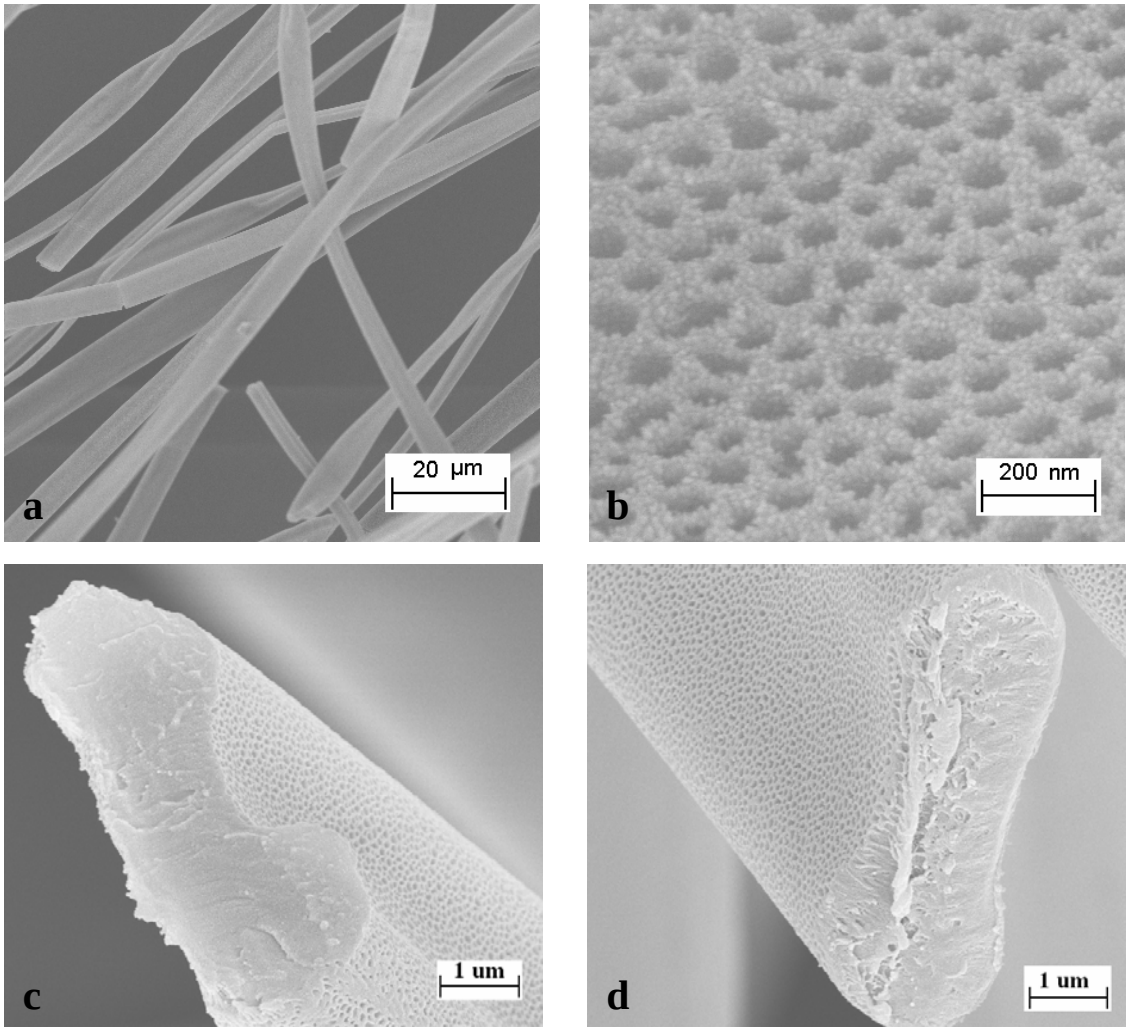

Figure 5.22. Polystyrene porous fibers electrospun from tetrahydrofuran solution at 29 wt% concentration: (a) and (b) are low and high magnification fiber surfaces, respectively. (c) and (d) are cross-sections of two different fibers showing that pores are only on the surface.

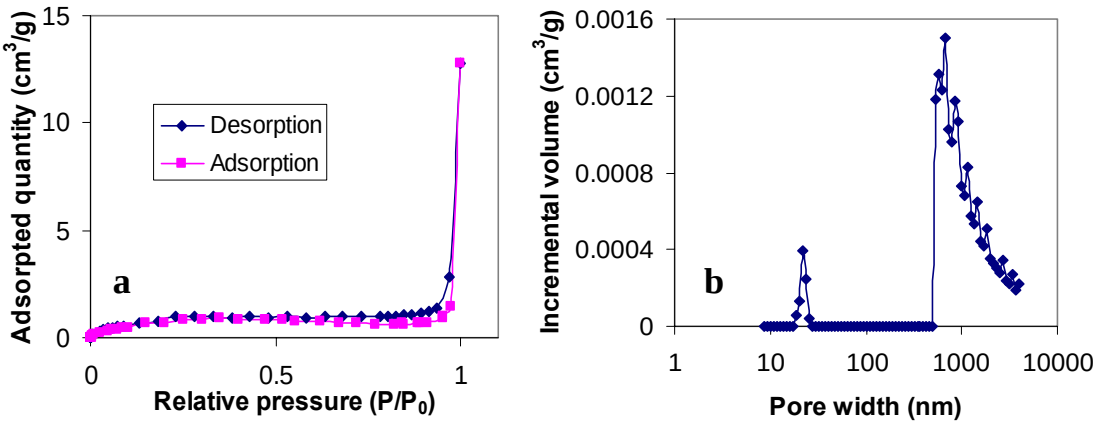

Figure 5.23. PS porous fibers electrospun from THF solution at 29 wt% concentration: (a) Adsorbed N_2 quantity as a function of relative pressure at 77 K, and (b) Pore size distribution.

Formation of a three-dimensionally ordered array of holes has been reported in a thin PS film[258]. The three dimensional pore structures were not observed when the films were formed in the absence of humidity. Another condition for the pore formation was using water immiscible solvent. The breath figure itself can not explain the electrospun PS fiber pore formation because THF is a water miscible solvent. The formation of pores by the electrospinning process is a much more complex process with many variables to be considered. Rabolt et al.[259] discussed about the humidity effect on polystyrene porous fibers. They found that humidity larger than 25% was the necessary condition to produce polystyrene porous fibers from THF solution, while in their another paper, polystyrene porous fibers were produced in air[251]. The authors hypothesized that both breath figure and phase separation were the porous fibers formation mechanisms. Phase separation techniques have been used to produce submicron structures by van de Witte et al[260]. Thermodynamic instability is the driving

force behind phase separation. Decreasing temperature, loss of solvent, or increase in nonsolvent causes a solution to become thermodynamically unstable during the electrospinning process, thus making phase separation a most likely mechanism of pore formation.

5.4. Conclusions

Both high molecular weight aPMMA/nitromethane and iPMMA/nitromethane solutions were utilized to explore the scaling relationship between viscosity and concentration and to investigate the effect of this relationship on the fiber formation during electrospinning. As polymer concentration increases, cups connected by fine fibers are observed in the semidilute unentangled regime, beaded fibers are observed in the semidilute entangled regime, and bead free fibers are observed in the concentrated regime. Dependence of the fiber diameter on concentration was also determined. Combining with the literature data, within the semidilute unentangled and concentrated regimes, fiber diameter shows dependence on solution concentration as $d_t \sim c^1$, while in the semidilute entangled region, fiber diameter has the relationship with solution concentration as $d_t \sim c^3$.

iPMMA electrospun fibers were produced using four solvents to investigate the influence of the solvent on fiber morphology. At 4 wt% concentration and at the same electrospinning conditions, various fiber morphologies including ribbon-shaped fibers from formic acid, order-structured fiber mat from acrylonitrile or nitromethane, and porous fibers from methylene chloride are obtained. Formation of different morphologies has been attributed to the solvent properties. In order to further explore porous fiber formation conditions, high molecular weight atactic PMMA was electrospun from MC

and polystyrene was electrospun from tetrahydrofuran. Although these three kinds of porous fibers have different pore morphologies, their formation is correlated with high volatility of the solvents used in the electrospinning process. Phase separation might be the most possible mechanism of porous fiber formation.

CHAPTER 6

CARBON NANOTUBE CORE – POLYMER SHELL ELECTROSPUN NANO FIBERS

6.1. Introduction

Incorporation of only a few percent of SWNT into many polymers leads to significant improvement in mechanical[40, 203] and electrical[29] properties. To fully explore their reinforcing potentiality, uniform SWNT dispersion, exfoliation and orientation[261] are important. SWNT have shown great potential as high-resolution AFM imaging probes[262] due to their small diameter, high mechanically properties, potential for chemical functionalization, high electrical conductivity, and thermal conductivity. High lateral resolution (better than 1 nm), and consistently and significantly better AFM image quality with nanotube tips than with the best silicon AFM tips have been reported[263]. There are several methods for attaching nanotubes to silicon AFM tips including manual assembly[264], direct growth[262], and pickup[262]. Recently, plasma-assisted deposition and polymerization of fluorocarbon polymer on the nanotubes for AFM tip application has been reported[265, 266]. Electrospinning is an active method to incorporate of CNTs into electrospun nanofibers resulting in improved mechanical properties and electrical conductivity[267]. Here, electrospun core (SWNT bundle) – shell (polymer) nanocomposite fibers were produced. These core – shell fibers have applications as AFM tips and in other nano devices. The interaction between PMMA and SWNT in the electrospun fibers has been studied using Raman spectroscopy.

6.2. Experimental

Purified HiPCO^{TM} SWNTs (containing 10 wt % catalyst based on the TGA analysis) were obtained from CNI, PMMA ($\overline{M_w} = 95{,}000 \sim 150{,}000$ g/mole) from Cyro industries, PAN ($\overline{M_w} = 100{,}000$ g/mole) from Exlan Corp., Japan. Both nitromethane and DMF were bought from Aldrich. All materials were used as received. 10 mg SWNTs were dispersed in 200 ml solvent (nitromethane for PMMA and DMF for PAN) by sonication (Branson water bath sonicator by Smithkline Company, model B-22-4, power 125 W, frequency 43 KHz) for 48 hours at room temperature. PMMA or PAN was added to this dispersion, followed by stirring for ten hours at 700 rpm. The polymer/SWNT/solvent dispersion was poured on a glass plate, and the solvent was allowed to evaporate in the hood over several days and the film was peeled off from the plate. This film was designated as "film A". A syringe pump (Fisher scientific), at a flow rate of 1 ml/h was used for electrospinning at 22,000 V, while the collection target (a grounded steel sheet) was placed at a distance of 10 cm from the syringe needle. The electrospun fiber mat was simply designated as "fiber mat". This fiber mat was heated in DSC from 25 °C to 150 °C at 10 °C/minute and then cooled at the same rate to room temperature, in order to relax any thermal strains in the sample. The DSC treated sample was designated as "film B". SEM (LEO 1530 thermally - assisted FEG) was done on gold coated samples. JEOL 4000EX (400 KV) was used for high resolution TEM. Raman spectroscopy was done on Holoprobe Raman microscope from Kaiser Optical Systems Inc. using 785 nm (E_{laser}=1.58 eV) excitation wavelength.

6.3. Results and discussion

SWNT/PAN and SWNT/PMMA composite fibers containing SWNT bundles as the core were processed by electrospinning (Figure 6.1). SWNT bundles (20 to 30 nm in

diameter) are aligned along the fiber axis as can be seen from the high resolution TEM (Figure 6.1 a). SEM of SWNT/PMMA fibers show SWNT bundle protruding at the end of the composite fiber. Some buckling[264] can be observed in the protruded SWNT bundles, and buckling is minimized if the SWNT tail is short (Figure 6.1 b). Fibers with sheath-core structure can be used as electrically conductive nanowires as well as nanoelectrodes in electrochemical devices where the nanotube core is used for conduction and the shell polymer as an insulator. Another important application is AFM probe tip, where the individual SWNT or small SWNT bundles can be used for achieving high resolution, while the larger diameter shell provides rigidity and ease of handling. The core diameter is the diameter of the individual nanotube or that of the nanotube bundle, depending on the extent of exfoliation. The highly exfoliated systems, such as PVA/PVP/SDS/SWNT[216] can be electrospun into nano fibers with different size nantoube AFM tips. One can tailor the tip length by etching the polymer using electron beam, as the electron beam resistivity of the carbon nanotubes is about 5 orders of magnitude higher than the flexible chain polymers such as PVA, poly (ethylene oxide), polyethylene, and PMMA. Electrospinning can also be done on the functionalized nanotubes/polymer composites. Use of chemically or biologically functionalized tips, as well tips with electrical and thermal conductivity provides additional capability to AFM. The electrospun fibers can typically be processed in the 100 nm to 2 μm diameter range by controlling solution properties and electrospinning conditions. Electrospinning can be used to process continuous core (nanotube) – shell (polymer) fibers using large number of polymers.

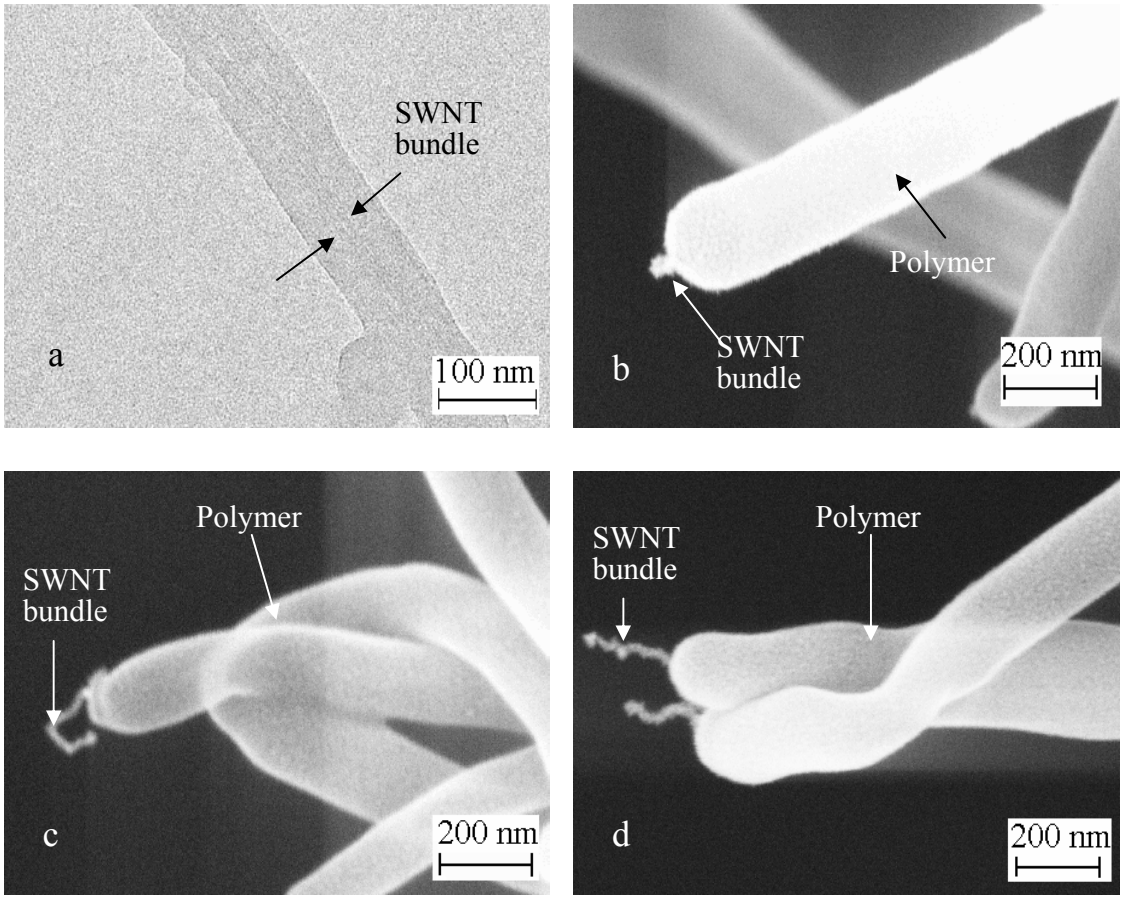

Figure 6.1. High resolution TEM (a) of electrospun PAN/SWNT composite fiber and SEM (b, c, d) of electrospun SWNT/PMMA fibers.

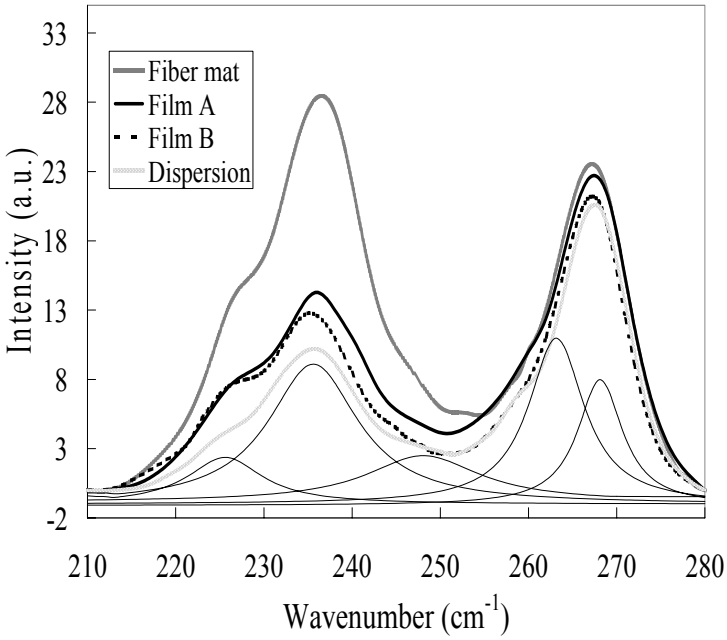

Figure 6.2. Raman radial breathing mode of PMMA/SWNT samples containing 1 wt% SWNT, with respect to the weight of PMMA.

Raman spectroscopy is a powerful and nondestructive method for characterizing SWNT and its interaction with other molecules, as well as the effect of pressure[268] and temperature[120]. According to the resonance theory, the intensity of the Raman bands depends on the difference between the laser excitation energy (E_{laser}) and the van Hove transition energy (E_{ii}). RBM intensity increases when the difference $|E_{ii} - E_{laser}|$ decreases, and vice versa and reach a maximum value when $E_{ii} = E_{laser}$. Raman RBM spectra of SWNT/PMMA composites (Figure 6.2) have been fitted with five Lorentzian components located at 226, 236, 248, 263 and 268 cm^{-1} and the fitted results of film A are also shown in Figure 6.2 as an example. Using d_t (nm) = 223.5/[ω_{RBM} (cm^{-1})-12.5][212] for the SWNT bundle, individual nanotube diameters in the 0.88 nm to 1.05 nm range were obtained. It is noted that only semi-conducting tubes are seen in RBM mode using

785 nm wavelength laser and the metallic tubes will require different excitation energy. The RBM intensities of various samples in Figure 6.2 have been normalized to the G band intensity. Following this normalization, the area of the peak at 265 cm^{-1} (composition of 263 cm^{-1} and 268 cm^{-1} peaks) is almost the same for the four samples for which data is shown in Figure 6.2. Following the treatment of Lucas and Young[215], one can show that under compressive strain, van Hove transition energy E_{22}^{s} increases for the tube corresponding to the 263 cm^{-1} RBM peak, and decreases for the tube corresponding to the 268 cm^{-1} peak[269]. The E_{22}^{s} values for both these tubes (1.8 eV to 1.90 eV) are quite far from the E_{laser}. Thus the other peak areas can also be normalized with respect to the 265 cm^{-1} peak. E_{22}^{s} of 236 cm^{-1} band is reported[213] to be between 1.59 and 1.67 eV. Under compressive strain, it decreases and approaches closer to the E_{laser} (1.58 eV) value. Therefore the intensity of 236 cm^{-1} band will increase under compression. The 236 cm^{-1} band intensities of film A, film B, and the dispersion are quite comparable, while the intensity of the electrospun fiber mat is much higher. This suggests that in the electrospun fiber, nanotube experience higher compressive strains than in the other three samples. Corresponding shifts have also been observed in the positions of G and G' Raman bands (Figure 6.3), as can be seen from the linear relationship between the 236 cm^{-1} band intensity and the G and G' band peak positions. These Raman results are consistent with SWNT/PMMA/different solvent dispersion study[269].

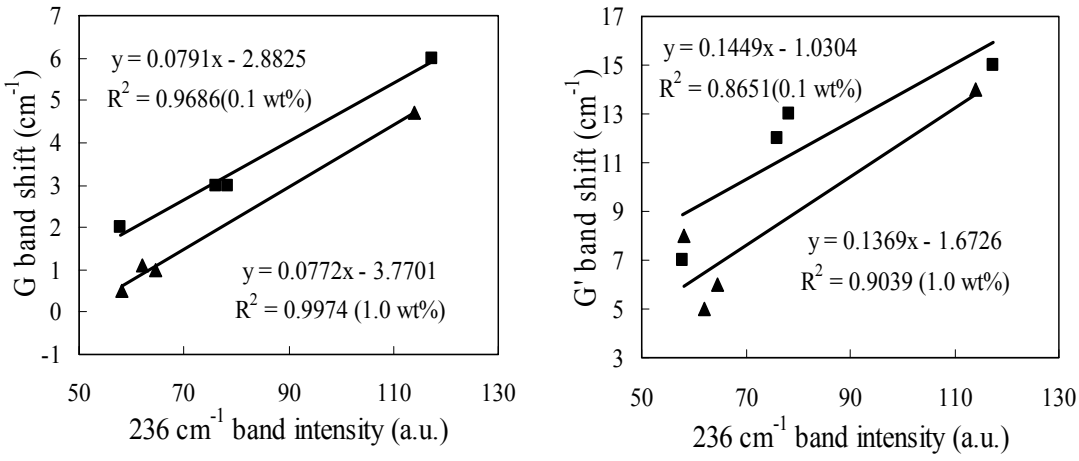

Figure 6.3. Raman G and G' band shift as a function of 236 cm^{-1} band intensity in PMMA/SWNT composites. Squares represent 0.1 wt % SWNT and triangles represent 1.0 wt % SWNT in PMMA. Samples from low to high 236 cm^{-1} band intensity (or from low to high G and G' shift) are dispersion, film B, film A, and the electrospun fiber mat.

6.4. Conclusions

SWNT/PMMA and SWNT/PAN composite fibers with hundreds of nanometer diameter containing SWNT bundle as the core were processed by electrospinning. Nanotubes in the electrospun fibers experience compressive strain, which results in enhanced intensity of the selected Raman RBM peak, as well as upshift in the G and G' band positions.

CHAPTER 7

CONCLUSIONS AND RECOMMENDATIONS

7.1 Conclusions

The key conclusions of this study are:

1. Single wall carbon nanotube (SWNT)/ polymethyl methacrylate (PMMA) dispersion study: SWNT dispersion in PMMA improved with increasing solvent polar solubility parameter (δ_p), and the most uniform dispersion is obtained in nitromethane, which is the most polar solvent employed in this study.
2. Carbon nanotube (CNT)/PMMA composites study: Based on dispersion study, nitromethane is chosen as the solvent to process CNT/PMMA composites. SWNT-A (35.0 wt% catalyst)/PMMA, SWNT-B (2.4 wt% catalyst)/PMMA, multi wall carbon nanotube (MWNT)/PMMA, and vapor grown carbon nanofiber (VGCNF)/PMMA composite films at 15 wt% CNT loadings have been processed. SWNT-B/PMMA composites at various carbon nanotube loadings of 0.5, 1, 5, 10, 15, 20, 35, and 50 wt% respectively, are processed. Conclusions of this composite study are given below:
   - *Morphology:* For all these composite films, CNT dispersed uniformly into PMMA matrix as evidenced by optical and scanning electron microscopy. The adhesion between PMMA and CNT appears to be less strong than between CNT and polyacrylonitrile.
   - *Tensile property, dimensional stability, and solvent resistance:* Among various CNT/PMMA composites at 15 wt% CNT, the SWNT-B/PMMA

composite film exhibit most enhancement in tensile modulus, tensile strength, dimensional stability (~70 % reduction in coefficient of thermal expansion (CTE)) and solvent resistance followed by composite of SWNT-A, MWNT and VGCNF.

- *Dynamic mechanical properties.* Enhancement in storage modulus for all CNT/PMMA composite films is observed. The highest increase in storage modulus is observed for SWNT-B/PMMA composite films. The magnitude of the tan δ peak decreases and shifts to higher temperature among all the CNT/PMMA composite films.
- *Electrical properties*. SWNT-A reinforced PMMA composite has the highest electrical conductivity among these four CNT/PMMA composites. The higher electrical conductivity in SWNT-A composites (1430 S/m) as compared to SWNT-B composites is due to additional conductivity network formed by the metal catalyst.
- *Decomposition temperature.* In nitrogen, PMMA has the same decomposition temperature in composites as for the control film, which indicates that CNT by itself does not affect PMMA decomposition. While in air, PMMA decomposes at lower temperature in the composite compared to control PMMA. This suggests that the presence of CNT assists in PMMA decomposition possibly by capturing more oxygen during TGA experiments in air.
- *Comparison between SWNT-A and SWNT-B composites.* Relatively poor mechanical properties and dimensional stability of SWNT-A composites

compared to SWNT-B/PMMA composites are attributed to the presence of metal impurities.

- *SWNT-B/PMMA composite.* With increasing SWNT-B loading, the dimensional stability (~90 % reduction in CTE at 50 wt% SWNT-B loading) and the solvent resistance is enhanced. Enhancement in storage modulus for all CNT/PMMA composite films is observed. The magnitude of the tan δ peak decreases and shifts to higher temperature among all these SWNT-B/PMMA composite films. The electrical conductivity of SWNT-B/PMMA is increased with increasing SWNT-B loading. The percolation volume is determined to be 0.5 wt%. The tensile modulus and the tensile strength do not increase linearly with increasing nanotube loading; they reach the maximum values at 35 wt% SWNT-B.

3. Novel micro- and nano-sturctured electrospun materials study: a series of polymers are electrospun over a wide concentration range from different solvents. With increasing solution concentration, electrospun material morphology changes from particles to fibers.

- At relatively low solution concentrations, micro- and nano-structured polymer particles such as cups, spheres, polygonal porous particles, polygonal solid particles, are produced. By electrospinning PMMA from seven different solvents and a series of poly (styrene-co-4-vinyl phenol) copolymers from methyl ethyl ketone solutions into particles, a qualitative relationship between solvent properties and particle morphologies is proposed.

- At high solution concentrations, isotactic PMMA electrospun fibers were produced using four solvents to investigate the influence of solvent on fiber morphology. At 4 wt% concentration and at the same electrospinning conditions, various fiber morphologies including ribbon-shaped fibers from formic acid, order-structured fiber mat from acrylonitrile or nitromethane, and porous fibers from methylene chloride are obtained. In order to further explore porous fiber formation conditions, atactic PMMA was electrospun from methylene chloride and polystyrene was electrospun from tetrahydrofuran. Polystyrene fiber pores have a smaller diameter (22 ± 5 nm) and a narrower size distribution. Isotactic PMMA have pores through the whole fiber. Although these three kinds of porous fibers have different pore morphologies, the pore formation is correlated with high volatility solvents. Phase separation might be the most possible mechanism of porous fiber formation.
- Both aPMMA/nitromethane and iPMMA/nitromethane solutions were utilized to explore the scaling relationship between viscosity and concentration and to investigate the impact of the relationship on the fiber formation during electrospinning. As concentration increases, cups connected by fine fibers are observed in the semidilute unentangled regime, beaded fibers are observed in the semidilute entangled regime, and the bead free fibers are observed in the concentrated regime. Dependence of the fiber diameter on concentration was also determined. Combining results of this study with the literature data, within semidilute unentangled and concentrated regimes, fiber diameter shows dependence on solution concentration as $d_t \sim c^1$, while in the semidilute

entangled region, fiber diameter has the relationship with solution concentration as $d_t \sim c^3$.

- SWNT/PMMA composite fibers with hundreds of nanometer diameter containing SWNT bundle as the core were processed by electrospinning. Nanotubes in the electrospun fibers experience compressive strain, which results in enhanced intensity of the selected Raman radial breathing mode peak, as well as upshift in the G and G' band positions.

7.2 Recommendations

Although many fruitful conclusions have been obtained in the present study, some aspects of this study need further investigation. Some suggestions for future studies are listed below.

1. Raman measurements on SWNT-B powder and composites reveal decrease in FWHM of G-band with increasing SWNT-B concentration. Reason for this change in FWHM is not clear and needs further investigation.
2. SWNT/polymer composites have better tensile properties than pure polymer or SWNT buckypaper. The reasons for SWNT buckypaper having inferior mechanical properties than the polymer/CNT composites needs further attention.
3. Porous fiber formation is related to the fast evaporation rate solvents. Porosity is attributed to polymer phase separation. However, exact phase separation conditions and porosity control remains unresolved issues.
4. Isotactic PMMA ribbon shaped fibers are formed from electrospinning in formic acid solution. Mechanism for ribbon shaped fiber formation is still not available.

APPENDIX A

ADDITIONAL TABLES AND FIGURES FOR SWNT-B/PMMA COMPOSITES

A. 1. E' (GPa) of SWNT-B/PMMA composite films at different temperatures at a frequency of 1.0 Hz.

	E' (GPa) at different temperature under 1 Hz						
SWNT-B (wt%)	30°C	50 °C	75 °C	100 °C	120 °C	125 °C	130 °C
0	2.52	2.08	1.64	0.99	0.10	0.02	
5	3.96	3.58	3.10	1.82	0.62	0.24	0.12
10	6.21	5.60	4.80	2.91	1.32	1.16	1.01
15	8.06	7.36	6.55	4.75	2.12	1.81	1.60
20	8.28	7.17	6.65	5.82	3.31	2.74	2.12
35	9.46	8.79	8.18	6.96	4.92	4.02	3.36
50	9.35	8.42	7.18	5.92	4.52	3.99	3.39

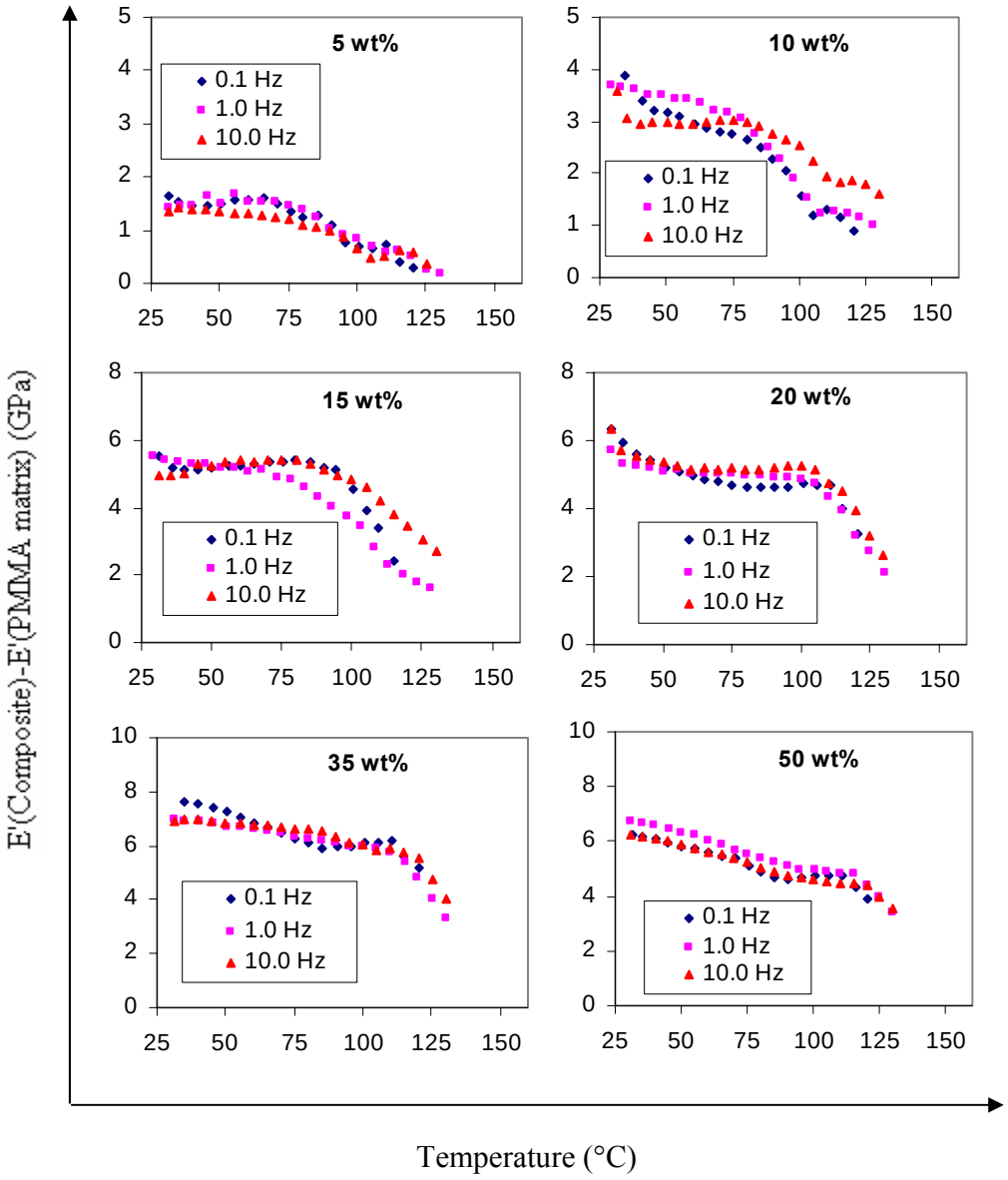

A. 2. E' (composite) - E' (PMMA matrix) as a function of temperature for SWNT-B/PMMA composites at various SWNT-B concentrations.

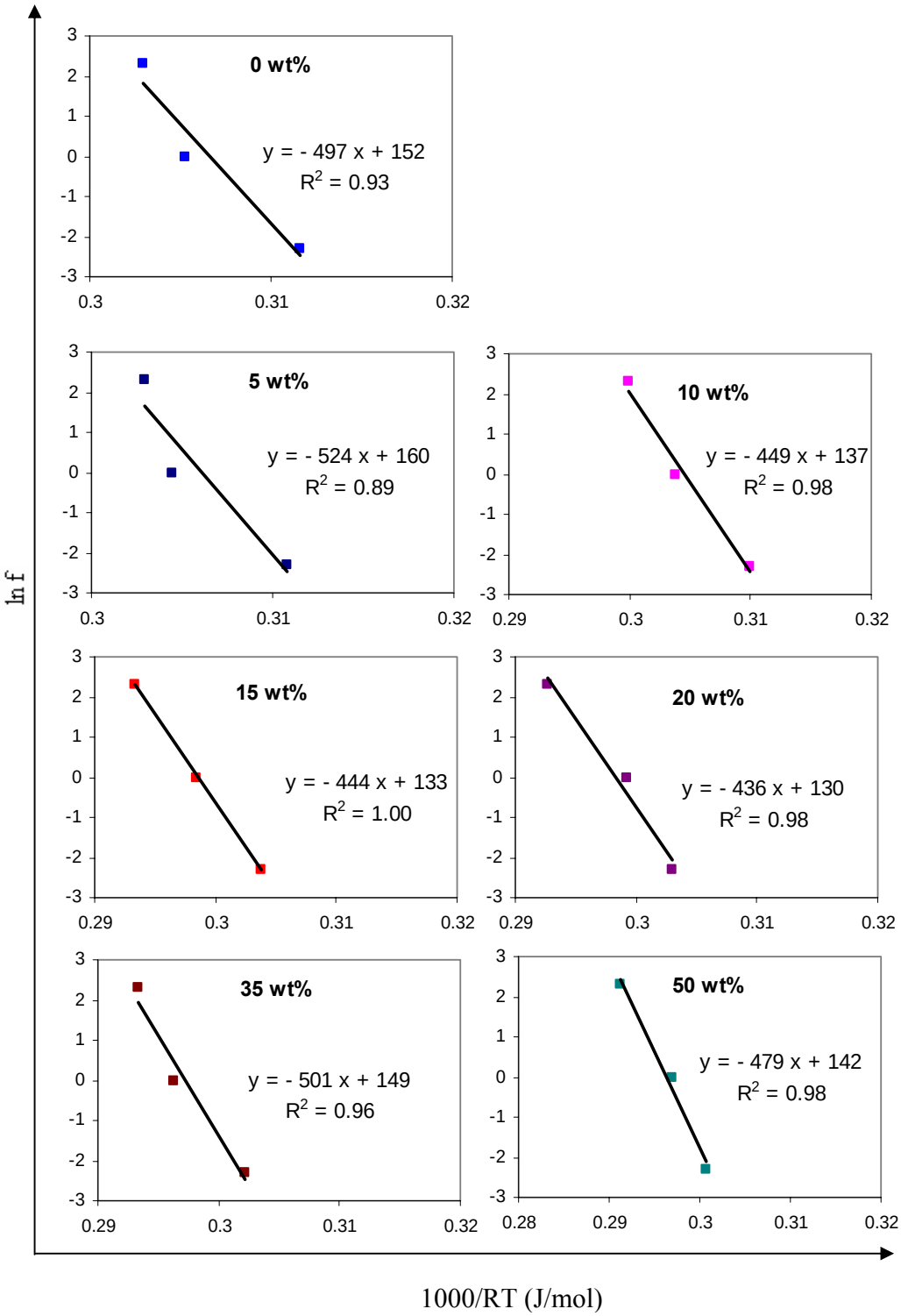

A. 3. Activation energy calculation of SWNT-B/PMMA composite films (The absolute value of the slope of the fitted line is the activation energy).

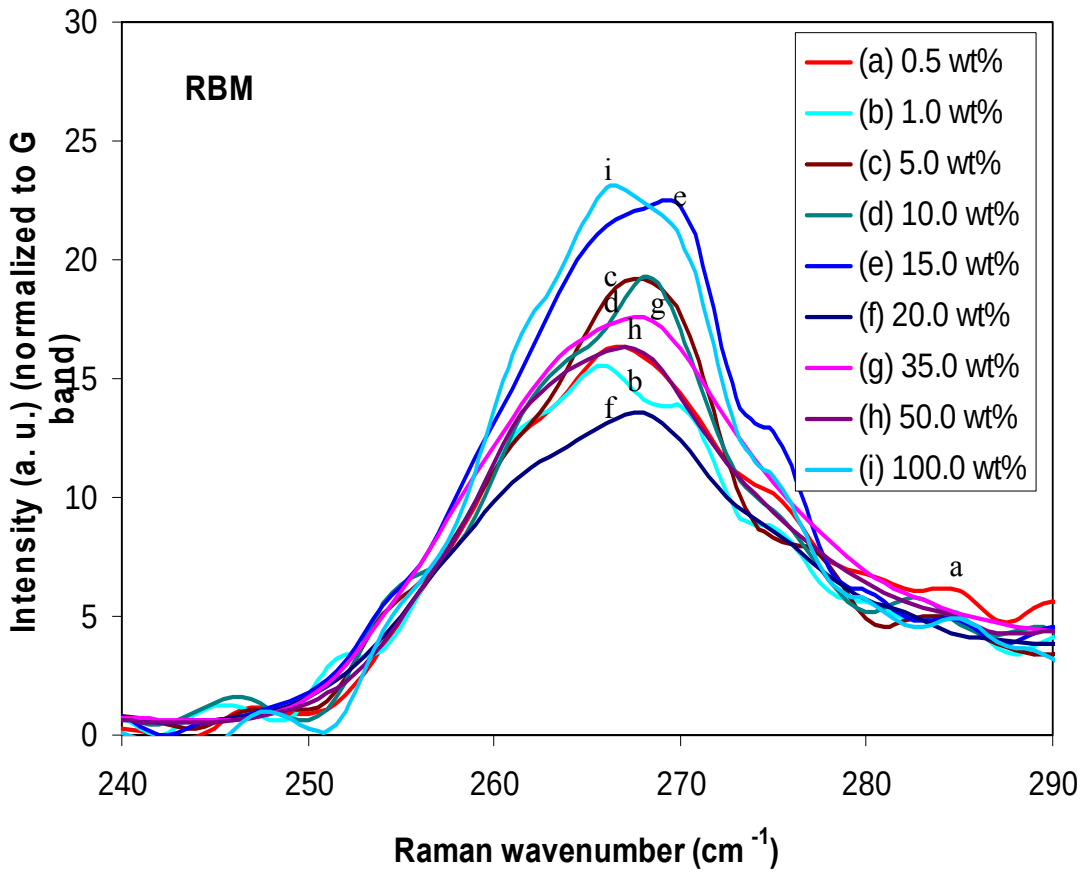

A. 4. Radial breathing mode (RBM) of SWNT-B/PMMA composite films at various SWNT-B concentrations (All intensities have been normalized assuming G band intensity to be 100).

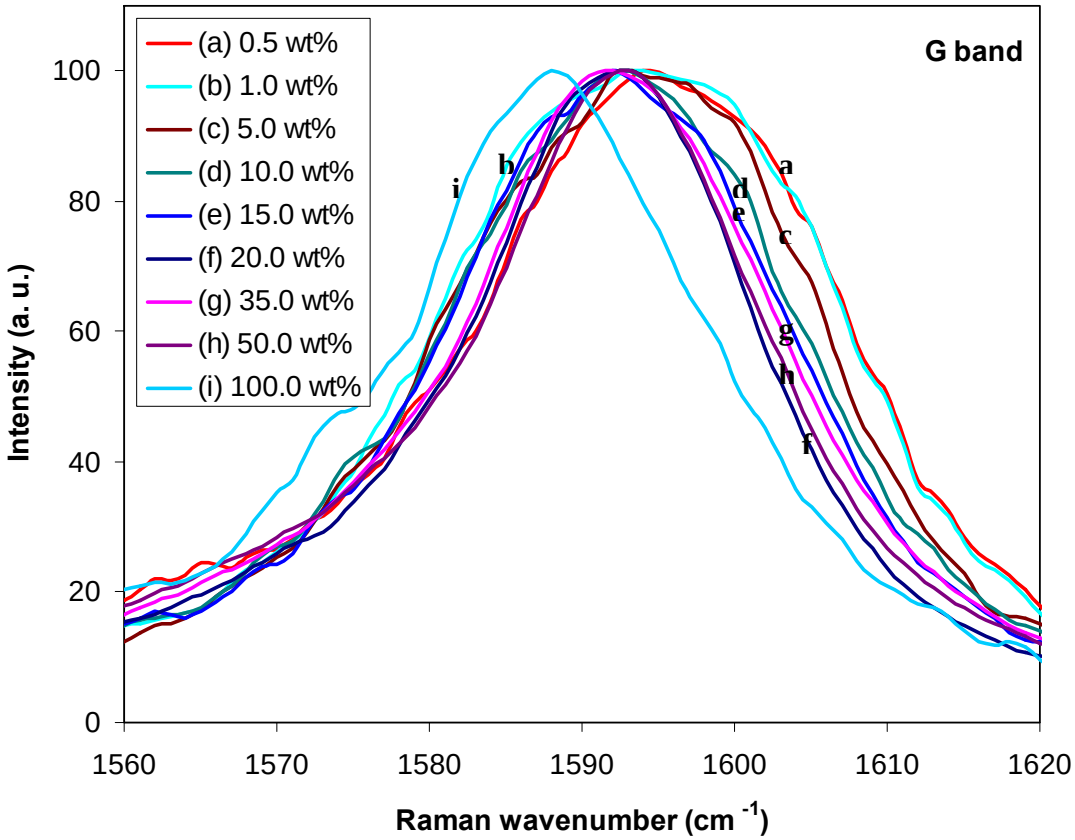

A. 5. G band of SWNT-B/PMMA composite films at various SWNT-B concentrations (All peak intensities have been normalized to 100).

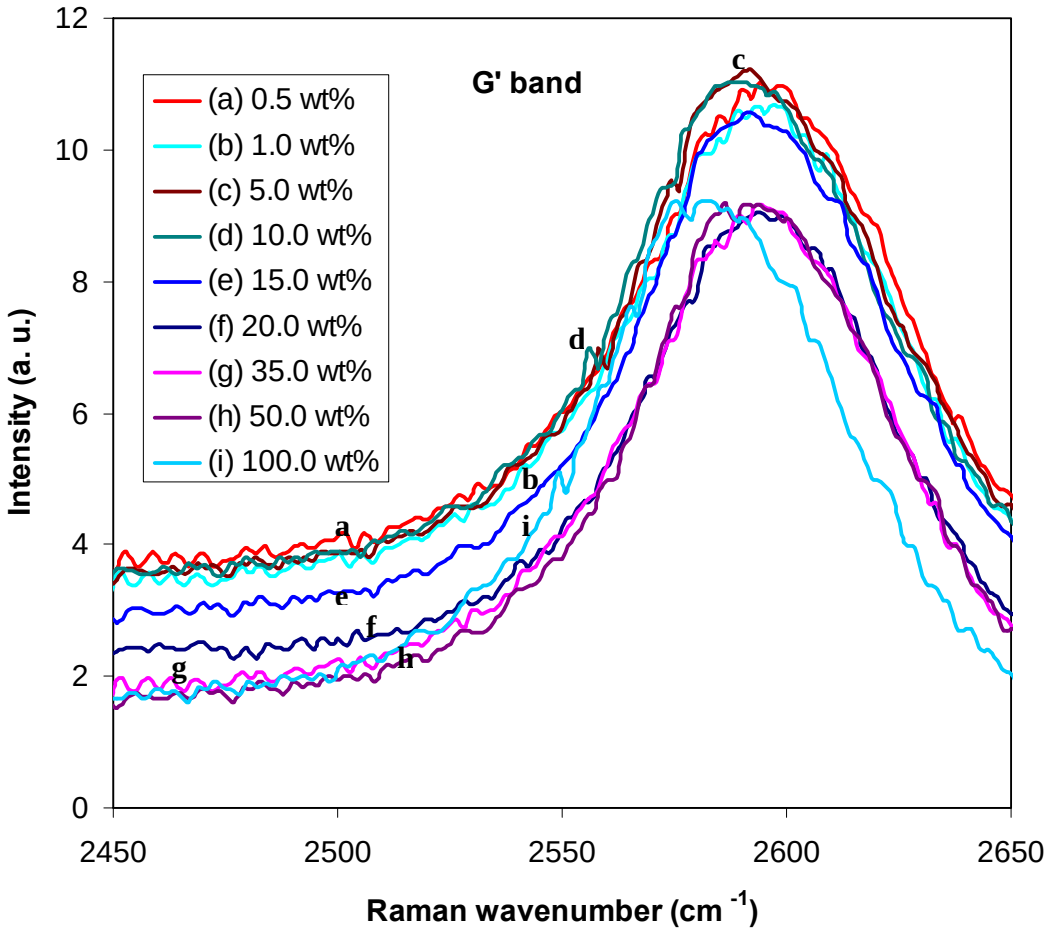

A. 6. G' band of SWNT-B/PMMA composite films at various SWNT-B concentrations (All intensities have been normalized to the G band intensity).

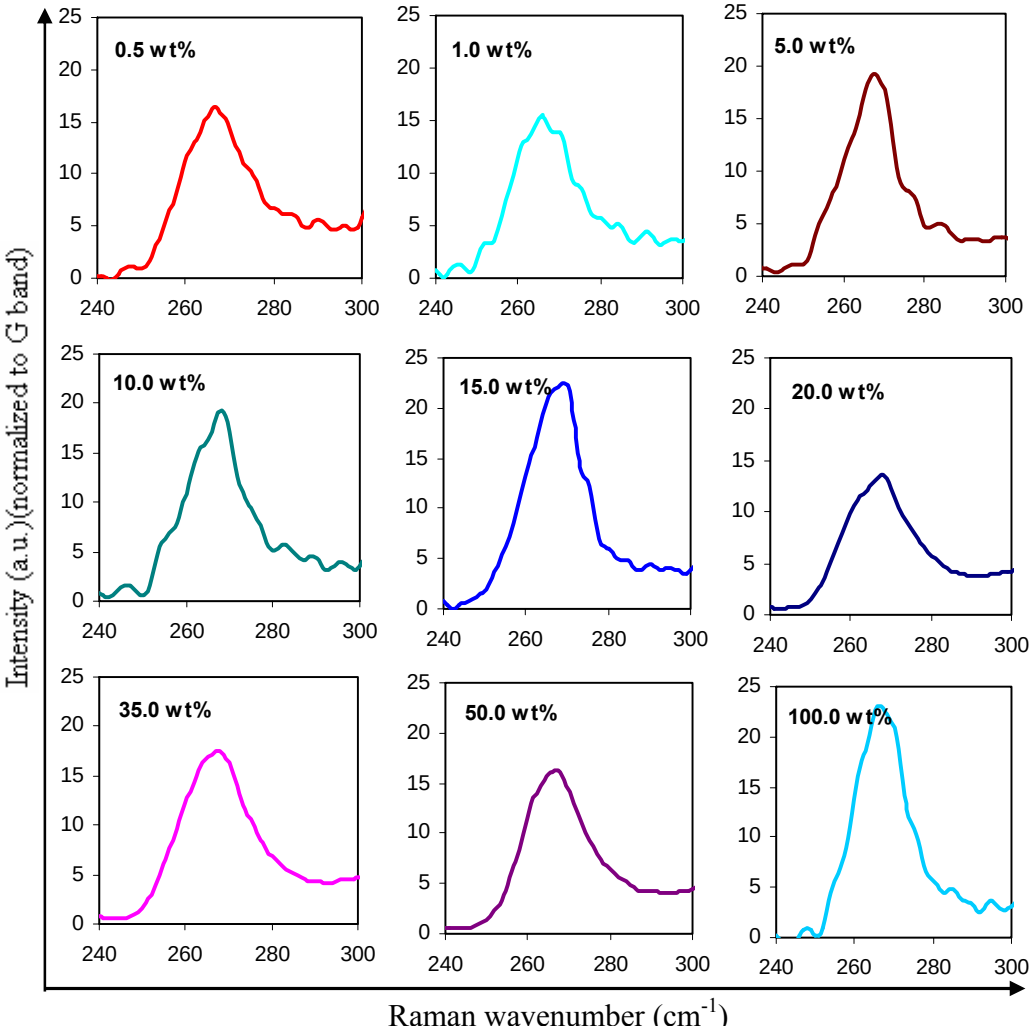

A. 7. Radial breathing mode (RBM) of SWNT-B/PMMA composite films at various SWNT-B concentrations (All intensities have been normalized to the G band intensity).

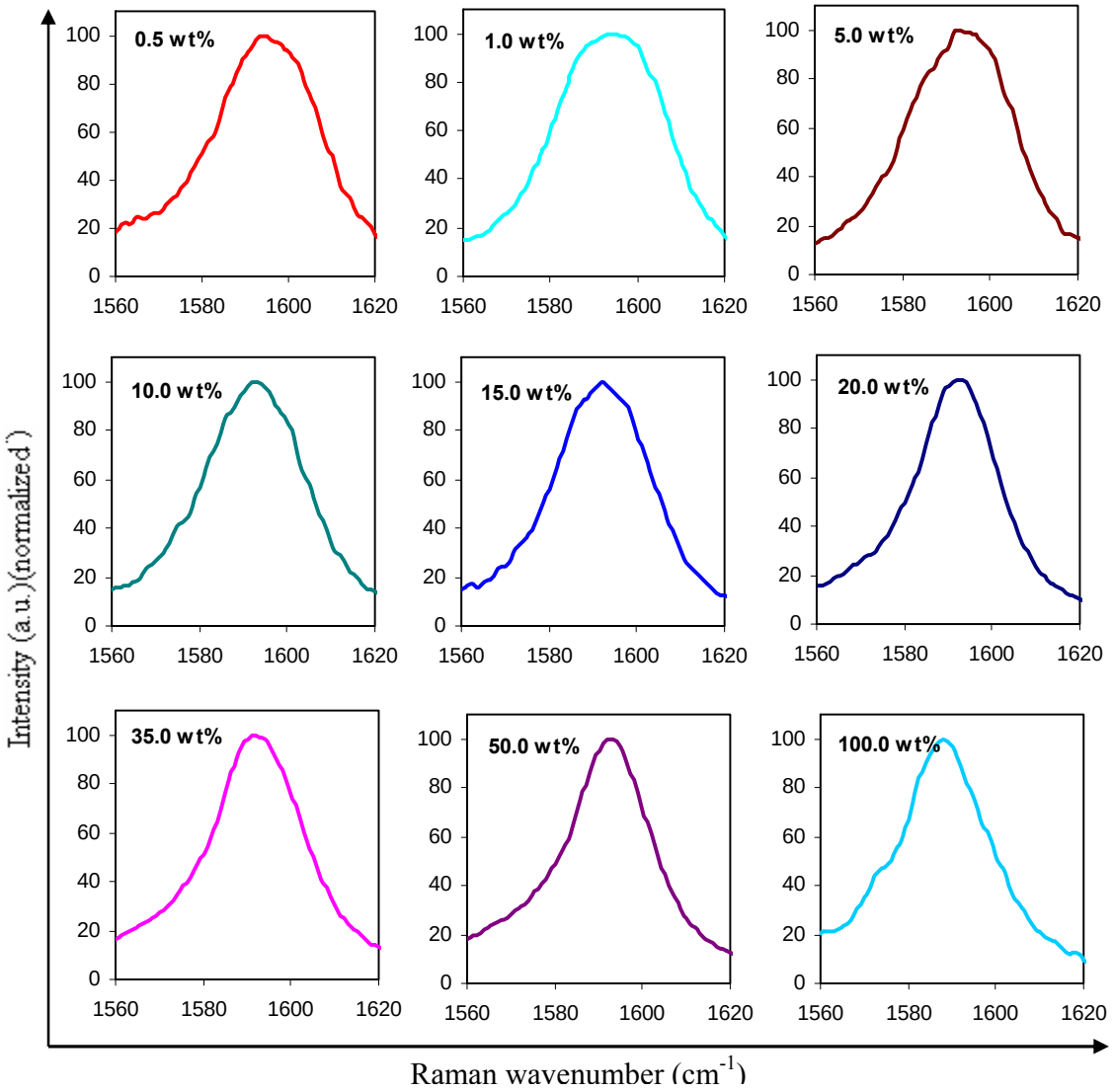

A. 8. G band of SWNT-B/PMMA composite films at various SWNT-B concentrations (All intensities have been normalized to100).

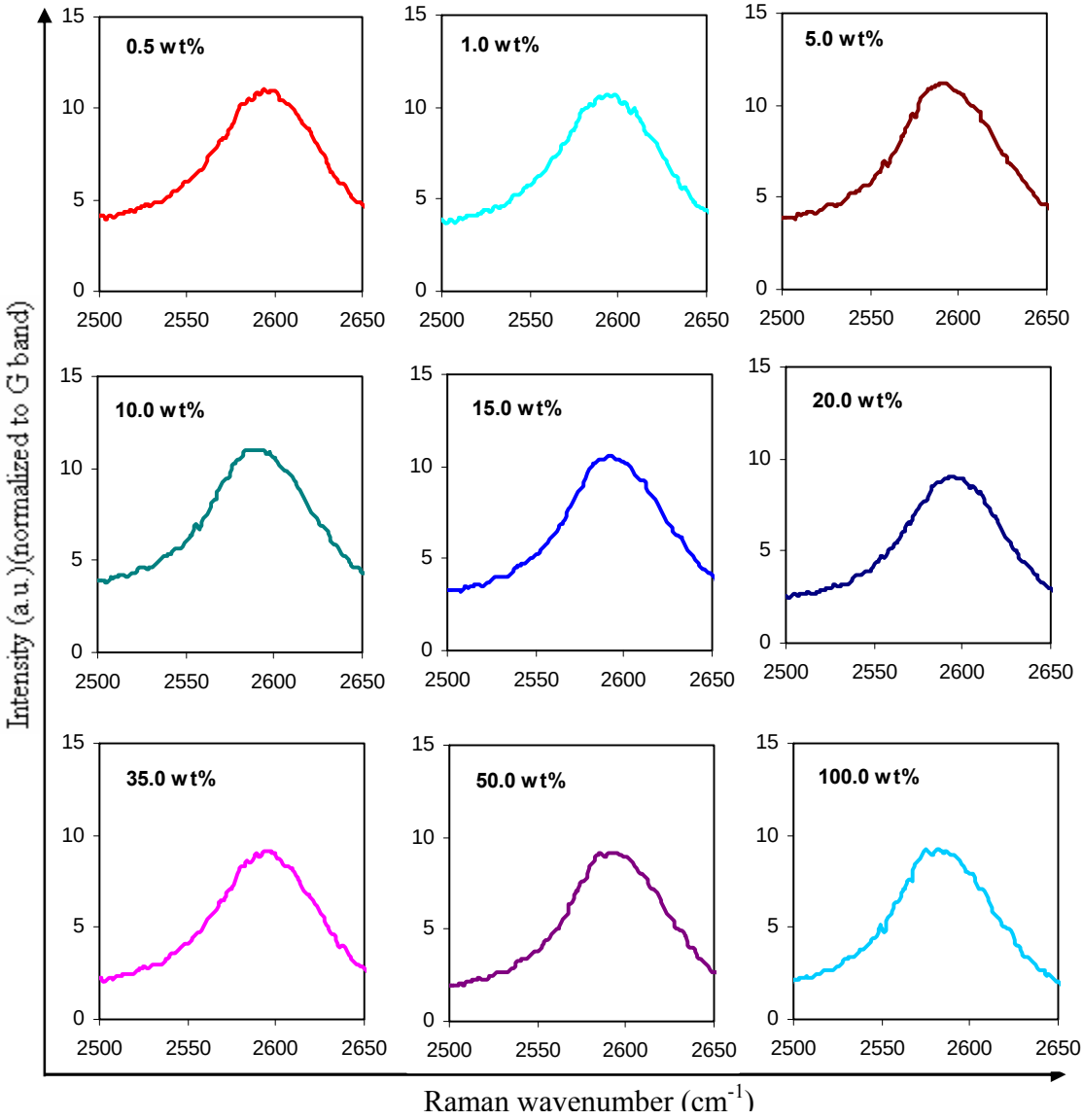

A. 9. G' band of SWNT-B/PMMA composite films at various SWNT-B concentrations (All intensities have been normalized to the G band intensity).

APPENDIX B

ADDITIONAL FIGURES RELATED TO THE ELECTROSPINNING STUDY

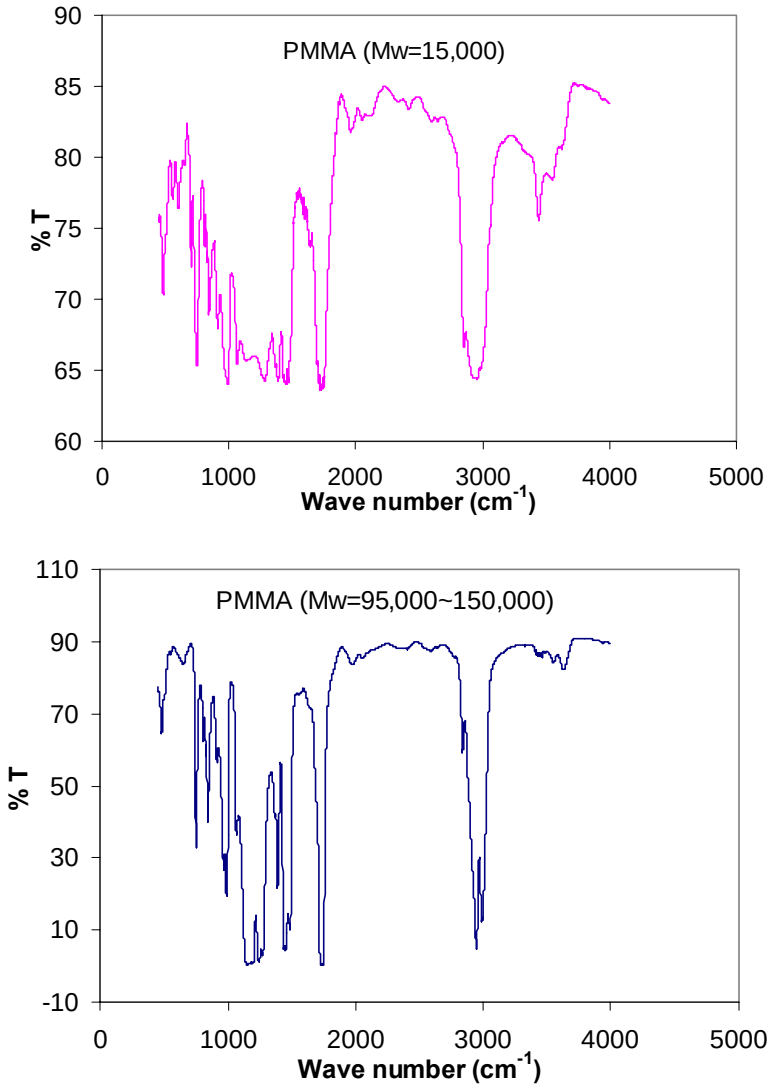

B. 1. Fourier transform infrared (FTIR) spectrum of ultra low molecular weight PMMA (Mw = 15,000 g/mole) (ULMW PMMA) and low molecular weight PMMA (Mw = 95,000 ~ 150,000 g/mole) (LMW PMMA).

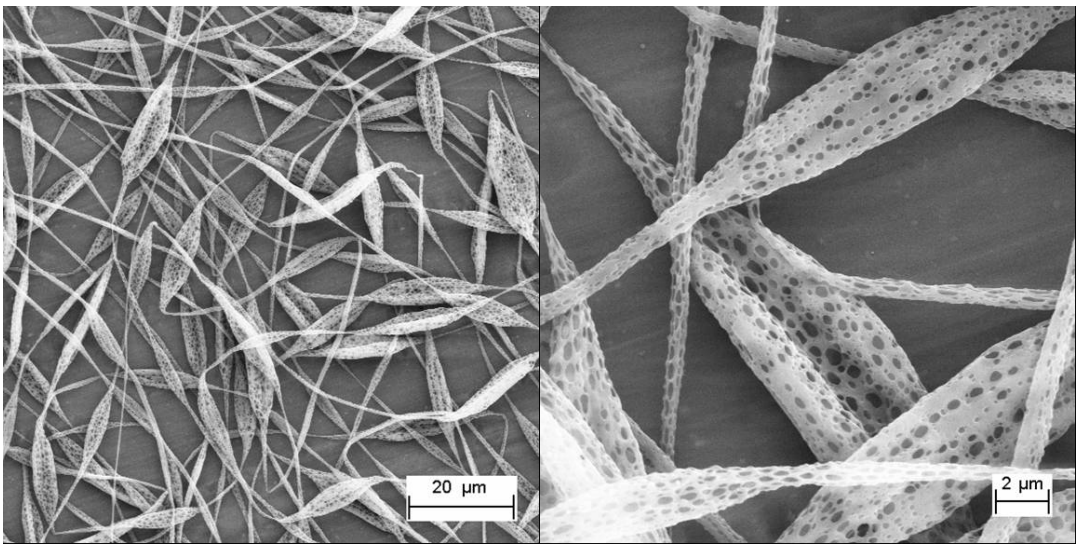

B. 2. Isotactic PMMA porous beaded fibers electrospun from methylene chloride at 2 wt% polymer concentration.

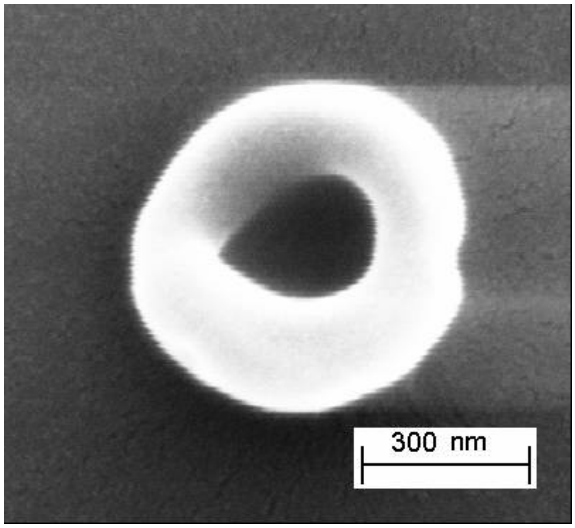

B. 3. PMMA ($\overline{M_w} = 95{,}000 \sim 150{,}000$ g/mole) cup electrospun from nitromethane at 1 wt% polymer concentration.

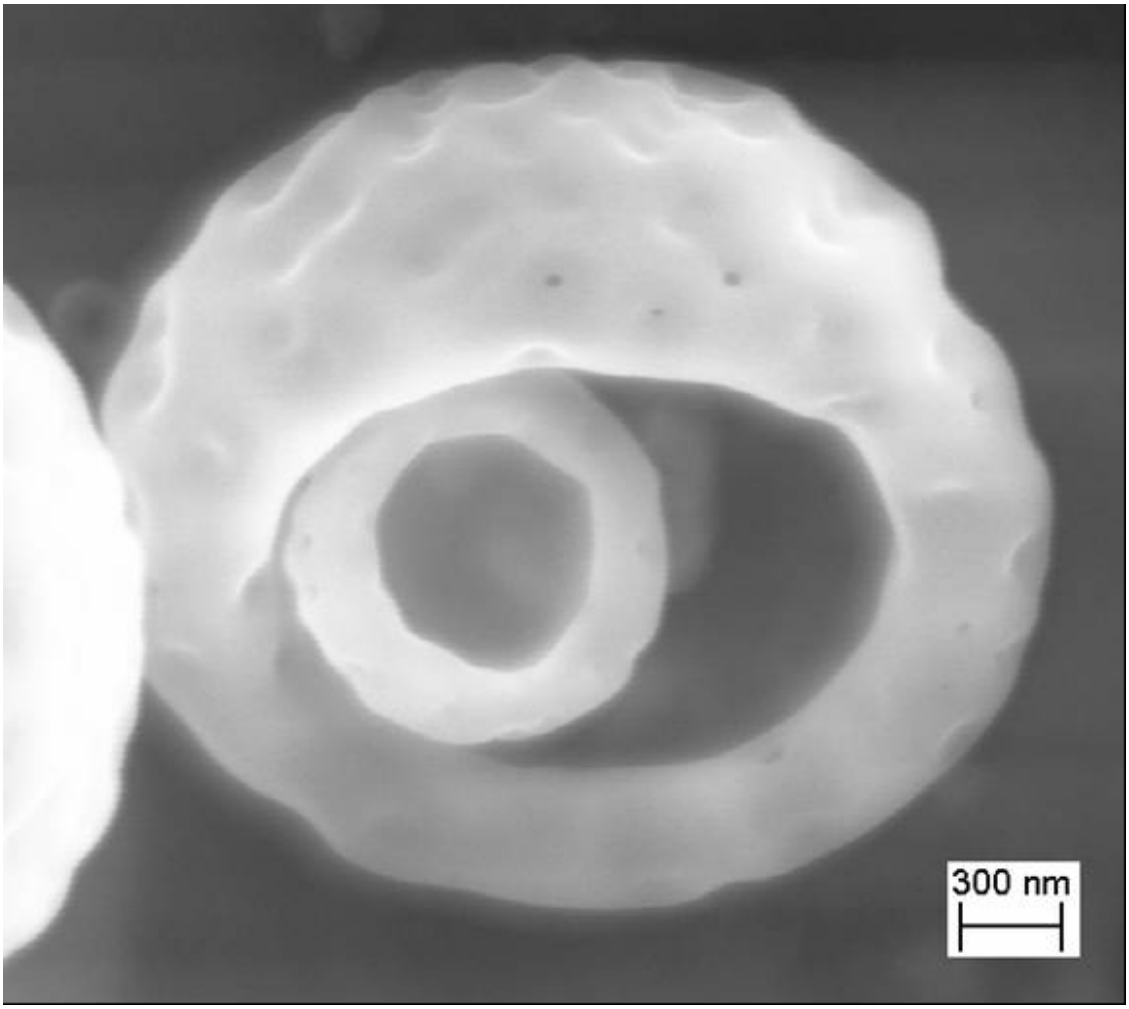

B. 4. PMMA ($\overline{M_w} = 95{,}000 \sim 150{,}000$ g/mole) cups electrospun from nitromethane solution at 6 wt% polymer concentration.

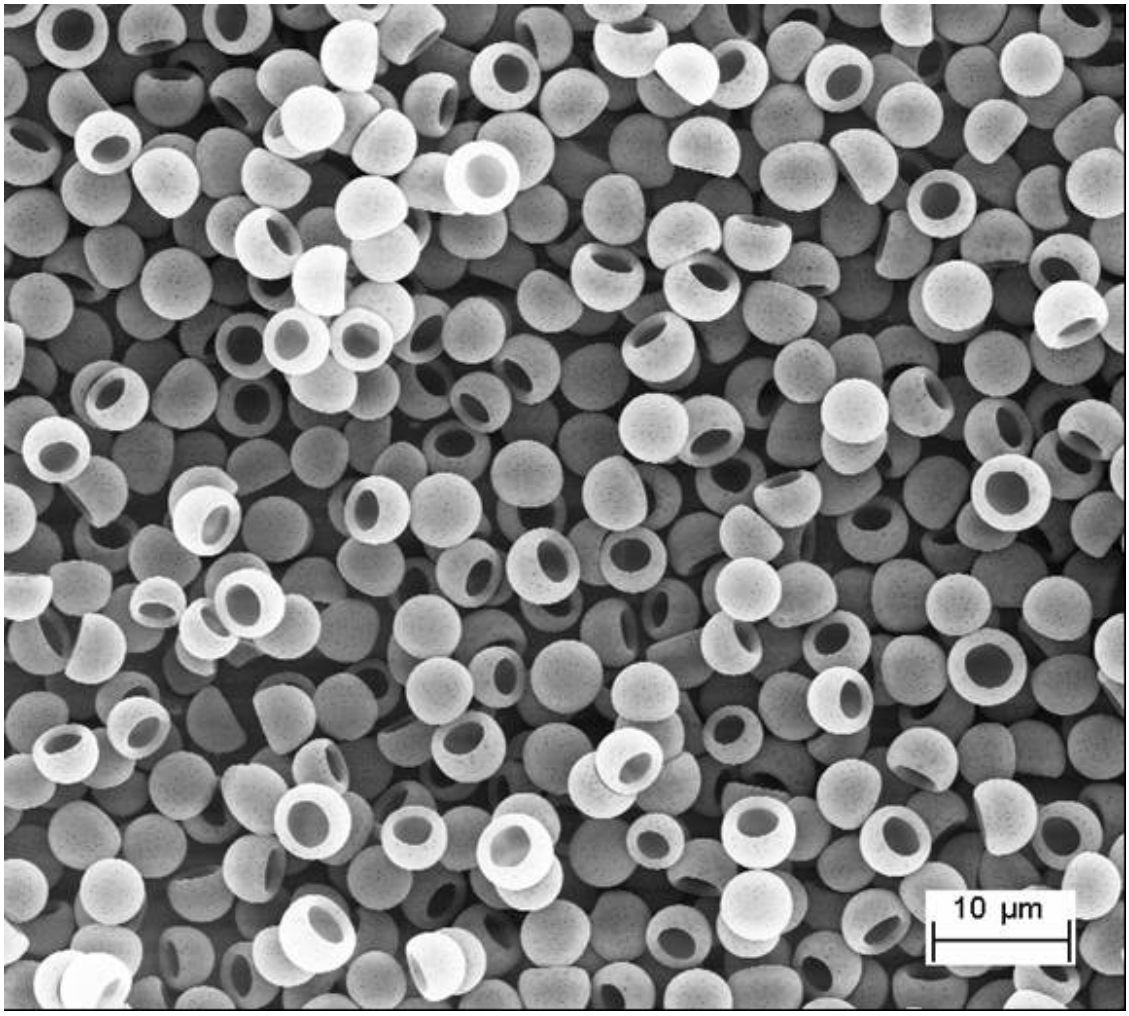

B. 5. PMMA ($\overline{M_w} = 95{,}000 \sim 150{,}000$ g/mole) cups electrospun from nitromethane solution at 8 wt% polymer concentration.

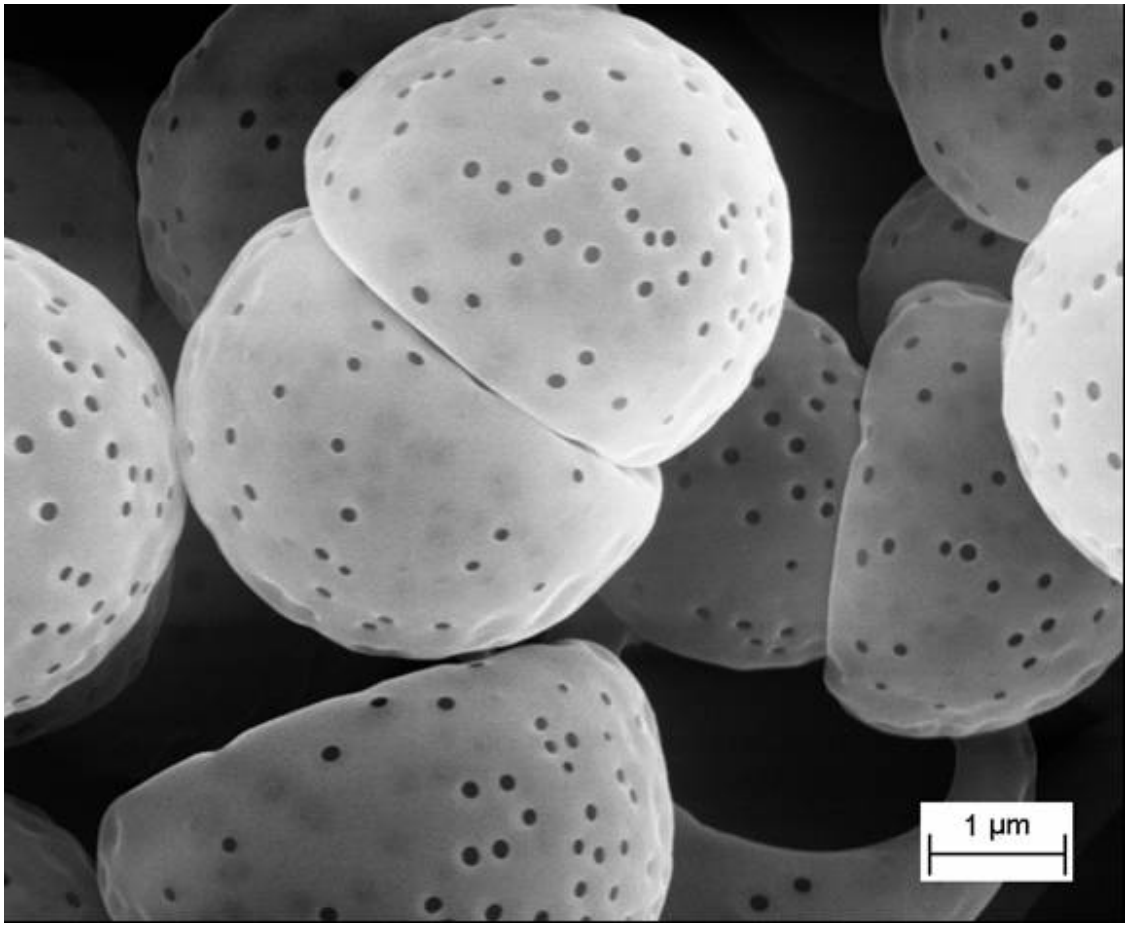

B. 6. PMMA ($\overline{M_w} = 95{,}000 \sim 150{,}000$ g/mole) cups electrospun from nitromethane solution at 8 wt% polymer concentration.

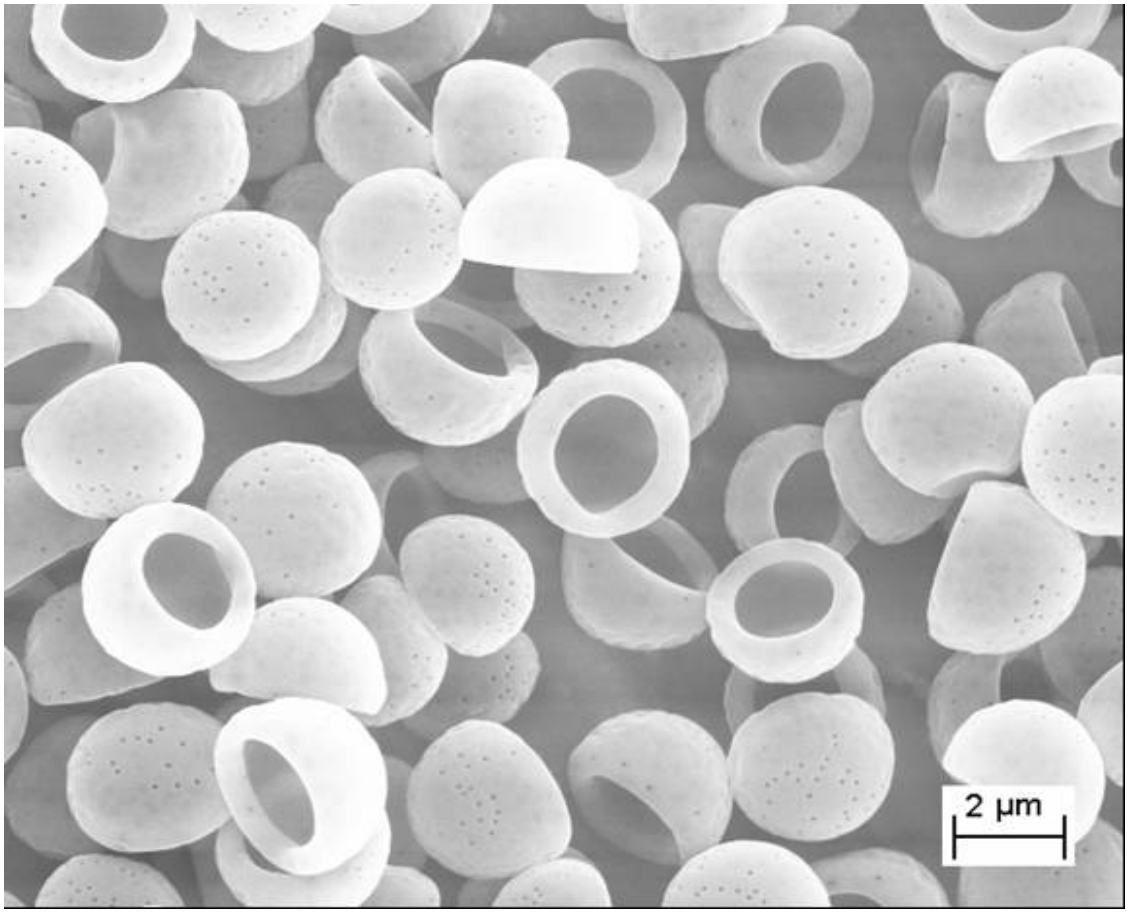

B. 7. PMMA ($\overline{M_w} = 95{,}000 \sim 150{,}000$ g/mole) cups electrospun from nitromethane solution at 6 wt% polymer concentration.

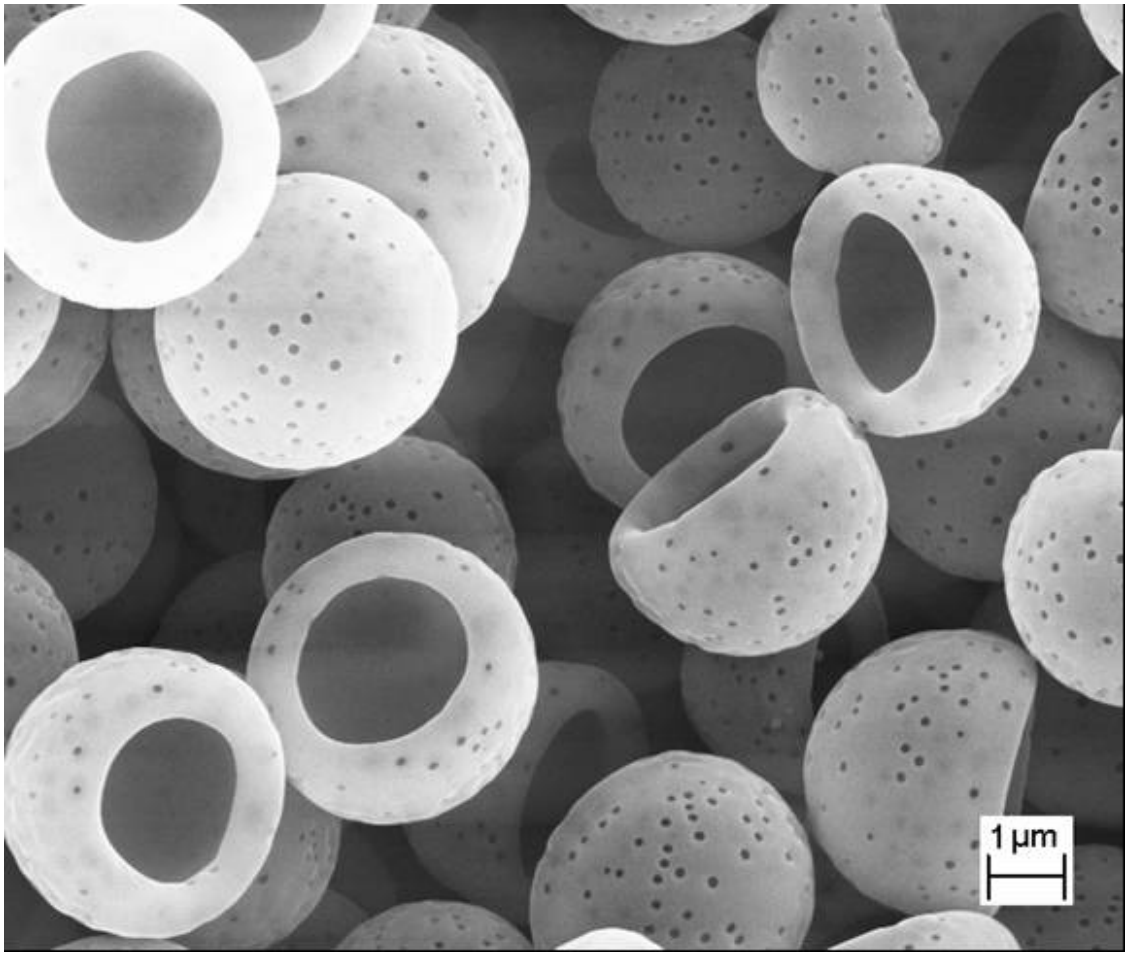

B. 8. PMMA ($\overline{M_w} = 95{,}000 \sim 150{,}000$ g/mole) cups electrospun from nitromethane solution at 8 wt% polymer concentration.

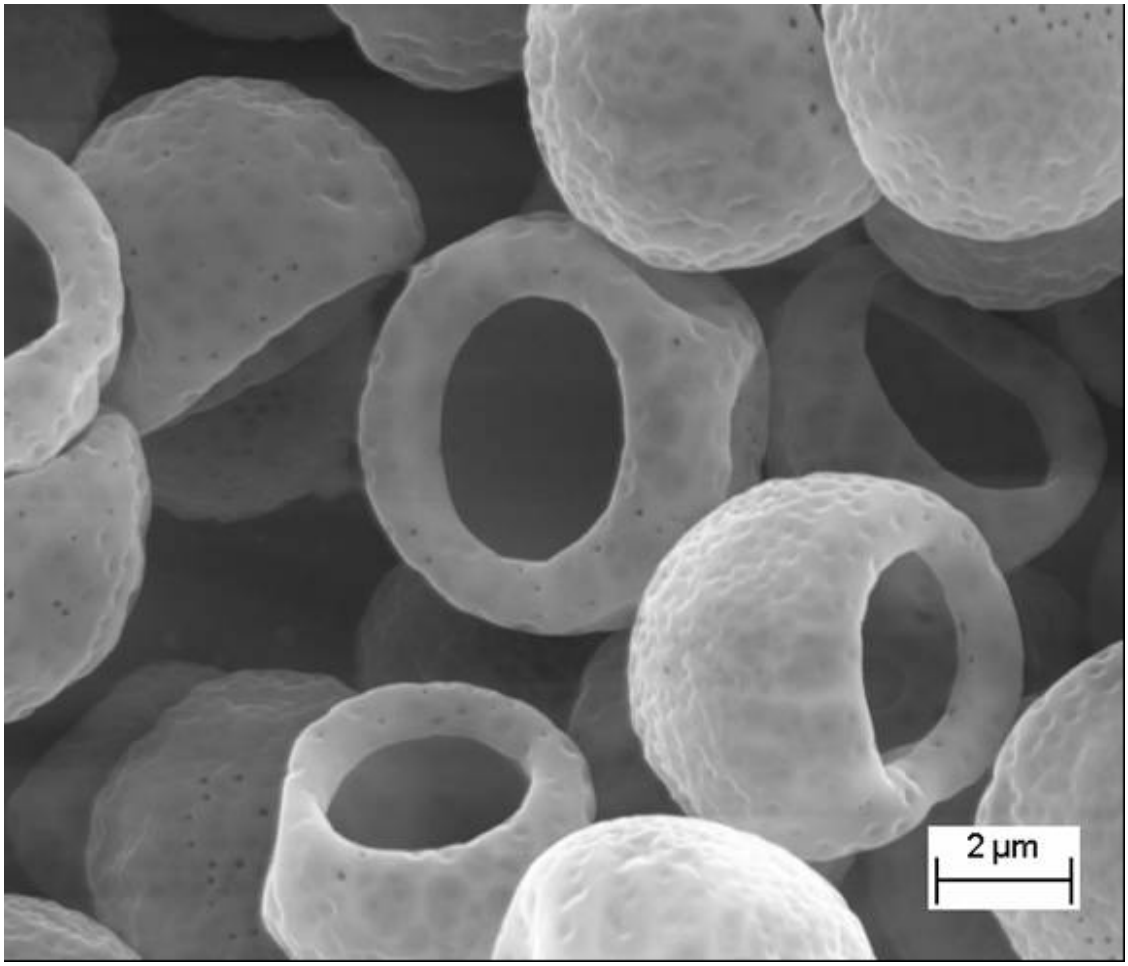

B. 9. PMMA ($\overline{M_w} = 95{,}000 \sim 150{,}000$ g/mole) cups electrospun from nitromethane solution at 10 wt% polymer concentration.

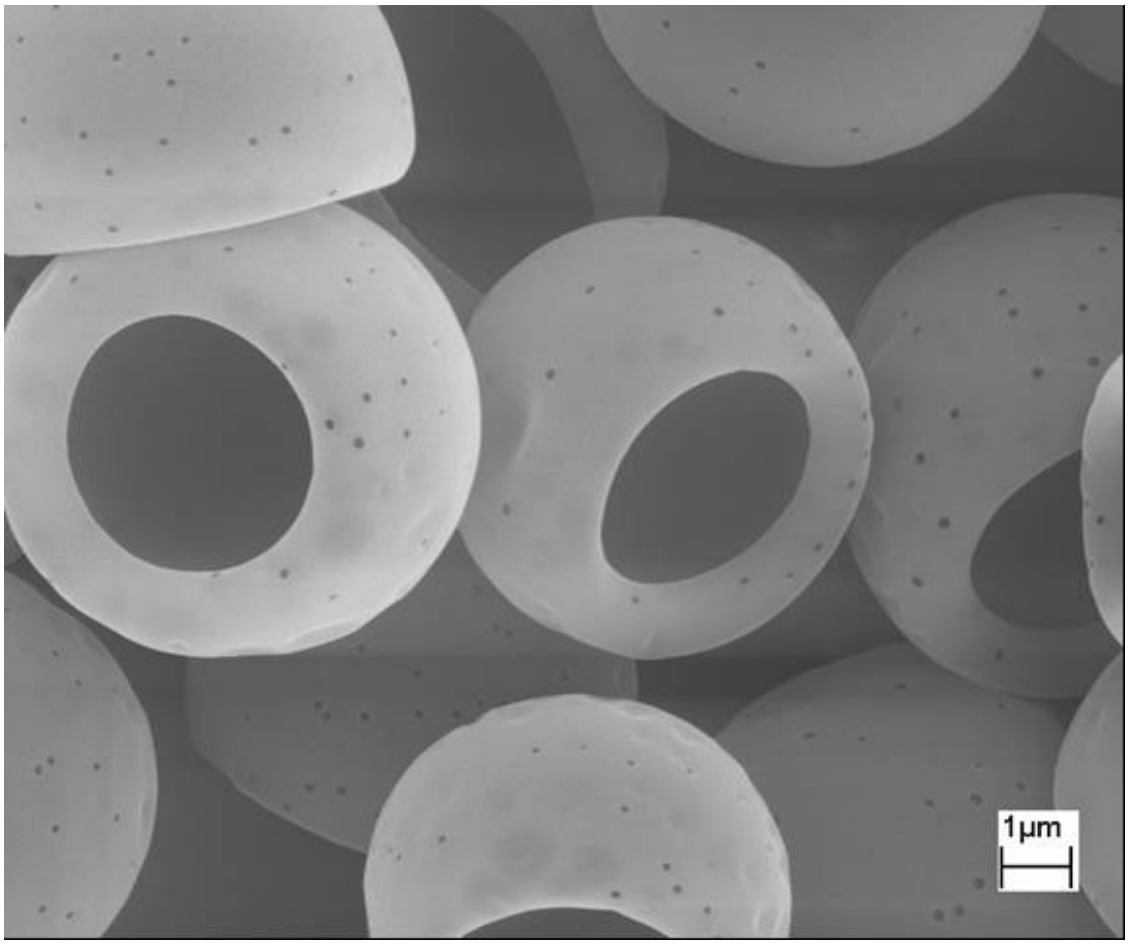

B. 10. PMMA ($\overline{M_w} = 95{,}000 \sim 150{,}000$ g/mole) cups electrospun from nitromethane solution at 12 wt% polymer concentration.

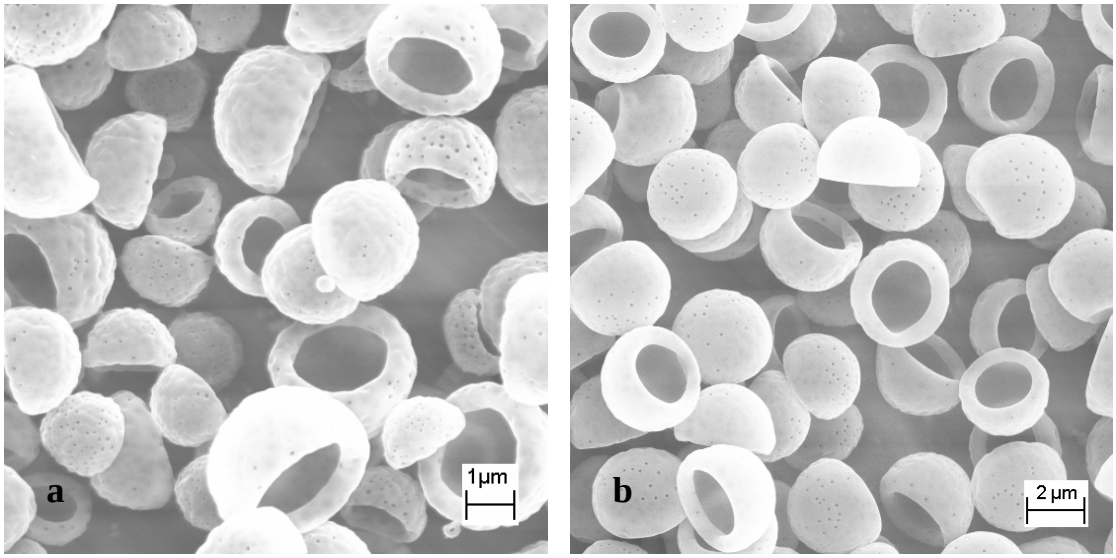

B. 11. PMMA cups electrsopun from nitromethane at 6 wt% concentration with different flow rate: (a) 0.2 ml/h and (b) 2.0 ml/h.

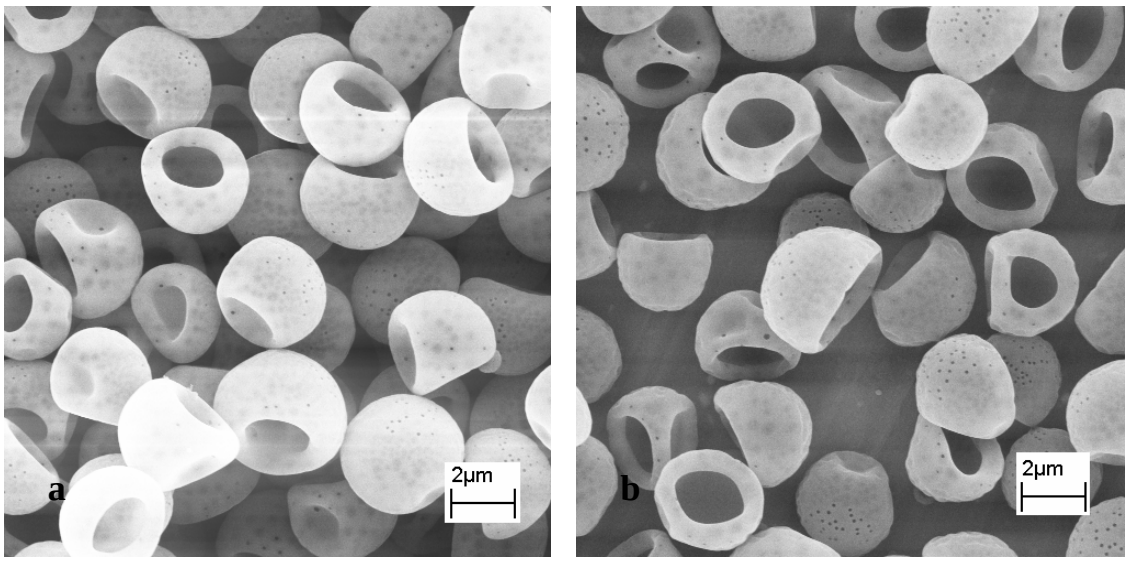

B. 12. PMMA cups electrsopun from nitromethane at 6 wt% concentration using 20# needle at 1 ml/h flow rate with different working distance: (a) 5 cm and (b) 10 cm.

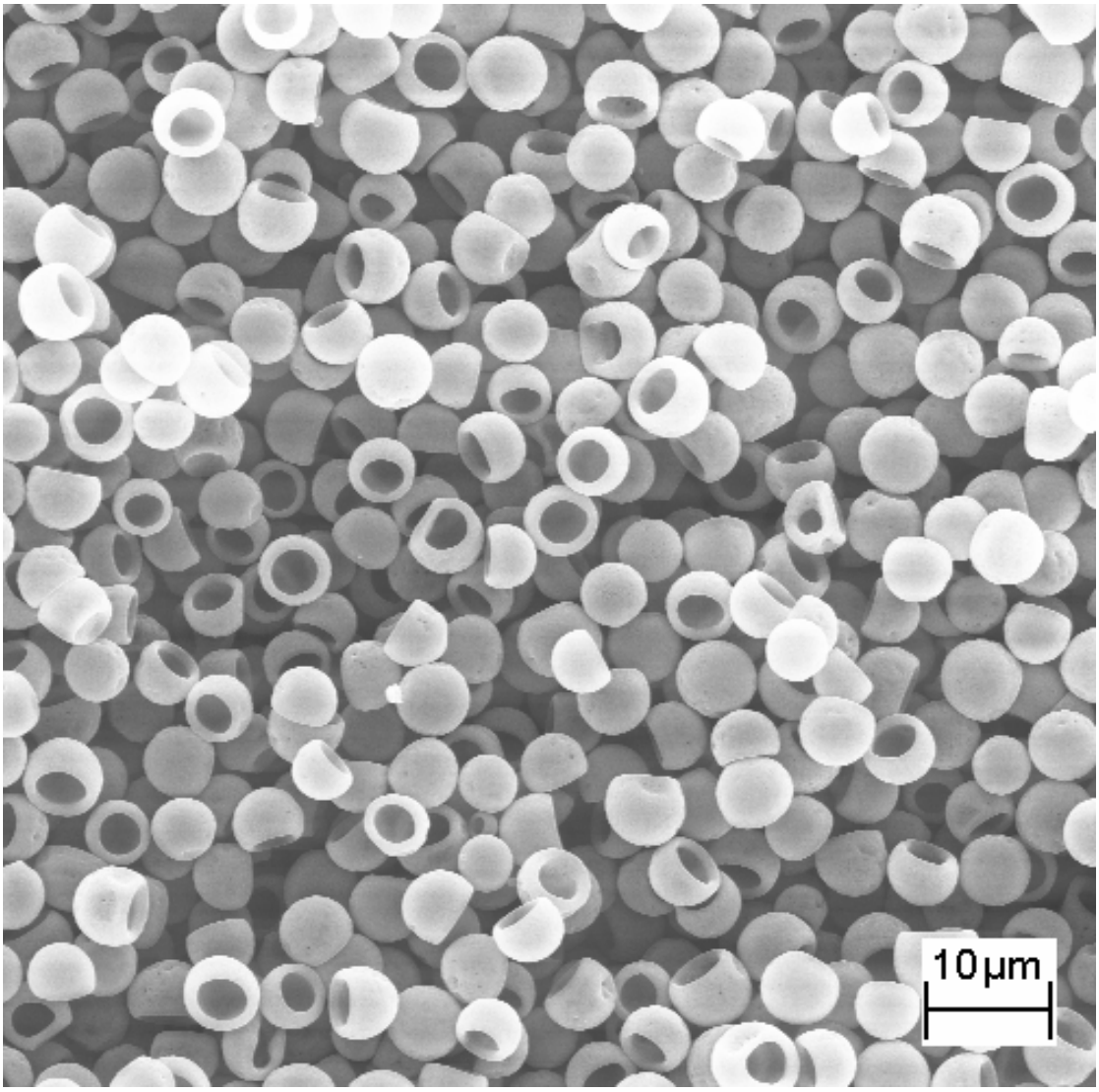

B. 13. PMMA ($\overline{M_w} = 95{,}000 \sim 150{,}000$ g/mole) cups electrospun from acrylonitrile at 8 wt% concentration.

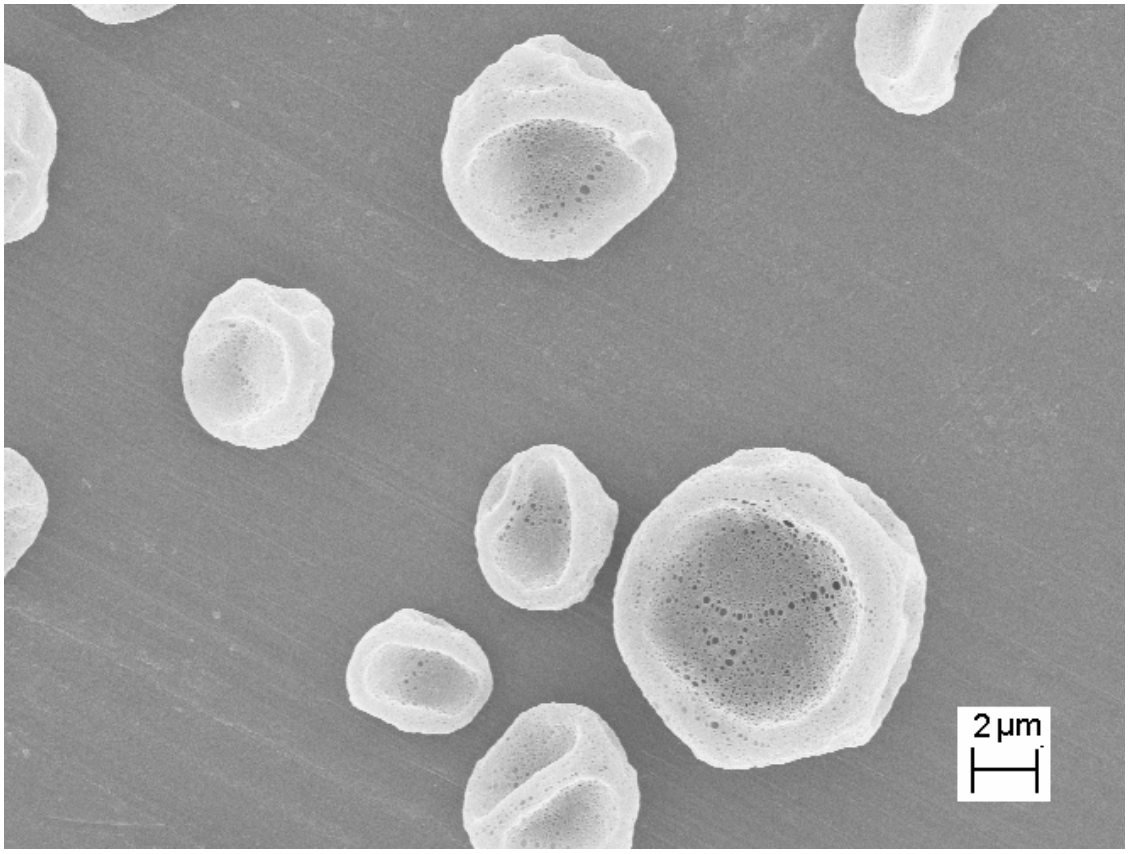

B. 14. PMMA ($\overline{M_w} = 95{,}000 \sim 150{,}000$ g/mole) particles electrospun from methylene chloride at 1 wt% concentration. Solution was maintained at room temperature, while the temperature of the target was maintained at about 5 °C using dry ice.

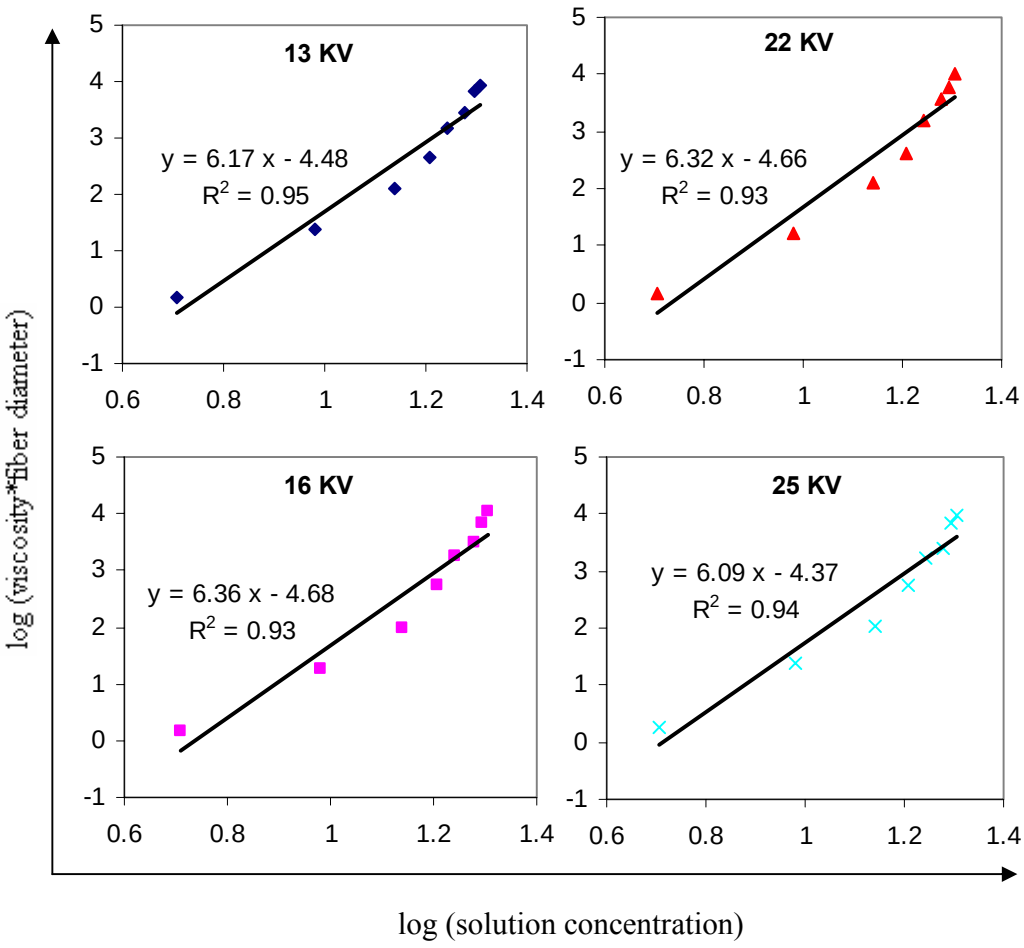

B. 15. The relationship between log (solution viscosity*fiber diameter) and log (concentration) of polyacrylonitrile electrospun from DMF at different applied voltages[230].

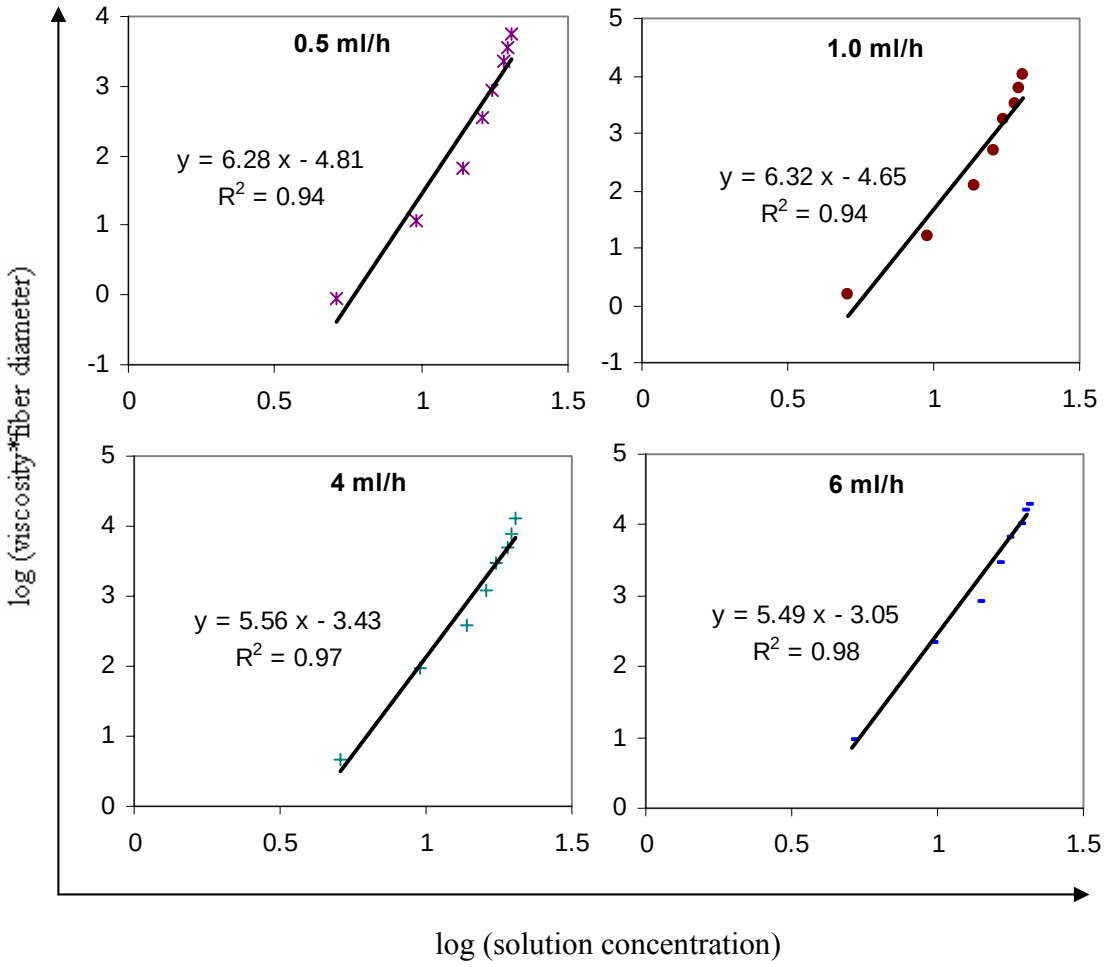

B. 16. The relationship between log (solution viscosity*fiber diameter) and log (concentration) of polyacrylonitrile electrospun from DMF at different flow rates[230].

REFERENCES

1. Bethune, D.S., C.H. Kiang, M.S. Devries, G. Gorman, R. Savoy, J. Vazquez, and R. Beyers, *Cobalt-Catalyzed Growth of Carbon Nanotubes with Single-Atomic-Layerwalls.* Nature, 1993. **363**(6430): p. 605-607.

2. Iijima, S. and T. Ichihashi, *Single-Shell Carbon Nanotubes of 1-Nm Diameter.* Nature, 1993. **363**(6430): p. 603-605.

3. Sugai, T., H. Yoshida, T. Shimada, T. Okazaki, and H. Shinohara, *New synthesis of high-quality double-walled carbon nanotubes by high-temperature pulsed arc discharge.* Nano Letters, 2003. **3**(6): p. 769-773.

4. Bandow, S., M. Takizawa, K. Hirahara, M. Yudasaka, and S. Iijima, *Raman scattering study of double-wall carbon nanotubes derived from the chains of fullerenes in single-wall carbon nanotubes.* Chemical Physics Letters, 2001. **337**(1-3): p. 48-54.

5. Iijima, S., *Helical microtubules of graphitic carbon.* Nature, 1991. **354**(6348): p. 56-58.

6. Minus, M.L. and S. Kumar, *The processing, properties, and structure of carbon fibers.* Journal of the Minerals, Metals, and Materials, 2005. **57**(2): p. 52-58.

7. Carneiro, O.S., J.A. Covas, C.A. Bernardo, G. Caldeira, F.W.J. Van Hattum, J.M. Ting, R.L. Alig, and M.L. Lake, *Production and assessment of polycarbonate composites reinforced with vapour-grown carbon fibres.* Composites Science and Technology, 1998. **58**(3-4): p. 401-407.

8. Bae, D.J., K.S. Kim, Y.S. Park, E.K. Suh, K.H. An, J.M. Moon, S.C. Lim, S.H. Park, Y.H. Jeong, and Y.H. Lee, *Transport phenomena in an anisotropically aligned single-wall carbon nanotube film.* Physical Review B, 2001. **64**(23): p. 233401.

9. Bozovic, I., N. Bozovic, and M. Damnjanovic, *Optical dichroism in nanotubes.* Physical Review B, 2000. **62**(11): p. 6971-6974.

10. Popov, V.N., V.E. Van Doren, and M. Balkanski, *Elastic properties of crystals of single-walled carbon nanotubes.* Solid State Communications, 2000. **114**(7): p. 395-399.

11. Che, J.W., T. Cagin, and W.A. Goddard, *Thermal conductivity of carbon nanotubes.* Nanotechnology, 2000. **11**(2): p. 65-69.

12. O'Connell, M.J., *Carbon Nanotubes: Properties and Applications.* Taylor & Francis, Boca Raton, FL, 2006: p. 211-265.

13. Baughman, R.H., A.A. Zakhidov, and W.A. de Heer, *Carbon nanotubes - the route toward applications.* Science, 2002. **297**(5582): p. 787-792.

14. Lu, J.P., *Elastic properties of carbon nanotubes and nanoropes.* Physical Review Letters, 1997. **79**(7): p. 1297-1300.

15. Gao, G.H., T. Cagin, and W.A. Goddard, *Energetics, structure, mechanical and vibrational properties of single-walled carbon nanotubes.* Nanotechnology, 1998. **9**(3): p. 184-191.

16. Sinnott, S.B., O.A. Shenderova, C.T. White, and D.W. Brenner, *Mechanical properties of nanotubule fibers and composites determined from theoretical calculations and simulations.* Carbon, 1998. **36**(1-2): p. 1-9.

17. Salvetat, J.P., G.A.D. Briggs, J.M. Bonard, R.R. Bacsa, A.J. Kulik, T. Stockli, N.A. Burnham, and L. Forro, *Elastic and shear moduli of single-walled carbon nanotube ropes.* Physical Review Letters, 1999. **82**(5): p. 944-947.

18. Li, M.Y., M.J. Mondrinos, M.R. Gandhi, F.K. Ko, A.S. Weiss, and P.I. Lelkes, *Electrospun protein fibers as matrices for tissue engineering.* Biomaterials, 2005. **26**(30): p. 5999-6008.

19. Yu, M.F., O. Lourie, M.J. Dyer, K. Moloni, T.F. Kelly, and R.S. Ruoff, *Strength and breaking mechanism of multiwalled carbon nanotubes under tensile load.* Science, 2000. **287**(5453): p. 637-640.

20. Pan, Z.W., S.S. Xie, L. Lu, B.H. Chang, L.F. Sun, W.Y. Zhou, G. Wang, and D.L. Zhang, *Tensile tests of ropes of very long aligned multiwall carbon nanotubes.* Applied Physics Letters, 1999. **74**(21): p. 3152-3154.

21. Liew, K.M., X.Q. He, and C.H. Wong, *On the study of elastic and plastic properties of multi-walled carbon nanotubes under axial tension using molecular dynamics simulation.* Acta Material, 2004. **52**(9): p. 2521-2527.

22. Johnson, W., *The structure of PAN based carbon fibers and relationship to the physical properties.* Handbook of Composites, New York, Elsevier Sicence, 1988. **1**: p. 393.

23. Toyobo, I., (http://www.toyobo.co.jp/e/seihin/kc/pbo/menu).

24. Chae, H.G., T.V. Sreekumar, T. Uchida, and S. Kumar, *A comparison of reinforcement efficiency of various types of carbon nanotubes in poly acrylonitrile fiber.* Polymer, 2005. **46**(24): p. 10925-10935.

25. Dupont, I., *Kevlar.* (http://www.dupont.com/kevlar).

26. Stephan, C., T.P. Nguyen, M.L. de la Chapelle, S. Lefrant, C. Journet, and P. Bernier, *Characterization of singlewalled carbon nanotubes-PMMA composites.* Synthetic Metals, 2000. **108**(2): p. 139-149.

27. Haggenmueller, R., H.H. Gommans, A.G. Rinzler, J.E. Fischer, and K.I. Winey, *Aligned single-wall carbon nanotubes in composites by melt processing methods.* Chemical Physics Letters, 2000. **330**(3-4): p. 219-225.

28. Cooper, C.A., D. Ravich, D. Lips, J. Mayer, and H.D. Wagner, *Distribution and alignment of carbon nanotubes and nanofibrils in a polymer matrix.* Composites Science and Technology, 2002. **62**(7-8): p. 1105-1112.

29. Benoit, J.M., B. Corraze, and O. Chauvet, *Localization, coulomb interactions, and electrical heating in single-wall carbon nanotubes/polymer composites.* Physical Review B, 2002. **65**(24): p. 241405.

30. Bhattacharyya, A.R., T.V. Sreekumar, T. Liu, S. Kumar, L.M. Ericson, R.H. Hauge, and R.E. Smalley, *Crystallization and orientation studies in polypropylene/single wall carbon nanotube composite.* Polymer, 2003. **44**(8): p. 2373-2377.

31. Kumar, S., H. Doshi, M. Srinivasarao, J.O. Park, and D.A. Schiraldi, *Fibers from polypropylene/nano carbon fiber composites.* Polymer, 2002. **43**(5): p. 1701-1703.

32. Sreekumar, T.V., T. Liu, B.G. Min, H. Guo, S. Kumar, R.H. Hauge, and R.E. Smalley, *Polyacrylonitrile single-walled carbon nanotube composite fibers.* Advanced Materials, 2004. **16**(1): p. 58-61.

33. Guo, H., T.V. Sreekumar, T. Liu, and S. Kumar, *Structure and properties of polyacrylonitrile/single wall carbon nanotube composite films.* Polymer, 2005. **46**(9): p. 3001-3005.

34. Pirlot, C., Z. Mekhalif, A. Fonseca, J.B. Nagy, G. Demortier, and J. Delhalle, *Surface modifications of carbon nanotube/polyacrylonitrile composite films by proton beams.* Chemical Physics Letters, 2003. **372**(3-4): p. 595-602.

35. Weisenberger, M.C., E.A. Grulke, D. Jacques, T. Rantell, and R. Andrews, *Enhanced mechanical properties of polyacrylonitrile/multiwall carbon nanotube composite fibers.* Journal of Nanoscience and Nanotechnology, 2003. **3**(6): p. 535-539.

36. Ko, F., Y. Gogotsi, A. Ali, N. Naguib, H.H. Ye, G.L. Yang, C. Li, and P. Willis, *Electrospinning of continuons carbon nanotube-filled nanofiber yarns.* Advanced Materials, 2003. **15**(14): p. 1161-1165.

37. Min, B.G., T.V. Sreekumar, T. Uchida, and S. Kumar, *Oxidative stabilization of PAN/SWNT composite fiber.* Carbon, 2005. **43**(3): p. 599-604.

38. Koganemaru, A., Y. Bin, Y. Agari, and M. Matsuo, *Composites of polyacrylonitrile and multiwalled carbon nanotubes prepared by gelation/crystallization from solution.* Advanced Functional Materials, 2004. **14**(9): p. 842-850.

39. Wang, B., J.W. Li, H.P. Wang, J.M. Jiang, and Y.Q. Liu, *Rheological behavior of spinning dope of multiwalled carbon nanotube/polyacrylonitrile composites.* Macromolecular Symposia, 2004. **216**: p. 189-194.

40. Kumar, S., T.D. Dang, F.E. Arnold, A.R. Bhattacharyya, B.G. Min, X.F. Zhang, R.A. Vaia, C. Park, W.W. Adams, R.H. Hauge, R.E. Smalley, S. Ramesh, and P.A. Willis, *Synthesis, structure, and properties of PBO/SWNT composites.* Macromolecules, 2002. **35**(24): p. 9039-9043.

41. Dalton, A.B., S. Collins, E. Munoz, J.M. Razal, V.H. Ebron, J.P. Ferraris, J.N. Coleman, B.G. Kim, and R.H. Baughman, *Super-tough carbon-nanotube fibres - These extraordinary composite fibres can be woven into electronic textiles.* Nature, 2003. **423**(6941): p. 703-703.

42. Dalton, A.B., S. Collins, J. Razal, E. Munoz, V.H. Ebron, B.G. Kim, J.N. Coleman, J.P. Ferraris, and R.H. Baughman, *Continuous carbon nanotube composite fibers: properties, potential applications, and problems.* Journal of Materials Chemistry, 2004. **14**(1): p. 1-3.

43. Wildoer, J.W.G., L.C. Venema, A.G. Rinzler, R.E. Smalley, and C. Dekker, *Electronic structure of atomically resolved carbon nanotubes.* Nature, 1998. **391**(6662): p. 59-62.

44. Dresselhaus, M.S., *Nanotechnology - New tricks with nanotubes.* Nature, 1998. **391**(6662): p. 19-20.

45. Saito, R., G. Dresselhaus, and M.S. Dresselhaus, *Trigonal warping effect of carbon nanotubes.* Physical Review B, 2000. **61**(4): p. 2981-2990.

46. Du, F.M., R.C. Scogna, W. Zhou, S. Brand, J.E. Fischer, and K.I. Winey, *Nanotube networks in polymer nanocomposites: Rheology and electrical conductivity.* Macromolecules, 2004. **37**(24): p. 9048-9055.

47. Kharchenko, S.B., J.F. Douglas, J. Obrzut, E.A. Grulke, and K.B. Migler, *Flow-induced properties of nanotube-filled polymer materials.* Nature Materials, 2004. **3**(8): p. 564-568.

48. Dresselhaus, M.S., G. Dresselhaus, A. Jorio, A.G. Souza, and R. Saito, *Raman spectroscopy on isolated single wall carbon nanotubes.* Carbon, 2002. **40**(12): p. 2043-2061.

49. Sandler, J., M.S.P. Shaffer, A.H. Windle, M.P. Halsall, M.A. Montes-Moran, C.A. Cooper, and R.J. Young, *Variations in the Raman peak shift as a function of*

hydrostatic pressure for various carbon nanostructures: A simple geometric effect. Physical Review B, 2003. **67**(3): p. 035417.

50. Venkateswaran, U.D., M.E. Gosselin, B. Postek, D.L. Masica, G. Chen, R. Gupta, and P.C. Eklund, *Radial and tangential vibrational modes of HiPCO-derived carbon nanotubes under pressure.* Physica Status Solidi B-Basic Research, 2003. **235**(2): p. 364-368.

51. Cooper, C.A., R.J. Young, and M. Halsall, *Investigation into the deformation of carbon nanotubes and their composites through the use of Raman spectroscopy.* Composites Part A-Applied Science and Manufacturing, 2001. **32**(3-4): p. 401-411.

52. Souza, A.G., A. Jorio, G.G. Samsonidze, G. Dresselhaus, R. Saito, and M.S. Dresselhaus, *Raman spectroscopy for probing chemically/physically induced phenomena in carbon nanotubes.* Nanotechnology, 2003. **14**(10): p. 1130-1139.

53. Huang, F.M., K.T. Yue, P.H. Tan, S.L. Zhang, Z.J. Shi, X.H. Zhou, and Z.N. Gu, *Temperature dependence of the Raman spectra of carbon nanotubes.* Journal of Applied Physics, 1998. **84**(7): p. 4022-4024.

54. Li, J., Y.J. Lu, Q. Ye, M. Cinke, J. Han, and M. Meyyappan, *Carbon nanotube sensors for gas and organic vapor detection.* Nano Letters, 2003. **3**(7): p. 929-933.

55. Heller, D.A., P.W. Barone, J.P. Swanson, R.M. Mayrhofer, and M.S. Strano, *Using Raman spectroscopy to elucidate the aggregation state of single-walled carbon nanotubes.* Journal of Physical Chemistry B, 2004. **108**(22): p. 6905-6909.

56. Sreekumar, T.V., T. Liu, S. Kumar, L.M. Ericson, R.H. Hauge, and R.E. Smalley, *Single-wall carbon nanotube films.* Chemistry of Materials, 2003. **15**(1): p. 175-178.

57. Coleman, J.N., W.J. Blau, A.B. Dalton, E. Munoz, S. Collins, B.G. Kim, J. Razal, M. Selvidge, G. Vieiro, and R.H. Baughman, *Improving the mechanical properties of single-walled carbon nanotube sheets by intercalation of polymeric adhesives.* Applied Physics Letters, 2003. **82**(11): p. 1682-1684.

58. Zhang, X.F., T. Liu, T.V. Sreekumar, S. Kumar, X.D. Hu, and K. Smith, *Gel spinning of PVA/SWNT composite fiber.* Polymer, 2004. **45**(26): p. 8801-8807.

59. Ericson, L.M., H. Fan, H.Q. Peng, V.A. Davis, W. Zhou, J. Sulpizio, Y.H. Wang, R. Booker, J. Vavro, C. Guthy, A.N.G. Parra-Vasquez, M.J. Kim, S. Ramesh, R.K. Saini, C. Kittrell, G. Lavin, H. Schmidt, W.W. Adams, W.E. Billups, M. Pasquali, W.F. Hwang, R.H. Hauge, J.E. Fischer, and R.E. Smalley, *Macroscopic, neat, single-walled carbon nanotube fibers.* Science, 2004. **305**(5689): p. 1447-1450.

60. Mallick, P.K., *Composites Engineering Handbook.* New York, Marcel Dekker Inc., 1997: p. 900-905.

61. Abraham, J.K., B. Philip, A. Witchurch, V.K. Varadan, and C.C. Reddy, *A compact wireless gas sensor using a carbon nanotube/PMMA thin film chemiresistor.* Smart Materials & Structures, 2004. **13**(5): p. 1045-1049.

62. Jia, Z.J., Z.Y. Wang, C.L. Xu, J. Liang, B.Q. Wei, D.H. Wu, and S.W. Zhu, *Study on poly(methyl methacrylate)/carbon nanotube composites.* Materials Science and Engineering A-Structural Materials Properties Microstructure and Processing, 1999. **271**(1-2): p. 395-400.

63. Sung, J.H., H.S. Kim, H.J. Jin, H.J. Choi, and I.J. Chin, *Nanofibrous membranes prepared by multiwalled carbon nanotube/poly(methyl methacrylate) composites.* Macromolecules, 2004. **37**(26): p. 9899-9902.

64. Du, F.M., J.E. Fischer, and K.I. Winey, *Coagulation method for preparing single-walled carbon nanotube/poly(methyl methacrylate) composites and their modulus, electrical conductivity, and thermal stability.* Journal of Polymer Science Part B-Polymer Physics, 2003. **41**(24): p. 3333-3338.

65. Sabba, Y. and E.L. Thomas, *High-concentration dispersion of single-wall carbon nanotubes (vol 37, pg 4815, 2004).* Macromolecules, 2004. **37**(17): p. 6662-6662.

66. Ramanathan, T., H. Liu, and L.C. Brinson, *Functionalized SWNT/polymer nanocomposites for dramatic property improvement.* Journal of Polymer Science Part B-Polymer Physics, 2005. **43**(17): p. 2269-2279.

67. Skakalova, V., U. Dettlaff-Weglikowska, and S. Roth, *Electrical and mechanical properties of nanocomposites of single wall carbon nanotubes with PMMA.* Synthetic Metals, 2005. **152**(1-3): p. 349-352.

68. Putz, K.W., C.A. Mitchell, R. Krishnamoorti, and P.F. Green, *Elastic modulus of single-walled carbon nanotube/poly(methyl methacrylate) nanocomposites.* Journal of Polymer Science Part B-Polymer Physics, 2004. **42**(12): p. 2286-2293.

69. de la Chapelle, M.L., C. Stephan, T.P. Nguyen, S. Lefrant, C. Journet, P. Bernier, E. Munoz, A. Benito, W.K. Maser, M.T. Martinez, G.F. de la Fuente, T. Guillard, G. Flamant, L. Alvarez, and D. Laplaze, *Raman characterization of singlewalled carbon nanotubes and PMMA-nanotubes composites.* Synthetic Metals, 1999. **103**(1-3): p. 2510-2512.

70. Zhang, M.F., M. Yudasaka, A. Koshio, and S. Iijima, *Effect of polymer and solvent on purification and cutting of single-wall carbon nanotubes.* Chemical Physics Letters, 2001. **349**(1-2): p. 25-30.

71. Jin, Z.X., K.P. Pramoda, S.H. Goh, and G.Q. Xu, *Poly(vinylidene fluoride)-assisted melt-blending of multi-walled carbon nanotube/poly(methyl methacrylate) composites.* Materials Research Bulletin, 2002. **37**(2): p. 271-278.

72. Jin, Z., K.P. Pramoda, G. Xu, and S.H. Goh, *Dynamic mechanical behavior of melt-processed multi-walled carbon nanotube/poly(methyl methacrylate) composites.* Chemical Physics Letters, 2001. **337**(1-3): p. 43-47.

73. Park, S.J., M.S. Cho, S.T. Lim, H.J. Cho, and M.S. Jhon, *Synthesis and dispersion characteristics of multi-walled carbon nanotube composites with poly(methyl methacrylate) prepared by in-situ bulk polymerization.* Macromolecular Rapid Communications, 2003. **24**(18): p. 1070-1073.

74. Hwang, G.L., Y.T. Shieh, and K.C. Hwang, *Efficient load transfer to polymer-grafted multiwalled carbon nanotubes in polymer composites.* Advanced Functional Materials, 2004. **14**(5): p. 487-491.

75. Gorga, R.E. and R.E. Cohen, *Toughness enhancements in poly(methyl methacrylate) by addition of oriented multiwall carbon nanotubes.* Journal of Polymer Science Part B-Polymer Physics, 2004. **42**(14): p. 2690-2702.

76. Grunlan, J.C., A.R. Mehrabi, M.V. Bannon, and J.L. Bahr, *Water-based single-walled-nanotube-filled polymer composite with an exceptionally low percolation threshold.* Advanced Materials, 2004. **16**(2): p. 150-153.

77. Ramasubramaniam, R., J. Chen, and H.Y. Liu, *Homogeneous carbon nanotube/polymer composites for electrical applications.* Applied Physics Letters, 2003. **83**(14): p. 2928-2930.

78. Seo, M.K. and S.J. Park, *Electrical resistivity and rheological behaviors of carbon nanotubes-filled polypropylene composites.* Chemical Physics Letters, 2004. **395**(1-3): p. 44-48.

79. Sandler, J.K.W., J.E. Kirk, I.A. Kinloch, M.S.P. Shaffer, and A.H. Windle, *Ultra-low electrical percolation threshold in carbon-nanotube-epoxy composites.* Polymer, 2003. **44**(19): p. 5893-5899.

80. Kymakis, E., I. Alexandou, and G.A.J. Amaratunga, *Single-walled carbon nanotube-polymer composites: electrical, optical and structural investigation.* Synthetic Metals, 2002. **127**(1-3): p. 59-62.

81. Kim, B., J. Lee, and I.S. Yu, *Electrical properties of single-wall carbon nanotube and epoxy composites.* Journal of Applied Physics, 2003. **94**(10): p. 6724-6728.

82. Robertson, J., *Realistic applications of CNTs.* Materials Today, 2004. **7**(10): p. 46-52.

83. Philip, B., J.K. Abraham, A. Chandrasekhar, and V.K. Varadan, *Carbon nanotube/PMMA composite thin films for gas-sensing applications.* Smart Materials & Structures, 2003. **12**(6): p. 935-939.

84. Xiong, J.W., Z. Zheng, X.M. Qin, M. Li, H.Q. Li, and X.L. Wang, *The thermal and mechanical properties of a polyurethane/multi-walled carbon nanotube composite.* Carbon, 2006. **44**(13): p. 2701-2707.

85. Li, J., L.F. Tong, Z.P. Fang, A.J. Gu, and Z.B. Xu, *Thermal degradation behavior of multi-walled carbon nanotubes/polyamide 6 composites.* Polymer Degradation and Stability, 2006. **91**(9): p. 2046-2052.

86. McNally, T., P. Potschke, P. Halley, M. Murphy, D. Martin, S.E.J. Bell, G.P. Brennan, D. Bein, P. Lemoine, and J.P. Quinn, *Polyethylene multiwalled carbon nanotube composites.* Polymer, 2005. **46**(19): p. 8222-8232.

87. Moon, S.I., F. Jin, C. Lee, S. Tsutsumi, and S.H. Hyon, *Novel carbon nanotube/poly(L-lactic acid) nanocomposites; Their modulus, thermal stability, and electrical conductivity.* Macromolecular Symposia, 2005. **224**: p. 287-295.

88. Wang, B., G.P. Sun, G. Sun, X.F. He, and J.J. Liu, *The thermal characterization and rheology behavior of PP/MWNTs nanocomposites.* Acta Polymerica Sinica, 2006(3): p. 408-413.

89. Yang, J., Y.H. Lin, J.F. Wang, M.F. Lai, J. Li, J.J. Liu, X. Tong, and H.M. Cheng, *Morphology, thermal stability, and dynamic mechanical properties of atactic polypropylene/carbon nanotube composites.* Journal of Applied Polymer Science, 2005. **98**(3): p. 1087-1091.

90. Costache, M.C., D.Y. Wang, M.J. Heidecker, E. Manias, and C.A. Wilkie, *The thermal degradation of poly(methyl methacrylate) nanocomposites with montmorillonite, layered double hydroxides and carbon nanotubes.* Polymers for Advanced Technologies, 2006. **17**(4): p. 272-280.

91. Gao, J.B., M.E. Itkis, A.P. Yu, E. Bekyarova, B. Zhao, and R.C. Haddon, *Continuous spinning of a single-walled carbon nanotube-nylon composite fiber.* Journal of the American Chemical Society, 2005. **127**(11): p. 3847-3854.

92. Xia, H.S. and M. Song, *Preparation and characterization of polyurethane-carbon nanotube composites.* Soft Matter, 2005. **1**(5): p. 386-394.

93. Choi, Y.K., K.I. Sugimoto, S.M. Song, and M. Endo, *Mechanical and thermal properties of vapor-grown carbon nanofiber and polycarbonate composite sheets.* Materials Letters, 2005. **59**(27): p. 3514-3520.

94. Xie, H.F., B.H. Liu, H. Yang, Z.L. Wang, J.Y. Shen, and R.S. Cheng, *Thermal characterization of carbon-nanofiber-reinforced tetraglycidyl-4,4 '-*

diaminodiphenylmethane/4,4 '-diaminodiphenylsulfone epoxy composites. Journal of Applied Polymer Science, 2006. **100**(1): p. 295-298.

95. Zeng, J.J., B. Saltysiak, W.S. Johnson, D.A. Schiraldi, and S. Kumar, *Processing and properties of poly(methyl methacrylate)/carbon nano fiber composites.* Composites Part B-Engineering, 2004. **35**(2): p. 173-178.

96. Yang, S.Y., J.R. Castilleja, E.V. Barrera, and K. Lozano, *Thermal analysis of an acrylonitrile-butadiene-styrene/SWNT composite.* Polymer Degradation and Stability, 2004. **83**(3): p. 383-388.

97. Xu, Y.S., G. Ray, and B. Abdel-Magid, *Thermal behavior of single-walled carbon nanotube polymer-matrix composites.* Composites Part A-Applied Science and Manufacturing, 2006. **37**(1): p. 114-121.

98. Probst, O., E.M. Moore, D.E. Resasco, and B.P. Grady, *Nucleation of polyvinyl alcohol crystallization by single-walled carbon nanotubes.* Polymer, 2004. **45**(13): p. 4437-4443.

99. Monthioux, M., B.W. Smith, B. Burteaux, A. Claye, J.E. Fischer, and D.E. Luzzi, *Sensitivity of single-wall carbon nanotubes to chemical processing: an electron microscopy investigation.* Carbon, 2001. **39**(8): p. 1251-1272.

100. Thess, A., R. Lee, P. Nikolaev, H.J. Dai, P. Petit, J. Robert, C.H. Xu, Y.H. Lee, S.G. Kim, A.G. Rinzler, D.T. Colbert, G.E. Scuseria, D. Tomanek, J.E. Fischer, and R.E. Smalley, *Crystalline ropes of metallic carbon nanotubes.* Science, 1996. **273**(5274): p. 483-487.

101. Girifalco, L.A., M. Hodak, and R.S. Lee, *Carbon nanotubes, buckyballs, ropes, and a universal graphitic potential.* Physical Review B, 2000. **62**(19): p. 13104-13110.

102. Liu, J., M.J. Casavant, M. Cox, D.A. Walters, P. Boul, W. Lu, A.J. Rimberg, K.A. Smith, D.T. Colbert, and R.E. Smalley, *Controlled deposition of individual single-walled carbon nanotubes on chemically functionalized templates.* Chemical Physics Letters, 1999. **303**(1-2): p. 125-129.

103. Ausman, K.D., R. Piner, O. Lourie, R.S. Ruoff, and M. Korobov, *Organic solvent dispersions of single-walled carbon nanotubes: Toward solutions of pristine nanotubes.* Journal of Physical Chemistry B, 2000. **104**(38): p. 8911-8915.

104. Rinzler, A.G., J. Liu, H. Dai, P. Nikolaev, C.B. Huffman, F.J. Rodriguez-Macias, P.J. Boul, A.H. Lu, D. Heymann, D.T. Colbert, R.S. Lee, J.E. Fischer, A.M. Rao, P.C. Eklund, and R.E. Smalley, *Large-scale purification of single-wall carbon nanotubes: process, product, and characterization.* Applied Physics A-Materials Science & Processing, 1998. **67**(1): p. 29-37.

105. Duesberg, G.S., J. Muster, V. Krstic, M. Burghard, and S. Roth, *Chromatographic size separation of single-wall carbon nanotubes.* Applied Physics A-Materials Science & Processing, 1998. **67**(1): p. 117-119.

106. Moore, V.C., M.S. Strano, E.H. Haroz, R.H. Hauge, R.E. Smalley, J. Schmidt, and Y. Talmon, *Individually suspended single-walled carbon nanotubes in various surfactants.* Nano Letters, 2003. **3**(10): p. 1379-1382.

107. Islam, M.F., E. Rojas, D.M. Bergey, A.T. Johnson, and A.G. Yodh, *High weight fraction surfactant solubilization of single-wall carbon nanotubes in water.* Nano Letters, 2003. **3**(2): p. 269-273.

108. Richard, C., F. Balavoine, P. Schultz, T.W. Ebbesen, and C. Mioskowski, *Supramolecular self-assembly of lipid derivatives on carbon nanotubes.* Science, 2003. **300**(5620): p. 775-778.

109. Penicaud, A., P. Poulin, A. Derre, E. Anglaret, and P. Petit, *Spontaneous dissolution of a single-wall carbon nanotube salt.* Journal of the American Chemical Society, 2005. **127**(1): p. 8-9.

110. Petit, P., C. Mathis, C. Journet, and P. Bernier, *Tuning and monitoring the electronic structure of carbon nanotubes.* Chemical Physics Letters, 1999. **305**(5-6): p. 370-374.

111. Jouguelet, E., C. Mathis, and P. Petit, *Controlling the electronic properties of single-wall carbon nanotubes by chemical doping.* Chemical Physics Letters, 2000. **318**(6): p. 561-564.

112. Zhang, M., K.R. Atkinson, and R.H. Baughman, *Multifunctional carbon nanotube yarns by downsizing an ancient technology.* Science, 2004. **306**(5700): p. 1358-1361.

113. Shaffer, M.S.P., X. Fan, and A.H. Windle, *Dispersion and packing of carbon nanotubes.* Carbon, 1998. **36**(11): p. 1603-1612.

114. Niyogi, S., M.A. Hamon, H. Hu, B. Zhao, P. Bhowmik, R. Sen, M.E. Itkis, and R.C. Haddon, *Chemistry of single-walled carbon nanotubes.* Accounts of Chemical Research, 2002. **35**(12): p. 1105-1113.

115. Zhou, O., R.M. Fleming, D.W. Murphy, C.H. Chen, R.C. Haddon, A.P. Ramirez, and S.H. Glarum, *Defects in carbon nanostructures.* Science, 1994. **263**(5154): p. 1744-1747.

116. Bahr, J.L. and J.M. Tour, *Highly functionalized carbon nanotubes using in situ generated diazonium compounds.* Chemistry of Materials, 2001. **13**(11): p. 3823-3824.

117. Holzinger, M., O. Vostrowsky, A. Hirsch, F. Hennrich, M. Kappes, R. Weiss, and F. Jellen, *Sidewall functionalization of carbon nanotubes.* Angewandte Chemie-International Edition, 2001. **40**(21): p. 4002-4005.

118. Mickelson, E.T., C.B. Huffman, A.G. Rinzler, R.E. Smalley, R.H. Hauge, and J.L. Margrave, *Fluorination of single-wall carbon nanotubes.* Chemical Physics Letters, 1998. **296**(1-2): p. 188-194.

119. Boul, P.J., J. Liu, E.T. Mickelson, C.B. Huffman, L.M. Ericson, I.W. Chiang, K.A. Smith, D.T. Colbert, R.H. Hauge, J.L. Margrave, and R.E. Smalley, *Reversible sidewall functionalization of buckytubes.* Chemical Physics Letters, 1999. **310**(3-4): p. 367-372.

120. Huang, J.E., X.H. Li, J.C. Xu, and H.L. Li, *Well-dispersed single-walled carbon nanotube/polyaniline composite films.* Carbon, 2003. **41**(14): p. 2731-2736.

121. Park, C., Z. Ounaies, K.A. Watson, R.E. Crooks, J. Smith, S.E. Lowther, J.W. Connell, E.J. Siochi, J.S. Harrison, and T.L.S. Clair, *Dispersion of single wall carbon nanotubes by in situ polymerization under sonication.* Chemical Physics Letters, 2002. **364**(3-4): p. 303-308.

122. Baek, J.B., C.B. Lyons, and L.S. Tan, *Grafting of vapor-grown carbon nanofibers via in-situ polycondensation of 3-phenoxybenzoic acid in poly(phosphoric acid).* Macromolecules, 2004. **37**(22): p. 8278-8285.

123. Jin, Z.X., L. Huang, S.H. Goh, G.Q. Xu, and W. Ji, *Characterization and nonlinear optical properties of a poly(acrylic acid)-surfactant-multi-walled carbon nanotube complex.* Chemical Physics Letters, 2000. **332**(5-6): p. 461-466.

124. Philip, B., J.I. Xie, J.K. Abraham, and V.K. Varadan, *A new synthetic route to enhance polyaniline assembly on carbon nanotubes in tubular composites.* Smart Materials & Structures, 2004. **13**(6): p. N105-N108.

125. Lin, Y., A.M. Rao, B. Sadanadan, E.A. Kenik, and Y.P. Sun, *Functionalizing multiple-walled carbon nanotubes with aminopolymers.* Journal of Physical Chemistry B, 2002. **106**(6): p. 1294-1298.

126. Hill, D.E., Y. Lin, A.M. Rao, L.F. Allard, and Y.P. Sun, *Functionalization of carbon nanotubes with polystyrene.* Macromolecules, 2002. **35**(25): p. 9466-9471.

127. Riggs, J.E., Z.X. Guo, D.L. Carroll, and Y.P. Sun, *Strong luminescence of solubilized carbon nanotubes.* Journal of the American Chemical Society, 2000. **122**(24): p. 5879-5880.

128. Tamura, K., N. Takashi, T. Akasaka, I.D. Roska, M. Uo, Y. Totsuka, and F. Watari, *Bioceramics 16 Key Engineering Materials*. 2004, TRANS TECH PUBLICATIONS LTD: BRANDRAIN 6, CH-8707 ZURICH-UETIKON, SWITZERLAND. p. 919-922.

129. Gartstein, Y.N., A.A. Zakhidov, and R.H. Baughman, *Mechanical and electromechanical coupling in carbon nanotube distortions.* Physical Review B, 2003. **68**(11).

130. Viswanathan, G., D.B. Kane, and P.J. Lipowicz, *High efficiency fine particulate filtration using carbon nanotube coatings.* Advanced Materials, 2004. **16**(22): p. 2045-2049.

131. Park, J.H., J.H. Choi, J.S. Moon, D.G. Kushinov, J.B. Yoo, C.Y. Park, J.W. Nam, C.K. Lee, J.H. Park, and D.H. Choe, *Simple approach for the fabrication of carbon nanotube field emitter using conducting paste.* Carbon, 2005. **43**(4): p. 698-703.

132. Kymakis, E. and G.A.J. Amaratunga, *Optical properties of polymer-nanotube composites.* Synthetic Metals, 2004. **142**(1-3): p. 161-167.

133. Zhou, C.F., T. Liu, T. Wang, and S. Kumar, *SWNT/PAN/SAN ternary composite film: A novel approach for high performance electrochemical supercapacitor.* Abstracts of Papers of the American Chemical Society, 2005. **229**: p. U1105-U1106.

134. Zhou, C.F., S. Kumar, C.D. Doyle, and J.M. Tour, *Functionalized single wall carbon nanotubes treated with pyrrole for electrochemical supercapacitor membranes.* Chemistry of Materials, 2005. **17**(8): p. 1997-2002.

135. Dzenis, Y., *Spinning continuous fibers for nanotechnology.* Science, 2004. **304**(5679): p. 1917-1919.

136. Li, D. and Y.N. Xia, *Electrospinning of nanofibers: Reinventing the wheel?* Advanced Materials, 2004. **16**(14): p. 1151-1170.

137. Yu, J.H., S.V. Fridrikh, and G.C. Rutledge, *Production of submicrometer diameter fibers by two-fluid electrospinning.* Advanced Materials, 2004. **16**(17): p. 1562-1566.

138. Jaeger, R., M.M. Bergshoef, C.M.I. Batlle, H. Schonherr, and G.J. Vancso, *Electrospinning of ultra-thin polymer fibers.* Macromolecular Symposia, 1998. **127**: p. 141-150.

139. Bailey, A.G., *Electrostatic Spraying of Liquids.* New York, Wiley, 1988.

140. Loscertales, I.G., A. Barrero, I. Guerrero, R. Cortijo, M. Marquez, and A.M. Ganan-Calvo, *Micro/nano encapsutation via electrified coaxial liquid jets.* Science, 2002. **295**(5560): p. 1695-1698.

141. Hull, P.J., J.L. Hutchison, O.V. Salata, and P.J. Dobson, *Synthesis of nanometer-scale silver crystallites via a room-temperature electrostatic spraying process.* Advanced Materials, 1997. **9**(5): p. 413-&.

142. Fenn, J.B., M. Mann, C.K. Meng, S.F. Wong, and C.M. Whitehouse, *Electrospray ionization for mass-spectrometry of large biomolecules.* Science, 1989. **246**(4926): p. 64-71.

143. Mathew, G., J.P. Hong, J.M. Rhee, H.S. Lee, and C. Nah, *Preparation and characterization of properties of electrospun poly(butylene terephthalate) nanofibers filled with carbon nanotubes.* Polymer Testing, 2005. **24**(6): p. 712-717.

144. Lyons, J., F.K. Ko, and C. Pastore, *Developments in melt-electrospinning of thermoplastic polymers.* Abstracts of Papers of the American Chemical Society, 2003. **226**: p. U400-U401.

145. Lyons, J., C. Li, and F. Ko, *Melt-electrospinning part I: processing parameters and geometric properties.* Polymer, 2004. **45**(22): p. 7597-7603.

146. Formhals, A., *United States Patent 4230650.* 1934. **1**(975): p. 504.

147. Katta, P., M. Alessandro, R.D. Ramsier, and G.G. Chase, *Continuous electrospinning of aligned polymer nanofibers onto a wire drum collector.* Nano Letters, 2004. **4**(11): p. 2215-2218.

148. Li, D., G. Ouyang, J.T. McCann, and Y.N. Xia, *Collecting electrospun nanofibers with patterned electrodes.* Nano Letters, 2005. **5**(5): p. 913-916.

149. Li, D., Y.L. Wang, and Y.N. Xia, *Electrospinning nanofibers as uniaxially aligned arrays and layer-by-layer stacked films.* Advanced Materials, 2004. **16**(4): p. 361-366.

150. Hao, X.F., Z.Y. Li, D.M. Li, and C. Wang, *Preparation of Cu(core)/PVA(shell) nanoparticles from electrospinning to electrospray ionization.* Chemical Journal of Chinese Universities-Chinese, 2005. **26**(2): p. 385-387.

151. McCann, J.T., D. Li, and Y.N. Xia, *Electrospinning of nanofibers with core-sheath, hollow, or porous structures.* Journal of Materials Chemistry, 2005. **15**(7): p. 735-738.

152. Sun, Z.C., E. Zussman, A.L. Yarin, J.H. Wendorff, and A. Greiner, *Compound core-shell polymer nanofibers by co-electrospinning.* Advanced Materials, 2003. **15**(22): p. 1929-1932.

153. Kim, G.M., G.H. Michler, and P. Potschke, *Deformation processes of ultrahigh porous multiwalled carbon nanotubes/polycarbonate composite fibers prepared by electrospinning.* Polymer, 2005. **46**(18): p. 7346-7351.

154. Li, D. and Y.N. Xia, *Direct fabrication of composite and ceramic hollow nanofibers by electrospinning.* Nano Letters, 2004. **4**(5): p. 933-938.

155. Yu, N., C.L. Shao, Y.C. Liu, H.Y. Guan, and X.H. Yang, *Nanofibers of LiMn2O4 by electrospinning.* Journal of Colloid and Interface Science, 2005. **285**(1): p. 163-166.

156. Li, D., T. Herricks, and Y.N. Xia, *Magnetic nanofibers of nickel ferrite prepared by electrospinning.* Applied Physics Letters, 2003. **83**(22): p. 4586-4588.

157. Kedem, S., J. Schmidt, Y. Paz, and Y. Cohen, *Composite polymer nanofibers with carbon nanotubes and titanium dioxide particles.* Langmuir, 2005. **21**(12): p. 5600-5604.

158. Li, D. and Y.N. Xia, *Fabrication of ceramic and composite nanofibers by electrospinning.* Abstracts of Papers of the American Chemical Society, 2003. **226**: p. U425-U425.

159. Kim, B., H. Park, S.H. Lee, and W.M. Sigmund, *Poly(acrylic acid) nanofibers by electrospinning.* Materials Letters, 2005. **59**(7): p. 829-832.

160. Shao, C.L., H.Y. Kim, J. Gong, B. Ding, D.R. Lee, and S.J. Park, *Fiber mats of poly(vinyl alcohol)/silica composite via electrospinning.* Materials Letters, 2003. **57**(9-10): p. 1579-1584.

161. Fong, H., W.D. Liu, C.S. Wang, and R.A. Vaia, *Generation of electrospun fibers of nylon 6 and nylon 6-montmorillonite nanocomposite.* Polymer, 2002. **43**(3): p. 775-780.

162. Fong, H., I. Chun, and D.H. Reneker, *Beaded nanofibers formed during electrospinning.* Polymer, 1999. **40**(16): p. 4585-4592.

163. Li, L. and Y.L. Hsieh, *Ultra-fine polyelectrolyte fibers from electrospinning of poly(acrylic acid).* Polymer, 2005. **46**(14): p. 5133-5139.

164. Mit-uppatham, C., M. Nithitanakul, and P. Supaphol, *Ultrafine electrospun polyamide-6 fibers: Effect of solution conditions on morphology and average fiber diameter.* Macromolecular Chemistry and Physics, 2004. **205**(17): p. 2327-2338.

165. http://vienna.che.uic.edu/RET/Reports/Final%20Reports/ZufanRETFinalReport.pdf, *Electrospinning setup.*

166. Taylor, G.I., *Disintegration of water droplets in an electric field.* Proc. R. Soc. London, 1964. **A 280**: p. 383–397.

167. http://en.wikipedia.org/wiki/Taylor_cone, *Taylor cone.*

168. Yarin, A.L., S. Koombhongse, and D.H. Reneker, *Taylor cone and jetting from liquid droplets in electrospinning of nanofibers.* Journal of Applied Physics, 2001. **90**(9): p. 4836-4846.

169. Yarin, A.L., W. Kataphinan, and D.H. Reneker, *Branching in electrospinning of nanofibers.* Journal of Applied Physics, 2005. **98**(6): p. 064501.

170. Fridrikh, S.V., J.H. Yu, M.P. Brenner, and G.C. Rutledge, *Controlling the fiber diameter during electrospinning.* Physical Review Letters, 2003. **90**(14).

171. Shin, Y.M., M.M. Hohman, M.P. Brenner, and G.C. Rutledge, *Experimental characterization of electrospinning: the electrically forced jet and instabilities.* Polymer, 2001. **42**(25): p. 9955-9967.

172. Hohman, M.M., M. Shin, G. Rutledge, and M.P. Brenner, *Electrospinning and electrically forced jets. I. Stability theory.* Physics of Fluids, 2001. **13**(8): p. 2201-2220.

173. Hohman, M.M., M. Shin, G. Rutledge, and M.P. Brenner, *Electrospinning and electrically forced jets. II. Applications.* Physics of Fluids, 2001. **13**(8): p. 2221-2236.

174. Feng, J.J., *Stretching of a straight electrically charged viscoelastic jet.* Journal of non-Newtonian Fluid Mechanics, 2003. **116**(1): p. 55-70.

175. Feng, J.J., *The stretching of an electrified non-Newtonian jet: A model for electrospinning.* Physics of Fluids, 2002. **14**(11): p. 3912-3926.

176. Tan, S.H., R. Inai, M. Kotaki, and S. Ramakrishna, *Systematic parameter study for ultra-fine fiber fabrication via electrospinning process.* Polymer, 2005. **46**(16): p. 6128-6134.

177. Theron, S.A., E. Zussman, and A.L. Yarin, *Experimental investigation of the governing parameters in the electrospinning of polymer solutions.* Polymer, 2004. **45**(6): p. 2017-2030.

178. Lee, K.H., H.Y. Kim, Y.M. La, D.R. Lee, and N.H. Sung, *Influence of a mixing solvent with tetrahydrofuran and N,N-dimethylformamide on electrospun poly(vinyl chloride) nonwoven mats.* Journal of Polymer Science Part B-Polymer Physics, 2002. **40**(19): p. 2259-2268.

179. Krishnappa, R.V.N., K. Desai, and C.M. Sung, *Morphological study of electrospun polycarbonates as a function of the solvent and processing voltage.* Journal of Materials Science, 2003. **38**(11): p. 2357-2365.

180. Wannatong, L., A. Sirivat, and P. Supaphol, *Effects of solvents on electrospun polymeric fibers: preliminary study on polystyrene.* Polymer International, 2004. **53**(11): p. 1851-1859.

181. Wu, X.H., L.G. Wang, H. Yu, and Y. Huang, *Effect of solvent on morphology of electrospinning ethyl cellulose fibers.* Journal of Applied Polymer Science, 2005. **97**(3): p. 1292-1297.

182. Lin, T., H.X. Wang, H.M. Wang, and X.G. Wang, *Effects of polymer concentration and cationic surfactant on the morphology of electrospun polyacrylonitrile nanofibres.* Journal of Materials Science & Technology, 2005. **21**: p. 9-12.

183. Kim, G., J. Park, and H. Han, *Production of microsized PMMA droplets using electrospraying with various auxiliary fields.* Journal of Colloid and Interface Science, 2006. **299**(2): p. 593-598.

184. Rietveld, I.B., K. Kobayashi, H. Yamada, and K. Matsushige, *Morphology control of poly(vinylidene fluoride) thin film made with electrospray.* Journal of Colloid and Interface Science, 2006. **298**(2): p. 639-651.

185. Deotare, P.B. and J. Kameoka, *Fabrication of silica nanocomposite-cups using electrospraying.* Nanotechnology, 2006. **17**(5): p. 1380-1383.

186. Qin, X.H., Y.Q. Wan, J.H. He, J. Zhang, J.Y. Yu, and S.Y. Wang, *Effect of LiCl on electrospinning of PAN polymer solution: theoretical analysis and experimental verification.* Polymer, 2004. **45**(18): p. 6409-6413.

187. Lin, T., H.X. Wang, H.M. Wang, and X.G. Wang, *The charge effect of cationic surfactants on the elimination of fibre beads in the electrospinning of polystyrene.* Nanotechnology, 2004. **15**(9): p. 1375-1381.

188. Li, X., C. Yao, F. Sun, and T. Song, *Conjugate electrospinning: continuous yarns from oppositely charged nanofibers.* ACS preprints: Polymeric Materials: Science & Engineering Division, 2006. **94**: p. 26.

189. Li, X.S. and G.Y. Nie, *Nano-porous ultra-high specific surface ultrafine fibers.* Chinese Science Bulletin, 2004. **49**(22): p. 2368-2371.

190. Kim, C.H., Y.H. Jung, H.Y. Kim, D.R. Lee, N. Dharmaraj, and K.E. Choi, *Effect of collector temperature on the porous structure of electrospun fibers.* Macromolecular Research, 2006. **14**(1): p. 59-65.

191. Han, S.O., W.K. Son, J.H. Youk, T.S. Lee, and W.H. Park, *Ultrafine porous fibers electrospun from cellulose triacetate.* Materials Letters, 2005. **59**(24-25): p. 2998-3001.

192. McCann, J.T., M. Marquez, and Y.N. Xia, *Highly porous fibers by electrospinning into a cryogenic liquid.* Journal of the American Chemical Society, 2006. **128**(5): p. 1436-1437.

193. Ge, J.J., H.Q. Hou, Q. Li, M.J. Graham, A. Greiner, D.H. Reneker, F.W. Harris, and S.Z.D. Cheng, *Assembly of well-aligned multiwalled carbon nanotubes in confined polyacrylonitrile environments: Electrospun composite nanofiber sheets.* Journal of the American Chemical Society, 2004. **126**(48): p. 15754-15761.

194. Hou, H.Q., J.J. Ge, J. Zeng, Q. Li, D.H. Reneker, A. Greiner, and S.Z.D. Cheng, *Electrospun polyacrylonitrile nanofibers containing a high concentration of well-aligned multiwall carbon nanotubes.* Chemistry of Materials, 2005. **17**(5): p. 967-973.

195. Sundaray, B., V. Subramanian, T.S. Natarajan, and K. Krishnamurthy, *Electrical conductivity of a single electrospun fiber of poly(methyl methacrylate) and multiwalled carbon nanotube nanocomposite.* Applied Physics Letters, 2006. **88**(14).

196. Salalha, W., Y. Dror, R.L. Khalfin, Y. Cohen, A.L. Yarin, and E. Zussman, *Single-walled carbon nanotubes embedded in oriented polymeric nanofibers by electrospinning.* Langmuir, 2004. **20**(22): p. 9852-9855.

197. Zong, X.H., H. Bien, C.Y. Chung, L.H. Yin, D.F. Fang, B.S. Hsiao, B. Chu, and E. Entcheva, *Electrospun fine-textured scaffolds for heart tissue constructs.* Biomaterials, 2005. **26**(26): p. 5330-5338.

198. Kim, C., K.S. Yang, and W.J. Lee, *The use of carbon nanofiber electrodes prepared by electrospinning for electrochemical supercapacitors.* Electrochemical and Solid State Letters, 2004. **7**(11): p. A397-A399.

199. Luu, Y.K., K. Kim, B.S. Hsiao, B. Chu, and M. Hadjiargyrou, *Development of a nanostructured DNA delivery scaffold via electrospinning of PLGA and PLA-PEG block copolymers.* Journal of Controlled Release, 2003. **89**(2): p. 341-353.

200. Nair, L.S., S. Bhattacharyya, and C.T. Laurencin, *Development of novel tissue engineering scaffolds via electrospinning.* Expert Opinion on Biological Therapy, 2004. **4**(5): p. 659-668.

201. Venugopal, J. and S. Ramakrishna, *Applications of polymer nanofibers in biomedicine and biotechnology.* Applied Biochemistry and Biotechnology, 2005. **125**(3): p. 147-157.

202. Ra, E.J., K.H. An, K.K. Kim, S.Y. Jeong, and Y.H. Lee, *Anisotropic electrical conductivity of MWCNT/PAN nanofiber paper.* Chemical Physics Letters, 2005. **413**(1-3): p. 188-193.

203. Sen, R., B. Zhao, D. Perea, M.E. Itkis, H. Hu, J. Love, E. Bekyarova, and R.C. Haddon, *Preparation of single-walled carbon nanotube reinforced polystyrene and polyurethane nanofibers and membranes by electrospinning.* Nano Letters, 2004. **4**(3): p. 459-464.

204. Wang, T., C.F. Zhou, and S. Kumar, *Electrospun poly (acrylonitrile)/poly(acrylonitrile-co-styrene)/carbon nanotube fiber mat for electrochemical supercapacitors.* Abstracts of Papers of the American Chemical Society, 2005. **229**: p. U1105-U1105.

205. Zhu, Y., J.C. Zhang, Y.M. Zheng, Z.B. Huang, L. Feng, and L. Jiang, *Stable, superhydrophobic, and conductive polyaniline/polystyrene films for corrosive enviromnents.* Advanced Functional Materials, 2006. **16**(4): p. 568-574.

206. Acatay, K., E. Simsek, C. Ow-Yang, and Y.Z. Menceloglu, *Generation of superhydrophobic surfaces by electrospinning process.* Abstracts of Papers of the American Chemical Society, 2005. **229**: p. U980-U980.

207. Smallwood, I.M., *Handbook of organic solvent properties.* London, Arnold, New York, Halsted, 1996.

208. Hummer, G., J.C. Rasaiah, and J.P. Noworyta, *Water conduction through the hydrophobic channel of a carbon nanotube.* Nature, 2001. **414**(6860): p. 188-190.

209. Ci, L.J., Z.P. Zhou, L. Song, X.Q. Yan, D.F. Liu, H.J. Yuan, Y. Gao, J.X. Wang, L.F. Liu, W.Y. Zhou, G. Wang, and S.S. Xie, *Temperature dependence of resonant Raman scattering in double-wall carbon nanotubes.* Applied Physics Letters, 2003. **82**(18): p. 3098-3100.

210. Li, H.D., K.T. Yue, Z.L. Lian, Y. Zhan, L.X. Zhou, S.L. Zhang, Z.J. Shi, Z.N. Gu, B.B. Liu, R.S. Yang, H.B. Yang, G.T. Zou, Y. Zhang, and S. Iijima, *Temperature dependence of the Raman spectra of single-wall carbon nanotubes.* Applied Physics Letters, 2000. **76**(15): p. 2053-2055.

211. Li, Z.L., P. Dharap, S. Nagarajaiah, E.V. Barrera, and J.D. Kim, *Carbon nanotube film sensors.* Advanced Materials, 2004. **16**(7): p. 640-643.

212. Bachilo, S.M., M.S. Strano, C. Kittrell, R.H. Hauge, R.E. Smalley, and R.B. Weisman, *Structure-assigned optical spectra of single-walled carbon nanotubes.* Science, 2002. **298**(5602): p. 2361-2366.

213. Dresselhaus, M.S. and P.C. Eklund, *Phonons in carbon nanotubes.* Advances in Physics, 2000. **49**(6): p. 705-814.

214. Kataura, H., Y. Kumazawa, Y. Maniwa, I. Umezu, S. Suzuki, Y. Ohtsuka, and Y. Achiba, *Optical properties of single-wall carbon nanotubes.* Synthetic Metals, 1999. **103**(1-3): p. 2555-2558.

215. Lucas, M. and R.J. Young, *Effect of uniaxial strain deformation upon the Raman radial breathing modes of single-wall carbon nanotubes in composites.* Physical Review B, 2004. **69**(8).

216. Zhang, X.F., T. Liu, T.V. Sreekumar, S. Kumar, V.C. Moore, R.H. Hauge, and R.E. Smalley, *Poly(vinyl alcohol)/SWNT composite film.* Nano Letters, 2003. **3**(9): p. 1285-1288.

217. Li, K., X.L. Gao, and A.K. Roy, *Micromechanical modeling of viscoelastic properties of carbon nanotube-reinforced polymer composites.* Mechanics of Advanced Materials and Structures, 2006. **13**(4): p. 317-328.

218. Pryamitsyn, V. and V. Ganesan, *Origins of linear viscoelastic behavior of polymer-nanoparticle composites.* Macromolecules, 2006. **39**(2): p. 844-856.

219. Stejskal, J., D. Hlavata, P. Holler, M. Trchova, J. Prokes, and I. Sapurina, *Polyaniline prepared in the presence of various acids: a conductivity study.* Polymer International, 2004. **53**(3): p. 294-300.

220. Rasheed, A., *SWNT buckypaper, unpublished results.* 2006.

221. Chae, H.G., M.L. Minus, and S. Kumar, *Oriented and exfoliated single wall carbon nanotubes in polyacrylonitrile.* Polymer, 2006. **47**(10): p. 3494-3504.

222. Fornes, T.D., J.W. Baur, Y. Sabba, and E.L. Thomas, *Morphology and properties of melt-spun polycarbonate fibers containing single- and multi-wall carbon nanotubes.* Polymer, 2006. **47**(5): p. 1704-1714.

223. Brandrup, J., E.H. Immergut, E.A. Grulke, A. Abe, and D.R. Bloch, *Polymer handbook.* New York Chichester Weinheim Brisbane Singapore Toronto, JOHN WlLEY & SONS, INC., 1999.

224. Shekhar, S., V. Prasad, and S. Subramanyam, *Structural and electrical properties of composites of polymer-iron carbide nanoparticles embedded in carbon.* Materials Science and Engineering B-Solid State Materials for Advanced Technology, 2006. **133**(1-3): p. 108-112.

225. Cadek, M., J.N. Coleman, V. Barron, K. Hedicke, and W.J. Blau, *Morphological and mechanical properties of carbon-nanotube-reinforced semicrystalline and amorphous polymer composites.* Applied Physics Letters, 2002. **81**(27): p. 5123-5125.

226. Chang, T.E., L.R. Jensen, A. Kisliuk, R.B. Pipes, R. Pyrz, and A.P. Sokolov, *Microscopic mechanism of reinforcement in single-wall carbon nanotube/polypropylene nanocomposite.* Polymer, 2005. **46**(2): p. 439-444.

227. Cadek, M., J.N. Coleman, K.P. Ryan, V. Nicolosi, G. Bister, A. Fonseca, J.B. Nagy, K. Szostak, F. Beguin, and W.J. Blau, *Reinforcement of polymers with carbon nanotubes: The role of nanotube surface area.* Nano Letters, 2004. **4**(2): p. 353-356.

228. Wu, G. and J.M. Dong, *Raman characteristic peaks induced by the topological defects of carbon nanotube intramolecular junctions.* Physical Review B, 2006. **73**(24).

229. Rasheed, A., H.G. Chae, S. Kumar, and M.D. Dadmun, *Polymer nanotube nanocomposites: Correlating intermolecular interaction to ultimate properties.* Polymer, 2006. **47**(13): p. 4734-4741.

230. Wang, T., *Ph.D thesis.* Georgia Institute of Technology, Atlanta, GA, May 2007.

231. http://www.newton.dep.anl.gov/askasci/chem00/chem00964.htm, *Evaporation rate dependence on concentration.*

232. Van Krevelen, D.W., *Properties of polymers.* Elsevier Science, Oxford, New York, 1990: p. 212-213.

233. Utracki, L.A. and R. Simha, *Statistical thermodynamics predictions of the solubility parameter.* Polymer International, 2004. **53**(3): p. 279-286.

234. Choi, P., *A re-examination of the concept of Hildebrand solubility parameter for polymers.* Macromolecular Rapid Communications, 2002. **23**(8): p. 484-487.

235. Viswanathan, S. and M.D. Dadmun, *Optimizing hydrogen-bonding in creating miscible liquid crystalline polymer blends by structural modification of the blend components.* Macromolecules, 2003. **36**(9): p. 3196-3205.

236. Dayal, P. and T. Kyu, *Porous fiber formation in polymer-solvent system undergoing solvent evaporation.* Journal of Applied Physics, 2006. **100**(4).

237. Colby, R.H., L.J. Fetters, W.G. Funk, and W.W. Graessley, *Effects of concentration and thermodynamic interaction on the viscoelastic properties of polymer-solutions.* Macromolecules, 1991. **24**(13): p. 3873-3882.

238. Krause, W.E., E.G. Bellomo, and R.H. Colby, *Rheology of sodium hyaluronate under physiological conditions.* Biomacromolecules, 2001. **2**(1): p. 65-69.

239. Graessley, W.W., *Polymer-chain dimensions and the dependence of viscoelastic properties on concentration, molecular-weight and solvent power.* Polymer, 1980. **21**(3): p. 258-262.

240. Gupta, P., C. Elkins, T.E. Long, and G.L. Wilkes, *Electrospinning of linear homopolymers of poly(methyl methacrylate): exploring relationships between fiber formation, viscosity, molecular weight and concentration in a good solvent.* Polymer, 2005. **46**(13): p. 4799-4810.

241. Lovell, R. and A.H. Windle, *Determination Of The Local Conformation Of Pmma From Wide-Angle X-Ray-Scattering.* Polymer, 1981. **22**(2): p. 175-184.

242. Yoon, D.Y. and P.J. Flory, *Small-Angle Neutron And X-Ray-Scattering By Poly(Methyl Methacrylate) Chains.2.* Macromolecules, 1976. **9**(2): p. 299-303.

243. De Gennes, P.G., *Scaling Concepts in Polymer Physics.* Ithaca, NY, Cornell University Press, 1979.

244. McKee, M.G., C.L. Elkins, and T.E. Long, *Influence of self-complementary hydrogen bonding on solution rheology/electrospinning relationships.* Polymer, 2004. **45**(26): p. 8705-8715.

245. Demir, M.M., I. Yilgor, E. Yilgor, and B. Erman, *Electrospinning of polyurethane fibers.* Polymer, 2002. **43**(11): p. 3303-3309.

246. Wnek, G.E., M.E. Carr, D.G. Simpson, and G.L. Bowlin, *Electrospinning of nanofiber fibrinogen structures.* Nano Letters, 2003. **3**(2): p. 213-216.

247. Deitzel, J.M., J. Kleinmeyer, D. Harris, and N.C.B. Tan, *The effect of processing variables on the morphology of electrospun nanofibers and textiles.* Polymer, 2001. **42**(1): p. 261-272.

248. Dong, H., V. Nyame, A.G. Macdiarmid, and W.E. Jones, *Polyaniline/poly(methyl methacrylate) coaxial fibers: The fabrication and effects of the solution properties on the morphology of electrospun core fibers.* Journal of Polymer Science Part B-Polymer Physics, 2004. **42**(21): p. 3934-3942.

249. Yang, Q.B., Z.Y. Li, Y.L. Hong, Y.Y. Zhao, S.L. Qiu, C. Wang, and Y. Wei, *Influence of solvents on the formation of ultrathin uniform poly(vinyl pyrrolidone) nanofibers with electrospinning.* Journal of Polymer Science Part B-Polymer Physics, 2004. **42**(20): p. 3721-3726.

250. Bognitzki, M., W. Czado, T. Frese, A. Schaper, M. Hellwig, M. Steinhart, A. Greiner, and J.H. Wendorff, *Nanostructured fibers via electrospinning.* Advanced Materials, 2001. **13**(1): p. 70-72.

251. Megelski, S., J.S. Stephens, D.B. Chase, and J.F. Rabolt, *Micro- and nanostructured surface morphology on electrospun polymer fibers.* Macromolecules, 2002. **35**(22): p. 8456-8466.

252. Huang, C.B., S.L. Chen, C.L. Lai, D.H. Reneker, H. Qiu, Y. Ye, and H.Q. Hou, *Electrospun polymer nanofibres with small diameters.* Nanotechnology, 2006. **17**(6): p. 1558-1563.

253. Wang, H., Y.P. Zhang, H.L. Shao, and X.C. Hu, *Electrospun ultra-fine silk fibroin fibers from aqueous solutions.* Journal of Materials Science, 2005. **40**(20): p. 5359-5363.

254. Zhang, C.X., X.Y. Yuan, L.L. Wu, Y. Han, and J. Sheng, *Study on morphology of electrospun poly(vinyl alcohol) mats.* European Polymer Journal, 2005. **41**(3): p. 423-432.

255. Choi, S.S., B. Chu, S.G. Lee, S.W. Lee, S.S. Im, S.H. Kim, and J.K. Park, *Titania-doped silica fibers prepared by electrospinning and sol-gel process.* Journal of Sol-Gel Science and Technology, 2004. **30**(3): p. 215-221.

256. Koombhongse, S., W.X. Liu, and D.H. Reneker, *Flat polymer ribbons and other shapes by electrospinning.* Journal of Polymer Science Part B-Polymer Physics, 2001. **39**(21): p. 2598-2606.

257. McCann, J.T., J.I.L. Chen, D. Li, Z.G. Ye, and Y.A. Xia, *Electrospinning of polycrystalline barium titanate nanofibers with controllable morphology and alignment.* Chemical Physics Letters, 2006. **424**(1-3): p. 162-166.

258. Srinivasarao, M., D. Collings, A. Philips, and S. Patel, *Three-dimensionally ordered array of air bubbles in a polymer film.* Science, 2001. **292**(5514): p. 79-83.

259. Casper, C.L., J.S. Stephens, N.G. Tassi, D.B. Chase, and J.F. Rabolt, *Controlling surface morphology of electrospun polystyrene fibers: Effect of humidity and molecular weight in the electrospinning process.* Macromolecules, 2004. **37**(2): p. 573-578.

260. Vandewitte, P., H. Esselbrugge, P.J. Dijkstra, J.W.A. VandenBerg, and J. Feijen, *Phase transitions during membrane formation of polylactides.1. A morphological study of membranes obtained from the system polylactide-chloroform-methanol.* Journal of Membrane Science, 1996. **113**(2): p. 223-236.

261. Liu, T. and S. Kumar, *Effect of orientation on the modulus of SWNT films and fibers.* Nano Letters, 2003. **3**(5): p. 647-650.

262. Hafner, J.H., C.L. Cheung, A.T. Woolley, and C.M. Lieber, *Structural and functional imaging with carbon nanotube AFM probes.* Progress in Biophysics & Molecular Biology, 2001. **77**(1): p. 73-110.

263. Wade, L.A., I.R. Shapiro, Z.Y. Ma, S.R. Quake, and C.P. Collier, *Correlating AFM probe morphology to image resolution for single-wall carbon nanotube tips.* Nano Letters, 2004. **4**(4): p. 725-731.

264. Dai, H.J., J.H. Hafner, A.G. Rinzler, D.T. Colbert, and R.E. Smalley, *Nanotubes as nanoprobes in scanning probe microscopy.* Nature, 1996. **384**(6605): p. 147-150.

265. Esplandiu, M.J., V.G. Bittner, K.P. Giapis, and C.P. Collier, *Nanoelectrode scanning probes from fluorocarbon-coated single-walled carbon nanotubes.* Nano Letters, 2004. **4**(10): p. 1873-1879.

266. Shapiro, I.R., S.D. Solares, M.J. Esplandiu, L.A. Wade, W.A. Goddard, and C.P. Collier, *Influence of elastic deformation on single-wall carbon nanotube atomic force microscopy probe resolution.* Journal of Physical Chemistry B, 2004. **108**(36): p. 13613-13618.

267. Seoul, C., Y.T. Kim, and C.K. Baek, *Electrospinning of poly(vinylidene fluoride)/dimethylformamide solutions with carbon nanotubes.* Journal of Polymer Science Part B-Polymer Physics, 2003. **41**(13): p. 1572-1577.

268. Dharap, P., Z.L. Li, S. Nagarajaiah, and E.V. Barrera, *Nanotube film based on single-wall carbon nanotubes for strain sensing.* Nanotechnology, 2004. **15**(3): p. 379-382.

269. Liu, J., T. Liu, and S. Kumar, *Effect of solvent solubility parameter on SWNT dispersion in PMMA.* Polymer, 2005. **46**: p. 3419-3424.